台灣顯微鏡學會

第三十四屆學術研討會

第十一屆海峽兩岸電子顯微鏡學術研討會

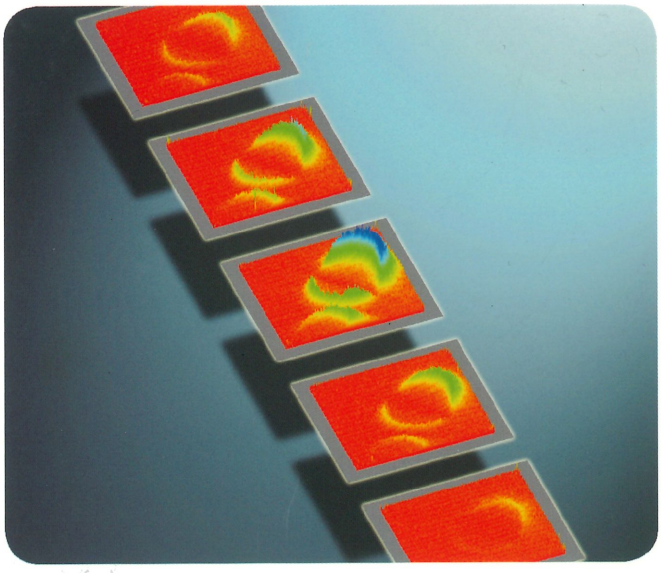

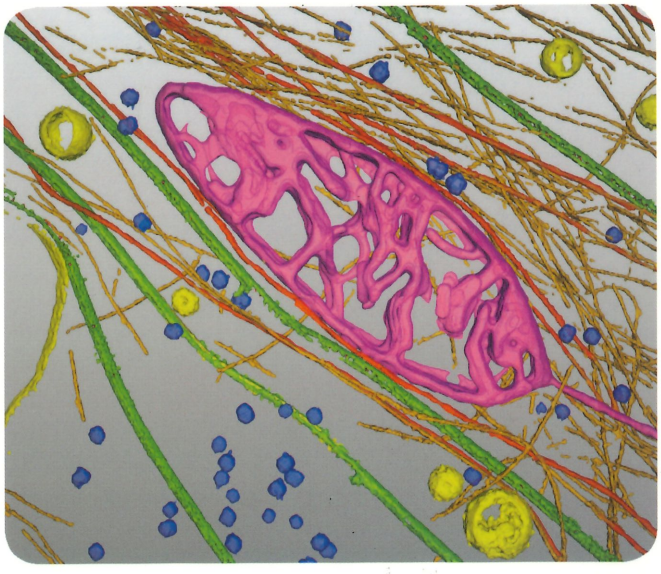

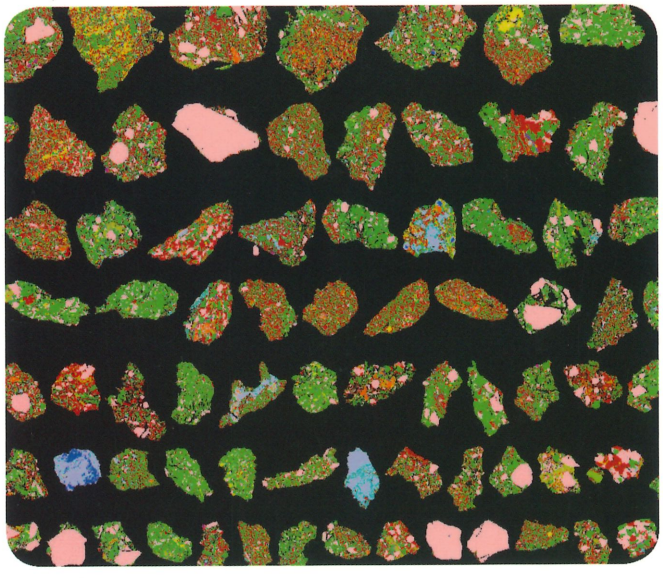

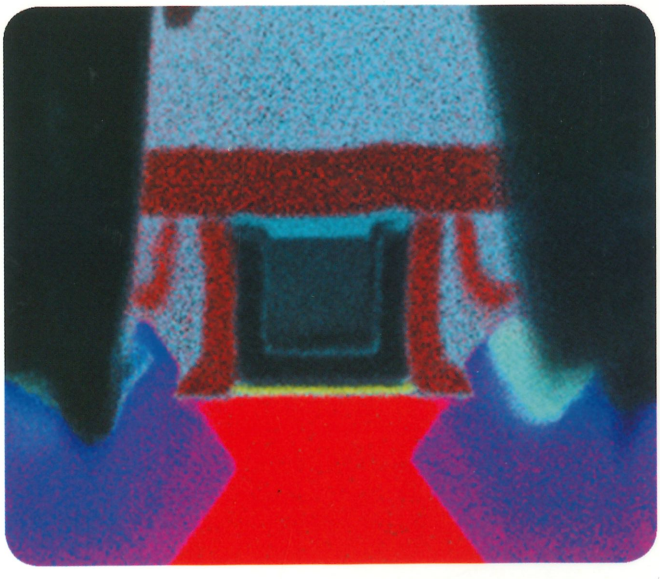

(Top left) Ultra-fast electron microscopy images of the evanescent field surrounding a protein sphere. Image courtesy of David J. Flannigan, Department of Chemical Engineering and Materials Science, University of Minnesota. **(Top right) Surface rendered cryo electron tomogram of mouse fibroblast cell.** Courtesy of Roman Koning. **(Bottom left) Drill cuttings from a CO_2 injection well.** Courtesy CO2CRC, Australia. **(Bottom right) 600 × 600 pixel maps, fully quantified, of a 45 nm PMOS transistor structure.** Courtesy of D. Klenov. FEI NanoPort. The Netherlands.

ATOMIC RESOLUTION S/TEM

Unrivaled raw data you can believe.

Atom-by-atom sub-angstrom imaging resolution, atom-to-atom chemical mapping, aberration correction, 2 and 3-D reconstruction, and optional Cold FEG. What can we help you achieve?

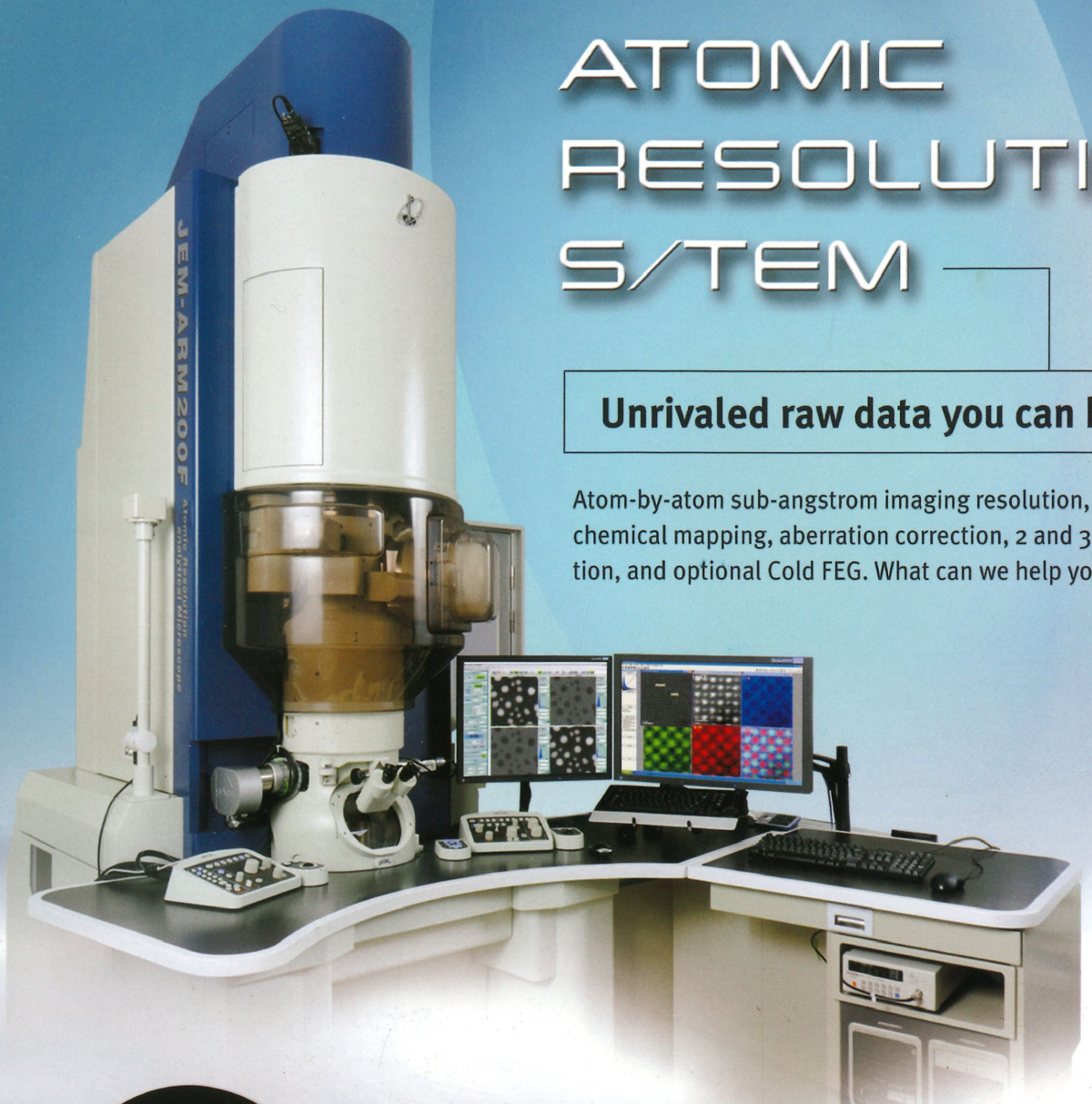

JEM-ARM200F

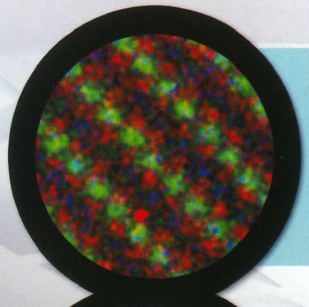

Dr. John Bradley
University of Hawaii
Commercial NCM Cathode Material for Li-Ion Batteries. Atomic EDS map. Overlay shows O (red), Ni (blue), Mn (green).
— 0.5nm

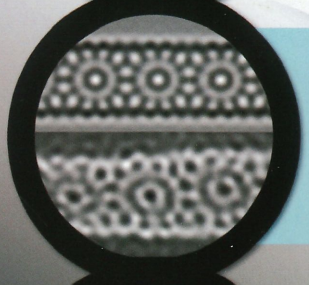

Dr. Miguel Jose Yacaman
University of Texas, San Antonio
Sample provided by Tour Lab, Rice University
Chiral Nanotube with parameters n=10 and m=4 (simulated and experimental).
— 0.5nm

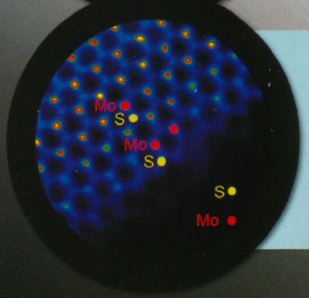

Dr. Moon Kim
University of Texas, Dallas
STEM HAADF image of transferred MoS_2, showing Mo and S atom positions and their 2H stacking sequence.
— 0.5nm

JEOL

Solutions for Innovation

捷東股份有限公司 www.jiedong.com.tw

5-on-1 of analytical tools for SEM

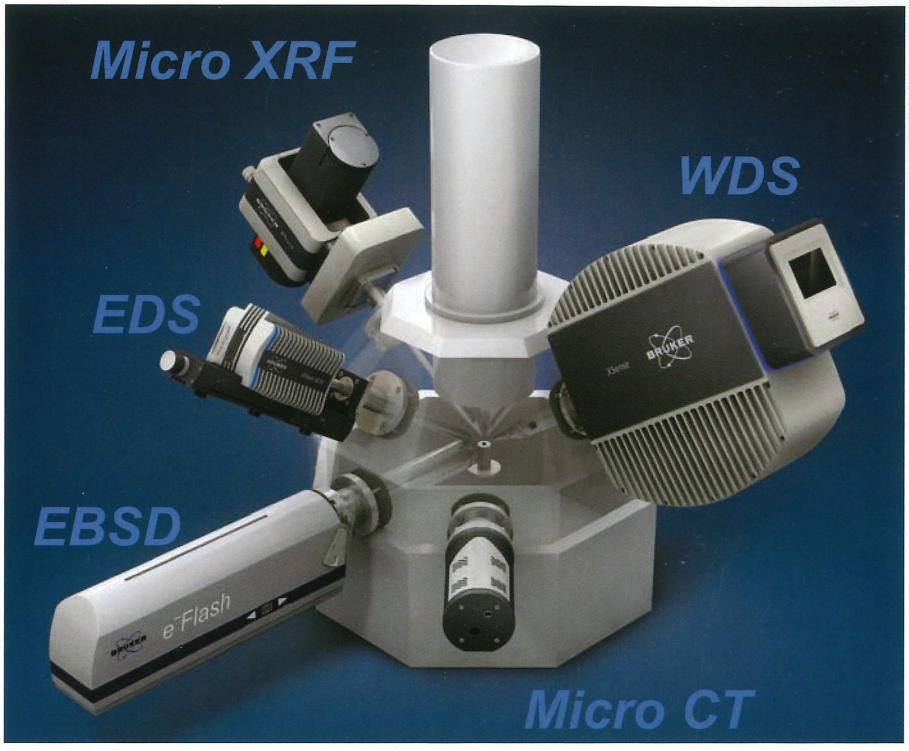

FQ5060 Low HV solution, High speed Mapping

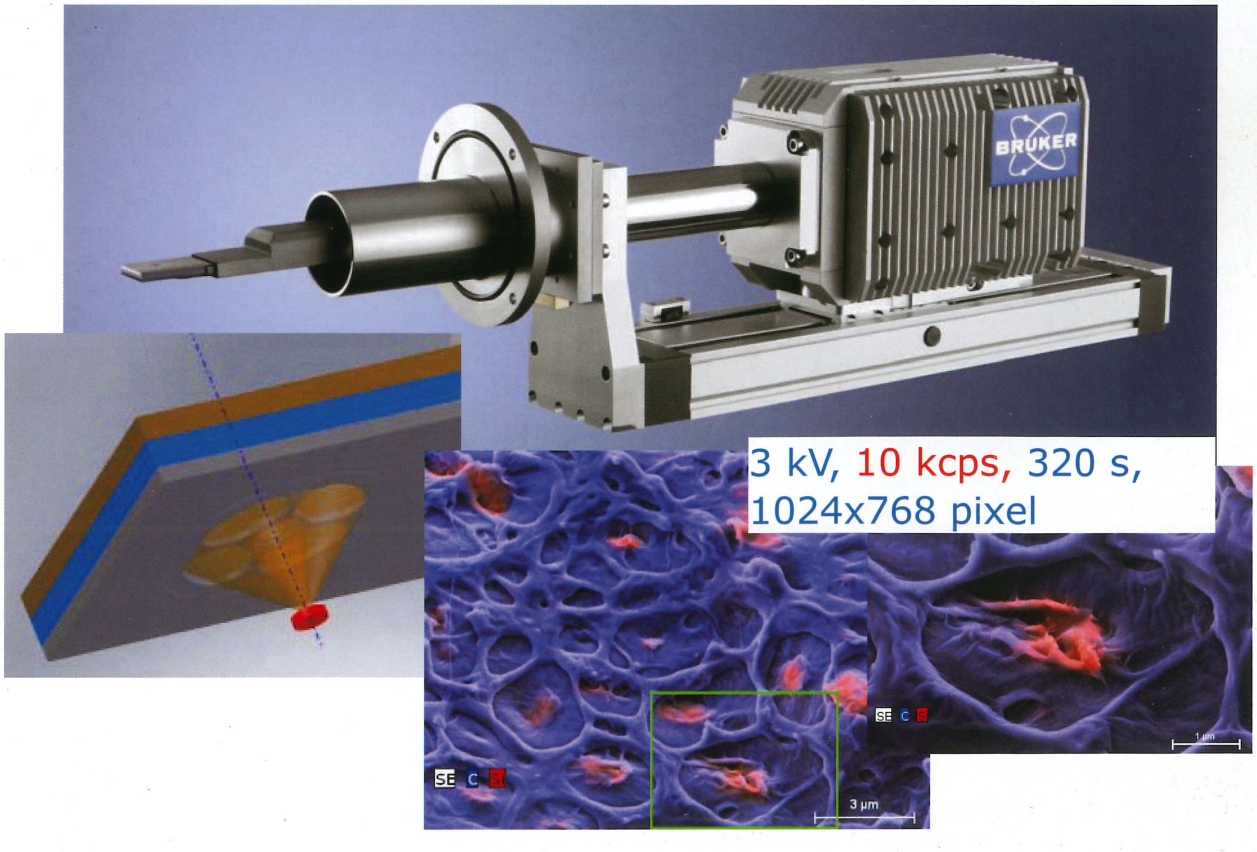

Touch panel for simple operation. Stylish and compact.

Benchtop Scanning Electron Microscope

NeoScope™ JCM-6000

Resolution and Analytical Performance

Superior technology – magnification range from ×10 to ×60,000
Optional EDS for elemental analysis

Simple to Use and Maintain

Intuitive software combined with a Multi-touch display
Automated alignment and image adjustment
Simple and quick sample exchange
Easy filament replacement

Excellent Value

Affordable imaging tool for high resolution and depth of field Space-saving design
Ideal for multiple users from novice to expert

Features

Both high-vacuum and low-vacuum imaging modes
Both Secondary and Backscattered Electron imaging
Feature measurement
Specimen tilt and rotation
Analytical capability with optional EDS system

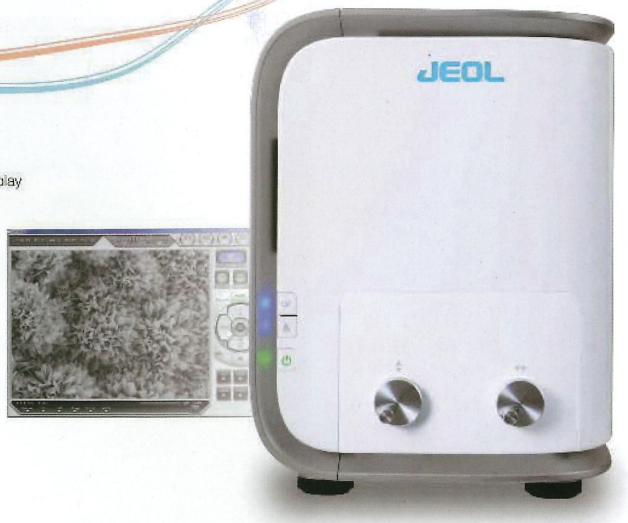

Versatile Functions

High-vacuum/low-vacuum modes are standard.

The high-vacuum mode offers a sharp image. The low-vacuum mode enables observation without coating.

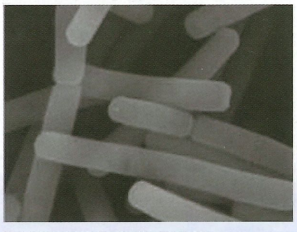

High-vacuum mode
Secondary electron image, Original mag : ×20,000, Specimen : yogurt fungus

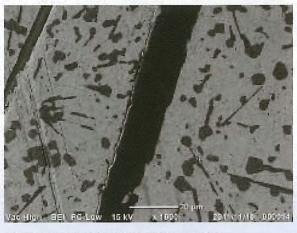

High-vacuum mode
Backscattered electron image, Original mag: ×1,000, Specimen: wood metal

Low-vacuum mode
Backscattered electron image, Original mag: ×540, Specimen: filter paper

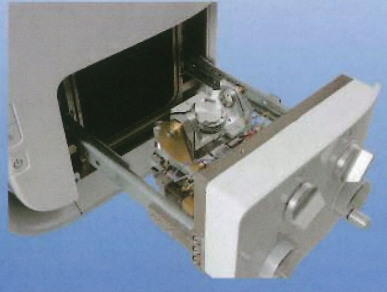

Use of the Tilting and Rotating Motor-Drive Holder enables observation at various angles, providing topographic information on a specimen.

※ Tilting and Rotating Motor-Drive Holder is optional.

Tilting and Rotating Motor-Drive Holder※

Tilt:0°, Original mag:×45, Specimen:Printed circuit board

Tilt:45°, Original mag:×45, Specimen:Printed circuit board

Elemental analysis

Pressing the Analysis button displays the EDS analysis screen.
EDS provides qualitative & quantitative analyses, point analysis and mapping (confirmation of elemental distribution).

"Analysis Assist" facilitates complicated analyses.

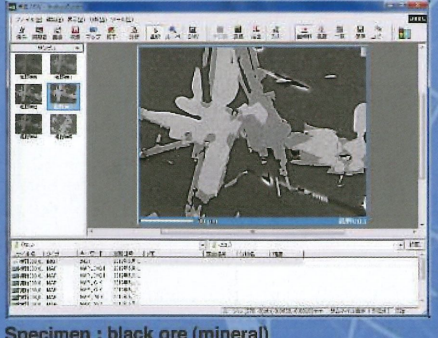

Specimen : black ore (mineral)

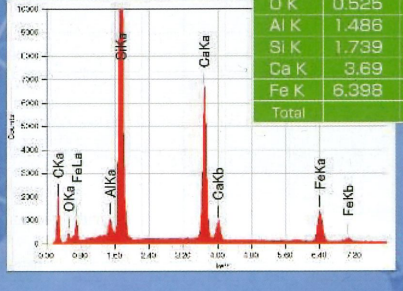

Element	(ke V)	Mass %	Number of atoms %
C K	0.277	45.65	70.06
O K	0.525	1.5	1.73
Al K	1.486	0.78	0.53
Si K	1.739	26.03	17.09
Ca K	3.69	15.38	7.07
Fe K	6.398	10.66	3.52
Total		100	100

捷東股份有限公司
www.jiedong.com.tw

JEOL
Serving Advanced Technology

Cathodoluminescence now for TEM

Imaging & Spectoscopy Optoelectronics Plasmonics Semiconductor Geological

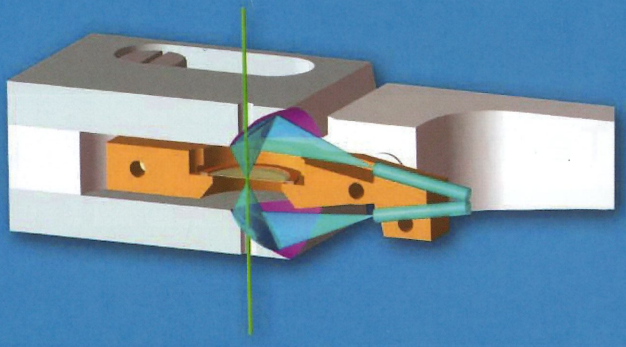

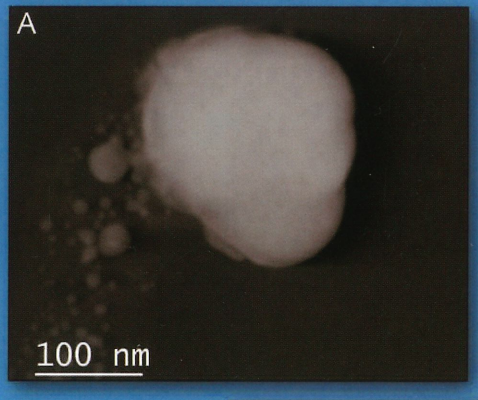

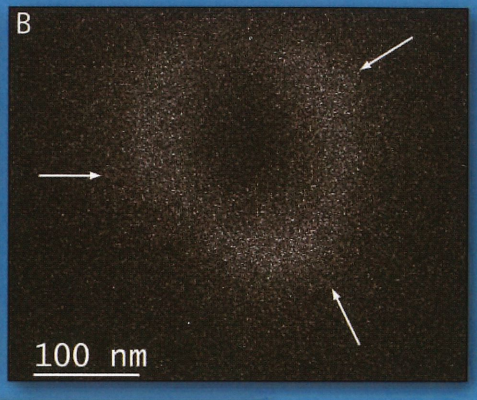

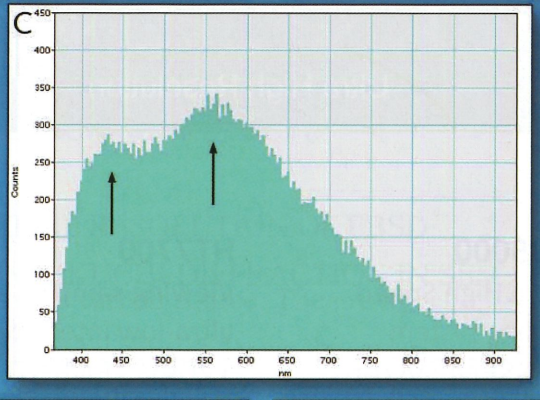

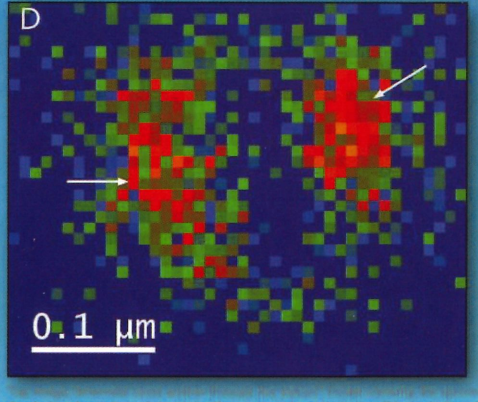

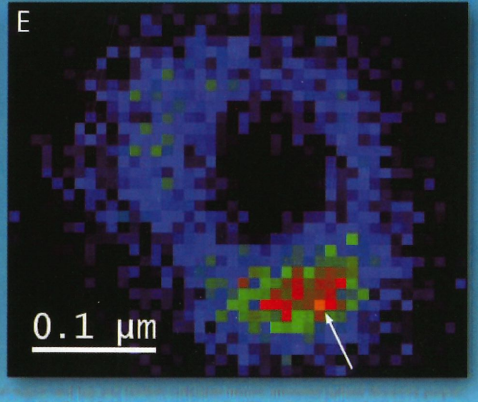

An electron beam (green) stimulates the specimen to emit photons (blue) which are focused by the collection mirrors into optical fibers situated away from the specimen region. Bottom images A-E: CL study of colloidal silver nanoparticle. A) HAADF image; B) panchromatic CL image (acquired simultaneously to the HAADF image) displaying three 'bright' resonance modes (indicated by arrow markers); C) cathodoluminescence spectrum with two peaks corresponding to spatially discrete resonance modes at 430 and 510 nm. D) and E) cathodoluminescence band pass images at 430 and 510 nm ±40 nm extracted from parent spectrum image showing resonance modes are separated spatially and spectrally.

Vulcan

Cathodoluminescence Detection and Analysis for Scanning TEMs

ANALYTICAL TEM DIGIAL IMAGING gatan SPECIMEN PREPARATION TEM HOLDER

Hitachi High-Technologies
HITACHI

HITACHI High-Technology.

SU8000 Series
Ultra High Resolution FE-SEM
STEM / EDS / EBSD

Excellent imaging performance
For a wide range of application

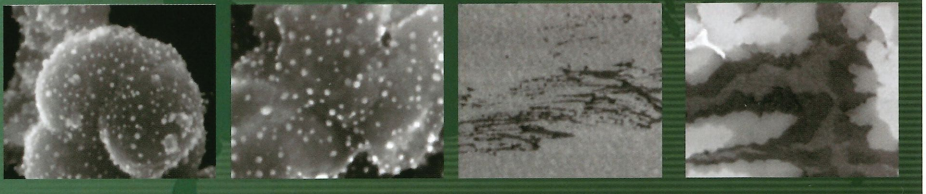

Ultra High Resolution　　Surface Voltage contrast

HF-3300
UHR-EELS
analysis system
Cold-FE-TEM

NB5000
Ultra High Speed
Milling system
FIB-SEM System

HT7700
Viewing samples at
ultra-low intensities
120kV TEM/STEM

SU3500
New Generation High
Performance SEM
Tungsten Filament

益弘儀器股份有限公司
E HONG INSTRUMENTS CO., LTD.

台北：02-27552266　新竹：03-5782020
台中：04-22452181　台南：06-2095135
高雄：07-3340407　www.ehong.com.tw

目錄

台灣顯微鏡學會

第十六屆理、監事名錄

理事長	楊哲人	台灣大學材料科學與工程學系	教授
副理事長	黃玲瓏	台灣大學生命科學系	教授
秘書長	溫政彥	台灣大學材料科學與工程學系	教授
常務理事	薛富盛	中興大學材料科學與工程學系	教授
	陳福榮	清華大學工程與系統科學系	教授
	劉康庭	友聯光學股份有限公司	董事長
理事	胡宇光	中央研究院物理研究所	研究員
	陳香君	台灣大學生命科學系	專任講師
	張立	交通大學材料科學與工程學系	教授
	劉全璞	成功大學材料科學與工程系	教授
	陳淑華	台灣大學生命科學院	教授
	朱明文	台灣大學凝態中心	研究員
	章為皓	中央研究院化學研究所	副研究員
	謝詠芬	閎康科技股份有限公司	董事長
	蔡定平	台灣大學物理系	教授
候補理事	李志浩	清華大學工程與系統科學系	教授
	高甫仁	陽明大學生醫光電研究所	教授
	簡萬能	中央研究院植物暨微生物學研究所	研究技師
	薛景中	中央研究院應用科學研究中心	副研究員
	孫啟光	台灣大學電機工程學系	教授
	蘇紘儀	台灣積體電路有限公司	故障分析處處長
常務監事	曾傳銘	中央研究院物理研究所	研究助技師
監事	羅聖全	工業技術研究院	研究員
	鮑忠興	成功大學奈米中心	教授
	張正	國立中興大學園藝學系	副教授
	林招松	台灣大學材料科學與工程學系	教授
候補監事	劉淦光	國家衛生研究院分子與基因醫學研究所	研究員

台灣顯微鏡學會

第34屆學術研討會 暨
第11屆海峽兩岸電子顯微學學術研討會

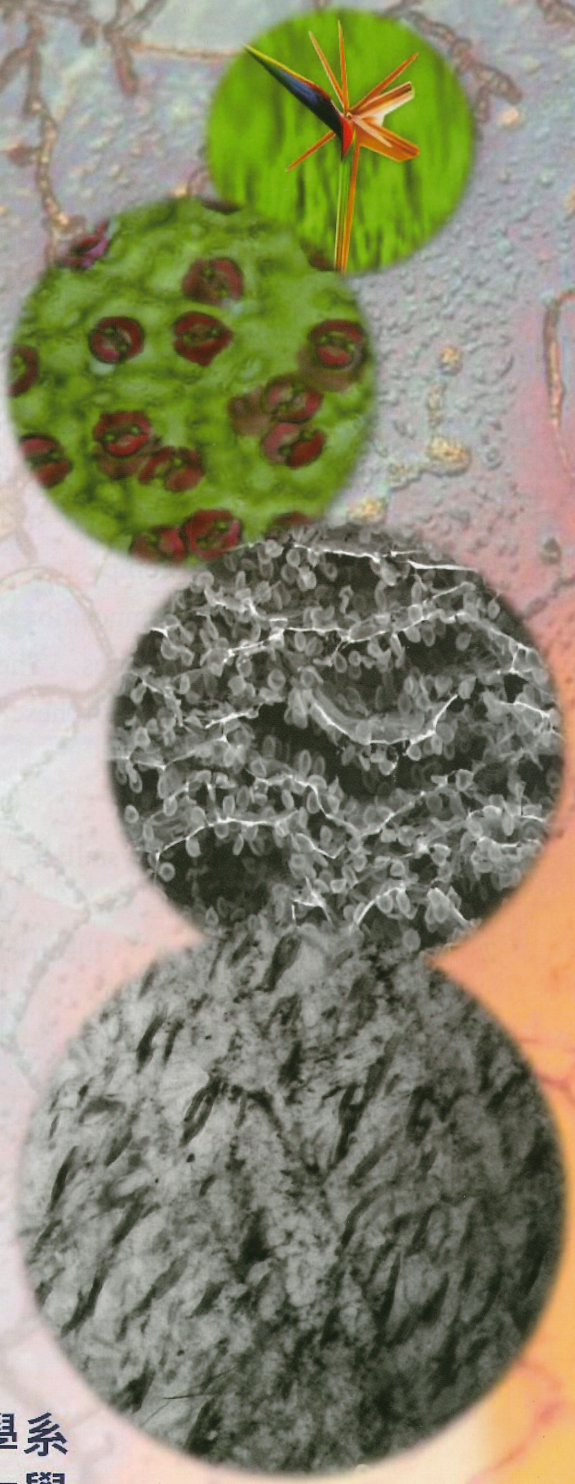

時間
103年6月22日至24日

地點
國立臺灣大學
應用力學館 國際會議廳

大會邀請演講
比利時 安特衛普大學
Dirk van Dyck 教授

論文徵稿
歡迎生物醫學及材料物理領域專家學者踴躍投稿，大會同時舉行學生論文壁報及顯微攝影照片競賽。

論文摘要與攝影作品截止日期
103年5月31日

詳細辦法請見台灣顯微鏡學會網頁
http://mst.ntu.edu.tw/~mst/

主辦單位 台灣顯微鏡學會
承辦單位 台灣大學材料科學與工程學系
協辦單位 科技部、台灣大學、清華大學

DYNAMIC EDS ANALYSIS OF THE LIGHT ELEMENT NANO-STRUCTURES AT HIGH TEMPERATURES

O. Lourie*, B. Barton, D. Sudfeld and B. Freitag

FEI Company, Achtseweg noord 5, P.O. Box 80066, 5600 KA, Eindhoven

The in situ chemical characterization of the nanostructures at high temperatures was a challenge for many years. With a new heating device based on the advanced MEMS technology and the state-of-the art SDD based EDS system, the fast analytical EDS studies at high temperatures can now be routinely performed, even on the light element materials such as Boron nanowires.

The refractory light materials such as Boron have shown a promising direction towards novel designs and application in nanoelectronics. For such applications the ideal 1D nanoscale interconnects are expected to be composed of electrically conductive ceramics or refractory elements possessing high crystallinities and high conductivities irrespective of chirality or crystallographic orientation. Here we present the in situ dynamic structural analysis of such nanocomposite structures, which naturally blend both high conductive properties and refractory composition.

The attached EDS compositional maps show presence of Ni nanowire as a core in the synthesized Boron nanowires. The growth model is proposed and the potential electro-mechanical properties of these composite nanostructures are evaluated and discussed.

References

1. CJ Otten, et al., "Crystalline Boron nanowires", J Am Chem Soc. 2002 May 1;124(17):4564-5.
2. D. Wang et al., " Electrical transport in boron nanowires", APL 2003, 183(25):5280-82.
3. W. Ding et al., "Mechanics of crystalline boron nanowires", Comp. Sci. and Techn. 2006, 66:1109-21.
4. J. Tian, et al., "Boron nanowires for flexible electronics",APL 2008 93:122105-7-5

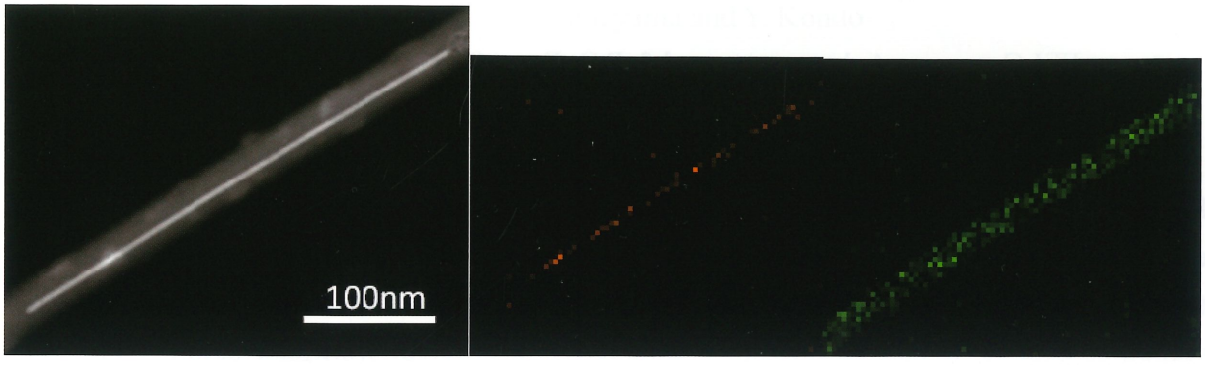

Fig.1. (left) STEM DF image of Boron/Ni composite nanowire ; (middle) Ni EDS map; (right) Boron EDS map;

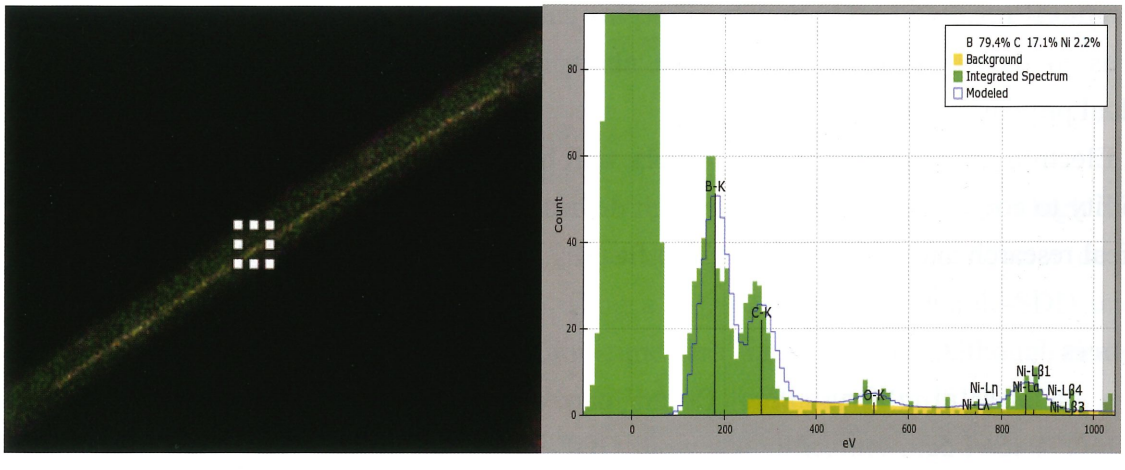

Fig.2. (left) combined EDS Boron/Ni map with indicated area where the EDS spectrum is acquired (right)

ELECTRON MICROSCOPY 4.0: HOW INTEGRATING TECHNOLOGIES HELP CURE DISEASES

Peter Fruhstorfer

FEI Company, Achtseweg noord 5, P.O. Box 80066, 5600 KA, Eindhoven

Electron microscopy has gone through a significant evolution the last few decades. From an elementary tool with an abundance of knobs and switches which required dedicated operators (EM 1.0) through development steps stabilizing the platforms, and increasing throughput (EM 2.0) it has arrived at the current situation (EM 3.0), a platform which is recognized for its ability to provide a complete and efficient workflow solution including sample preparation, imaging platforms, image acquisition, data output and data analysis.

Electron Microscopy 4.0 (EM 4.0) is the next step, and it is going to revolutionize microscopy both at the molecular and cellular level. In Cell biology the combination of various microscopy modalities, called correlative microscopy, will reveal cellular changes in-depth merging dynamics, labeling specificity and nanometer resolution - from a single experiment.

A similar evolution can be observed in the field of Structural Biology, which aim is to resolve protein structures at the molecular or atomic detail. Usually referred to as Integrated Structural Biology, the combination of XRD/NMR and Cryo-Electron Microscopy is quickly being adopted as the next step, gaining insight at the molecular level as the combination of these methods results in a continuum of scales and resolutions over a broad range, adding dynamics to the equation as well as the ability to study protein complexes rather than individual proteins only.

Electron microscopy 4.0, at all levels, will have a significant impact moving forward. The ability to combine technologies through dedicated workflow solutions will revolutionize biological research and will contribute significantly to curing disease.

References

1. CJ Otten, et al., "Crystalline Boron nanowires", J Am Chem Soc. 2002 May 1;124(17):4564-5.
2. D. Wang et al., " Electrical transport in boron nanowires", APL 2003, 183(25):5280-82.
3. W. Ding et al., "Mechanics of crystalline boron nanowires", Comp. Sci. and Techn. 2006, 66:1109-21.
4. J. Tian, et al., "Boron nanowires for flexible electronics",APL 2008 93:122105-7-5

FAST AND HIGHLY SENSITIVE ANALYSIS SYSTEM WITH TWO SILICON DRIFT-TYPE DETECTORS FOR TRANSMISSION ELECTRON MICROSCOPY

I. Ohnishi, S. Kawai, T. Ishikawa, K. Yagi, T. Iwama, K. Miyatake, Y. Iwasawa, M. Matsushita, T. Kaneyama and Y. Kondo

JEOL Ltd., 1-2 Musashino 3-chome, Akishima, Tokyo 196-8558, Japan

An energy dispersive X-ray spectrometer (EDS) has been one of the most important devices for analytical transmission electron microscopy (TEM), since it can provide simultaneous multi-elemental analysis for any specimen and can be used easily for any user. However, it needs long time for collecting the X-rays of sufficient intensity, due to a small ionization cross section for core electrons of a specimen and a small solid angle for a detector. Therefore, an analyzing specimen sometimes suffers electron beam damage and/or contamination. In order to solve this problem, we have developed a new analysis system for TEM, which is composed of two silicon drift-type detectors (SDDs). Here we report its features and applications.

Figure 1 shows the schematic configuration of our newly developed analysis system for a field emission TEM (JEM-2800). The system consists of two SDDs (double-SDD) with a large sensor area (100 mm^2). A new TEM column has two ports for the detectors. The total X-ray intensity of the new system has increased, because the X-ray signals collected from two detectors are integrated. For example, the peak intensity of Al K line obtained with a double-SDD has increased to be approximately 1.7 times higher than that obtained with a single SDD as shown in Fig. 2.

Since the new analysis system has high sensitivity, an elemental map with a high S/N ratio can be acquired. Elemental maps sized 256 x 256 pixels for a semiconductor device are shown in Fig. 3. They were obtained by using a single SDD and a double-SDD under the same analytical condition. X-ray acquisition time was just 1 minute. Although these maps clearly show Si_xN_y and SiO_x layers on Si substrate, the intensity profiles for oxygen and nitrogen K lines acquired with the double-SDD show a significantly improved S/N ratio with respect to the ones with the single SDD.

We have successfully developed a new analysis system with significantly high X-ray collection ability. The system provides a shorter acquisition time than a single SDD system, and helps us to analyze a beam sensitive specimen and to detect trace elements in a specimen.

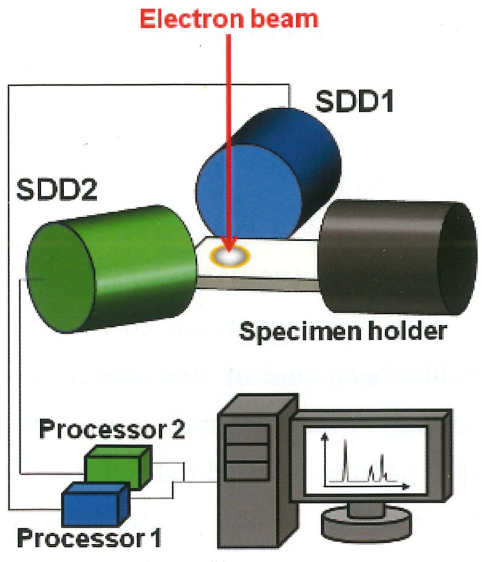

Fig. 1. Schematic configuration of an EDS analysis system with a double SDD for a field emission TEM (JEM-2800).

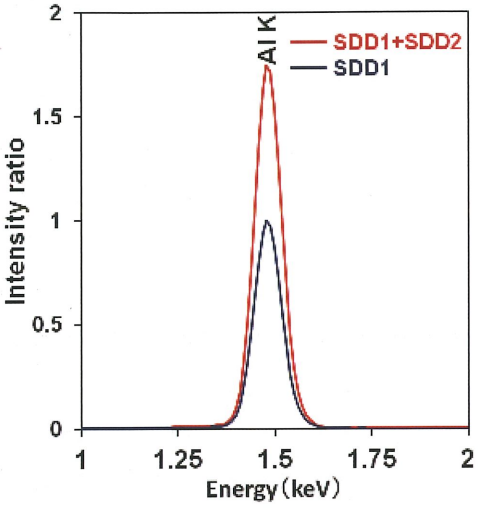

Fig. 2. EDS spectra of an Al foil specimen, obtained using JEM-2800 (200 kV) with SDD1+SDD2 (red) and SDD1 (blue). The vertical axis has been normalized by the peak intensity of Al K line, obtained with SDD1.

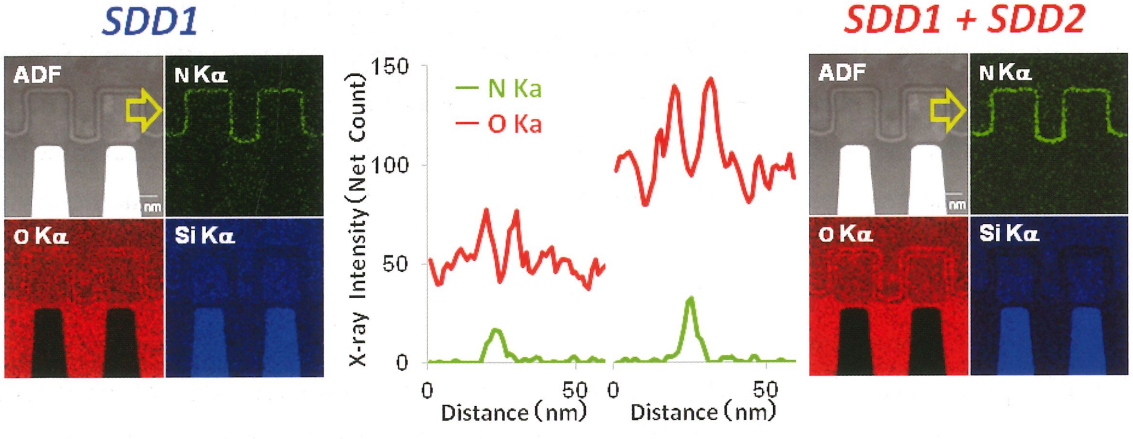

Fig. 3. Two sets of STEM-ADF image and elemental maps (N, O, Si) for a semiconductor device, obtained with JEM-2800 (200 kV) with SDD1 (left) and SDD1+SDD2 (right). The mapping size is 256 x 256 pixels. Line profiles of the net intensity of N Kα and O Kα along yellow arrowed lines in ADF images are shown in the middle.

BIOLOGICAL APPLICATIONS WITH MODERN TRANSMISSION ELECTRON MICROSCOPE

Naoki Hosogi

JEOL Ltd., 3-1-2 Musashino, Akishima, Tokyo 196-8558, Japan

We present biological applications with a transmission electron microscope (TEM). JEM-1400Plus is the TEM developed for biological application in our products. The microscope has many suitable features for biological applications such as simplified operation panel, user friendly software, 8M pixel camera fully integrated in TEM, "Stage Navigation" function ("Ultra Low Mag" mode and "Point & Shoot") and so on. These features allow us to observe biological specimens easily and at high-throughput.

With the "Stage Navigation" function and "Picture Overlay Program" software, we have developed a workflow of correlative light and electron microscopy (CLEM). The "Picture Overlay Program" software allows us to share the coordinates of LM and TEM images. After the sharing of the coordinates, we can place the region specified in an LM image with the "Stage Navigation" function in the center of the field of TEM view. Then, we can increase the magnification to examine a detailed structure of the region (Fig. 1).

Frozen-hydrated biological specimens can be observed using a cryo-transfer holder and a minimum dose system (Fig. 2). The cryo-TEM specimen is usually observed without chemical fixing and staining. Because of the non fixing and staining procedure, we can observe the structure of the specimen close to natural state without any disturbance due to the specimen preparation.

To observe frozen-hydrated specimens, we have developed more suitable TEMs, which are JEM-2200FS and JEM-3200FSC. They are equipped with a field emission gun and an in-column energy filter (omega filter). The omega filter is used to obtain high-contrast images using only zero-loss energy electrons by eliminating inelastically scattered electrons, which are contributed to back ground noise (Fig. 3). In addition, these TEMs are compatible with a Zernike phase plate. The Zernike phase plate can retard the phase of electron waves by half π so that the contrast transfer function (CTF) changes from sine functions to cosine functions. It allows us to observe high-contrast images of non-stained specimens with just in-focus (Fig. 4).

We are certain that these TEMs, with the attached instruments and the software, offer significant advantages to structural characterizations of biological specimens at high throughput.

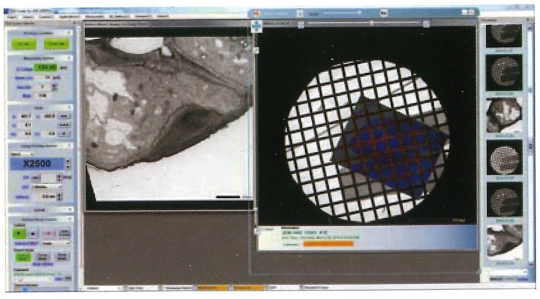

Figure 1. Screenshot of windows for CLEM, running "Picture Overlay Program" on a TEM operation monitor. The software superimposes LM and TEM images and shares their coordinates.

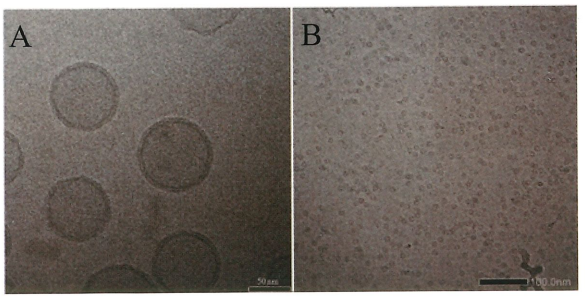

Figure 2. Cryo-TEM images of ice-embedded liposomes (A) and apoferritin particles (B). These images were taken with JEM-1400Plus.

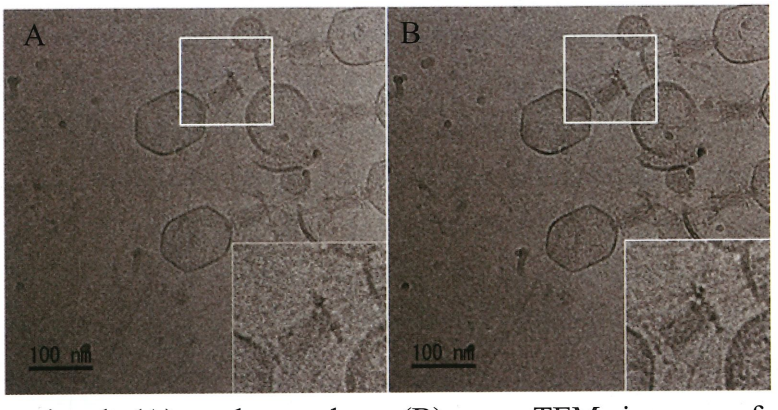

Figure 3. Conventional (A) and zero-loss (B) cryo-TEM images of ice-embedded bacteriophage T4. The zero-loss image shows improved image contrast compared with the conventional image. These images were taken with JEM-2200FS.

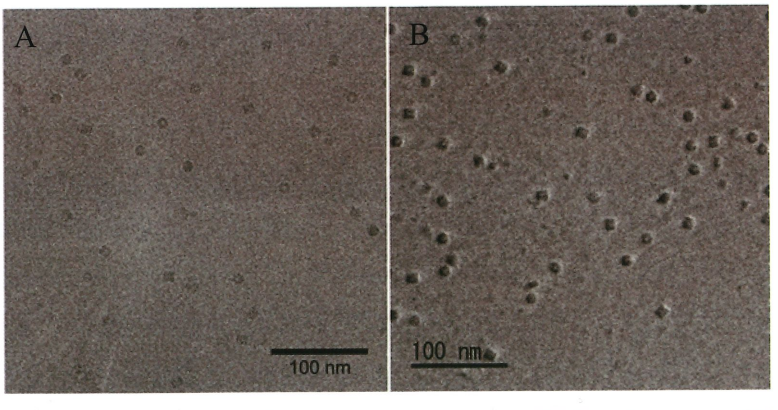

Figure 4. Zero-loss (A) and Zernike phase contrast (ZPC) (B) cryo-TEM images of ice-embedded Gro-EL particles. The zero-loss image was taken at a defocus of 2 μm. The ZPC image was taken at in-focus. The ZPC image shows improved image contrast compared with the zero-loss image. These images were taken with JEM-2200FS.

IMPROVING THE SPATIAL RESOLUTION OF EBSD WITH TRANSMISSION KIKUCHI DIFFRACTION IN SEM

[1] Kip Goi, [2]Ian Brough, [2] Ali Gholinia and [3]P Trimby

[1]Oxford Instrument, HsinChu, Taiwan
[2]School of Materials, Manchester University
[3]P Trimby, Australian Centre for Microscopy & Micro Analysis, The University of Sydney.

It is becoming increasingly important to be able to characterise materials on the nanoscale. Despite significant technological developments in recent years, the EBSD technique is still limited by the pattern source volume to resolutions in the order of 25-100nm; this is insufficient to measure accurately truly nanostructured materials (with mean grain sizes below 100nm). A new approach to SEM-based diffraction has emerged, namely using an electron transparent sample coupled with conventional EBSD hardware and software. This technique, referred to as transmission EBSD (t-EBSD: Keller and Geiss, 2012) or SEM Transmission Kikuchi Diffraction (TKD: Trimby, 2012) [1] has been proven to enable spatial resolutions better than 10nm, and is ideal for routine EBSD characterisation of both nanostructured and highly deformed samples.

Describes the set up required for working with an EBSD system in transmission mode, using a NordlysNano EBSD detector and AZtecHKL. Utilizing the high performance of FE-SEM, the sensitivity of the NordlysNano EBSD detector design coupled with the refine indexing of AZtecHKL software. The characterizations of grain size in a few nanometer ranges are possible. It illustrates the application of TKD to a nanostructured nickel sample and a highly deformed stainless steel, both of which were impossible to characterise using conventional EBSD.

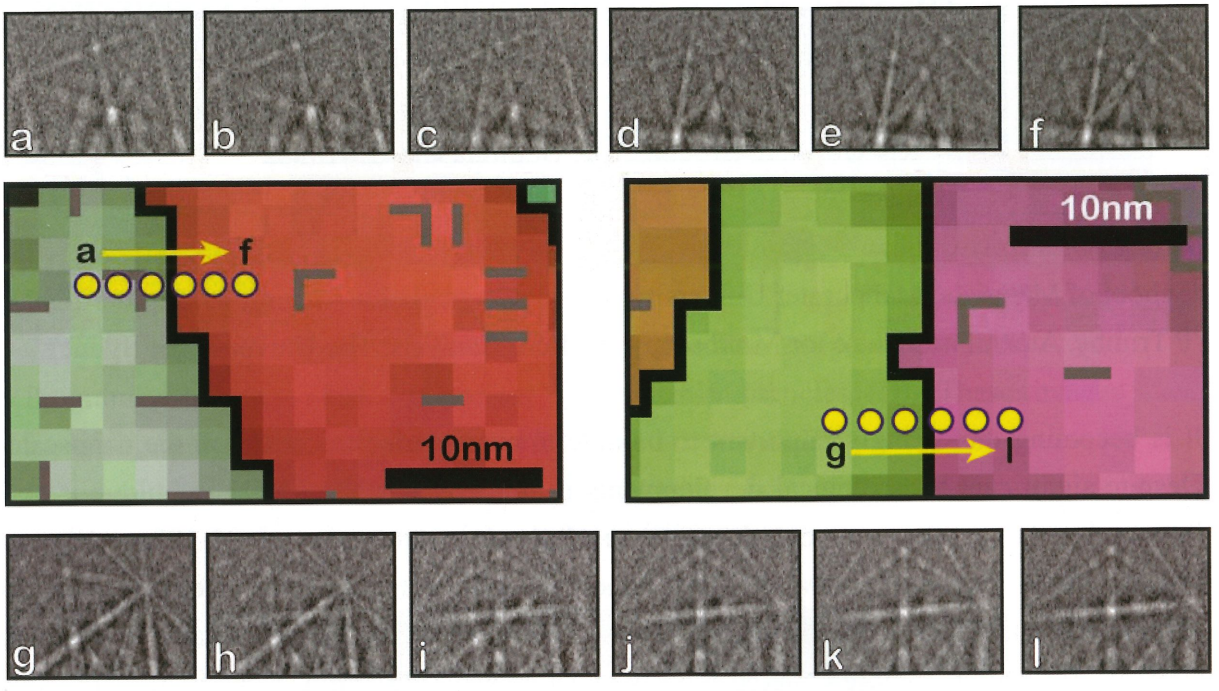

Figure 1 Show the spatial resolution of Transmission Kikuchi Diffraction(TKD)

References

1. P Trimby, Australian Centre for Microscopy & Micro Analysis, The University of Sydney.

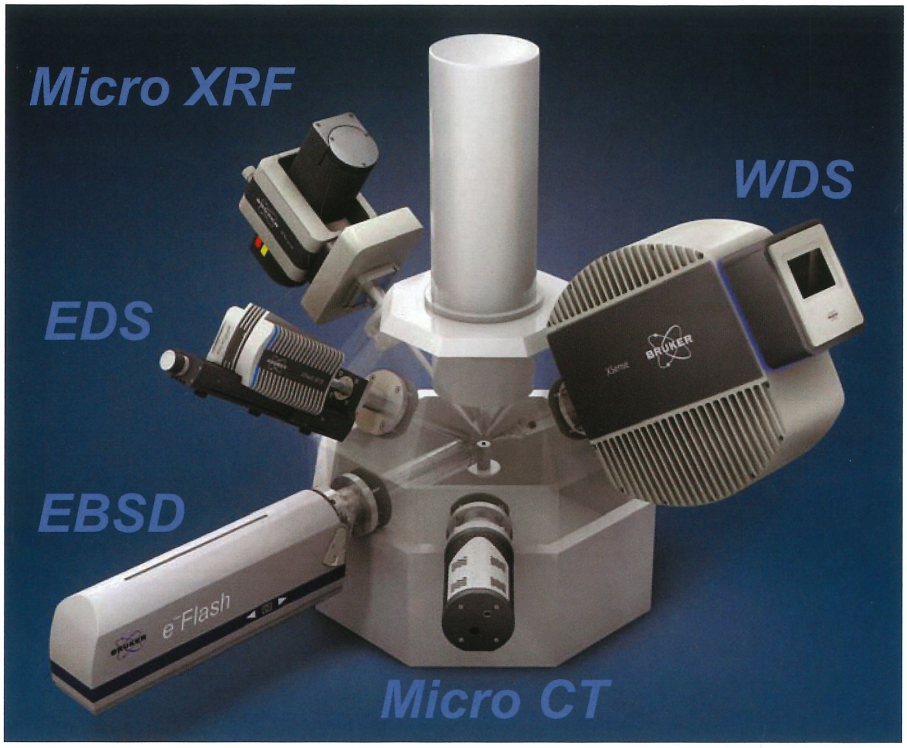

EDS: 121eV 最佳能量解析度，低能量分析更精確。600kcps output count rate 極高速處理器。快速完成 mapping 不是夢

EBSD: 最快速的 EDS/EBSD 同時量測與分析，獨家 Argus FSE/BSE 彩色微觀可視成像系統，快速判斷分析區域

WDS: 設定簡單，快速開始量測光學系統自動調整，確保最佳的量測條件

μXRF: 超過 EDS 20~50 倍的偵測極限，量測到 EDS 無法量測的微量元素與 EDS 結果整合，增加定量結果的可信度

μCT: 非破壞量測可以看到樣品內部的 3D 形貌解析度可達 400nm pixel size

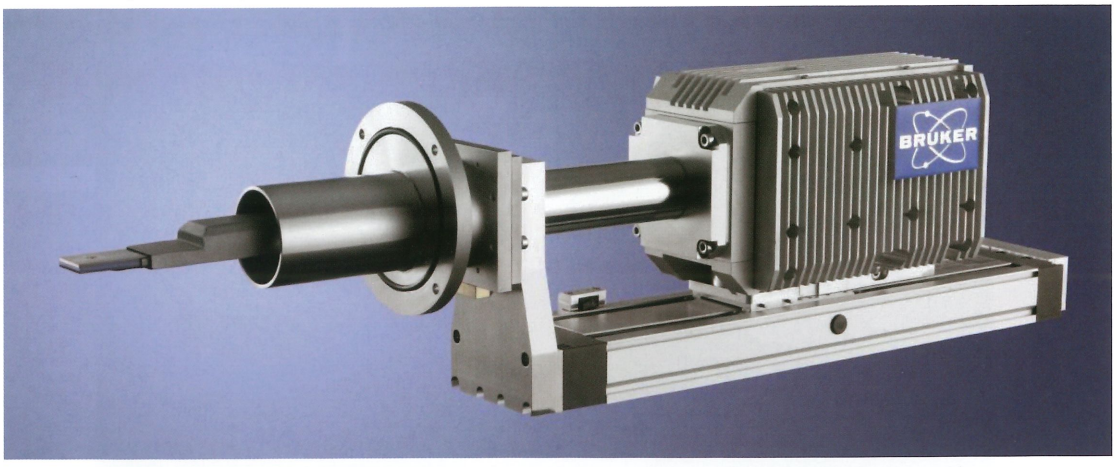

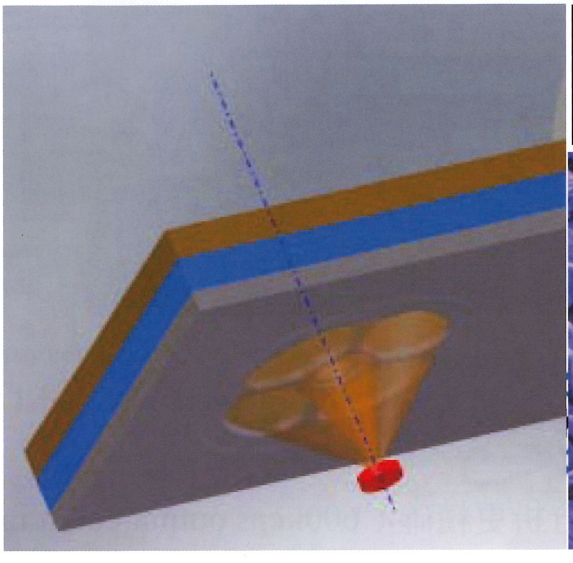

3 kV, 10 kcps, 320 s,
1024x768 pixel

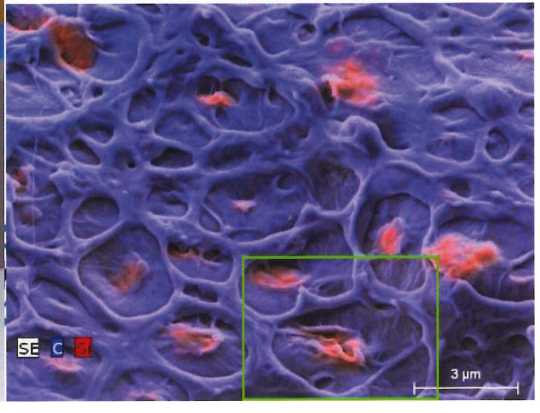

Bruker FQ5060

- Ultra large solid angle $\Omega \approx 1.1$ sr,
- Good and sufficient statistics even for low HV

- beam sensitive samples

- nano-structures and/or thin samples

- Minimize shadow effects at topographic samples

第三十四屆台灣顯微鏡學會學術研討會

材料物理與生物醫農組　學生論文海報競賽

材料物理組		
M-P-01	**TRANSMISSION ELECTRON MICROSCOPY STUDY OF THE STABILITY OF SILVER NANOWIRES** Chia-Hao Yu（余家濠）and Cheng-Yen Wen（溫政彥） Department of Materials Science and Engineering, National Taiwan University, Taipei, Taiwan	9
M-P-02	**CHARACTERIZATION OF ULTRA-THIN NI SILICIDE FILM BY STEM-EELS** Chien-Ting Wu (吳建霆), Yao-Jen Lee (李耀仁) National Nano Device Laboratories, National Applied Research Laboratories, Hsinchu City, Taiwan	11
M-P-03	**ELECTRON MICROSCOPY ANALYSIS OF SIGE ALLOY AND SIGE/SI AXIAL HETEROJUNCTION NANOWIRE STRUCTURES** Yun-Yi Tsai（蔡昀嶧), Sheng-You Taso (曹勝宥), and Cheng-Yen Wen（溫政彥） Department of Materials Science and Engineering, National Taiwan University, Taipei, Taiwan	13
M-P-04	**THE INVESTIGATION IN YIELD STRENGTH OF NB-MO LOW CARBON BAINITIC STRIP WITH AGING PROCESS** Bo-Ming Huang (黃柏銘),[1] Hung-Wei Yen(顏鴻威),[2] Simon P. Ringer,[2] Ya-Ling Chang（張雅齡), [1] Yu-Chuan Chien（簡佑全), [1] and Jer-Ren Yang（楊哲人), [1] [1]Department of Materials Science and Engineering, National Taiwan University, Taipei, Taiwan [2] Australian Centre for Microscopy and Microanalysis, The University of Sydney, 2006, NSW, Australia	15
M-P-05	**IN-SITU ENGINEERING AND CHARACTERIZATION OF GRAPHENE IN TEM** Chia-Hao Tu（涂嘉豪)[1], Jing-GuO Wen（文建國)[2], Dean Miller[2], and Chuan-Pu Liu（劉全璞)[1] [1]Department of Materials Science and Engineering, National Cheng Kung University, Tainan, Taiwan [2] Electron Microscopy Center, Argonne National Laboratory, Illinois, USA	17

	[1]Department of Biochemical Science and Technology, National Taiwan University, Taipei, Taiwan [2]Department of Marine Science, National Sun Yat Sen University, Kaohsiung, Taiwan [3]Department of Engineering System, National Tsing-Hua University, Hsinchu, Taiwan, [4]Divion of Structural Biology, National Institutes of Physiology, Okazaki, Japan [5]Institute of Chemistry, [6]Institute of Statistics and [7]Institute of Physics, Academia Sinica, Taipei, Taiwan	
B-P-06	**THE PRELIMINARY STUDY OF THE STRUCTURE OF *SAPINDUS MUKOROSSI* SEED AND ITS PHYSICAL DORMANCY MECHANISM** [1]WANG, Ming-Wei (王名偉), [1]KUO-HUANG, Ling-Long (黃玲瓏) and [2]Ching-Te Chien (簡慶德) [1]Institute of Ecology and Evolutionary Biology, National Taiwan University, Taipei, Taiwan [2]Taiwan Forestry Research Institute, Taipei, Taiwan	75

M-P-01

TRANSMISSION ELECTRON MICROSCOPY STUDY OF THE STABILITY OF SILVER NANOWIRES

Chia-Hao Yu（余家濠）and Cheng-Yen Wen（溫政彥）

Department of Materials Science and Engineering, National Taiwan University, Taipei, Taiwan

Using silver nanowires in transparent conductive thin film can potentially replace current indium tin oxide (ITO) based transparent electrode for its low-cost, flexibility, good conductivity and transparency [1]. However, silver nanowires are very unstable due to oxidation and sulfurization in the ambient environment [2]. This corrosion problem is very troublesome for their applications. It has been reported that applying oxide coating on the surfaces is an effective method for protecting silver nanowires or nanoparticles from degradation [3-4], but there are relatively few researches regarding applying the atomic layer deposition (ALD) for the growth of oxide protection layer on silver nanowires. ALD can provide large-area uniform deposition of oxide on complicated surfaces, and we believe that the oxide protection layer grown by ALD would be more helpful for relieving the corrosion problem of silver nanowires [5].

In this presentation, we first discuss the evolution of the silver nanowires in air. We find that silver nanowires are subject to phase transformation and gradually decompose to Ag_2S in the ambient environment (Fig. 1). To avoid this problem, we try to deposit titanium oxide layers and aluminum oxide layers on the sidewalls of silver nanowires using the ALD method. It is found that deposition of TiO_2 layers onto silver nanowires is rather difficult, due to the low reactivity of the precursor gas [6], and the silver nanowires are still corroded and transform to Ag_2S (Fig. 2). On the contrary, uniform aluminum oxide protection layer can form and protect silver nanowires well from oxidation and sulfurization (Fig. 3). The long-term stability of silver nanowires coated with ALD-Al_2O_3 protection layer is therefore useful for future applications.

References

1. Jung-Yong Lee, Stephen T. Connor, Yi Cui, and Peter Peumans, Nano Lett., 8 689 (2008).
2. J. L. Elechiguerra, L. Larios-Lopez, C. Liu, D. Garcia-Gutierrez, A. Camacho-Bragado, and M. J. Yacaman, Chem. Mat., 17 6042 (2005).
3. G. Baraldi, M. Carrada, J. Toudert, F. J. Ferrer, A. Arbouet, V. Paillard, and J. Gonzalo, J. of Phys. Chem. C, 117 9431 (2013).
4. P. Ramasamy, D. M. Seo, S. H. Kim, and J. Kim, J. Mater. Chem., 22 11651 (2012).

5. S. M. George, Chem. Rev., 110 111 (2010).
6. Stacey D. Standridge, George C. Schatz, and Joseph T. Hupp, Langmuir, 25 2596 (2009).

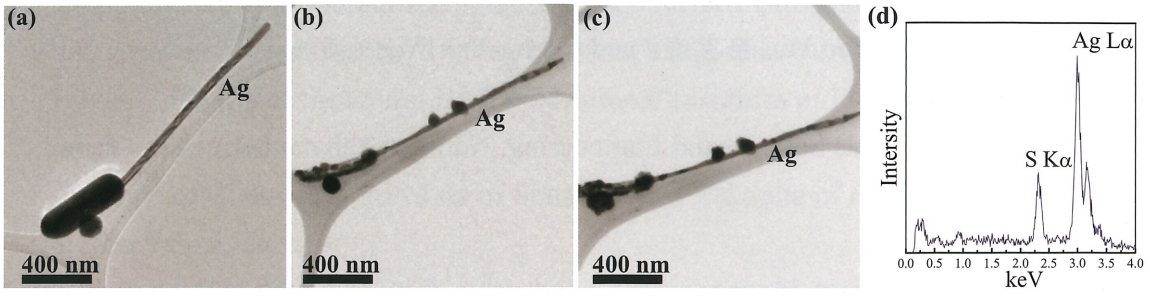

Figure 1. (a-c) TEM images of the evolution of a silver nanowire. The silver nanowire prepared by the polyol method (a) was stored in N_2 for 3 weeks (b), followed by being stored in air for another week (c). (d) Energy dispersive spectrum (EDS) of a nanoparticle formed on the surface of the silver nanowire in (c).

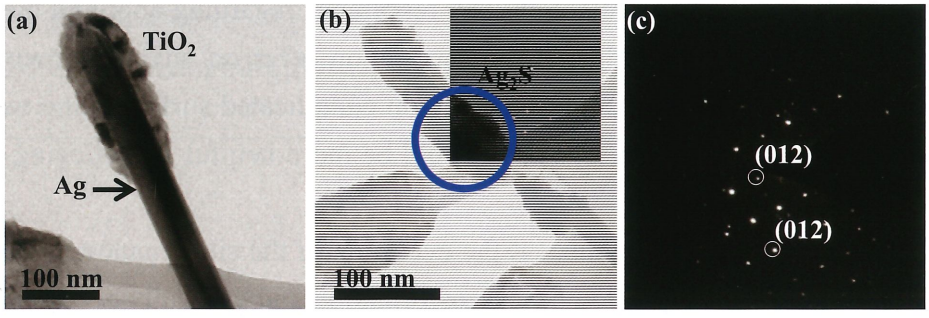

Figure 2. (a) TEM image of a silver nanowire coated with TiO_2. 20 nm thick TiO_2 was expected to be grown uniformly on the nanowire surface at 250 °C, but only the nanowire tip has obvious TiO_2 deposition. (b) TEM image of the silver nanowire in (a) after being placed in air for one week. (c) Selected-area diffraction pattern taken from area marked by the blue circle in (b), showing the diffraction pattern of acanthite Ag_2S along its $[02\bar{1}]$ axis.

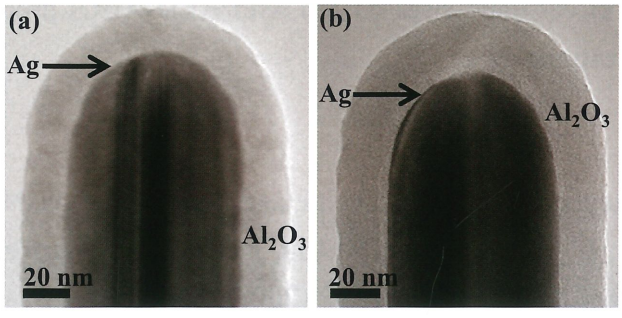

Figure 3. (a) TEM image of silver nanowire soon after coated with an Al_2O_3 layer. (b) TEM image of an Al_2O_3-coated silver nanowire stored in air for 9 months. No significant changes in the morphology are observed.

M-P-02

CHARACTERIZATION OF ULTRA-THIN NI SILICIDE FILM BY STEM-EELS

Chien-Ting Wu (吳建霆), Yao-Jen Lee (李耀仁)

National Nano Device Laboratories, National Applied Research Laboratories, Hsinchu City, Taiwan

We reports a novel silicide process that achieves Ni silicide thickness of 10 nm while maintaining low resistance of 18 ohm/sq. with two-step low temperature microwave annealing (MWA), and an ultra-thin Ni silicide film, only 4.5 nm, has been realized. In this study, we use electron energy-loss spectroscopy and energy dispersive X-ray spectroscopy in conjunction with scanning transmission electron microscopy (STEM-EELS/EDS) in order to identify the nickel silicide phases concentrating primarily on the Z-contrast image with atomic spatial resolution, elemental analysis, bulk plasmon excitaions and the Ni-$L_{2,3}$ edge ELNES.[1] Figure 1 shows the $[1\text{-}10]_{\text{Si substrate}}$ high-resolution HAADF image of the 4.5 nm NiSi sample, with the brightest contrast signifying NiSi (green inset, Fig. 1) and the bright one in the right inset directing to $NiSi_2$ (red inset, Fig. 1) taking into account the weight sensitivity of the STEM-HAADF technique. It clearly shows a 4.5 nm NiSi thin film formed with a few, small and non-penetrating epi-$NiSi_2$ (10~20 nm) regions at Si surface. By the HAADF imaging, lattice parameters of Si and $NiSi_2$ are similar (Si: 0.5430 nm, $NiSi_2$: 0.5406 nm), and the in-plane mismatch between the atomic spacing on the $NiSi_2$ (111) and Si (111) planes is only 0.5%. In addition, Fig. 2 shows portion of the STEM-EELS spectra taken across the interface with the electron probe pinpointing the observed Si, NiSi and $NiSi_2$, respectively. Upon positioning the electron probe at Si, we observed the characteristic bulk-plasmon excitation, 16.7 eV, of the material. The readily observed bulk-plasmon excitations of $NiSi_2$ (19.7 eV) and NiSi (20.3 eV) in Fig. 2(a) are also nicely consistent with the known values of the respective materials, in agreement with the STEM-HAADF characterizations in Fig. 1. The dash-square (green color) and triangular-line (red color) curves in Fig. 2(b) are the Ni-$L_{2,3}$ edge ELNES spectra of NiSi and $NiSi_2$, respectively, after background subtraction and Fourier-ratio deconvolution of the plural scattering effects. The intensities had been normalized to the L_2 maximum peak of each phase. It is clear that L_3 peak becomes smaller relative to the L_2 peak if the Si concentration increases. The branching ratio, which is defined as $I(L_3)/[I(L_2)+I(L_3)]$, of NiSi and $NiSi_2$ are respectively 0.73 and 0.70, respectively.

References

1. C.-T. Wu, Y.-J. Lee, F.-K. Hsueh, P.-J. Sung, T.-C. Cho, M. I. Current and T.-S. Chao, ECS Journal of Solid State Science and Technology **3**, P122-P125 (2014).

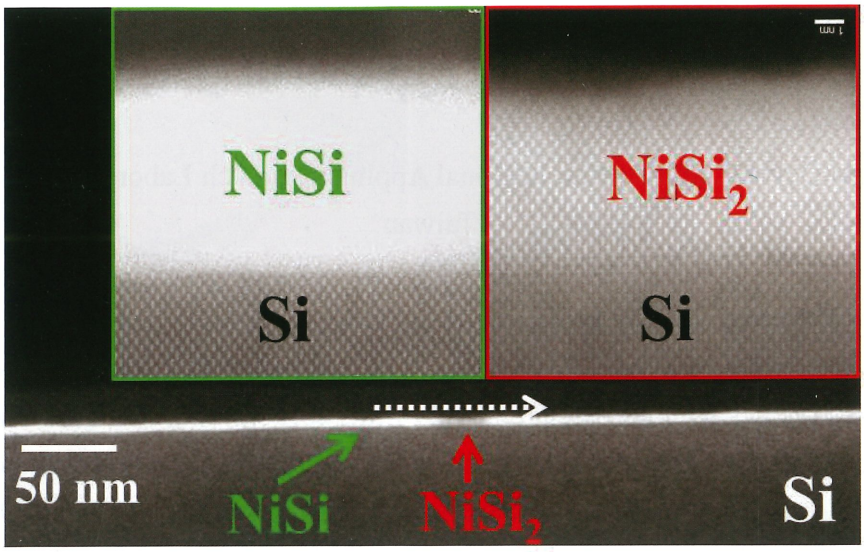

Figure 1. The [110] cross-sectional HAADF image of 4.5 nm NiSi sample. In this imaging mode, the intensity of scattering scales with the atomic number Z as $Z^{1.7}$, so the brightest features are NiSi (left insert), the gray-white features are epi-$NiSi_2$ (right insert), and the Si substrates are weakly visible.

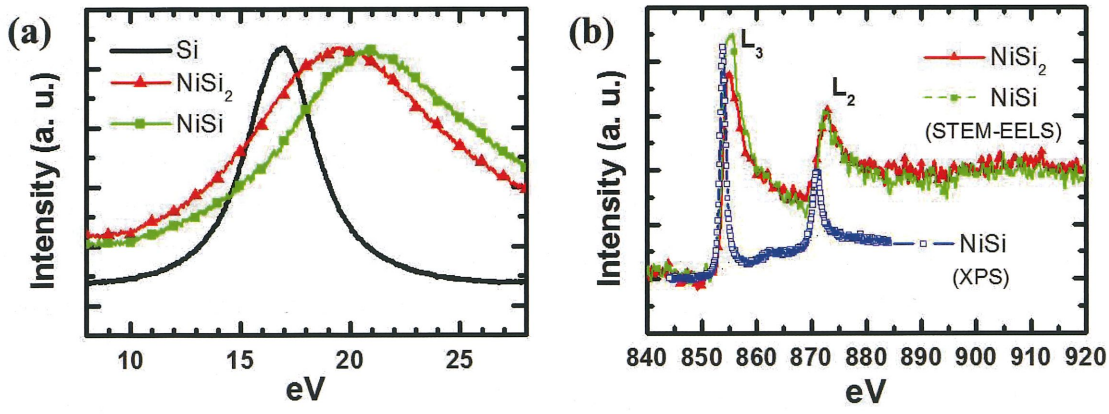

Figure 2. (a) EELS low-loss spetra of Si, $NiSi_2$ and NiSi. (b) A typical XPS Ni-$L_{2,3}$ edge spectrum of NiSi film. And the ELNES Ni-$L_{2,3}$ edge spectra of $NiSi_2$ and NiSi films.

M-P-03

ELECTRON MICROSCOPY ANALYSIS OF SIGE ALLOY AND SIGE/SI AXIAL HETEROJUNCTION NANOWIRE STRUCTURES

Yun-Yi Tsai (蔡昀嶧), Sheng-You Taso (曹勝宥), and Cheng-Yen Wen (溫政彥)

Department of Materials Science and Engineering, National Taiwan University, Taipei, Taiwan

Silicon (Si) and germanium (Ge) nanowires are potential candidates for future applications in semiconductor devices [1, 2]. SiGe alloy nanowires also exhibit excellent transport properties for thermoelectric applications [3, 4]. To realize these applications, controlling the morphology, growth direction, number density, and composition distribution of nanowires are very important. In this study, we grow Si, SiGe alloy and SiGe/Si heterojunction nanowires via the vapor-liquid-solid (VLS) mechanism [5] in a chemical vapor deposition (CVD) reactor. Si nanowires with high aspect ratios and controllable distribution are fabricated (Figs. 1a and 1b). Straight epitaxial SiGe alloy nanowires can also be grown by the same fabrication method (Fig. 1c). But for some SiGe nanowires grown with lower flow ratios of Si to Ge gas precursors, the axial nanowire growth is accompanied by significant side-wall deposition (Fig. 2a). Defects also appear at the interface between the SiGe nanowire and the Si substrate (Figs. 2b and 2c). In these SiGe nanowires, Si and Ge compositional distribution is rather uniform (Fig. 3). We notice that gold migration is significant (Figs. 3d and 4b), presumably due to the instability of catalysts during nanowire growth or in the cooling process after growth. This metal migration can be a serious problem for future nanowire-based device fabrication. Finally, axial SiGe/Si heterojunction nanowires are fabricated using a mixture of Au and Ag [6] as the catalysts. The contrast in the TEM image (Fig. 4a) shows a distinct boundary between the SiGe and Si segments in the nanowire.

References

1. S. T. Le, P. Jannaty, X. Luo, A. Zaslavsky, D. E. Perea, S. A. Dayeh, and S. T. Picraux, Nano Lett., **12** 5850 (2012).
2. J. Goldberger, A. I. Hochbaum, R. Fan, and P. D. Yang, Nano Lett., **6** 973 (2006).
3. E. K. Lee, L. Yin, Y. Lee, J. W. Lee, S. J. Lee, J. Lee, S. N. Cha, D. Whang, G. S. Hwang, K. Hippalgaonkar, A. Majumdar, C. Yu, B. L. Choi, J. M. Kim, and K. Kim, Nano Lett., **12** 2918 (2012).
4. A. I. Boukai, Y. Bunimovich, J. Tahir-Kheli, J. K. Yu, W. A. Goddard, and J. R. Heath, Nature, **451** 168 (2008).
5. R. S. Wagner and W. C. Ellis, Appl. Phys. Lett., **4** 89 (1964).
6. Y. C. Chou, C. Y. Wen, M. C. Reuter, D. Su, E. A. Stach, and F. M. Ross, Acs Nano, **6** 6407 (2012).

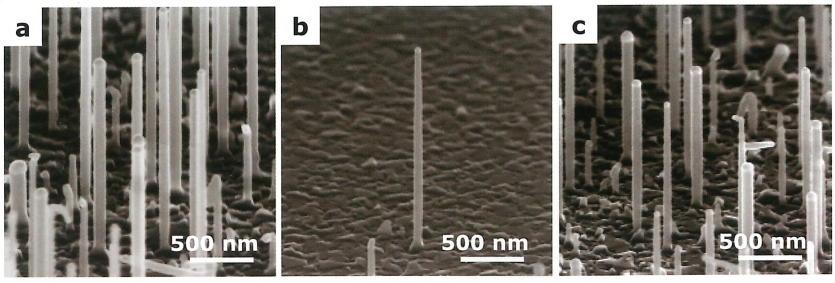

Figure 1. (a-b) SEM images of high aspect-ratio silicon nanowires with controllable number densities. (c) SEM image of SiGe nanowires.

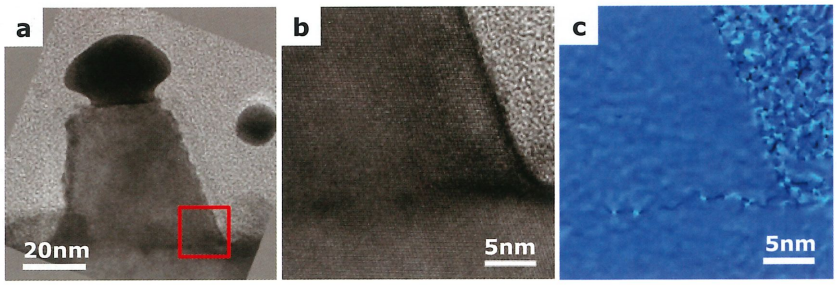

Figure 2. (a) TEM image of a SiGe nanowire grown on Si(111) substrate with a low flow ratio of Si to Ge gas precursors. (b) HRTEM image of the epitaxial growth of the SiGe nanowire and the Si substrate in (a). (c) Geometric Phase Analysis (GPA) rigid body rotation map at the interface, showing no lattice rotation between the SiGe nanowire and the Si substrate.

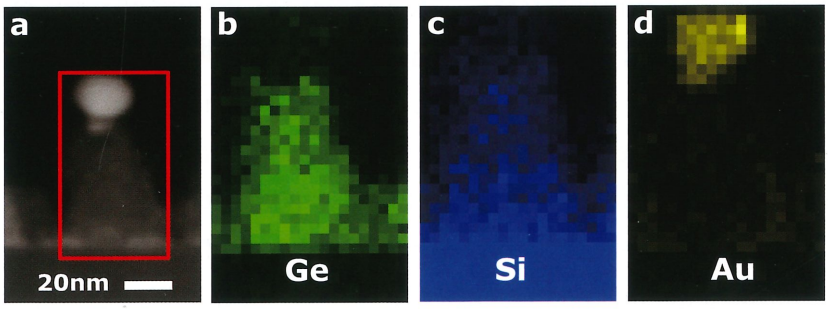

Figure 3. (a) HAADF-STEM image of a SiGe nanowire on the Si substrate. (b-d) STEM-EDS compositional maps of the area marked in (a). Si and Ge distribute uniformly in the nanowire. Au is found not only in the catalyst but also on nanowire sidewalls.

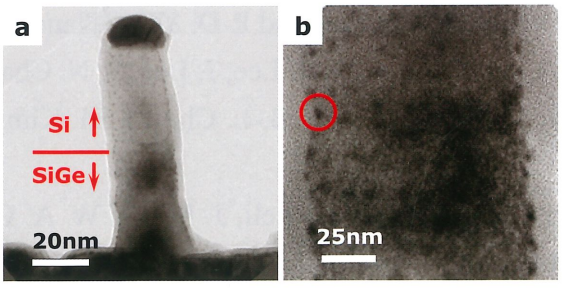

Figure 4. (a) TEM image of a SiGe/Si axial heterojunction nanowire. (b) TEM image of the nanowire body, showing strong migration of metal from the catalyst to nanowire sidewalls.

M-P-04

THE INVESTIGATION IN YIELD STRENGTH OF NB-MO LOW CARBON BAINITIC STRIP WITH AGING PROCESS

Bo-Ming Huang(黃柏銘),[1] Hung-Wei Yen(顏鴻威),[2] Simon P. Ringer,[2] Ya-Ling Chang(張雅齡), [1] Yu-Chuan Chien(簡佑全), [1] and Jer-Ren Yang(楊哲人), [1]

[1]Department of Materials Science and Engineering, National Taiwan University, Taipei, Taiwan

[2] Australian Centre for Microscopy and Microanalysis, The University of Sydney, 2006, NSW, Australia

Present work aims to study the change in secondary hardening in Nb-Mo low carbon bainitic strip during aging. The hardness of studied strip achieves maximum value at 600°C for 1 hour. At the aging condition, there is 100 MPa increment in yield strength but only 40 MPa in tensile strength. The yield/tensile stress ratio increases from 0.85 to 0.93. In detailed analysis, coalescence of bainitic ferrite and dislocation structure are excluded in affecting yield strength due to no significant change during aging. The Cottrell atmosphere and the nanometer-sized (Nb,Mo) carbides are dominant in secondary hardening in yield strength with aging process. In investigation of Cottrell effect, the Nb-Mo-C clusters segregate along dislocation line in 3-D distribution of atom probe tomography (APT) as shown in Fig.1. In conventional concept of Cottrell effect,[1] only interstitial atoms, carbon atoms are well-known to create dominant increment in yield strength during aging. In the study, Nb and Mo solute combine with carbon atoms to synergistically suppress slipping of dislocation and results from high yield/tensile stress ratio.

References

1. A. H. Cottrell and B. A. Bilby, *Proc. Phys. Soc. A,* 62 49 (1949).

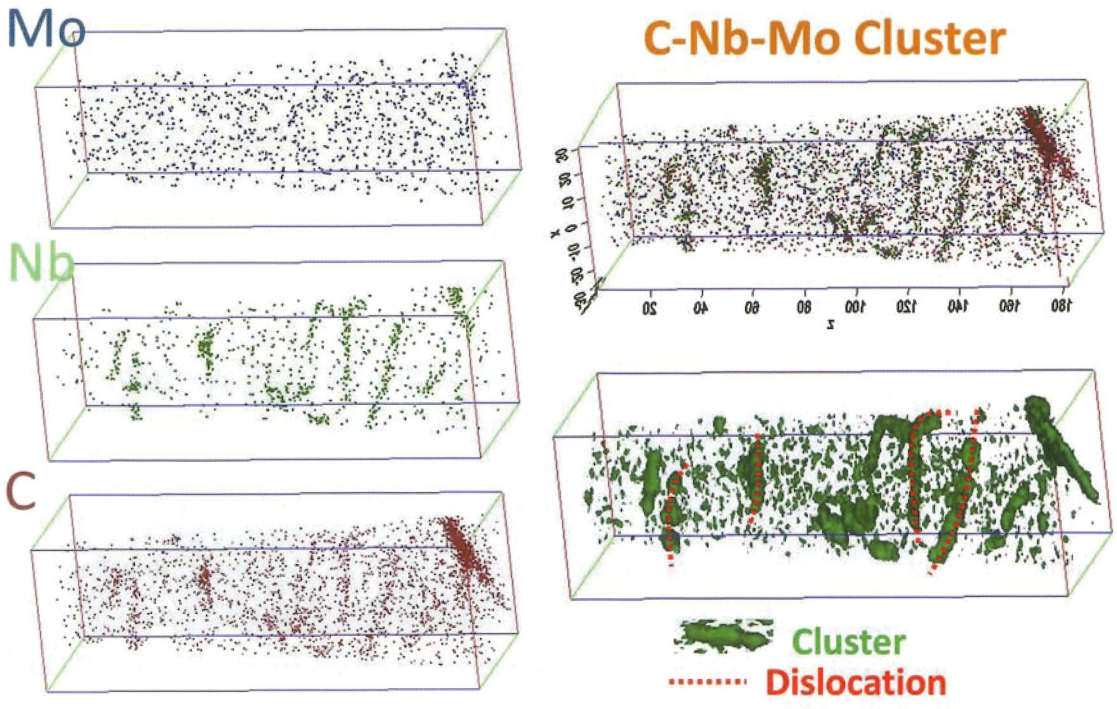

Figure 1. The distribution of C, Nb, and Mo and the corresponding cluster in granular bainite ferrite.

M-P-05

IN-SITU ENGINEERING AND CHARACTERIZATION OF GRAPHENE IN TEM

Chia-Hao Tu (涂嘉豪)[1], Jing-GuO Wen (文建國)[2], Dean Miller[2], and Chuan-Pu Liu (劉全璞)[1]

[1]Department of Materials Science and Engineering, National Cheng Kung University, Tainan, Taiwan
[2] Electron Microscopy Center, Argonne National Laboratory, Illinois, USA

This paper demonstrates the graphene sheets can be engineered by electron beam. With the electron irradiation the amorphous layer on top of the graphene sheet grown by CVD on copper foil can be cleaned away. The width of graphene nanoribbons also can be shrunk under electron beam irradiation, as shown in Fig. 1. The shape of the edge of graphene nanoribbons can be tuned as well. At the same condition, multi-layer graphene grown by solid state diffusion can peeled to single-layer. These phenomena were all recorded by high-resolution TEM with Cs and Cc aberration corrector.

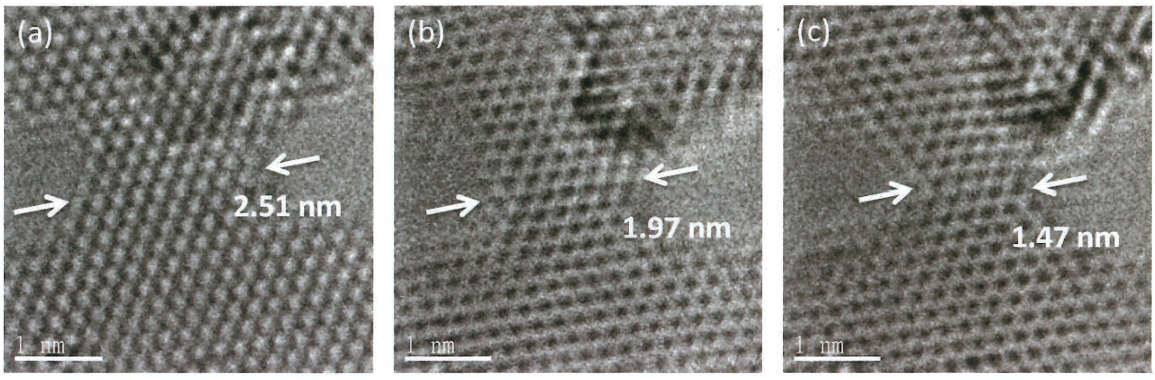

Figure 1. (a) to (c) The width of graphene nanobridge becomes from 2.51 to 1.47 nm by electron beam radiation.

M-P-06

STRUCTURAL INVESTIGATION OF ZNO:AL FILMS DEPOSITED ON THE SI SUBSTRATES BY RADIO FREQUENCY MAGNETRON SPUTTERING

Yi-Yan Chen (陳苡諺),[1] Jer-Ren Yang (楊哲人),[1] Shao-Liang Cheng (鄭紹良), [2] and Makoto Shiojiri[3]

[1] Department of Materials Science and Engineering, National Taiwan University, Taipei, Taiwan

[2] Department of Chemical and Materials Science Engineering, National Central University, Taoyuan, Taiwan

[3] Professor Emeritus of Kyoto Institute of Technology, 1-297 Wakiyama, Kyoto, Japan

Transparent conducting oxide (TCO) films are widely applied in optical and electronic devices.[1,2] Among these TCO materials, ZnO:Al has attracted much attention because it is an abundant, inexpensive, non-toxic and environmentally friendly raw material with high crystallinity and good conductivity that is easy to prepare. In this study, ZnO:Al films 400 nm thick were prepared on (100) Si substrates by magnetron sputtering at room temperature and no bias was applied on the substrate. The present samples were not treated with post-deposition annealing. From EDS and TEM, seen in Figures 1 and 2, the resulting film consisted of three layers: an amorphous silicon oxide layer, a crystalline Si layer including a small amount of Zn, and the ZnO:Al main film. It revealed that in the initial stage of the deposition, an amorphous silicon oxide layer about 4 nm thick formed from damage to the Si substrate due to sputtered particle bombardment and the incorporation of Si atoms with oxygen. Then a crystalline Si (Zn) layer about 30 nm thick grew on the silicon oxide layer by co-deposition of Si atoms sputtered away from the substrate with Zn atoms from the target. When the deposited film grew over the critical thickness of 30 nm, Si atoms were no longer ejected from the substrate. Finally, a ZnO:Al film with columnar grains normal to the substrate surface was deposited on the Si (Zn) layer. The sputtered particle bombardment greatly influenced the structure of the object films. The (0001) lattice fringes of the ZnO:Al film were observed in high-resolution TEM images, seen in Figure 3, and the forbidden 0001 reflection spots in electron diffraction patterns were attributed to double diffraction. It should be emphasized that the energetic particles and/or ions bombarding the substrate, in particular at an early stage of deposition, form layers in unexpected phases on the substrate, which may greatly influence the optical and electrical properties of the fabricated ZnO:Al films.

References

1. S. Fernández, O. de Abril, F.B. Naranjo, J.J. Gandía, Sol. Energy Mater. Sol. Cells, 95 2281 (2011).
2. J.K. Jeong, Semicond. Sci. Technol., 26 034008 (2011).

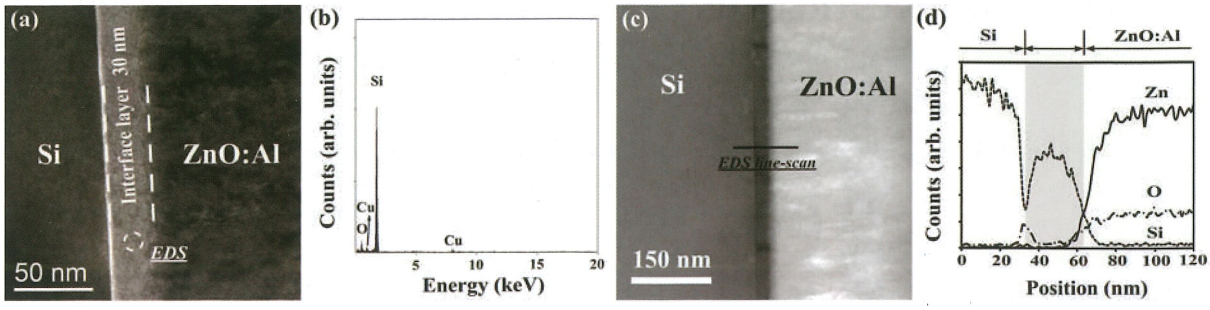

Figure 1 (a) TEM image of ZnO:Al film deposited on the (001) Si substrate by RF magnetron sputtering. (b) EDS from the dotted circle area in (a). (c) HAADF STEM image of the ZnO:Al/Si. (d) EDS line-scan profiles along the line indicated in (c). An interface layer with brighter contrast in (a) and with darker contrast in (c) was formed.

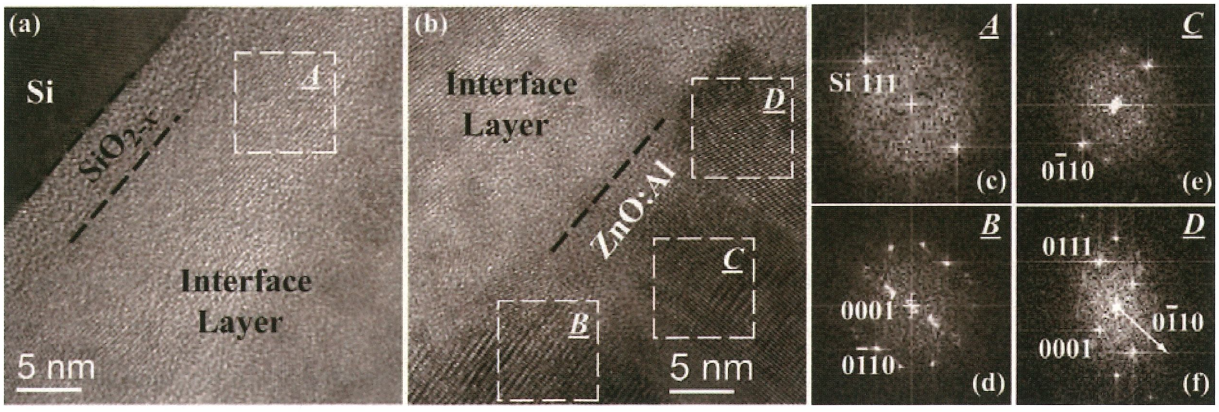

Figure 2 (a) HR-TEM image of the interface layer/Si substrate. (b) HR-TEM image of the ZnO:Al film/interface layer. (c)-(f) The corresponding FFT images to the images in areas A-D, respectively.

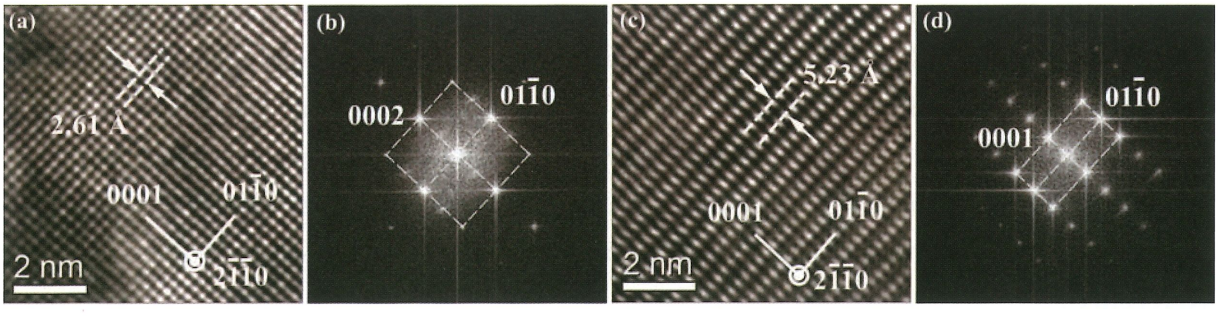

Figure 3 (a) and (c) HR-TEM images of different areas in the ZnO:Al film. (b) and (d) the corresponding FFT images to the images in (a) and (d), respectively.

M-P-07

VERTICALLY-ALIGNED ZINC OXIDE NANOWIRE GROWTH AT LOW TEMPERATURES

Kuan-Hung Chen (陳冠宏), Yun-Yi Tsai (蔡昀嶧), Chia-Hao Yu (余家濠), and Cheng-Yen Wen (溫政彥)

Department of Materials Science and Engineering, National Taiwan University, Taiwan

Zinc oxide (ZnO) nanowires possess novel electronic and optical properties, which make them promising candidates for future device applications. For facilitating these applications, controlling the morphology, alignment, and aspect ratio of ZnO nanowires is very important. In this study, we focus on the growth of vertical ZnO nanowires on substrates at low temperatures by two methods: catalyst-free physical vapor deposition (PVD) and the seeded hydrothermal synthesis process. The orientation of ZnO nanowires and the effects of growth parameters on their morphology are studied using scanning electron microscopy (SEM) and high-resolution transmission electron microscopy (HRTEM) analysis. Well-distributed vertical ZnO nanowires can be grown on Si substrates by the PVD method as shown in Fig. 1(a). An interfacial layer is found between the substrate and the nanowire array, suggesting that the growth of ZnO nanowires follows the self-catalyzed mechanism [1], but it is interesting to know that the growth direction is along the c-axis of ZnO wurzite structure, as shown in Fig. 1(b). In contrast, forming a seed layer is a more effective approach to control the growth direction of the ZnO nanowire array on substrates [2]. TEM analysis of the ZnO seed layer prepared by thermal decomposition of zinc acetate shows that a layer of ZnO grains is formed on substrates as shown in Figs. 2(a, b). The well-distributed ZnO grains with their c-axes normal to the substrate provide nucleation sites for vertical nanowire growth in the hydrothermal synthesis [3]. The ZnO nanowire arrays can therefore have a high aspect ratio and good alignment on substrates under adequate growth conditions [4, 5], as shown in Figs. 3(a, b).

References

1. S. C. Lyu, Y. Zhang, C. J. Lee, H. Ruh, and H. J. Lee, Chem. Mater., 15 3294 (2003).
2. L. E. Greene, M. Law, D. H. Tan, M. Montano, J. Goldberger, G. Somorjai, and P. D. Yang, Nano Lett., 5 1231 (2005).
3. L. E. Greene, B. D. Yuhas, M. Law, D. Zitoun, and P. D. Yang, Inorg. Chem., 45 7535 (2006).
4. Y. Zhou, W. B. Wu, G. D. Hu, H. T. Wu, and S. G. Cui, Mater. Res. Bull., 43 2113 (2008).
5. J. H. Tian, J. Hu, S. S. Li, F. Zhang, J. Liu, J. Shi, X. Li, Z. Q. Tian, and Y. Chen, Nanotechnology, 22 245601 (2011).

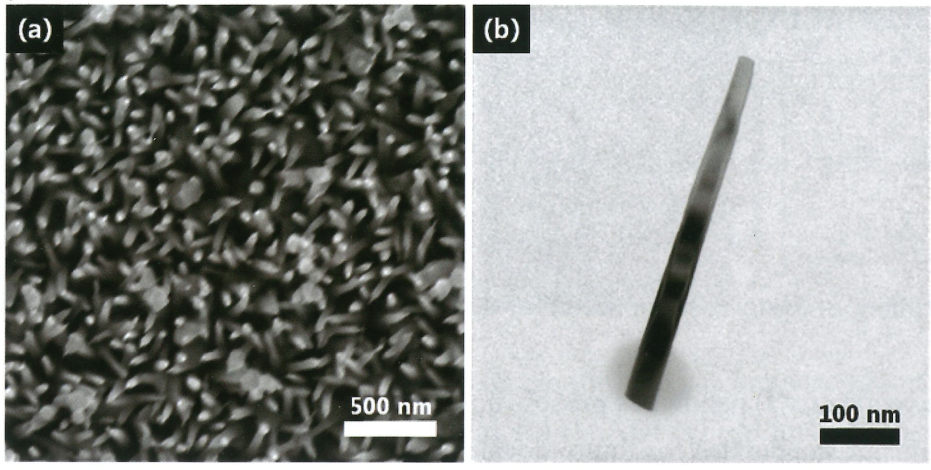

Figure 1. (a) SEM image of ZnO nanowire arrays grown on the Si substrate. (b) TEM image of the ZnO nanowire prepared by catalyst-free physical vapor deposition.

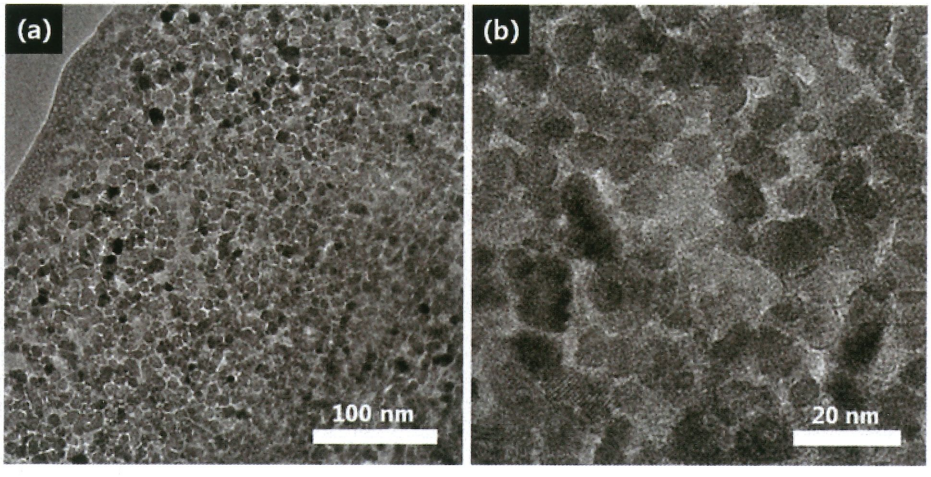

Figure 2. (a, b) TEM images of the ZnO seed layer prepared by thermal decomposition of zinc acetate.

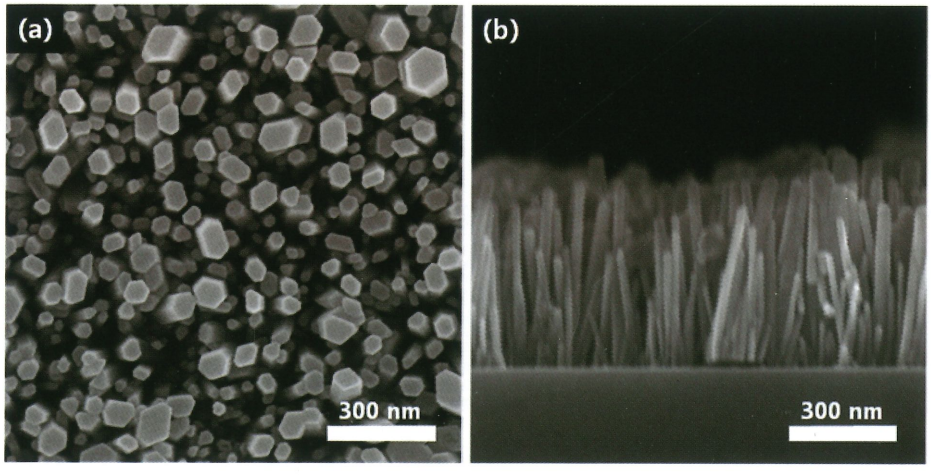

Figure 3. (a) Plan-view and (b) cross-sectional SEM image of the hydrothermal synthesized ZnO nanowire arrays grown on the ZnO seed layer.

M-P-08

ATOMIC-SCALE PROBING OF THE CHARGE DISTRIBUTION CHARACTERISTICS AT THE OXIDE INTERFACES

Ching-Pin Chang (張景斌),[12] Ming-Wen Chu (朱明文),[1] Jauyn Grace Lin (林昭吟),[1] Su-Ling Cheng (鄭淑齡),[12] Jer-Ren Yang (楊哲人),[2] and Cheng-Hsuan Chen (陳正弦)[1]

[1] Center for Condensed Matter Sciences, National Taiwan University, Taipei, Taiwan
[2] Department of Materials Science and Engineering, National Taiwan University, Taipei, Taiwan

Upon joining the non-polar $(Ti^{4+}O_2)^0$ plane of band-insulating $Sr^{2+}Ti^{4+}O_3$ (STO) with the polar plane of an insulating oxide, the polar-discontinuous interface can become metallic. This exotic phenomenon has been generally described by the charge transfer from the polar to non-polar planes to avoid the polar discontinuity, forming a conductive two-dimensional electron gas (2DEG) near the interface in STO. The 2DEG at the metallic interfaces of $La^{3+}Al^{3+}O_3$/STO and $La^{3+}Ti^{3+}O_3$/STO, primitively $(LaO)^{1+}$-$(TiO_2)^0$, represents a grand classic. Nevertheless, there exist a vast group of oxides other than $LaAlO_3$ and $LaTiO_3$, such as the strongly-correlated, mixed-valence manganites characterized by intricate interplays among the characteristic charge, lattice, orbital, and spin degrees of freedom. Growing such strongly-correlated oxides on STO with a designated primitive polar discontinuity, would the established wisdom of 2DEG in STO be still observed? Furthermore, the film-substrate misfit strains can be relaxed by one-dimensional misfit dislocations, forming semi-coherent interfaces characterized by strained dislocation cores and inter-dislocation epitaxial regions with vanishing strains. How the localized strain field of one-dimensional misfit dislocations would affect the extended oxide-interfacial charges is intriguing and remains unresolved. To explore these emergent questions, we have grown two different morphologies, coherent (defect free) and semi-coherent (misfit dislocations), $(Nd_{0.35}Sr_{0.65})MnO_3$/STO heterostructures with a primitively polar-discontinuous interface of $(Mn^{3.65+}O_2)^{0.35-}$-$(Nd_{0.35}Sr_{0.65}O)^{0.35+}$-$(TiO_2)^0$-$(SrO)^0$. The interface was tackled using atomically-resolved electron energy-loss spectroscopy (EELS) in an aberration-corrected scanning transmission electron microscope (STEM; electron probe, ~1.2 Å).

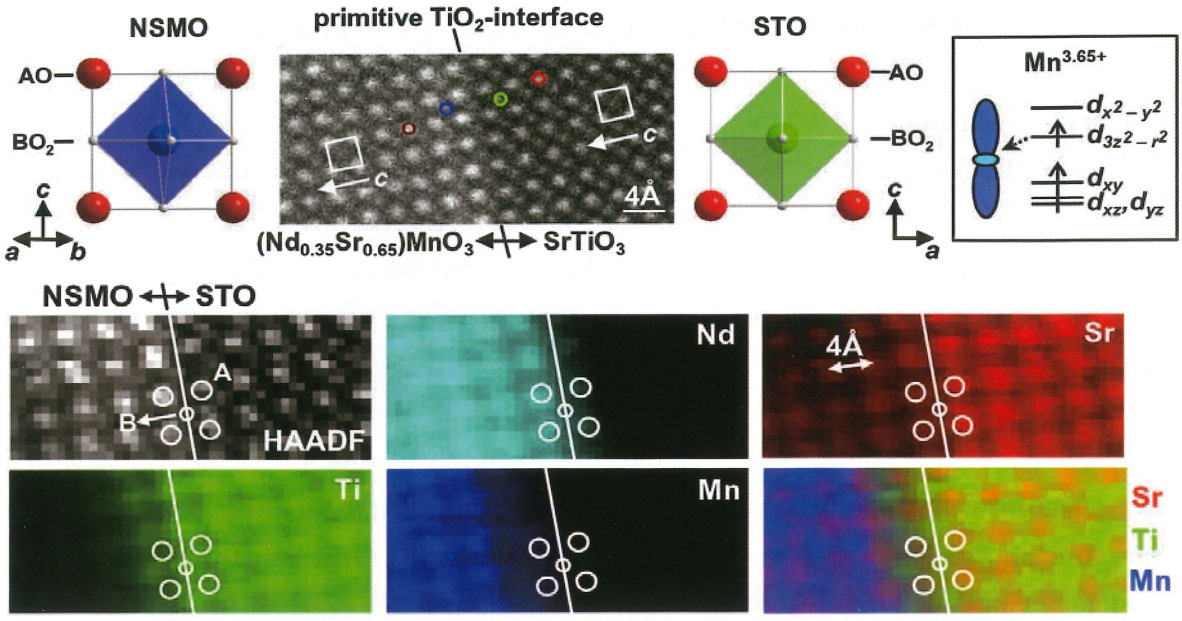

Figure 1. STEM imaging and STEM-EELS chemical mapping of the coherent (defect free) $(Nd_{0.35}Sr_{0.65})MnO_3/SrTiO_3$ interfaces.

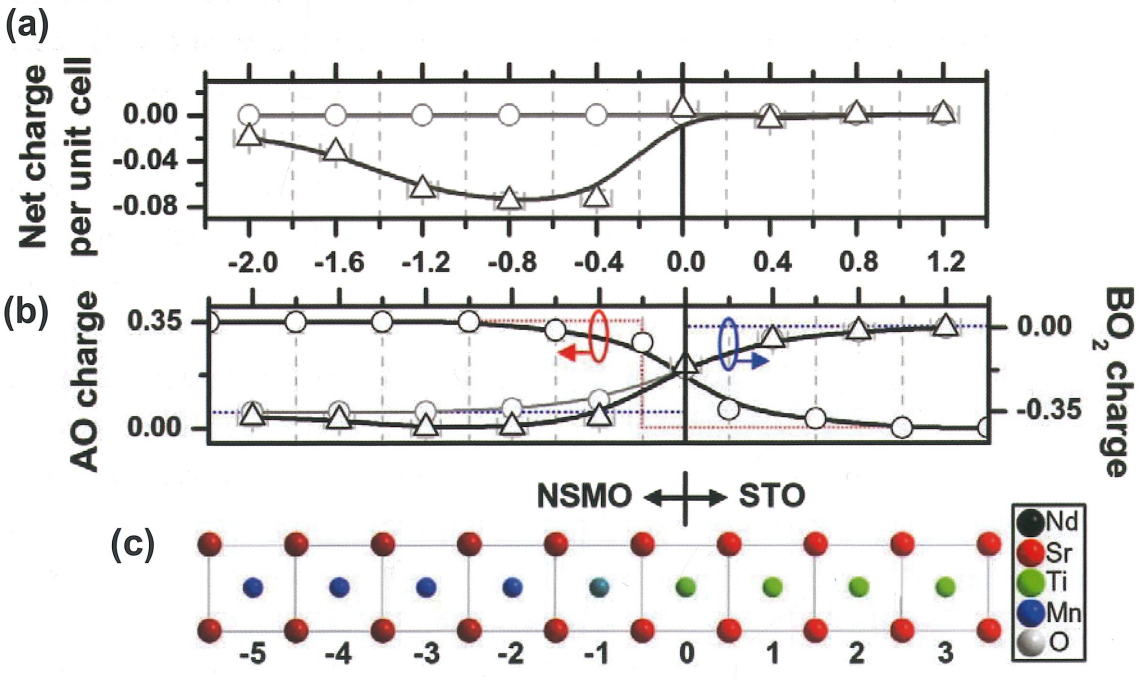

Figure 2. Interfacial charge characteristics

M-P-09

FABRICATION AND STUDY OF HIGH ENERGY RESOLUTION SILICON DRIFT DETECTOR FOR ENERGY DISPERSIVE X-RAY SPECTROMETER

Chiao-Chun Hsu (許喬竣),[1] Fan-Gang Tseng (曾繁根),[1] Fu-Rong Chen (陳福榮),[1] Chih-Hao Lee (李志浩),[1] Yun-Ju Chuang (莊昀儒)[2]

[1]Department of Engineering and System Science, National Tsing Hua University, Hsinchu, Taiwan

[2]Department of Biomedical Engineering, Ming Chuan University, Taipei, Taiwan

Energy Dispersive X-ray Spectrometer (EDS) is the most common analytical tool in SEM and TEM used for the elemental analysis or chemical characterization of a sample. The most critical part in EDS system is the x-ray detector. In the past, the most solid-state detectors used in X-ray spectroscopy system are made of Si(Li) crystal. The incorporation of lithium atoms into silicon can greatly reduce the space charge from the bulk of silicon and thick detectors could be fabricated and operated at reasonable biasing voltage. The major drawback of Si(Li) detector is that they require hours to cool down by liquid nitrogen to reduce electrical noise before use, and cannot be allowed to warm up during operation. Besides, the increase of Si(Li) detection area will increase the capacitance and electronic noise that will lead to lower response time and sensitivity. There is a trend towards a new EDS detector over past decade, called the silicon drift detector (SDD).[1] The key advantage of the SDD is the very lower anode capacitance compared with conventional Si(Li) detectors of the same active detection area. This unique feature reduces electronic noise and shortens processing shaping time to achieve higher energy resolution and counting rate. Due to the small anode in the SDD the leakage current is so low that the SDD can be operated with moderate cooling simply by Peltier cooler.

Silicon Drift detector for EDS has been designed, fabricated and tested.(Fig.2) The SDDs were fabricated on n-type <111> and a resistivity of more than 4kΩ.cm silicon substrates with a thickness of 400μm. The SDD consists of fully depleted silicon, in which an electric field with a strong component parallel to the surface drives electrons generated by the absorption of x-ray towards a small sized collecting anode. The electric field is generated by a number of increasingly reverse biased cathodes on one side surface of the device. The radiation entrance window on the opposite side is made by a non-structured shallow implanted junction giving a homogeneous X-ray entrance surface over the whole detection area and allows lower energy x-ray can be detected.

SDD comprise non-structured shallow implanted junction and the anode guard ring for improving the energy resolution of detector. (Fig.1) First, if the p-n junction is located at deep depth, the thickness of dead layer will to thick. Therefore the non-structured shallow implanted junction allows minimizing the dead layer of detector and also prevents the unnecessary absorption of X-ray by the structure metal layer on the surface of entrance

window. Second, the electrons attracted by positive fixed charges at the Si/SiO_2 interface are collected by the anode guard ring rather than contributing to the leakage current of detector. It is helpful to reduce leakage current and increasing signal to noise ratio.

SDD were characterized to extract critical I-V performance parameter like total leakage current at anode. The value of leakage current of ring_2 is 248 nA without anode guard ring, and reduces to 4 nA with anode guard ring. (Fig.3)And will test the response for detector exposed to the X-ray source in the future. The goal of the testing have shown a FWHM at $Mn_{K\alpha}$ line of a radioactive ^{55}Fe source of 170 eV at -20℃.

References

[1] E. Gatti and P. Rehak, "Semiconductor drift chamber—an application of a novel charge transport scheme," Nuclear Instruments and Methods in Physics Research, vol. 225, pp. 608-614, 1984.

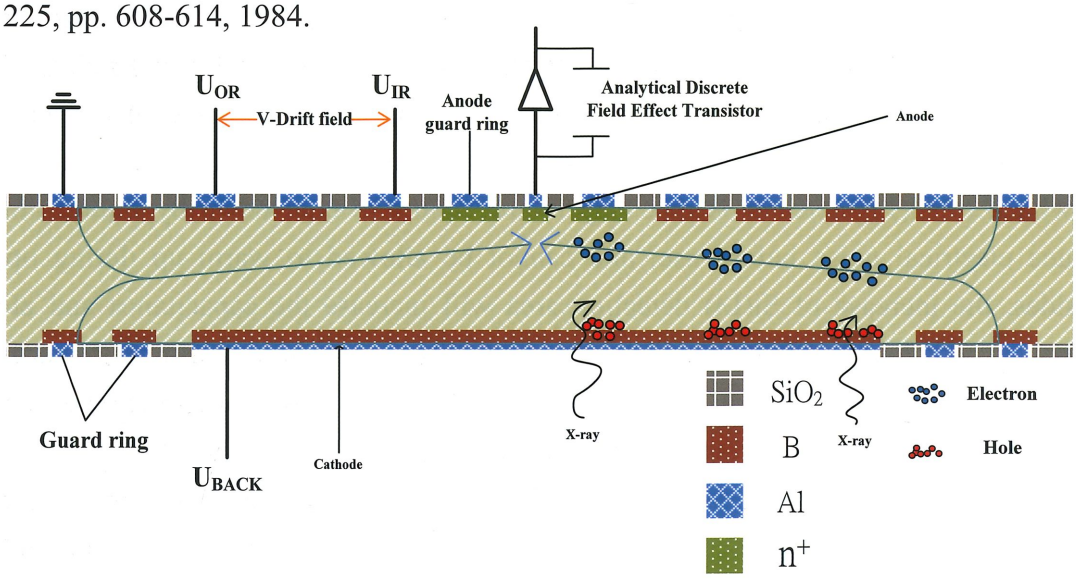

Fig.1 Cross section and operation scheme of a SDD detector with anode guard rings and non-structured homogeneous x-ray entrance window.

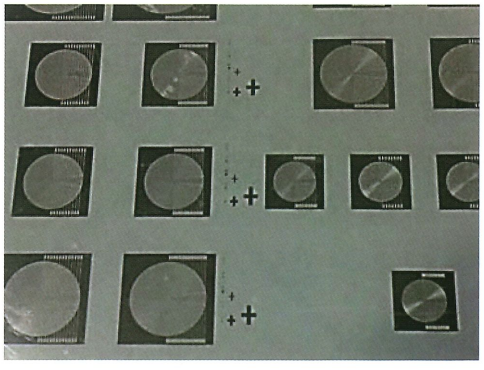

Fig. 2 Photo image of a fabricated silicon drift detectors.

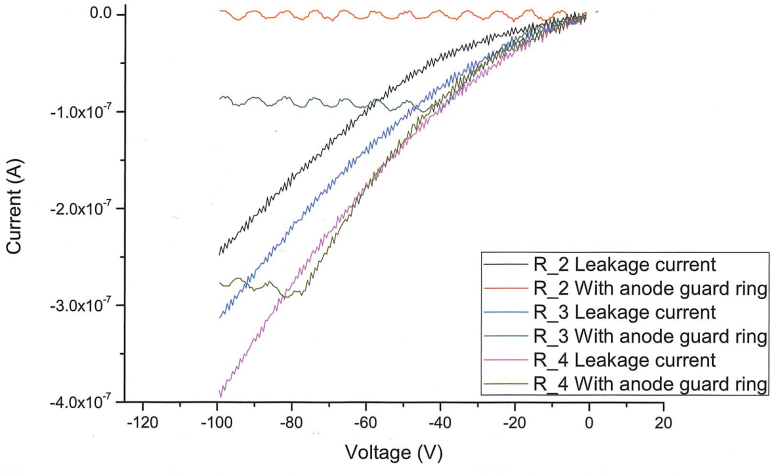

Fig. 3 Leakage current of SDD with testing anode guard ring

M-P-10

DIRECT IMAGING OF ATOMIC STRUCTURE OF TIN/MGO(001) INTERFACE BY CS-CORRECTED STEM

Lin-Lung Wei (魏伶容), Hien Do (杜氏賢), Li Chang (張立)

Department of Materials Science and Engineering, National Chiao Tung University, Hsinchu, Taiwan

Thin films of titanium nitride (TiN) have a wide range of industrial applications because of its good electrical property, high hardness, excellent heat resistance and chemical stability [1,2]. High-quality TiN coating on oxides may extend its applications if the interfacial properties can be understood. Here we characterize the TiN/MgO interface using STEM annual dark field (ADF) imaging technique and make a comparison of image contrast among the different elements. Though ADF images can easily provide direct visualization of atomic column positions of heavy atoms, for light elements it is usually invisible even at high resolution.

STEM ADF imaging was performed in a Cs-corrected JEOL ARM200F microscope with a Schottky gun at 200 kV with 0.08 nm probe and inner collection angle of 90 mrad. High-quality epitaxial TiN thin films were grown on MgO substrate by pulsed laser deposition method as sevidenced by the (002) X-ray rocking curve of full-width at half-maximum in 60 arcsec. Cross-sectional STEM specimens were prepared by tripod polishing method, followed by Ar-ion milling at angle of 4-5° and 3 - 4.5 kV.

In all acquired ADF images, atomic positions of Ti and Mg exhibit strong bright contrast with O in weak but visible bright contrast, whereas the contrast of N atoms is hardly observed, as shown in Fig. 1. The contrast can be further improved as shown in the filtered images (the insets in Fig. 1) in which O positions are more clearly visible while N ones are still barely seen. Also, the interfacial region shows s distinctly different contrast from TiN and MgO. From the line profile analysis, the intensity variation across the interface is detectable in the range of 2 - 3 atomic layers, suggesting that interdiffusion between MgO and TiN may occur. Also, it can be shown from the ADF images that TiN and MgO is almost fully coherent cross the diffuse interface layer with epitaxial relationships of $(001)_{TiN}//(001)_{MgO}$ and $[1\bar{1}0]_{TiN}//[1\bar{1}0]_{MgO}$ because of a small lattice mismatch (δ=0.466%) between MgO and TiN for both of which have NaCl-type structure with lattice parameter of a_{MgO} = 0.428nm and a_{TiN} = 0.430 nm, respectively.

References

1. M. Popović*, M. Novaković, Z. Rakočević, N. Bibić, Processing and Application of Ceramics 19 (2011).
2. D. Chen, X. L. Ma, Y. M. Wang, and L. Chen, PHYSICAL REVIEW 69 155401 (2004).

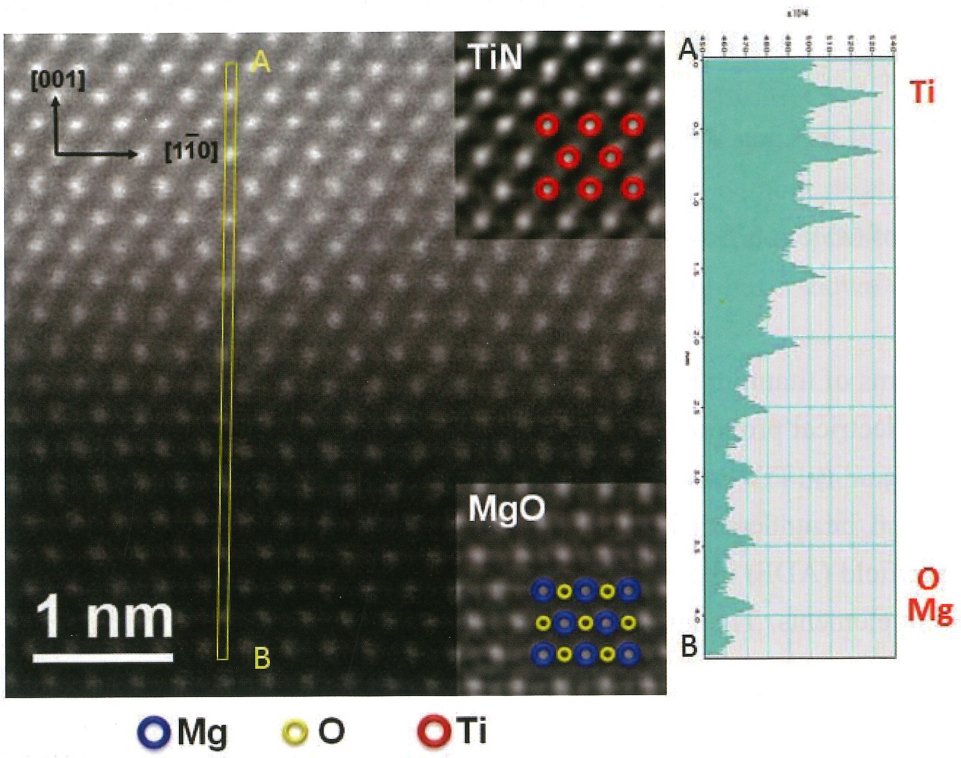

Figure 1. ADF image of the TiN/MgO interface [110] zone axis. Ti, Mg and O atomic positions as marked in TiN and MgO filtered images in the insets. The line profile (from A to B) showing the gradual variation in intensity from TiN to MgO.

M-P-11

CHARGE-DENSITY WAVE AND DOMAIN-CONTRAST REVERSALS IN A THREE-DIMENSIONAL MATERIAL SYSTEM OBSERVED BY TRANSMISSION ELECTRON MICROSCOPY

MING-HAO LEE （李明浩）, C. H. Chen（陳正弦）, and M.-W. Chu（朱明文）

Center for Condensed Matter Sciences, National Taiwan University, Taipei 106, Taiwan

The charge-density wave (CDW) is an electronic ground state with broken translational symmetry brought by correlated electron-phonon interactions. Decades of studies on the subject have established that a highly anisotropic band structure is essential for the emergence of this ground state and is characteristic to a wide spectrum of low-dimensional materials. Indeed, CDW has been largely found in one-dimensional (1D) and two-dimensional (2D) material systems such as $NbSe_3$ and $TaSe_2$. The existence of CDW in three-dimensional materials is usually not expected.

It is not found until recently that the tetragonal rare-earth transition-metal silicide system with three-dimensional crystallographic structure $R_5T_4Si_{10}$, where R is Dy, Ho, Er, Tm, and Lu, and T = Ir and Rh, can exhibit CDW phase transitions. Here, we report the investigations of CDW in $Dy_5Ir_4Si_{10}$ at different temperatures using transmission electron microscopy (TEM) techniques including electron diffraction (Figure 1) and dark-field superlattice imaging. Incommensurate superlattice diffraction spots along c axis were observed in the electron diffraction patterns (Figure 2) when the sample was cooled below the well-known CDW transition temperature at ~208 K. CDW becomes commensurate with further cooling and configurations of CDW dislocations imaged by the dark-field technique convincingly show that the CDW phase transition is accompanied by a concomitant cell-doubling structural phase transition. Intriguingly, the cell-doubling transition is featured by an inversion-symmetry breaking observed by further convergent beam electron diffraction. A disparity in the CDW modulation vectors, q_+ and q_-, readily arises, breaking the CDW principle that the associated modulations should remain invariant upon spatial inversion. Upon dark-field imaging using respective q_+ and q_-, we surprisingly observed the contrast reversal of the CDW domains (Figure 3), a phenomenon largely undocumented in the past. The potential linking of this discovery to the emergent chiral CDW, which allow the breakdown of the spatial-invariant principle, was discussed.

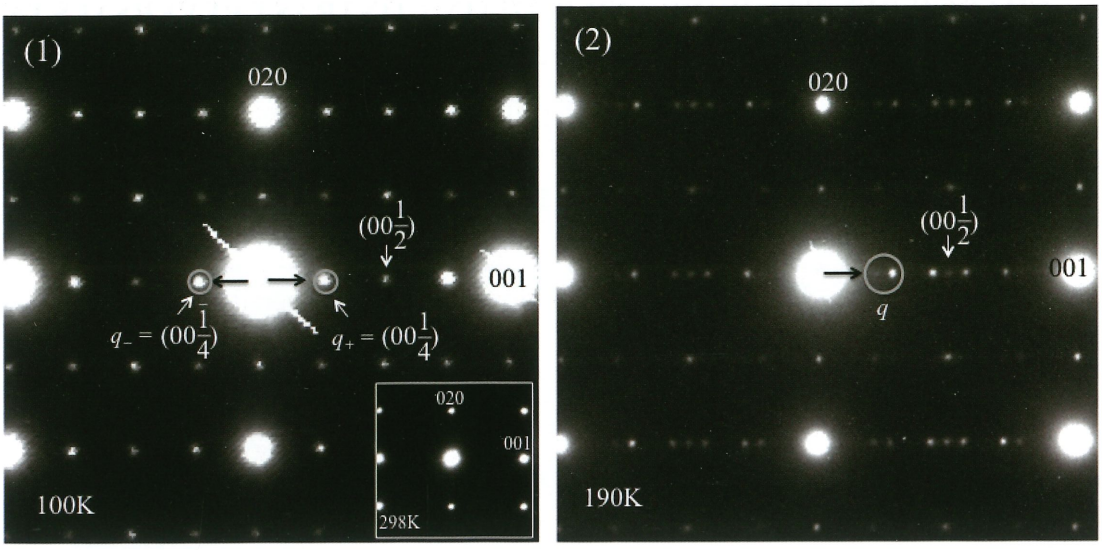

(1) Electron-diffraction pattern along the [100] zone axis obtained at 100 K, which shows the commensurate superlattice spots of CDW modulations characterized by q_+ = (0, 0, ¼) and q_- = (0, 0, –¼). The length between center to (001) Bragg peak corresponds to 1.48 $Å^{-1}$. The room-temperature pattern along the same projection is also shown (inset). (2) [100]-zone-axis diffraction pattern taken at the same sample region to (1) at otherwise 190 K, showing the emergence of incommensurate superlattice peaks as indicated by the white circle.

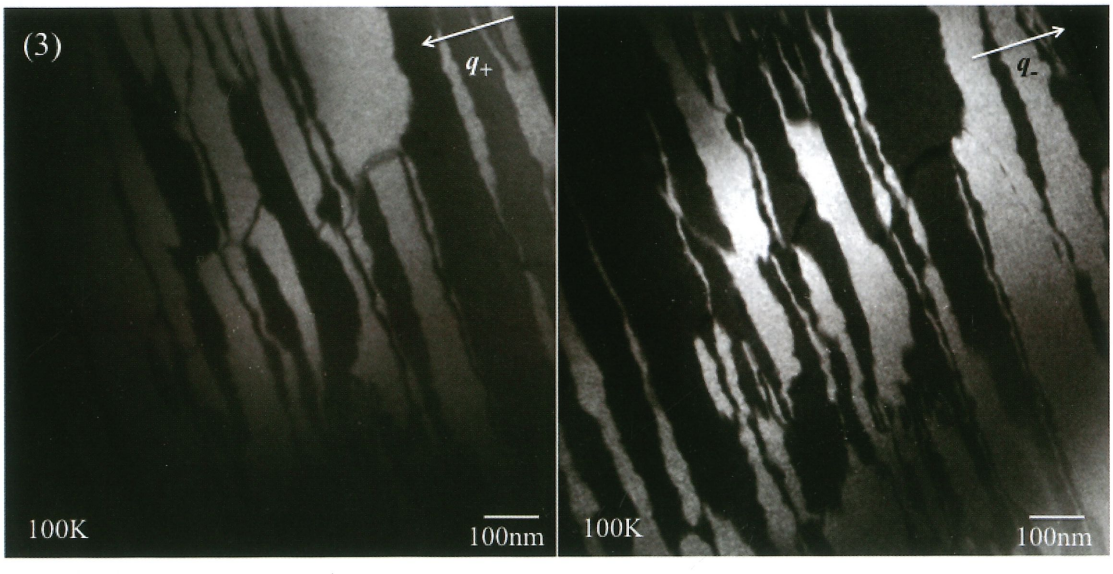

(3), the superlattice dark-field TEM images obtained from the respective commensurate q_+ = (0, 0, ¼) and q_- = (0, 0, –¼) vectors in Fig. 1. The reversed contrasts of one to the other clearly indicate that the modulation vectors, q_+ and q_-, actually come from different domains as a result of the symmetry breaking along *c* axis upon the CDW modulation.

M-P-12

THE GROWTH OF LENTICULAR MARTENSITE IN AISI 440C STAINLESS STEEL

*Ya-Ling Chang (張雅齡),[1] Yi-Ling Tsai (蔡宇庭),[1] Po-Yu Chen (陳伯宇), [1] and Jer-Ren Yang (楊哲人)[1]

[1]Department of Materials Science and Engineering, National Taiwan University, Taipei, Taiwan

This research focuses on the microstructure of lenticular martensite in AISI 440C stainless steel. By adjusting the austenization temperature, the lenticular martensite structure can be observed after deep cryogenic treatment. The most appropriate austenization temperature for analyzing is about 1150°C due to its large austenite grain size and almost no lenticular martensite impinging on each other, which is important for analyzing the orientation of martensite units. The growing arrangement of lenticular martensite was investigated by EBSD technique, which showed that the misorientation between each lenticular martensite grains tends to be high angle. In the TEM observation result, it indicated that there are three regions in lenticular martensite: midrib, twinned region, and untwinned region. The screw dislocation a/2[1$\bar{1}$1] in untwinned region can be seen as the product of martensite transformation, which also showed that the lenticular martensite transformation is a combination of twin mode and slip mode.

References

1. M. Umemoto, C. M. Wayman, Acta Metallurgica, Vol. 26, 1978, p. 1529-1549.
2. Y. Liu and J. Pietikainen, Scripta Metallurgica et Materialia, Vol. 27, 1992, p.887-892.
3. A. Stormvinter, P. Hedstrom and A. Borgenstam, J. Mater. Sci. Technol, Vol. 29, 2013, pp. 373-379
4. H. Okamoto, M. Oka and I. Tamura, Trans. JIM, Vol. 19, 1978, pp. 674-684
5. A. Stormvinter, G. Miyamoto, T. Furuhara, P. Hedstrom and A. Borgenstam, Acta Materialia, Vol. 60, 2012, pp.7265-7274
6. T. Chiba, G. Miyamoto and T. Furuhara, Scripta Materialia, Vol. 67, 2012, pp.324-327
7. T. Chiba, G. Miyamoto and T. Furuhara, ISIJ International, Vol. 53, 2013, pp.915-919
8. C. M. Wayman, Martensite, pp. 215
9. X. M. Zhang, X, Zhao, J. X. Zhong and Y. Qi, Scripta Metallurgica et Materialia, Vol. 24, 1990, p.1953-1958
10. A. Shibata, S. Morito, T. Furuhara, T. Maki, Scripta Materialia, Vol. 53, 2005, pp. 597-602
11. G. Miyamoyo, A. Shibata, T. Maki, T. Furuhara, Acta Materialia, Vol. 57, 2009, pp.

1120-1131.

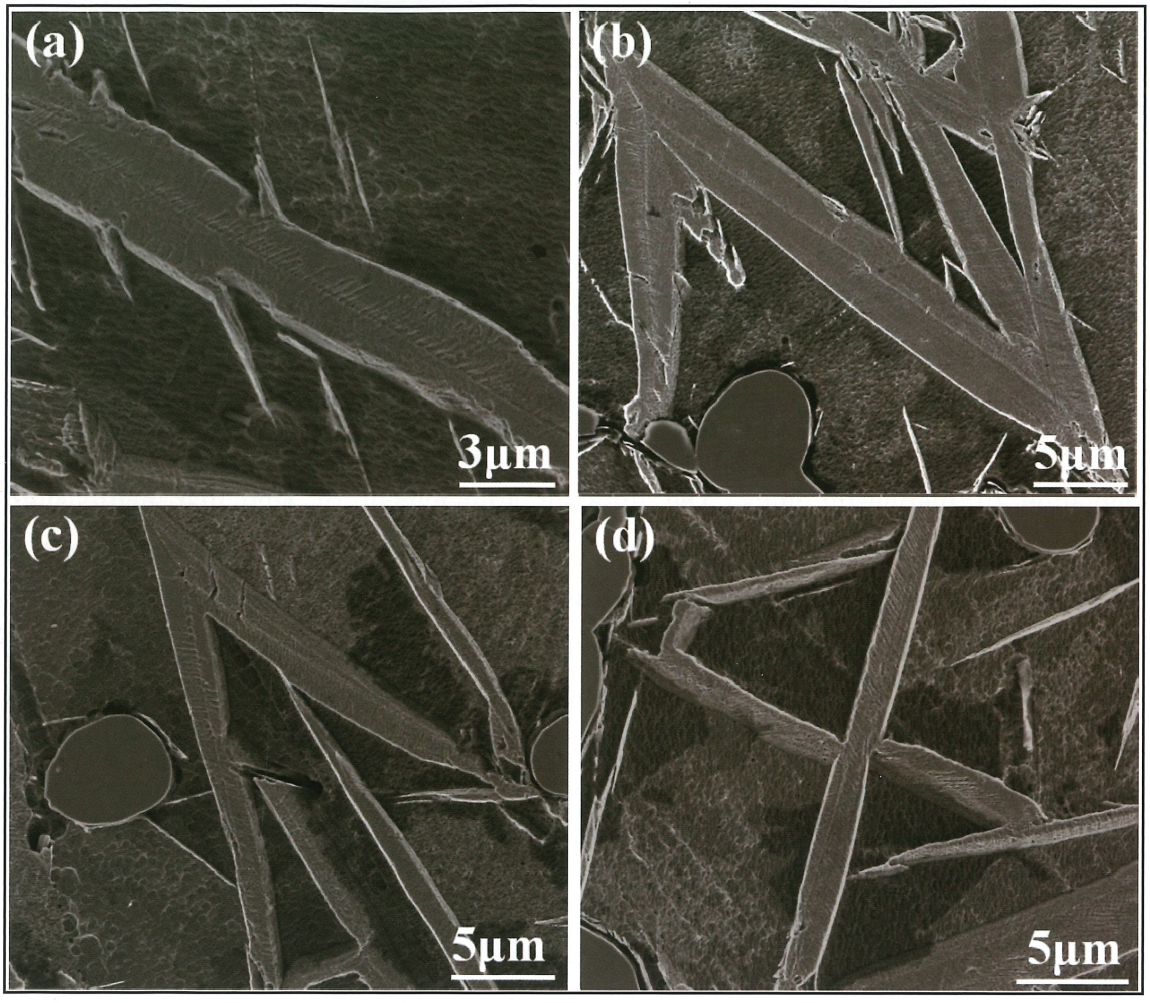

Fig. 1 SEM image shown the(a) kink (b) zigzag array (c) spear (d) crossed region morphology of lenticular martensite.

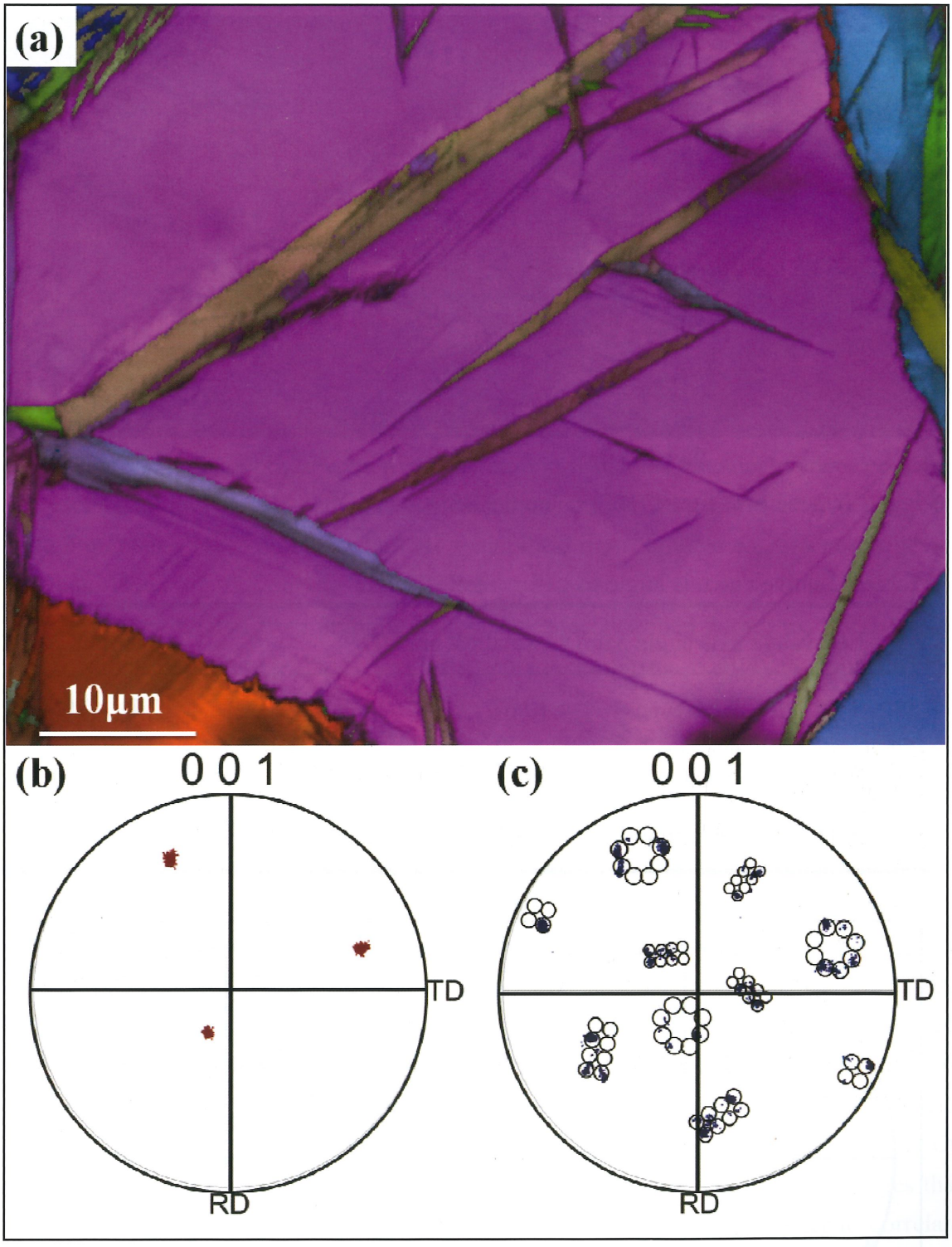

Fig. 2 (a)Inverse pole figure (IPF) colored EBSD map. The {100} pole figure of (c)simulated K-S OR variants containing lenticular martensite crystal orientations inside an (b)austenite grain.

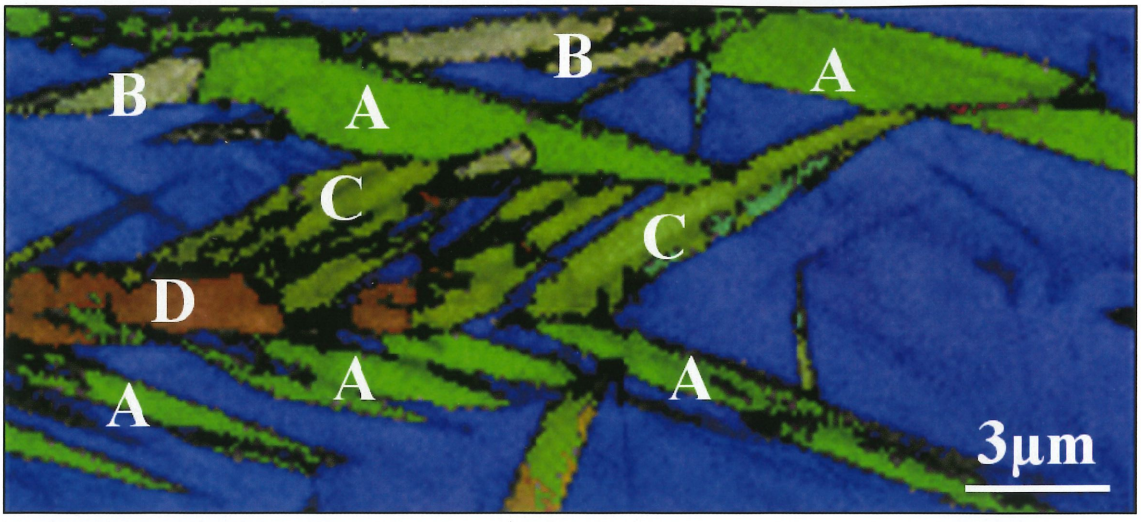

Fig. 3 Inverse pole figure (IPF) colored EBSD map.

Table 1 Equivalent axis/angle pair (for smallest angle)

Equivalent axis/angle pair (for smallest angle)				Variant pair
A-B	Kink type	[0.67 0.31 -0.68]	16.4	1a—10b
A-C	Spear type	[0.37 0.66 -0.65]	53.8	1a—11a
A-D	Spear type	[-0.71 -0.71 0.01]	50.7	1a— 3b

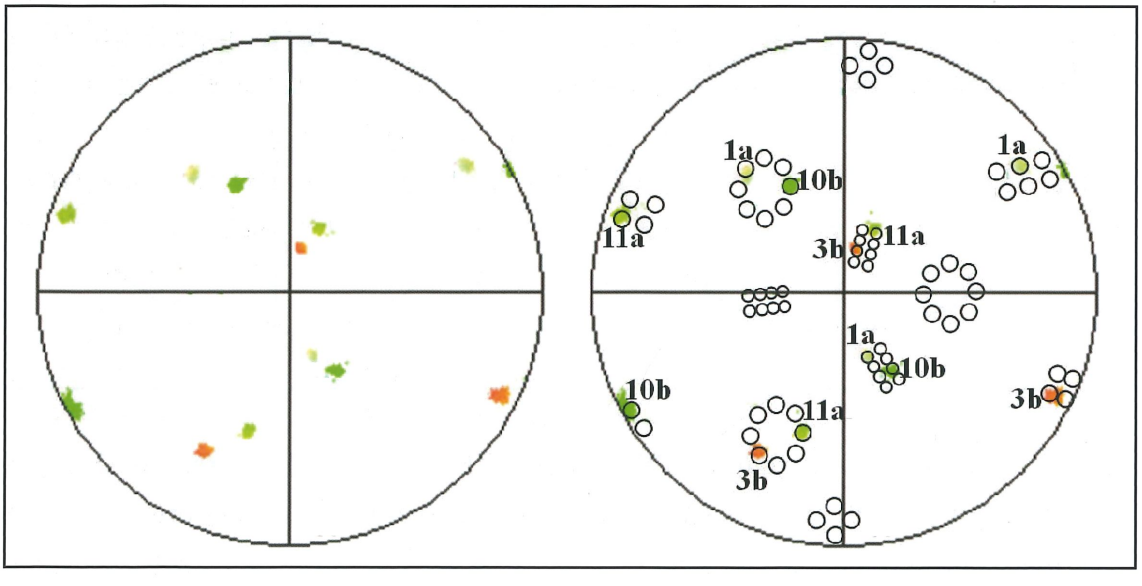

Fig. 4 The {100} pole figure of simulated K-S OR variants containing lenticular martensite crystal orientations.

M-P-13

MICROSCOPIC CHARACTERIZATION FOR THE ISLAND GROWTH OF GRAPHENE ON COPPER SUBSTRATES BY CHEMICAL VAPOR DEPOSITION

Ren-Jie Chang (張仁頡), Yun-Yi Tsai (蔡昀嶧), and Cheng-Yen Wen (溫政彥)

Department of Materials Science and Engineering, National Taiwan University, Taipei, Taiwan

Graphene is a two-dimensional single atomic layer of sp^2-hybridized carbon atoms arranged in a hexagonal honeycomb structure. Since its discovery, a variety of physical phenomena have been explored, making various novel graphene-based applications. Graphene can be fabricated by several methods, among which the chemical vapor deposition (CVD) method shows several advantages, including simple fabrication procedures, easy control of graphene layer numbers, and its scalability, most suitable for electronic device applications. However, the quality of CVD-grown graphene is not as good as that of the graphene layers exfoliated from graphite flakes; the defects formed during the CVD growth graphene, such as domain boundaries, seriously degrade the carrier mobility in graphene [1].

In order to improve the quality of the CVD-grown graphene, understanding the nucleation and growth mechanisms in this growth method is necessary. Reliable analytical tools are therefore very essential. In this study, we apply several useful methods for characterizing the growth behavior and structural properties of graphene. Optical microscopy is a convenient tool to measure the size and distribution of the as-grown graphene islands on Cu substrates. To enhance the contrast for optical observations, the as-grown graphene sample is annealed in air at 200°C to form Cu oxide on the bare substrate areas, which are not covered by graphene [2]. Figure 1 shows a series of such optical images of graphene with different pre-treatments before graphene growth; the contrast of graphene is strongly raised. From these images, we find that using the electro-chemically polished Cu substrate does not reduce the nucleation density of graphene. In contrast, introducing oxygen prior to graphene growth forms copper oxide layers, which passivate the active sites for nucleation on the Cu substrate, greatly reducing the nucleation density. We also find from the optical images that the shapes of graphene domains varies on different Cu grains (Fig. 2). In order to correlate the morphology of graphene islands with the orientation of Cu grains in the substrate, we apply electron backscatter diffraction (EBSD) analysis in SEM. As shown in Fig. 3, the shape and facets of graphene domains are strongly influenced by the crystallographic orientations of the Cu grains in the substrate. The graphene islands on Cu (100) grains exhibit four-lobed dendritic morphology, and those on Cu (311) grains have nearly rectangular shapes with two grooves on opposite edges. It is noted that the graphene domains can be larger than Cu grains; in other words, the graphene growth can cross Cu grain boundaries, showing the possibility

of synthesizing large-area single crystalline graphene on polycrystalline Cu substrates.

References

1. O.V. Yazyev and S.G. Louie, Nat. Mater., **9** 806 (2010).
2. C. Jia, J. Jiang, L. Gan, X. Guo, Sci. Rep., **2** 707 (2012).

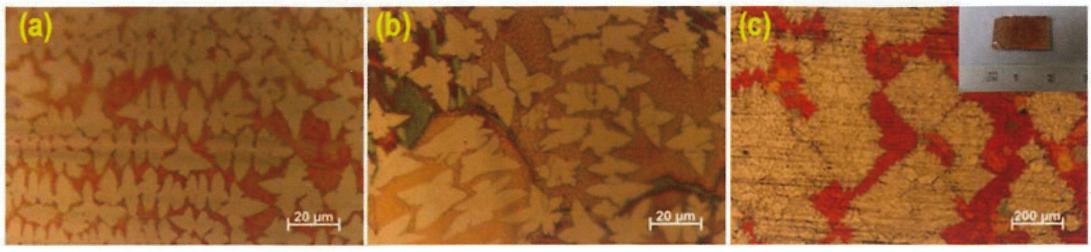

Figure 1. (a-b) Optical images of graphene grown in 20 mtorr CH_4 at 1030°C with and without electropolishing treatment of the Cu substrates, respectively. (c) Optical image of graphene grown by the O_2-assisted CVD process.

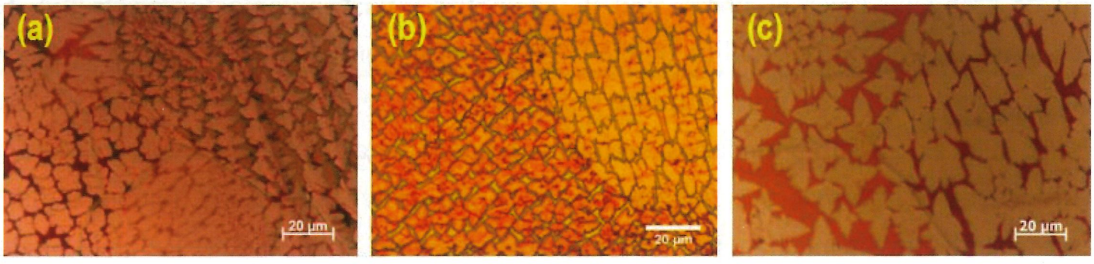

Figure 2. (a-c) Optical images of graphene grown in 20 mtorr CH_4 at 1030°C for 2 min. The samples were oxidized at 200°C to enhance the contrast of graphene. The morphology of graphene domains on different Cu grains in the substrate have different shapes.

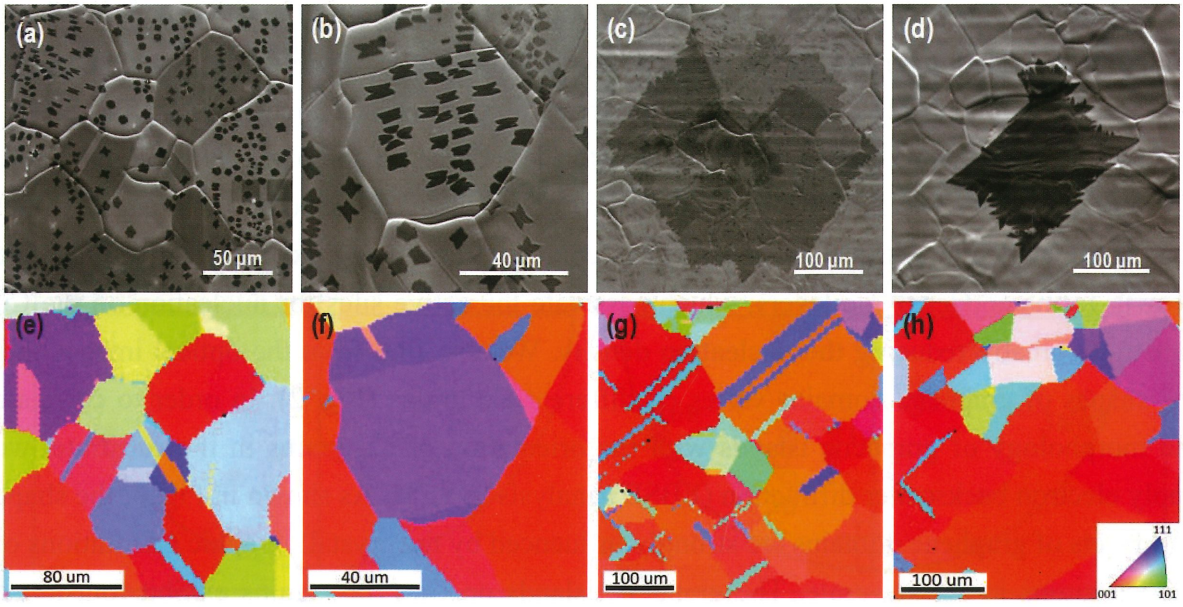

Figure 3. SEM images of graphene domains grown on Cu foil by (a-b) regular CVD and (c-d) O_2-assisted CVD growth method. (e-h) EBSD mapping of the Cu grain orientation in the area of (a-d), respectively.

M-P-14

INVESTIGATION ON THE DISLOCATION STRUCTURES OF 2205 DUPLEX STAINLESS STEEL BY ANNULAR DARK FIELD IMAGING

Yu-Ting Tsai(蔡宇庭),[1] Yi-Chieh Hsieh(謝亦傑)[1] and J.R. Yang(楊哲人)[1]

[1]Department of Materials Science and Engineering, National Taiwan University, Taipei, Taiwan

2205 duplex stainless steel (DSS), with high resistance to general corrosion and to stress corrosion cracking in extreme environment, have become the most widely used DSS grade. However, the well-known 475°C embrittlement, resulting from spinodal decompositions of the ferritic component, has restricted this steel grade from high temperature applications. The interaction of spinodal product and dislocations structure was therefore of engineering importance.

In this research, the dislocation structures of 2205 DSS were investigated. scanning transmission electron microscopy annular dark field imaging (STEM-ADF) was applied, and interfering diffraction contrast in conventional TEM two-beam condition was therefore absent. It was also found that in ADF the angular tolerance for clear dislocations imaging is larger than in weak beam dark field (WBDF) imaging, with slight sacrifice in spatial resolution. STEM-ADF technique is therefore full of potential in the analysis of dislocation structures in large grains, and successful attempt was made for the ferritic component of 2205 DSS. Total dislocation structures of single ferrite grain, can be categorized and analyzed simultaneously. Near ferrite/austenite grain boundary, high density of dislocations and dislocation tangles were found, while near the low angle boundary between ferrite and adjacent ferrite grain, the dislocations were of same type, were evenly distributed, and could passed from one grain to another. Dislocations density and the morphology as a function of distance from grain boundaries was made and discussed.

References

1. C.J. Humphreys, Ultramicroscopy, 7, 7, (1981)
2. D.M. Maher, D.C. Joyc., Ultramicroscopy, 1, 239, (1976)

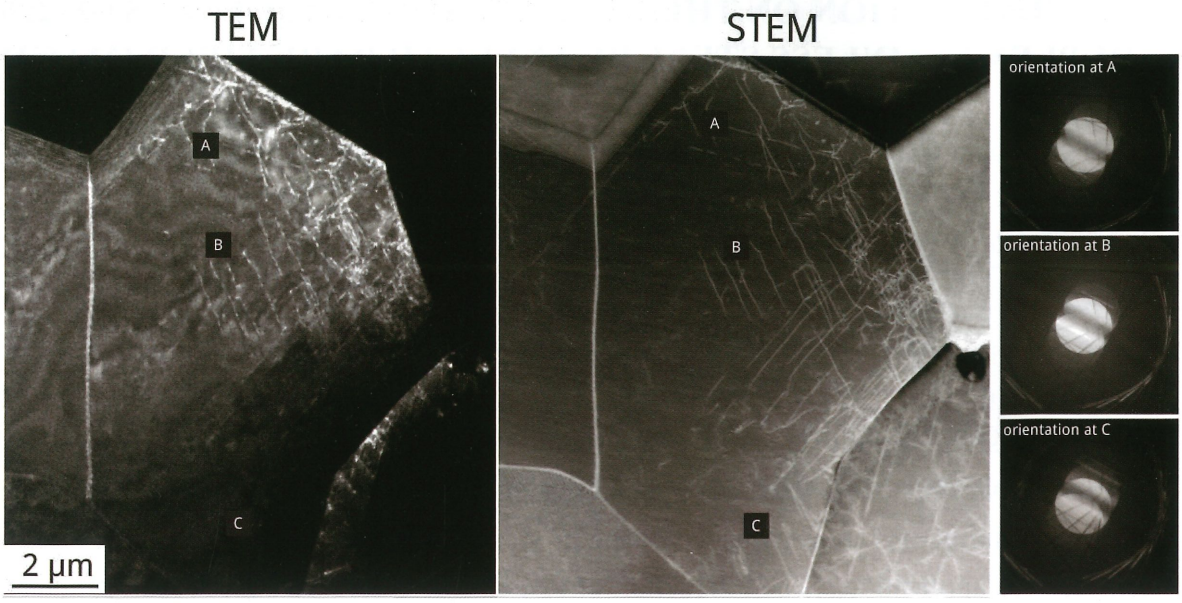

Figure 1. Illustration of degradation of diffraction contrast in CTEM due to misorientation inside a single large grain. Relatively good contrast can be obtained in STEM mode, suggesting higher angular resolution of STEM dislocation imaging. Misorientation from A to C is measured to be about 10 mrad.

M-P-15

TRANSMISSION ELECTRON MICROSCOPY ANALYSES FOR TiO_2 THIN FILMS GROWN BY ATOMIC LAYER DEPOSITION FOR RESISTANCE SWITCHING RANDOM ACCESS MEMORIES

Shih-Chun Chao (趙士鈞) and Cheng-Yen Wen (溫政彥)

Department of Materials Science and Engineering, National Taiwan University, Taipei, Taiwan

Resistance switching random access memory (ReRAM) is an emerging nonvolatile memory technology, which is based on bistable and multistable switchable resistance states of transition metal binary oxide [1]. Among them, TiO_2 is one of the most studied materials due to several advantages [2], such as good chemical, thermal stability, and earth abundance.

Atomic layer deposition (ALD) is a proven way for conformal growth of uniform TiO_2 thin films for ReRAM applications. In this study, we use titanium isopropoxide (TTIP) and H_2O as precursors to deposit TiO_2 thin films on Si substrates at different temperatures. The cross-sectional TEM images (Fig. 1(a-d)) suggest that uniform TiO_2 thin films are deposited on Si substrates. It is interesting to note that for the same thickness, thin films deposited at 120-200℃ are amorphous, but that grown at 250℃ is crystalline. This phenomenon is attributed to the critical thickness in ALD thin film deposition: an amorphous TiO_2 layer is formed in the initial stage of growth and sustains the amorphous state until the critical thickness for crystallization is reached. This critical thickness decreases with an increasing thin film deposition temperature [3].

Fracture of the TiO_2 thin films sometimes occurs, especially for those with the crystalline state (Fig. 2a). This fracture is related to the residual stress after thin film deposition, as observed from the strain contrast in TEM image (Fig. 2b) or the curvature of free-standing TiO_2 film/thin Si substrate cantilevers (Figs. 2c and 2d). Such a fracture is an important issue for applying ALD TiO_2 thin films for ReRAM device materials. Finally, we attempt to quantify the stress (based on the Stoney relation, Fig. 3a) by measuring the specimen thickness (Fig. 3b) and the bending curvature (Fig. 3c) of the curved lamellas after thinning down the substrate [4].

References

1. R. Waser, R. Dittmann, G.Staikov, and K.Szot, Adv. Mater., **21** 2632 (2009).
2. D. H. Kwon, K. M. Kim, J. H. Jang, J. M. Jeon, M. H. Lee, G. H. Kim, X. S. Li, G. S. Park, B. Lee, S. Han, M. Kim, and C. S. Hwang, Nat. Nanotechnol., **5** 148 (2010).
3. D. R. G. Mitchell, D. J. Attard, and G. Triani, Thin Solid Films, **441** 85 (2003).
4. M. Cabié, A. Ponchet, A. Rocher, L. Durand, and A. Altibelli, Appl. Phys. Lett., **86**

191901 (2005).

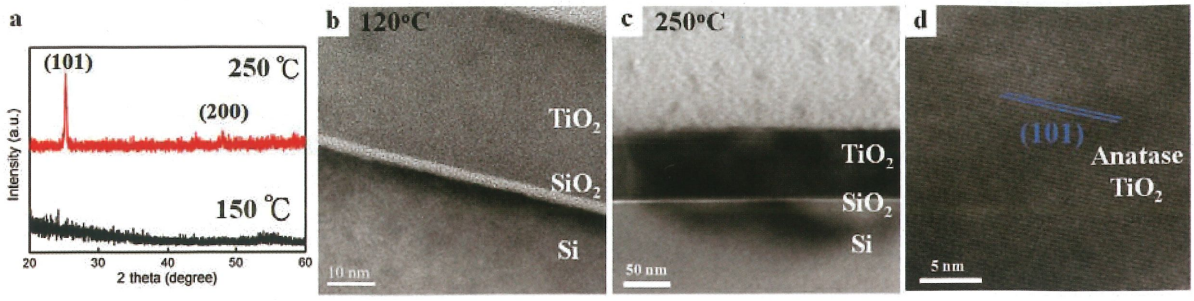

Figure 1. (a) X-ray diffraction patterns of TiO_2 films deposited at 150℃ and 250℃, showing the amorphous and polycrystalline anatase structure, respectively. (b-c) Cross-sectional TEM images of 35 nm TiO_2 films deposited at 150℃ and 250℃ on silicon substrates, respectively. The films are respectively amorphous and crystalline. (d) High-resolution TEM (HRTEM) image of a TiO_2 grain in (c), with lattice fringes in a spacing of 3.5 Å, corresponding to the (101) plane of the anatase TiO_2 phase.

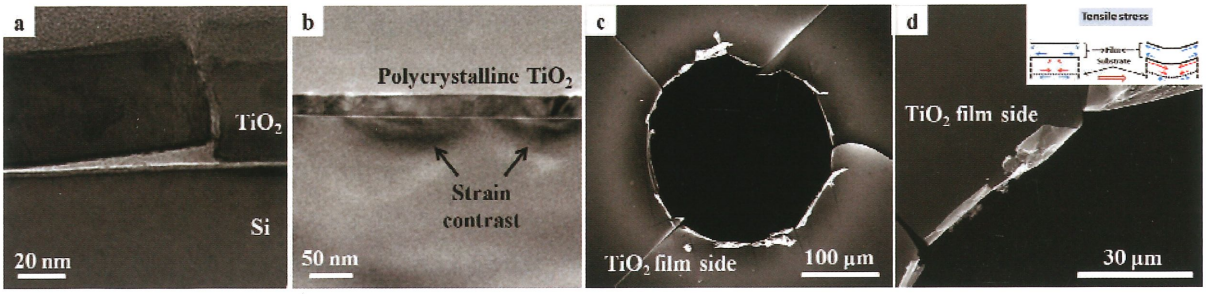

Figure 2. (a) Cross-sectional TEM image of the fractured crystalline TiO_2 thin films. (b) The cross-sectional TEM image showing strain contrast, suggesting the existence of residual stress after thin film deposition. (c-d) SEM images of the bending of TiO_2 films on thin Si substrates. From the bending direction, the stress is determined to be tensile.

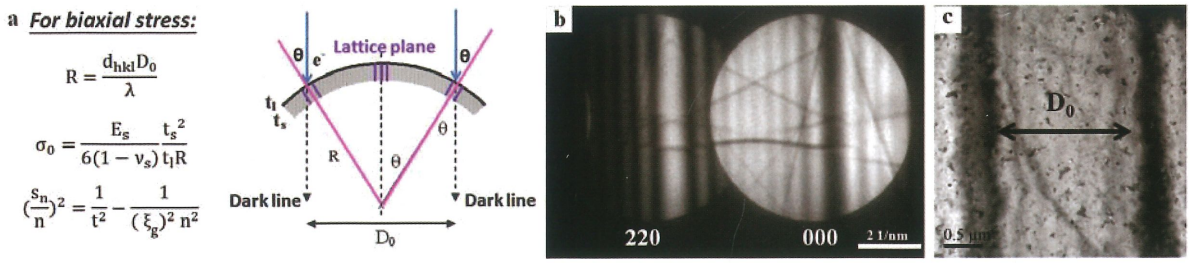

Figure 3. Illustration of using the Stoney formula to determine the biaxial stress (a), with the specimen thickness measured from the convergent beam electron diffraction pattern (CBED) (b) and the curvature measured from the bend contours in the TEM image (c).

M-P-16

EFFECT OF MARTENSITE VOLUME FRACTION AND PLASTICITY ON THE MECHANICAL PROPERTIES OF DUAL-PHASE (DP) STEEL

Cheng-Han Li (李承翰),[1] Shao-Pu Tsai (蔡劭璞),[1] Chih-Hung Jen (鄭至閎),[1] Yuan-Tsuong Wang (王元聰), [2] Ching-Yuan Huang (黃慶淵), [2] and Jer-Ren Yang (楊哲人)[1]

[1]Department of Materials Science and Engineering, National Taiwan University, Taipei, Taiwan

[2]Department of Research and Development, China Steel Corporation, Kaohsiung, Taiwan

The inhomogeneous deformation behavior of dual-phase (DP) steel is well known. However, there is little research about the relationship between quantitative analysis of inhomogeneous deformation behavior of dual-phase steel and true deformation behavior of dual-phase steel. In this research, mechanical properties of dual-phase steel with different martensite volume percent (30% and 40%) are investigated. Eshelby model modified by Weng is adopted to estimate the partitioning effect of stress-strain relations of the constituents in dual-phase steel. Empirical formulae are also adopted to estimate the yield strength of martensite and ferrite with the aid of Thermo-Calc to estimate the content of carbon in both phases. SEM morphology is analyzed to support this research.

Partitioning stress in dual-phase steel is found to be independent of martensite volume percent. High martensite volume percent that induces more dislocations in ferrite could enhance yield strength of ferrite and ultimate tensile strength of DP steel. The calculated yield strength of martensite is much higher than partitioning stress of martensite in DP steel so there is little plastic deformation of martensite. According to SEM morphology, specimen of higher martensite volume fraction has more interfacial cracks between martensite and ferrite, which is thought to have direct impact on lower ductility during deformation.

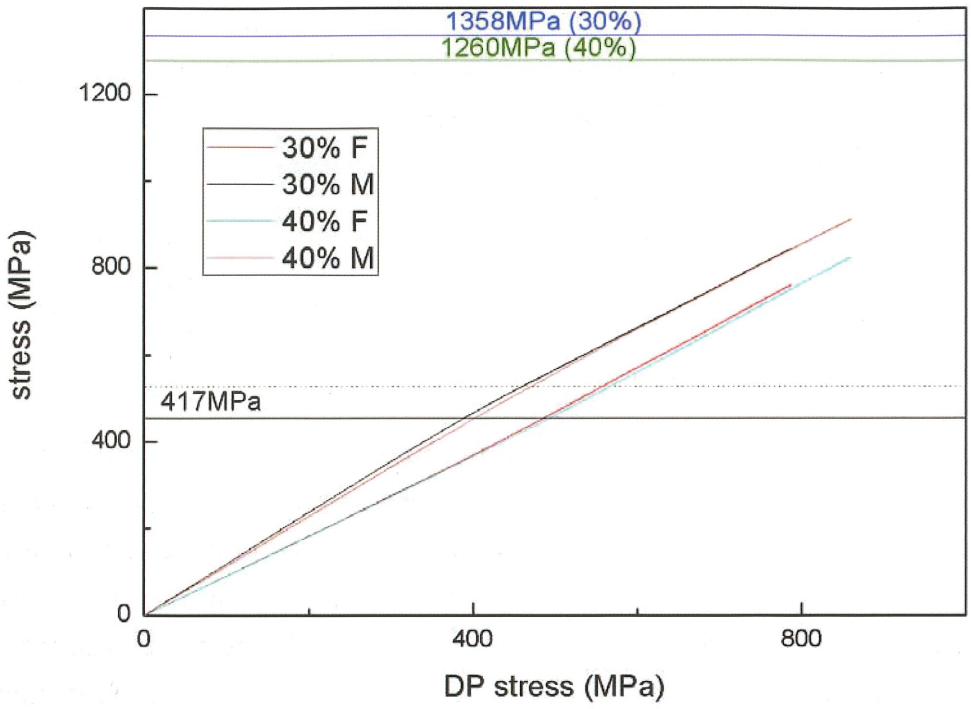

Figure 1. Stress partitioning effect and calculated yield strength of ferrite and martensite.

M-P-17

DISLOCATION SUBSTRUCTURE EVOLUTION IN FERRITE OF DP STEELS UNDER DEFORMATION

Chih-Hung Jen (鄭至閎),[1] Shao-Pu Tsai (蔡劭璞),[1] Yu-Ting Tsai (蔡宇庭),[1] Bo-Ming Huang (黃柏銘),[1] Yuan-Tsuong Wang (王元聰), [2] Ching-Yuan Huang (黃慶淵), [2] and Jer-Ren Yang (楊哲人)[1]

[1]Department of Materials Science and Engineering, National Taiwan University, Taipei, Taiwan

[2]Department of Research and Development, China Steel Corporation, Kaohsiung, Taiwan

The dual-phase (DP) steels are widely used in automobile industry due to its good formability. Strain hardening rate of DP steels decreases during plastic deformation, which can be divided into 3 stages in this study. This deformation behavior is believed to associate with the transformation of structure of dislocations in ferrite. In order to make a linkage between substructure and mechanical property, dislocation structure and density at different stages were observed by TEM and STEM ADF in this work. The specimens were pre-strained to transition points (5.1 and 16.1%) between stage I, II and III. In this experiment, dislocation density increased very fast in initial deformation, causing high strain hardening rate at stage I. Since dislocations started to tangle, the strain hardening rate would be reduced. In stage II, more dislocation tangled together and the wall of dislocation cell became thicker. As a result, the strain hardening rate were low and nearly remained constant. Since the dislocation cell were well-developed and dislocation structure couldn't change with larger strain. The strain hardening rate would decrease dramatically, causing the transition of deformation behavior from stage II to stage III.

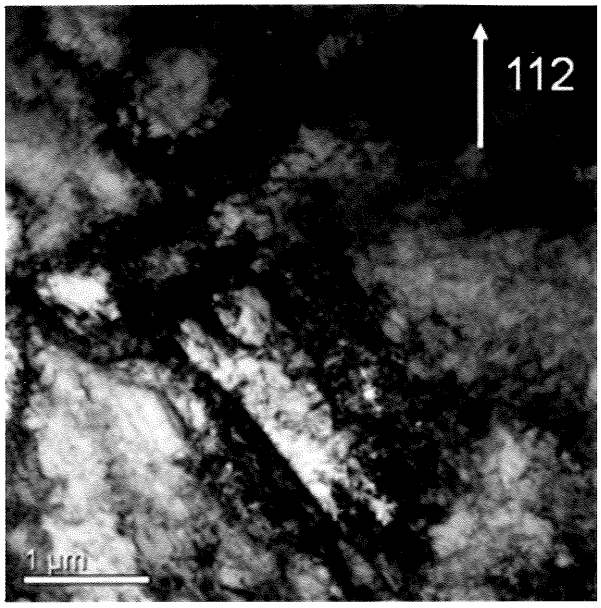

Figure 1. Cell structure under engineering strain of 16.1%.

M-P-18

FABRICATION OF TWO-DIMENSIONAL POSITION SENSITIVITY SINGLE-SIDED SILICON STRIP-PIXEL DETECTOR

Yu-Ting Liao (廖鈺婷),[1] Fan-Gang Tseng (曾繁根),[1] Fu-Rong Chen (陳福榮),[1] Chih-Hao Lee (李志浩),[1] Yun-Ju Chuang (莊昀儒)[2]

[1]Department of Engineering and System Science, National Tsing Hua University, Hsinchu, Taiwan

[2]Department of Biomedical Engineering, Ming Chuan University, Taipei, Taiwan

From the early times of the electron microscopy, film has been used for recording the electron images in TEM. A standard detector option commonly used instead of film is the charged coupled device (CCD), which started to be used in electron microscopy in the late 1980s. CCD systems have enabled the immediate access to images in real-time, and have significantly increased throughput in the electron microscopy field. The CCD camera system is indirect imaging detection systems which are composed by CCD and scintillator due to radiation damage and charge saturation. A scintillator is thus needed to convert the electron image to a photonic image, which is then relayed to the CCD cameras for image acquisition. Hence, indirect imaging detection systems have some inherent restrictions, including spatial and temporal resolution, efficiency and frame rate. In order to improve performance of electron detection systems, the application of silicon strip detector in TEM as a direct imaging systems was proposed [1]. The application of silicon strip detector in TEM can meet the requirements for two-dimensional position sensitivity, spatial resolution and frame rate with direct sensing.

Compared to pixel detector like CCD, silicon strip detector has advantages of simple structure, less number of readout circuits and lower manufacturing complexity. But silicon strip detector has one major issue, ghost images, which is unavoidable. If more than one particle hits the silicon strip detector, the measured particles position is no longer unambiguous and ghost hits appear. In this work, we proposed a direct electron detector with special metal strip arrangement, called silicon strip-pixel detector, to improve multi-hits problems and greatly reduce the number of readout circuits. Owing to characteristics integration of silicon strip detector and pixel detector, it was called silicon strip-pixel detector. Fig. 1 shows a schematic cross section of the silicon strip-pixel detector.

Fig. 2 illustrates the metal strip arrangement of silicon strip-pixel detector where X-strip and Y-strip are orthogonal. We distinguish the exact 2-D position of incident particles according to the strip which output the signal current. As shown in Fig. 2(a), strip layout of silicon strip detector, the X1, X6 metal strip and Y1, Y6 metal strip have higher signal while two particles hit on position A and B simultaneously. Thus, it is hard to distinguish the exact

position A(X1, Y1), B(X6, Y6), C(X6, Y1) or D(X1, Y6) of incident particles. With proper disconnection of the metal strips as shown in Fig. 2(b), the multi-hits problems can be relieved. Besides, for n x n pixel, the traditional pixel detector needs n^2 readouts while our strip-pixel detector only needs 2n readouts.

The silicon strip-pixel detector is produced by single-sided process on high resistivity n-doped 4 inch diameter silicon wafer with a thickness of 250 um. The pitch of strips determines the spatial resolution of the detector. The performance of P-N junction can be obtained by fine-tuning of implantation energy, dose and annealing parameters. The guard rings are designed around the active area to reduce leakage current and improve signal to noise ratio. The process flow of silicon strip-pixel detector is shown in Fig. 3.

The leakage currents as a function of reverse bias voltage have been measured to evaluate basic properties of the detector. The leakage current of silicon strip-pixel detector is 8 uA. The breakdown voltage is about -50 V. Furthermore, the dark current is 1.63 pA. We are still working on the follow-up signal to image conversion.

References

[1] G. Moldovan, X. Li, P. Wilshaw, and A. Kirkland, "Thin silicon strip devices for direct electron detection in transmission electron microscopy," *Nuclear Instruments and Methods in Physics Research Section A: Accelerators, Spectrometers, Detectors and Associated Equipment,* vol. 591, pp. 134-137, 2008.

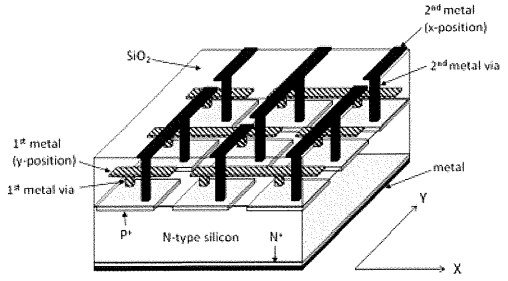

Figure 1. Schematic structure of the silicon strip-pixel detector.

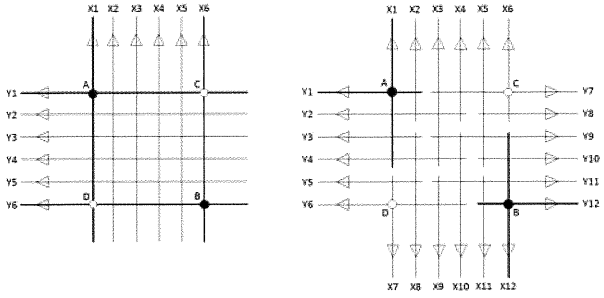

(a) (b)

Figure 2. Illustration of the metal strip arrangement.

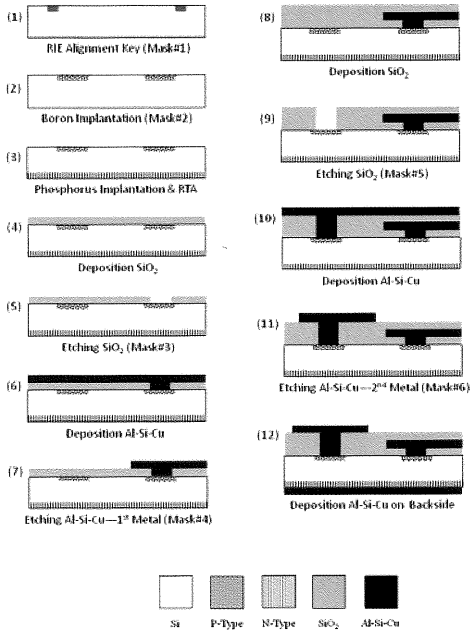

Figure 3. The process flow of silicon strip-pixel detector

M-P-19

RESISTIVE MEMORY DEVICES WITH HIGH SWITCHING ENDURANCE THROUGH SINGLE FILAMENTS IN BI-CRYSTAL CUO NANOWIRES

Yen-Chih Chen (陳彥志) ,[1] Chia-Hao Tu (涂嘉豪) ,[1] Che-Chia Chang (張哲嘉),[1] Chao-Hung Wang (王超鴻),[1] Yi-Chang Li (李奕錩),[1] and Chuan-Pu Liu (劉全璞) [1]

[1] Department of Materials Science and Engineering, National Cheng Kung University, Tainan 70101, Taiwan

We propose a simple system to investigate the influence of microstructure on the resistive switching behavior via bi-crystal CuO nanowires. CuO nanowires are prepared by thermally oxidizing transmission electron microscopy copper grids in air, shown in Figure1. The devices made of single-crystal nanowires follow Ohm's law, with a high resistance, within the sweeping voltage range of 0 to 4 V, whereas those made of bi-crystal nanowires exhibit threshold and memory resistive switching behaviors, which are due to the enrichment of copper ions in the grain boundaries of bi-crystal CuO nanowires providing sources for the formation of conductive filaments. Futhermore, the bi-crystal nanowires with higher defect densities in grain boundaries result in lower threshold voltages of switching from high to low resistance states. The threshold resistive switching behavior can be turned into memory resistive switching behavior by increasing the thickness of the device electrodes or reducing the compliance current. The endurance of memory resistive switching through the pre-defined conduction paths in the single grain boundaries of bi-crystal CuO nanowires is at least 1000 cycles without any performance deterioration. This high reliability is ascribed to the single conductive filaments.

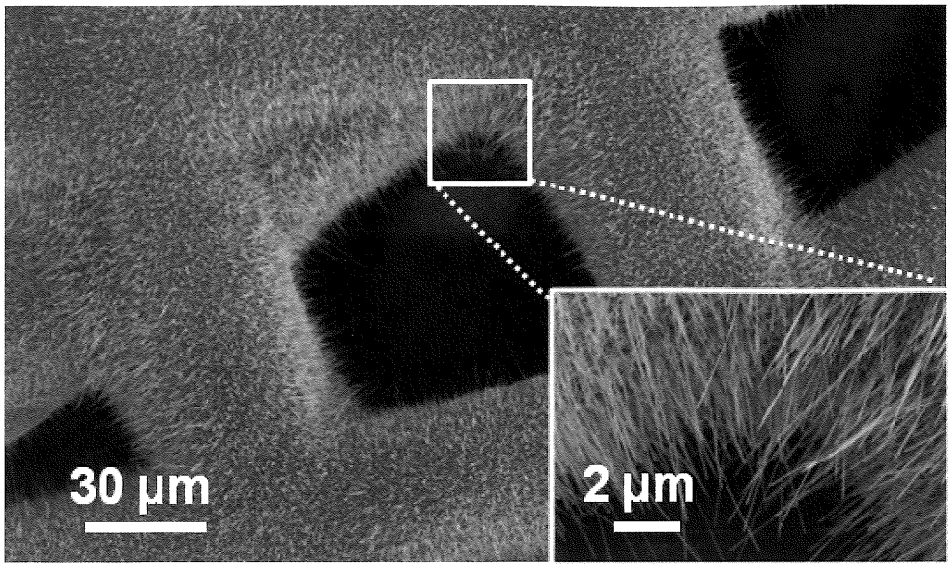

Figure 1. SEM image of the CuO nanowires.

M-P-20

GROWTH OF GRAPHENE ON EPITAXIAL NICKEL DISILICIDE FILMS

Chia-Hao Lee (李家豪) and Cheng-Yen Wen (溫政彥)

Department of Materials Science and Engineering, National Taiwan University, Taipei, Taiwan

Graphene is a two-dimensional crystal of carbon atoms packed in a honeycomb structure, and it has been in the focus of intensive researches due to its unique physical properties. For almost ten years, the synthesis of large-area high-quality graphene has been an important but unsolved problem. There are several methods for graphene fabrication [1], including mechanical exfoliation, epitaxial growth on silicon carbide substrate, and the chemical vapor deposition (CVD) growth on metal substrates. Among these methods, the CVD process provides a simple fabrication route for making large area graphene [2]. However, there are still some problems in the CVD-grown graphene. First of all, the high growth temperature in the CVD method is unfavorable for integrating it with the current Si-based VLSI technology – the high temperature may roughen the sample surface and damage the circuit structures Secondly, even graphene can be grown on other metal substrates, application of graphene still requires complicated transfer procedures, which usually damage graphene, lowering its quality.

In order to improve the quality of CVD-grown graphene, we propose to use epitaxial nickel disilicide thin film on Si(111) wafer as the growth substrate and use acetylene (C_2H_2) instead of methane (CH_4) as the carbon source. The growth results are shown in Fig. 1. There are two reasons to choose nickel disilicide as the growth substrate: firstly, nickel-based materials are good catalysts for graphene growth (it has been shown that several metal silicides can decompose hydrocarbons); secondly, the lattice constant of nickel disilicide ($NiSi_2$, a=5.406 Å) is very close to Si (a=5.432Å), with a lattice mismatch as low as 0.4%. Nickel disilicide can be grown epitaxially on the Si(111) wafer, offering an excellent crystal quality and atomically flat surface for graphene growth. Epitaxial growth of graphene on nickel disilicide can therefore produce less grain boundaries. In this research, we use transmission electron microscopy (TEM) and scanning electron microscopy (SEM) to study the surface morphology and crystal quality of the $NiSi_2$ growth substrates, as shown in Fig. 2. We also use Raman spectroscopy to evaluate the quality of graphene (Fig. 3).

References

1. W. Choi, I. Lahiri, R. Seelaboyina, Y. S. Kang, Cri Rev. Solid State Mater. Sci., **35** 52 (2010).
2. S. Bae, H. Kim, Y. Lee, X. Xu, J.-S. Park, Y. Zheng, J. Balakrishnan, T. Lei, H. R. Kim, Y. I. Song, Nat. Nanotechnol., **5** 574 (2010).

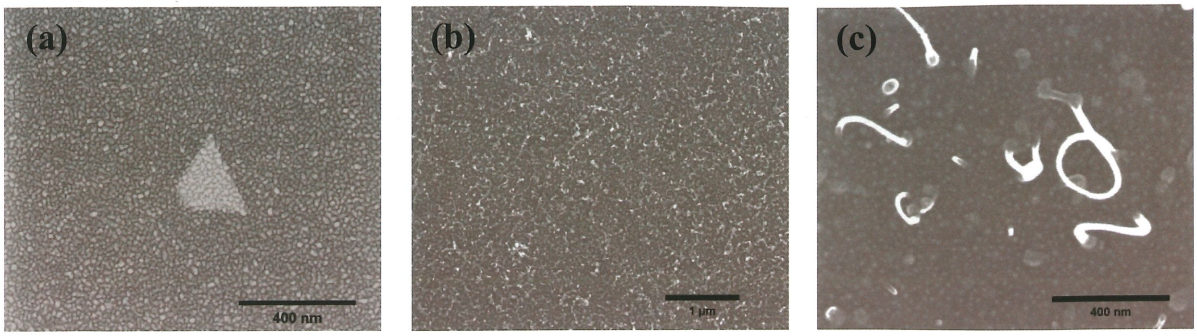

Figure 1. (a) SEM image of an epitaxial $NiSi_2$ island. (b-c) SEM images of graphene grown at 600℃. Some surface structures were observed in addition to graphene growth.

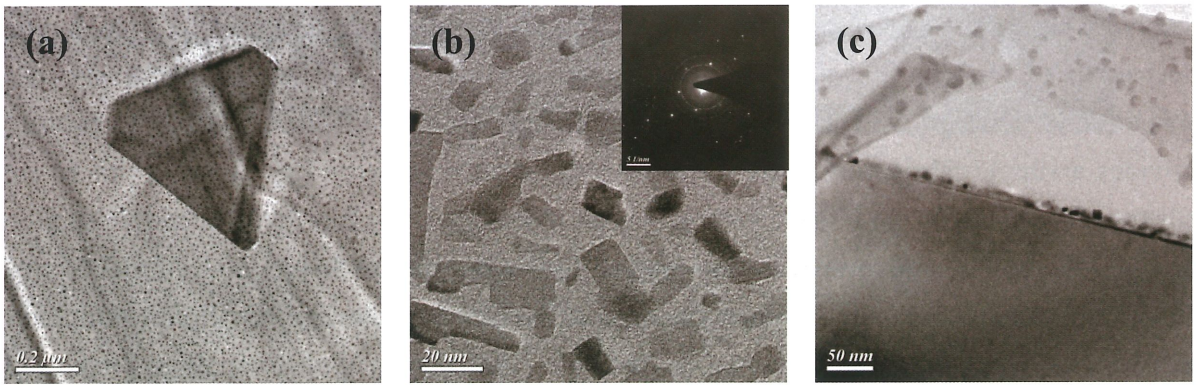

Figure 2. (a) TEM image of an epitaxial $NiSi_2$ island. (b) TEM image of the particles in the background of (a), which are likely the unreacted NiSi particles. (c) Cross-sectional TEM image of the nickel disilicide film. The contrast implies the polycrystalline structure in the thin film.

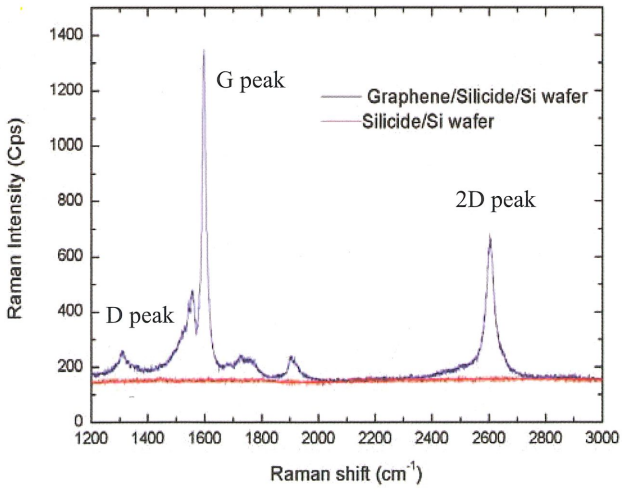

Figure 3. Raman spectrum of the graphene on $NiSi_2$/Si wafer. The intensity ratio between 2D peak and G peak shows that the graphene grown on $NiSi_2$ is multilayer.

M-P-21

SI_3N_4 THICKNESS EFFECT OF GROEL/GNP IN WET CELL TEM OBSERVATION

Chih-Hsiang Kuo (郭至翔),[1] Chun-Ying Tsai (蔡俊穎),[1] Yuan-Chih Chang (張淵智)[2] Hsin-Yu Lin (林信余),[1] Yu-Hung Wong (翁宇弘)[1], Fu-Rong Chen (陳福榮)[1] and Fan-Gang Tseng (曾繁根)[1]

[1]Department of Engineering and System Science, National Tsing Hua University, Hsinchu, Taiwan

[2]Institute of Cellular and Organismic Biology ,Academia Sinica, Taipei , Taiwan

Transmission Electron microscopy (TEM) has been a key technique of observation about the bio-samples by several major approaches: negative staining and Cryo-electron microscopy. Imaging of negative staining and frozen samples are not in their native states, only static snapshots along the way and the critical moment may be ignored. Wet cell in situ TEM is a burgeoning technique that makes it possible to observe processing taking place in liquid state with an electron microscopy and has the potential to produce new insights in many branches of science.

In this literature, we demonstrated a wet cell chips fabricated by MEMS process to create a micro chamber, which encapsulated aqueous samples by two chips contain a window of 50 nm silicon nitride membrane to sustain pressure different between the TEM vacuum and the vapor pressure within the liquid chamber[1]. To test the wet cell chips, we used the negative stained chaperoning protein GroEL as a standard model. As to detect low Z materials in TEM, there is one major limitation: scattering and absorption of electrons attribute to 50 nm silicon nitride membrane. Thus, we use hydrogen fluoride (HF) to thin down the silicon nitride membrane in order to minimize the interaction between electron and silicon nitride membrane[2]. The signal to noise ratio improvement is visually evident as shown in three negative staining GroEL images of different Si3N4 thickness (Fig.1 a-c). Fig. 1d shows the line plot of single to noise ratio verse Si_3N_4 thickness. The signal to noise ratio of 2.1 nm membrane thickness GroEL image is about 1.32 times higher as compared to the corresponding 35.1 nm membrane thickness GroEL image. Furthermore, the gold nanoparticles (GNPs) solution was selected to test the strength of membrane against vacuum. Fig. 2 shows the in situ GNPs images in liquid state by sealing two 15 nm Si_3N_4 membrane wet cell chips. It should make the trade-off between resolution and ability of vacuum sustaining which is not the problem for wet cell nanoparticle image but should breakthrough for wet cell protein image.

References

[1] T. W. Huang, S. Y. Liu, Y. J. Chuang, H. Y. Hsieh, C. Y. Tsai, Y. T. Huang, et al., Lab

Chip, vol. 12, pp. 340-7, Jan 21 2012.
[2] U. M. Mirsaidov, H. Zheng, Y. Casana, and P. Matsudaira, Biophys J, vol. 102, pp. L15-7, Feb 22 2012.

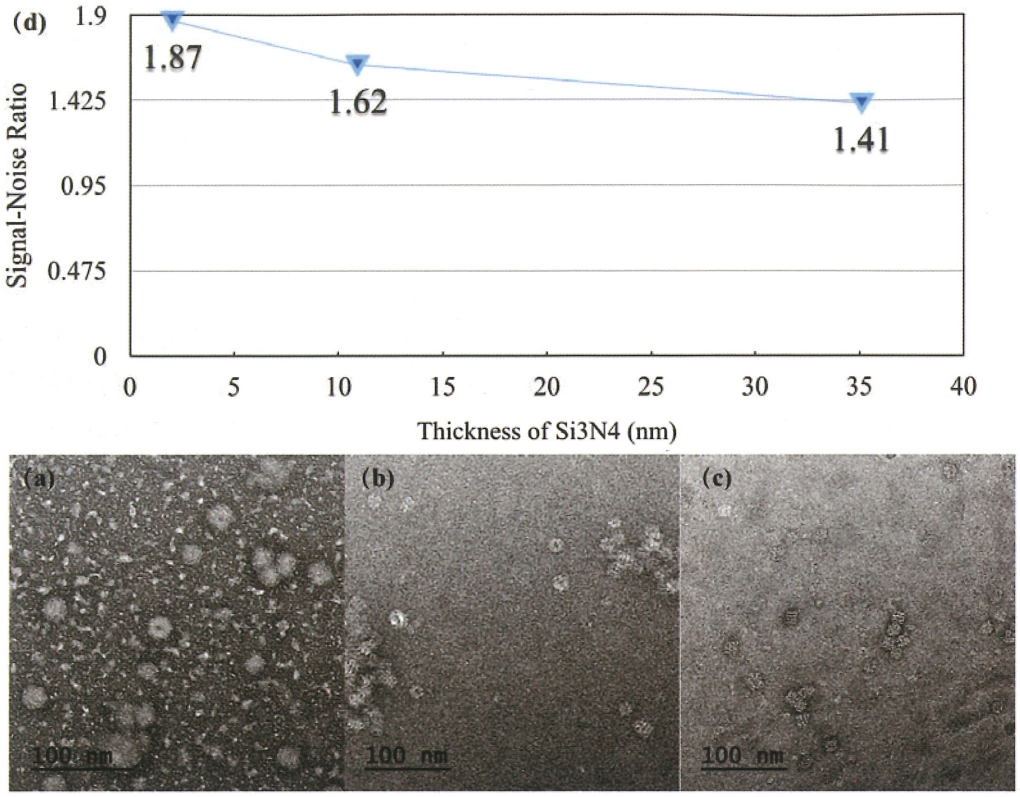

Fig. 1 Signal-Noise Ratio decrease while resoultion increase as the thickness of silicon nitride membrane increase. Thicknesses of silicon nitride film are respectively (a) 35.1 nm (b) 10.9 nm (c) 2.1 nm

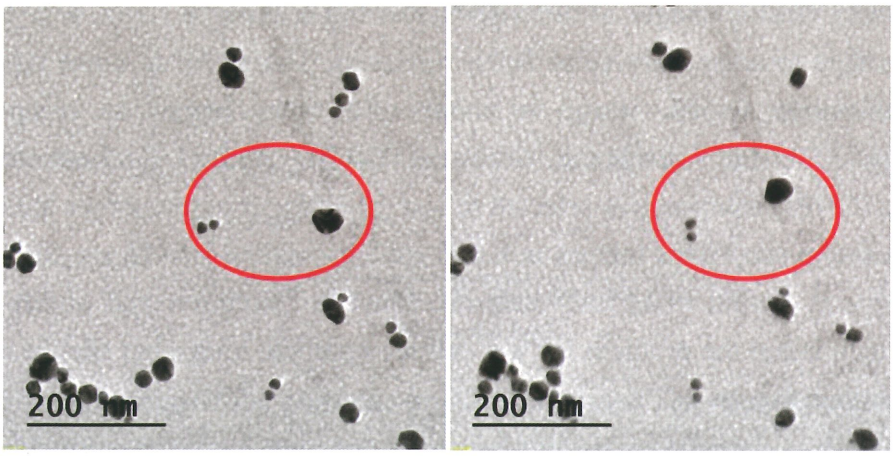

Fig. 2 GNPs with liquid were sealed by two wet-cell chips with 15 nm silicon nitride membrane.

M-P-22

HIGH-RESOLUTION TEM STUDY OF MICROSTRUCTURAL EVOLUTION OF TI-6AL-4V ALLOY FOLLOWING THERMAL HYDROGENATION PROCESSING

[1]Wang, Le-Min (王樂民), [2]Tsai, Chih-Jen (蔡智仁)

[1]Department of Power Vehicle and Systems Engineering, Chung Cheng Institute of Technology, National Defense University, Taoyuan, Taiwan
[2]School of Defense Science, Chung Cheng Institute of Technology, National Defense University, Taoyuan, Taiwan

Recently, an increased understanding of titanium metallurgy has demonstrated that the thermal hydrogenation processing (THP) is an effective technique in which hydrogen is used as a temporary alloying element to control the microstructure and improve the final mechanical properties [1-4] and the corrosion resistance by growing controlled thin oxide layers on the surface of Ti-6Al-4V alloy [5]. In this study, we further investigate the effects of hydrogen loading of THP treatment on the microstructural evolution at the atomic level using high-resolution transmission electron microscope. It appears that the micro-hardness of THP treated Ti–6Al–4V alloy increased with increasing hydrogen loading due to the effect of grain refinement. The THP treatments with a hydrogen loading of 0.3 H/M (the ratio of hydrogen to metal atoms) or higher hydrogen concentration resulted in the formation of an ill-defined lattice area within the existed matrix as well as the produced phase (α_2-Ti_3Al), leading to the α phases being isolated and refined (Figure 1).

References

1. O. N. Senkov and F. H. Froes, Int. J. Hydrogen Energy, 24 565 (1999).
2. N. Eliaz, D. Eliezer, and D. L. Olson, Mater. Sci. Eng., A, 289 41 (2000).
3. D. Eliezer, N. Eliaz, O. N. Senkov, and F. H. Froes, Mater. Sci. Eng., A, 280 220 (2000).
4. F. H. Froes, Int. Mater. Rev, 49 227 (2004).
5. C. J. Tsai and L. M. Wang, J. Electrochem. Soc., 160 C560 (2013).

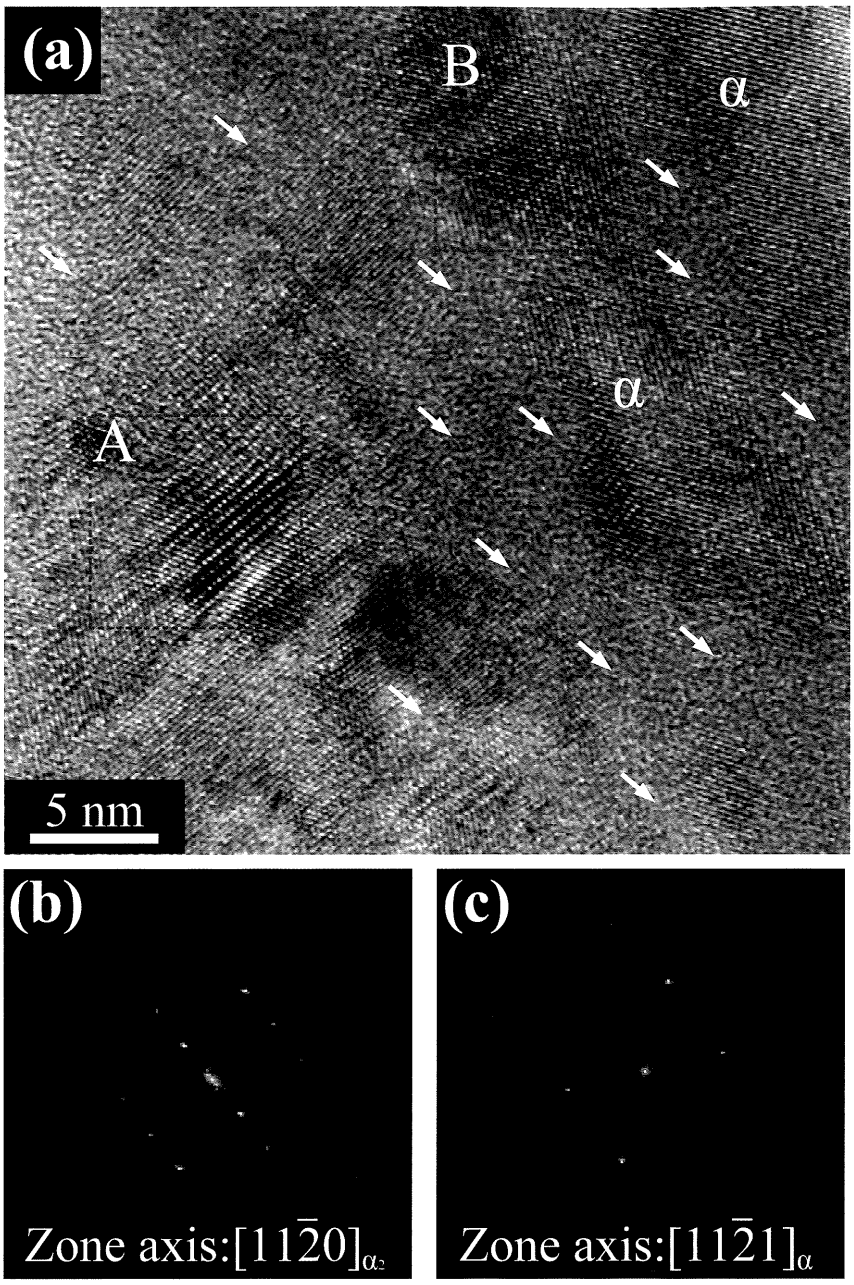

Figure 1. (a) HRTEM micrograph of Ti-6Al-4V alloy following THP with a hydrogen loading of 0.3 H/M.The ill-defined regions around the α_2-Ti_3Al and the refined α phases are arrowed. (b) The FFT analysis of the framed area A in (a) shows the zone axis of [11$\bar{2}$0]α_2 and (c)The FFT analysis of the framed area B in (a) shows the zone axis of [11$\bar{2}$1]α.

M-P-23

DEVELOPMENT OF IN-SITU WET-CELL ELECTRON MICROSCOPE HOLDER FOR OXYGEN NANO-BUBBLES BY PLATINUM

H.T. Zheng (鄭弘田)[1], S. Y. Liu (劉鈰誼)[1], C.T. Tsai (蔡承廷)[2], T. W. Haung (黃祖緯)[1], F. G. Tseng (曾繁根)[1] and F. R. Chen (陳福榮)[1]

[1] Engineering and System Science Department/National Tsing Hua University, Hsinchu, Taiwan
[2]Dept. of Material Science and Engineering, National Chung Hsing University, Tai-Chung, Taiwan

Recently, wet-cell electron microscopy provides a new method for investigating crucial scientific issues within liquid which beyond the conventional electron microscopy. The progress in electron microscopy pushes the capability of viewing as close as the original phenomena occur and thus may open new scientific windows in multidiscipline due to the spatial resolution in sub-nanometer as well as tens of millisecond time-resolved power. Much more researches have been published and included various field such as electrochemistry, catalyst material, and biophysics. Heimei et al firstly visualize growth dynamics of Platinum nanocrystal with nanometer resolution in wet cell TEM [1]. These techniques provide the key to understanding toward whole mechanism for synthesizing more efficient catalyst materials. In this research, owing to the significance of catalyst, we put more focus on investigating catalytic process of Platinum. For this purpose and to approach real case, we built up the platform with function of liquid importation to fit with currently TEM (JEOL, JEM-2010 LaB_6 equipped with Gatan multi-scan CCD) observation respectively, that is in-situ wet-cell electron microscope holder. The wet-cell chip is made by micro electro mechanical systems (MEMS) process and the observing window is 50nm Si_3N_4 [2, 3].

For TEM observation, the platinum nanoparticles carried by multi-wall carbon nanotube was dropped onto wet-cell chip with electron transparent Si_3N_4 membrane then sealing was completed by a set of o-rings. The solution contains 0.08wt% of H_2O_2 have been transported into the observation area by syringe pump; additionally, the flow rate was accurately controlled below 0.15 mL/hr that is the key to preventing membranes broken. The bubble formation is due to the well-known equation: $2H_2O_2 \rightarrow 2H_2O+O_2$. Platinum serves as catalyst to promote hydrogen peroxide decomposed into water and oxygen, which contribute to the source of bubble generation.

References:

[1] H. Zheng, R. K. Smith, Y. W. Jun, C. Kisielowski, U. Dahmen and A. P. Alivisatos, Science 324 (2009), p. 1309.

[2] T. W. Huang, S. Y. Liu, Y. J. Chuang, H. Y. Hsieh, C. Y. Tsai, Y. T. Huang, U. Mirsaidov, P. Matsudaira, F. G. Tseng, C. S. Chang, and F. R. Chen, Lab chip **12** (2012), p. 340

[3] T. W. Huang, S. Y. Liu, Y. J. Chuang, H. Y. Hsieh, C. Y. Tsai, W. J. Wu, C. T. Tsai, Utkur Mirsaidov, P. Matsudaira, C. S. Chang, F. G. Tseng and F. R. Chen, Soft Matter **9** (2013), p.8854

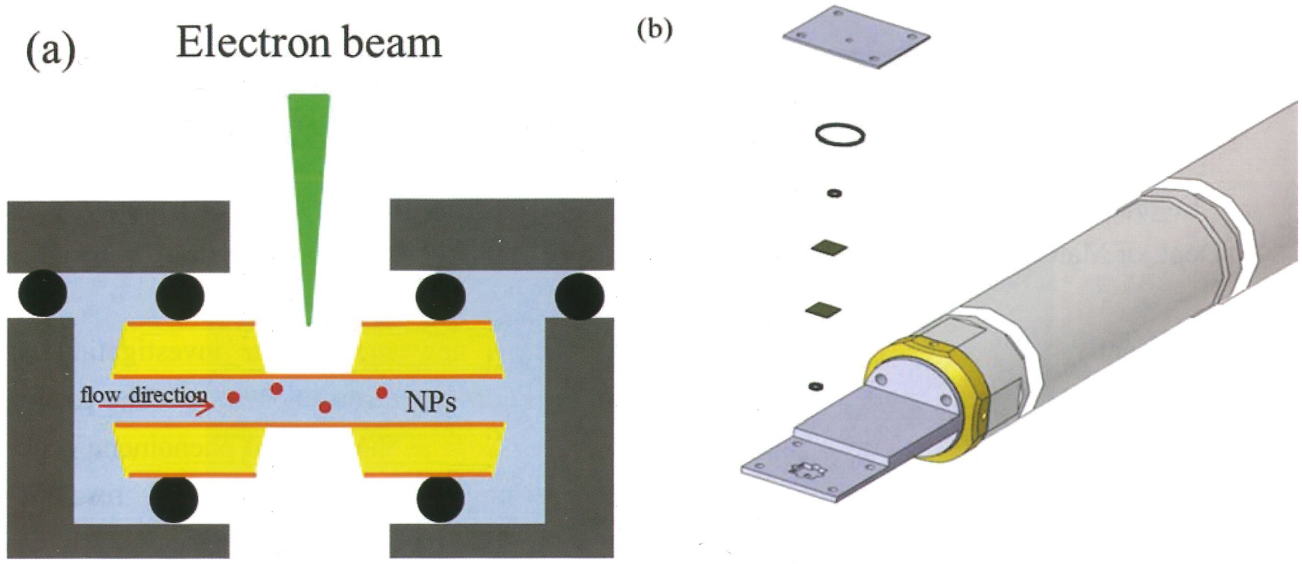

Fig. 1(a) The cross section view of TEM liquid holder tip: electron beam penetrate the liquid thickness which defined by metal spacer between chips and sets of o-rings are used for vacuum sealing. The nitride membrane is 50 nm for each piece and (b) assembling diagram of TEM liquid holder.

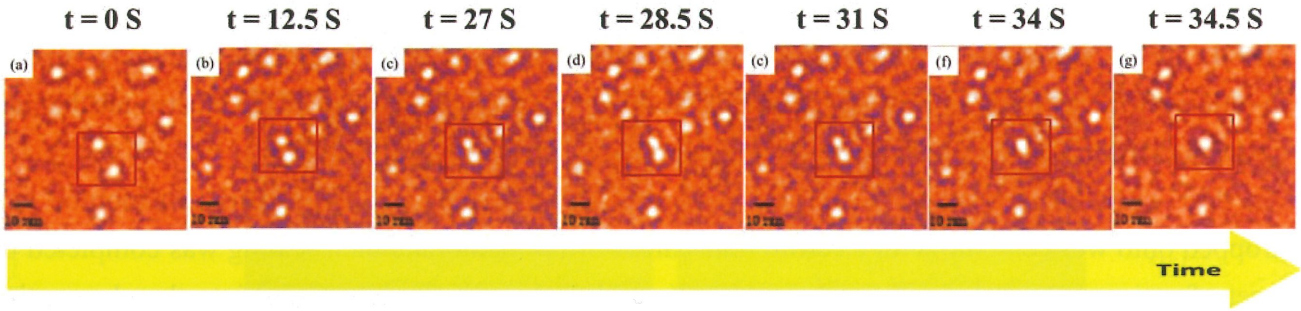

Fig. 2, TEM images of nano-bubbles, phenomena of the bubbles merge as indicated in dash line region with time by injecting H_2O_2 solution (a) ~ (g).

M-P-24

E-BEAM CROSSLINKING AND THERMAL DEGRADATION OF HYDROGEL UNDER ELECTRON MICROSCOPE

Yu-Hung Wong (翁宇弘)‡[1], Chih-Hsiang Kuo (郭至翔)‡[1], Tsu-wei Huang (黃祖緯)[1], Shih-Yi Liu (劉鈰誼)[1], Hsin-Yi Hsieh[23] (謝馨儀),Fu-Rong Chen (陳福榮)[1]and Fan-Gang Tseng (曾繁根)[14]

[1]Department of Engineering and System Science, National Tsing Hua University, Taiwan
[2]Department of Mechanical Engineering, National Taiwan University, Taiwan
[3]Institute of NanoEngineering and MicroSystems, National Tsing Hua University, Taiwan
[4]Division of Mechanics, Research Center for Applied Science, Academia Sinica, Taiwan

In the past decades, hydrogel has been becoming an important medium for incorporating cells together to from 2D or 3D structures for tissue engineering applications. Electron beam can be used to pattern the resulting hydrogels on silicon or glass surfaces with nanometric and micrometric feature sizes by radiation crosslinking [1]. The water content plays a role to form the hydrogen and hydroxyl radicals which initialize the polymerization reaction. To visualize the dynamic evolution of hydrogel, we use a hermetic micro-device (wet-cell) to preserve the hydrated hydrogel in vacuum system under electron illumination. We have utilized the innovated self-aligned wet-cell to demonstrate the TEM examination of hydrated D. Radiodurans in our previous work [2]. In this paper, we furthermore integrated miniature heater on wet-cell to achieve temperature manipulation for the rapid recovering of hydrogel.

The multiple-electrode wet-cell device is composed of two silicon chips with complementary structure, as shown in Fig. 1. The "cover piece", a 3mm x 3mm square-shaped device made of 250μm-thick Si wafer, has an observing window which is formed by the bulk micromachining and covered by a silicon nitride membrane; the "electrode piece", a 3mm x 6mm rectangle-shaped device made of 250μm-thick Si wafer, consists of a similar observing window with additional Ni/Cr heater (200nm/50nm, 20.07 kΩ) as well as the extended metal pad for wire connecting. The wet cell incorporated onto the SEM (Hitachi TM-1000) through an additional circuit of SEM side port, so that we can apply tunable voltage and investigate wet hydrogel under vacuum condition.

To measure the temperature rising with increasing applied voltage, we use an infrared-thermal microscope to visualize the distribution and variation of temperature around the heater. Several different applied voltages and their corresponding temperatures are shown in Fig. 2. We can control our heater temperature ranging from 30 to 70 °C, reversibly.

References:

1. P. Krsko, I. Saaem, R. Clancy, H. Geller, P. Soteropoulos, M. Libera, , Proc. of SPIE 6002, 600201-1.
2. T.W Huang, S.Y Liu, Y.J Chuang, H.Y Hsieh, C.Y Tsai, Y.T Huang, F.G Tseng, C.S Chang,F.R Chen , Lab on a chip 12 , 340-347

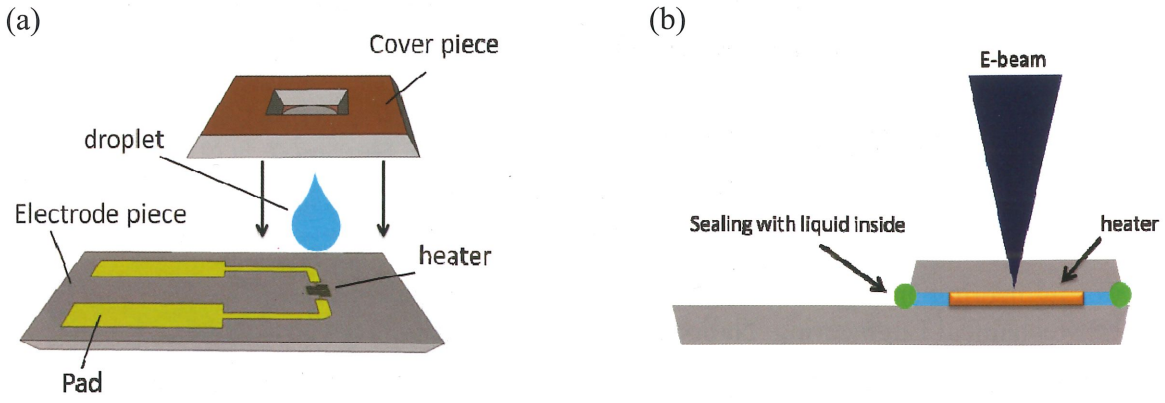

Figure 1.(a)Schematic of two parts of our device assembly
(b)Schematic of E-beam and chip observing area.

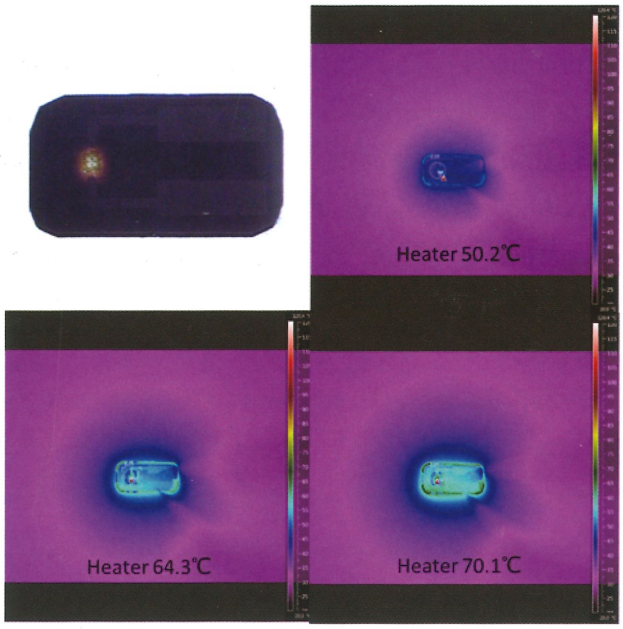

Figure 2.IR microscope image of our device heating
by applied voltage from 50.2℃ to 70.1℃

Acknowledgements: This work was supported by National Science Council (NSC102-2321-B-007-007 and NSC 102-2120-M-007-006-CC1).

M-P-25

INTEGRATION OF A LIGHT MICROSCOPE INTO A DESKTOP SCANNING ELECTRON MICROSCOPE

Lian-Sheng Tsai (蔡濂聲),[1] Yi-Chang Chen (陳義昌),[2] Fu-Rong Chen (陳福榮),[3] and Yi-Sha Ku (顧逸霞)[2]

[1]Department of Science and Technology of Synchrotron Light Source, National Tsing Hua University, Hsinchu, Taiwan

[2]Center for Measurement Standards, Industrial Technology Research Institute

[3]Department of Engineering and System Science, National Tsing Hua University, Hsinchu, Taiwan

We have developed a new CLEM (Correlative Light Electron Microscope) with a merged system combining a light microscope module and a commercial desktop electron microscope (TEMIC-EM100). A 10X objective lens with long working distance is positioned in between the BSED (Backscatter Electron Detector) and the sample stage of a scanning electron microscope (SEM) as shown in Fig.1 (a). A 45° mirror mounted on a home-built objective nose piece guides the light from the objective lens to the sample and vice versa. The system is designed in such a way that all components of the light microscope except the objective lens and the reflection mirror are positioned outside the vacuum. In order to guide the light microscope module into and out of the vacuum chamber, a flexible bellow is mounted in the door plate as shown in Fig.1 (b), and an optical window is sealed inside the end of the objective lens. All components inside the vacuum chamber are compatible with a vacuum base pressure of at least 10^{-2} mBar. With the new system development, the SEM objective lens and the light objective lens have a common axis and focal plane, allowing high-resolution optical microscopy and scanning electron microscopy on the same area of a sample by simply moving and repositioning the light microscope module, thus leading to correlative imaging.

We demonstrate the use of our light microscope module as a kind of "preview option" for SEM as shown in Fig.2. The light microscope gives visibility to the copper mesh (grid size : 5 μm*5 μm), individual grid can be clearly identified in the image in Fig.2(a). Based on this image, a region can be selected for SEM inspection at high magnification, as indicated in Fig.2 (b) and 2(c).

Our future work is to extend a fluorescence analysis function in the module to study living cells. We have developed a fluorescence microscope module on the original low magnification "preview" module, according to the scheme depicted in Figure 3(a). A 350 W Xenon lamp light source with collimator lens is used to illuminate polystyrene particle sample(Fluoro-Max R400 ; particle size 400 nm), and an emission of orange 612 nm fluorescence image taken by the 100X objective lens is shown in Fig.3(b).

References

[1] S. e. al., "<Electron microscope with optical microscope," *United State Patent,* p. 4266128, 1979.

[2] T. e. al., "<Scanning electron microscope with an optical microscope," *United State Patent,* p. 4537477, 1983.

[3] T. Kanemaru, K. Hirata, S. Takasu, S. Isobe, K. Mizuki, S. Mataka, *et al.*, "A fluorescence scanning electron microscope," *Ultramicroscopy,* vol. 109, pp. 344-9, Mar 2009.

[4] H. Nishiyama, M. Suga, T. Ogura, Y. Maruyama, M. Koizumi, K. Mio, *et al.*, "Reprint of: Atmospheric scanning electron microscope observes cells and tissues in open medium through silicon nitride film," *J Struct Biol,* vol. 172, pp. 191-202, Nov 2010.

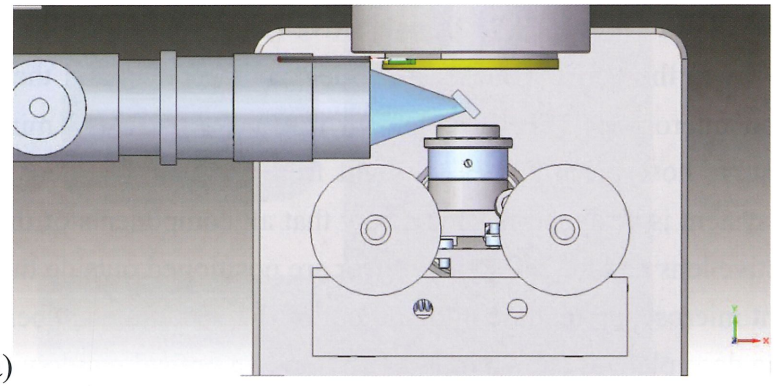

(a)

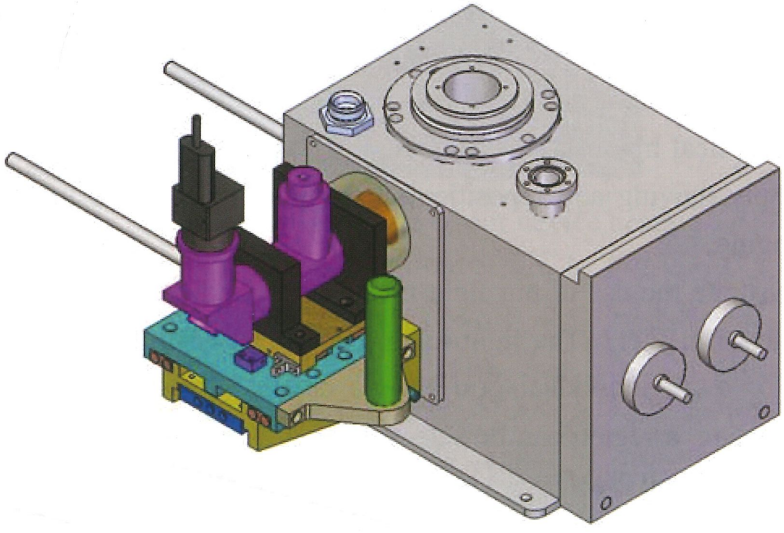

(b)

Fig 1. Schematic of CLEM (a) Perspective view (b) Side view

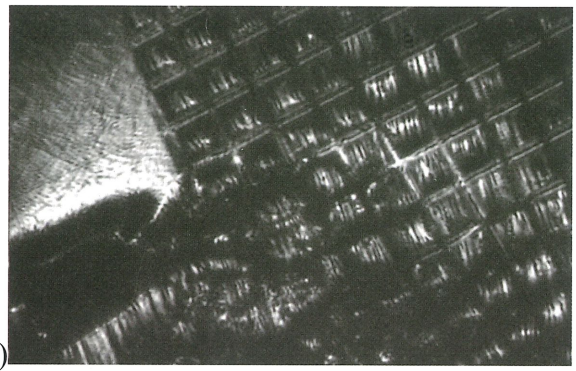

(a)

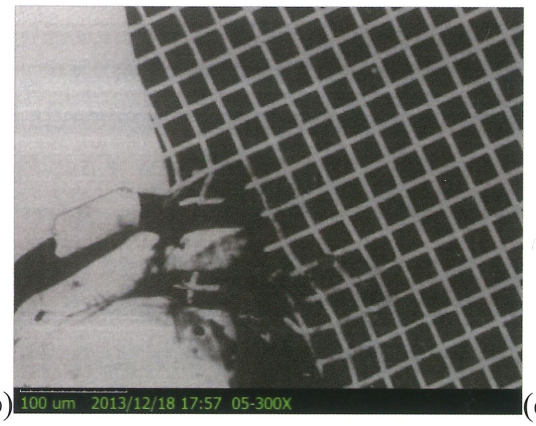

(b)

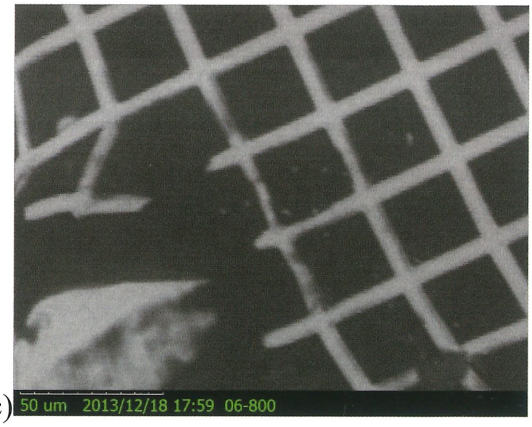

(c)

Fig 2. (a) OM 10x image (b) SEM 300x image (c) SEM 800x image

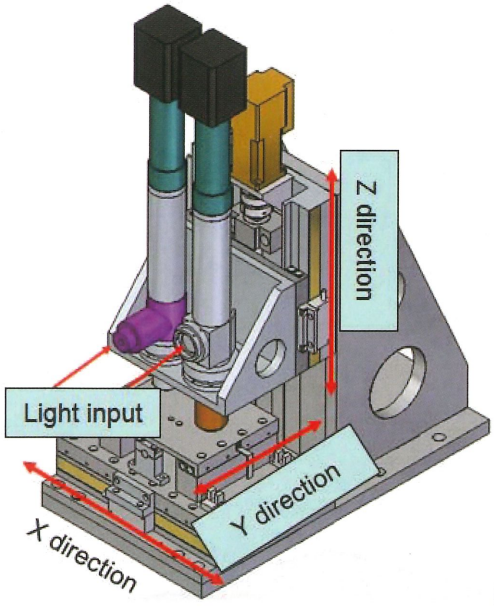

(a)

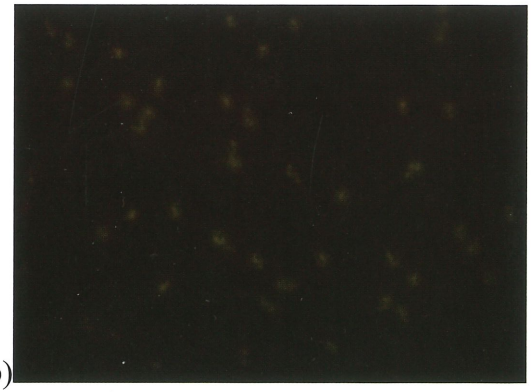

(b)

Fig 3. (a) testing stage for fluorescence light microscope (b) 100x fluorescence light microscope image for 400 nm polystyrene

M-P-26

SI EFFECT ON STRENGTHENING OF DUAL-PHASE STEELS

Shao-Pu Tsai (蔡劭璞),[1] Chih-Hung Jen (鄭至閎),[1] Yuan-Tsuong Wang (王元聰), [2] Ching-Yuan Huang (黃慶淵), [2] and Jer-Ren Yang (楊哲人)[1]

[1]Department of Materials Science and Engineering, National Taiwan University, Taipei, Taiwan

[2]Department of Research and Development, China Steel Corporation, Kaohsiung, Taiwan

Two alloys which are heat treated by step quenching to obtain dual-phase (ferrite+martensite) morphology with different Si addition are studied. Specimens from each alloy with similar martensite volume fraction are picked out for comparison so that martensite strengthening effect can be ruled out. It is discovered that Si can slightly raise the hardness of both ferrite and martensite phase in that Si as solute atoms has effective strengthening effect. Tensile tests further show that Si content increment can either improve ultimate tensile strength or elongation while not sacrificing the other in the mean time. Thus, in this study, Si addition is thought to improve mechanical properties of dual-phase steels.

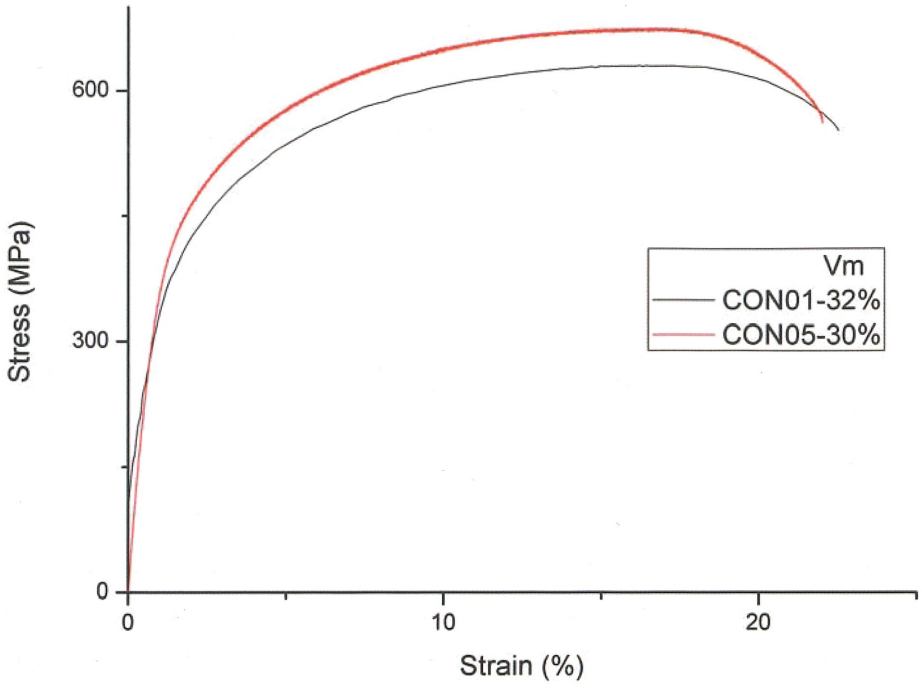

Figure 1. Si effect on increasing yield strength and ultimate tensile strength while not sacrificing elongation.

B-P-01

INFLORESCENCE AND FLORAL DEVELOPMENT IN *TROCHODENDRA ARALIOIDES* SIEBOLD & ZUCC. (TROCHODENDRACEAE)

Yu-Chwen Hsu (許毓純) [1,2], Wann-Neng Jane (簡萬能)[3] and Su-Hwa Chen (陳淑華)[1]

[1]Institute of Ecology and Evolutionary Biology, National Taiwan University, Taipei, Taiwan
[2]Collection Management Department, National Taiwan Museum, Taipei, Taiwan
[3]Institute of Plant and Microbial Biology, Academia Sinica, Taipei, Taiwan

Trochodendron aralioides is a monotypic species of genus *Trochodendron* in the basal eudicot family Trochodendraceae. In the sudy, the flower development was examined using scanning electron microscopy. The floral primodia spirally arranged in the inflorescence and covered by a floral subtending bract (pherophyll) that was developing earlier. The two prophylls initiated in the transversal position of floral primodium, and some scales like tepal rudiments appeared between the prophylls and androecium in some flowers. The numerous anthers spirally initiated within a narrow area in the terminal flower and the developments of androeium at the abaxial side are delayed in lateral flowers. The numerous carpels arised in a whorl. The residual floral apex could be obviously visible at the early developmental stage and then coated by carpels at anthesis. The floral development of *Trochodendron aralioides* would provide the developing floral parts in an elegant orientation for revealing the ones of the basal eudicot plants.

References

1. APG, 2009. An update of the Angiosperm Phylogeny Group classification for the orders and families of flowering plants: APG III. Bot. J. Linn. Soc. 161, 105-121.
2. Endress PK (1986) Floral structure, systematics, and phylogeny in Trochodendrales. Ann Missouri Bot Gard 73:297-324
3. Wu H-C, Su H-J, Hu J-M (2007) The identification of A-, B-, C-, and E-class MADS-box genes and implications for perianth evolution in the basal eudicot *Trochodendron aralioides* (Trochodendraceae). Int J Plant Sci 168(6):775-799

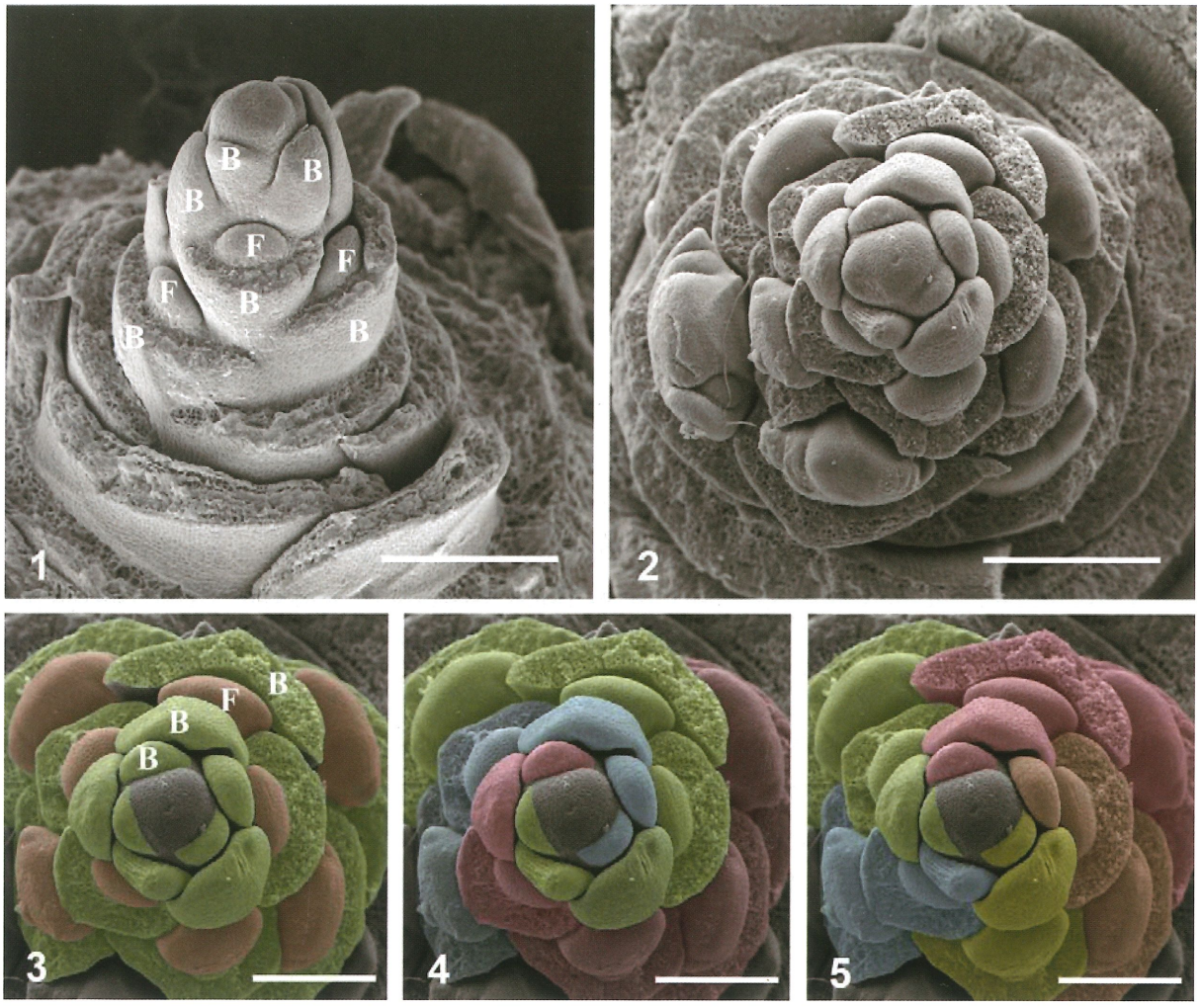

Fig. 1-5 Young inflorescence. Fig. 1 Entire inflorescence form the side, floral pherophylls were removed in lower part to show floral primordia. Fig. 2 Entire inflorescence form above, floral pherophylls were removed also to show the arrangement of the floral primordia. Fig. 3 The same orientation as fig. 2 floral primordia colored by orange and pherophylls colored by green. Fig. 4 & 5 Same as fig. 2 colored floral primordia to show the phyllotaxis in set of 5 clockwise and set of 3 anticlockwise. (B: subtending bract (pherophyll), F: floral primordium). Bars: Fig. 1&2 = 300 μm; Fig. 3-5 = 200 μm.

B-P-02

BLUE IRIDESCENCE IN AQUATIC AROID, *Bucephalandra*

[1]FAN, Kang-Yu (范綱祐) and [1] KUO-HUANG, Ling-Long (黃玲瓏)

[1]Institute of Ecological and Evolutionary Biology, National Taiwan University, Taipei, Taiwan

Bucephalandra, a genus of rheophytic aroids, is endemic to Borneo. Currently, there are 5 species scientifically accepted and at least 20 undescribed new species. They are understory plants living in or along the streams. Some species adapt the underwater environment well, but the rest of them tend to grow emerse. Particularly, those underwater species show blue iridescence in submerged leaves. The anatomical results show that the epidermal cell walls are partially lamellated (Figure 1.). So far, this kind of multi-layer structure has only been discovered in terrestrial plants. It's the first report of blue leaf iridescence in submerged leaves of aquatic plants.

References

1. B. J. Glover, H. M. Whitney. Structural color and iridescence in plants: the poorly studied relations of pigment color, *Ann Bot*. 105 (2010) 505.
2. K. R. Thomas, M. Kolle, H. M. Whitney, B. J. Glover, U. Steiner. Function of blue iridescence in tropical understory plants. *J R Soc Interface*. 7 (2010) 1699.
3. P. Vukusic, J. R. Sambles. Photonic structures in biology, *Nature*. 424 (2003) 852.

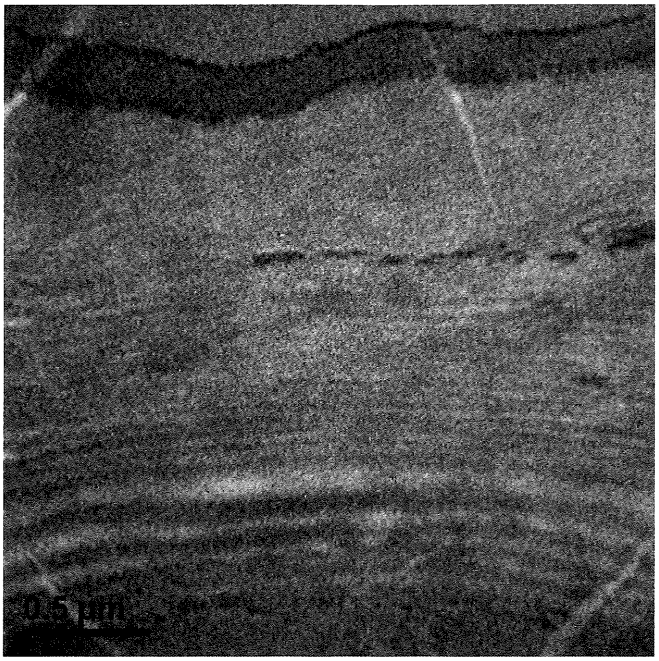

Figure 1. TEM micrograph of multi-layer structure in outer cell wall.

B-P-03

DEVELOPMENT OF FEMALE GAMETOPHYTE AND YOUNG SEED OF *NEONOTONIA WIGHTII* (WIGHT & ARN.) J.A. LACKEY (LEGUMINOSAE)

Tian-Jyun Liu (劉恬君),[1] Chi-Chih Wu (吳啟智)[2], and Ling-Long Kuo-Huang (黃玲瓏) [1]

[1] Institute of Ecology and Evolutionary, National Taiwan University, Taipei, Taiwan, 10617

[2] Institute of Plant and Microbial Biology, Academia Sinica, Taipei, Taiwan, 11529

The genus *Neonotonia* was early grouped with the genus *Glycine* [1,2] and is closely related to the *Glycine* that contains cultivated soybean, *Glycine max*[3]. The *Neonotonia* consists of only two species that are perennial and have smaller seeds compared to *G. max*. The development of the seed, especially in the female gametophyte, embryo and endosperm, has been studied for cultivated soybean[4-6]; however, little is known about these components of sexual reproduction in wild related species of soybean, such as the genus *Neonotonia*. In order to understand the developmental and evolutionary transition of these traits of cultivated soybean from its wild relatives, we used a comparative developmental and morphological approach to study megagametogenesis, embryogenesis and the formation of young fruit of a wild relative of cultivated soybean, *Neonotonia wightii*. In addition, we investigated the timing of key features of sexual reproduction, including double fertilization, the first mitotic division of the zygote and the primary endosperm nucleus, and the cellularization of endosperm. Our results show that, in general, the pattern of the female gametophyte of *N. wightii* is similar to that of cultivated soybean, *G. max*. Both are the Polygonum type in which a functional megaspore undergoes three runs of mitotic divisions to form an eight-nucleate, seven-celled mature female gametophyte (embryo sac). After double fertilization, many features of embryo and endosperm development were observed and compared with those of cultivated soybean. The development of an endosperm is the nuclear type. In addition, the timing of reproductive features is reported.

References

1 Hermann, F. J. *A revision of the genus Glycine and its immediate allies*. (Washington : U.S. Dept. of Agriculture, 1962).

2 Verdcourt, B. A Proposal concerning Glycine L. *Taxon* **15**, 34-36.

3 Zhu, T., Shi, L., Doyle, J. J. & Keim, P. A single nuclear locus phylogeny of soybean based on DNA sequence. *Theoretical and Applied Genetics* **90**, 991-999 (1995).

4 Folsom, M. W. & Peterson, C. M. Ultrastructural Aspects of the Mature Embryo Sac of Soybean, Glycine-Max (L) Merr. *Bot Gaz* **145**, 1-10, doi:Doi 10.1086/337418 (1984).

5 Dute, R. R., Peterson, C. M. & Rushing, A. E. Ultrastructural Changes of the Egg ApparatusAssociated with Fertilization and Proembryo Development of Soybean, Glycine max (Fabaceae). *Ann Bot-London* **64**, 123-135 (1989).

6 Folsom, M. W. & Cass, D. D. Embryo Sac Development in Soybean - the Central Cell and Aspects of Fertilization. *Am J Bot* **79**, 1407-1417, doi:Doi 10.2307/2445140 (1992).

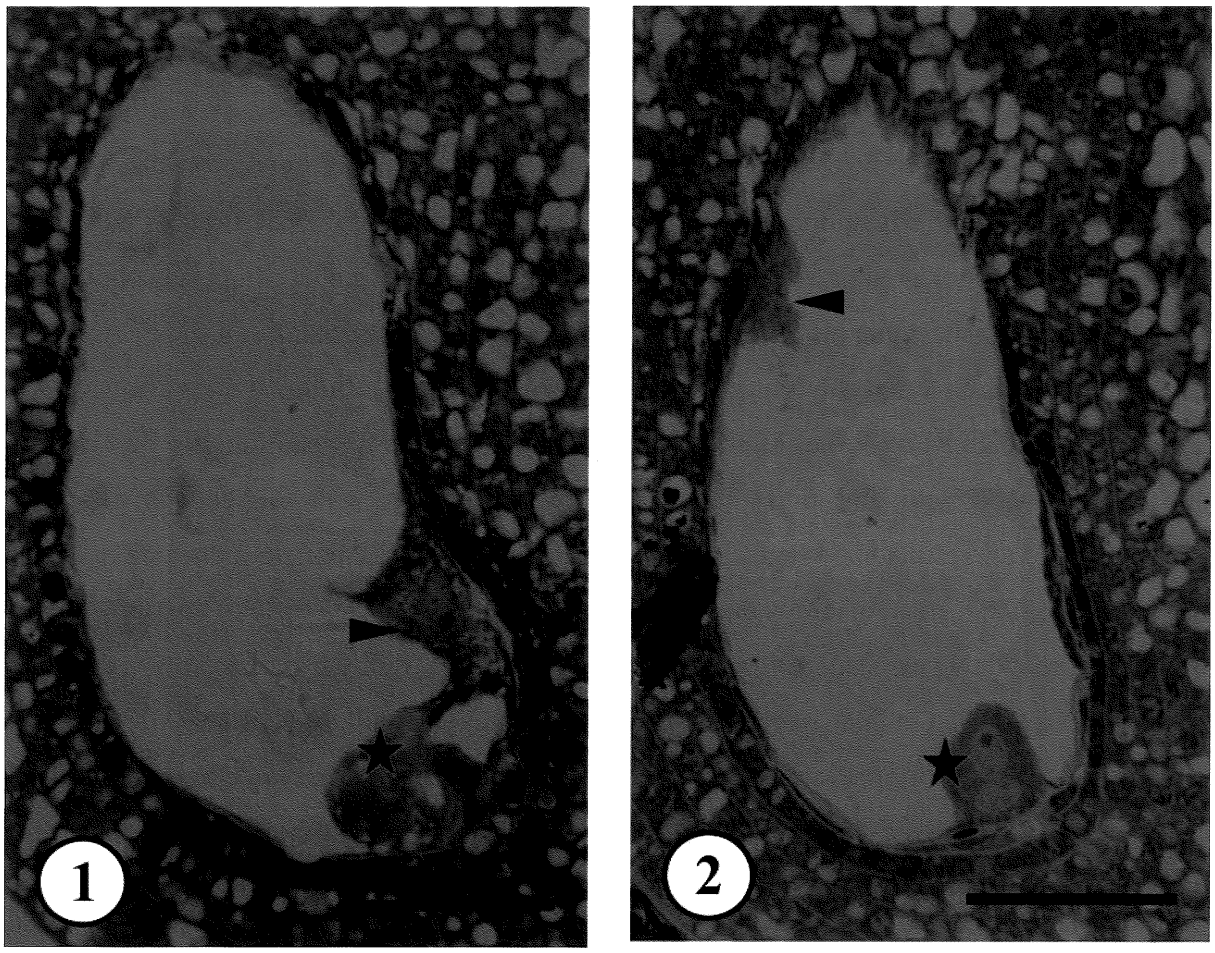

Fig. 1 Zygote in metaphase. Scale bar: 50μm

Fig. 2 Zygote in telophase. Scale bar: 50μm

Asterisks denote zygotes, and arrows denote free endosperm nuclei.

B-P-04

REVEALING a 2-nm DOMAIN in a 13-nm PROTEIN COMPLEX by IN-FOCUS CRYO ELECTRON MICROSCPOY

[1]WU, Yi-Min (吳逸民), [1]CHANG, Jen-Wei(張荏韋), [2]NAGAYAMA, Kuniaki(永山國昭), [2]MURATA, Kazuyoshi(村田和義) and [1]CHANG, Wei-Hau(章為皓)

[1]Institute of Chemistry, Academia Sinica, Taipei, Taiwan
[2]Division of Structural Biology, National Institutes of Physiology, Okazaki, Japan

In the transcription process through RNA polymerase (RNAP), the elongation factor Spt4/5 is the only conserved between bacteria, archaea, and eukaryota domains. The function of Spt4/5 complex related a dual role in both stimulating transcription elongation and causing the promoter-proximal pausing together with the negative elongation factor NELF. To understand the structure basis on which Spt4/5 regulates the transcription elongation process, the molecular architecture of RNAP with Spt4/5 is required. Recently, a cryo-EM reconstruction of archaeal RNAP-Spt4/5 and a partial crystal structure of yeast Spt4/5 bound to the RNAP clamp domain have been reported [1, 2], disagreeing on the location of Spt4/5 on RNAP. According to our previous finding that a Zernike phase plate (ZPP) could extend the lower size limit of cryo-EM to ~100 kDa [3], we applied ZPP cryo-EM to yeast Spt4/5 of 100 kDa as it was associated with RNAP. As the structure of RNAP-Spt4/5 is compared with RNAP, a conspicuous density on the Rpb1 clamp is revealed. (Fig. 1).

References

1. B. J. Klein, *Proc Natl Acad Sci U S A.* 108 (2011) 546.
2. F. W. Martinez-Rucobo, *EMBO J.* 30 (2011) 1302.
3. Y. M. Wu, *J. Phys. D: Appl. Phys.* 46 (2013) 494008.

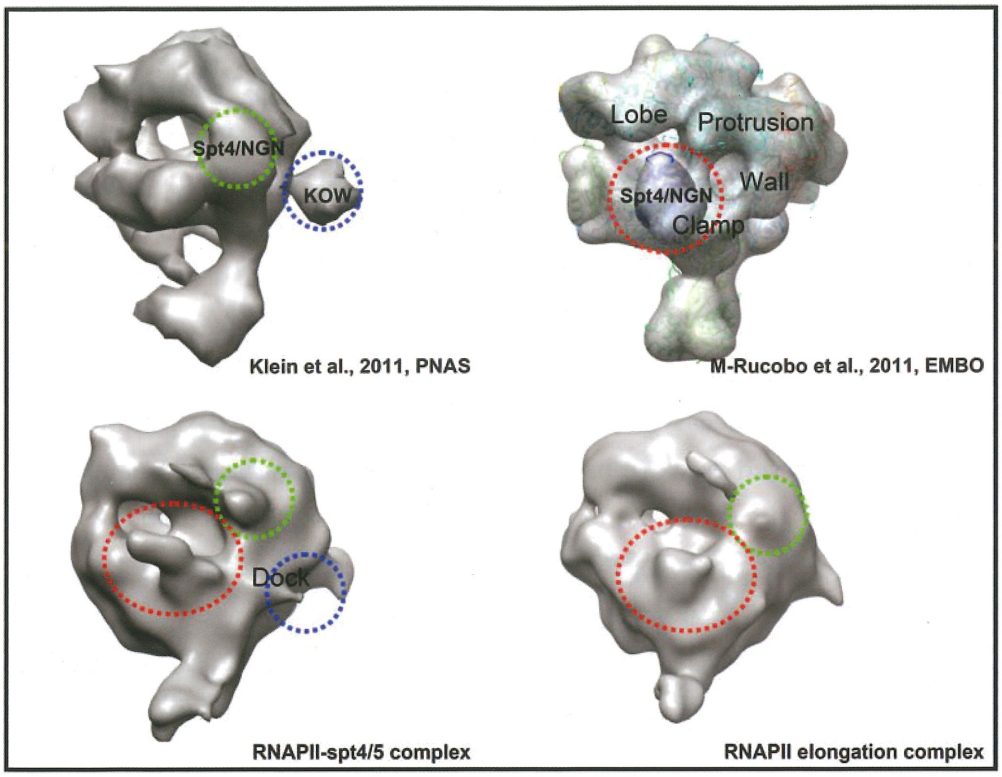

Figure 1. Cryo-EM reconstructions of RNAP and RNAP-Spt4/5 complex. In the upper panel, left is the Klein archeal RNAP-Spt4/5 by conventional cryo-EM while in the right represents of a filtered model of RNAP-Spt4/5 based on partial X-ray structure by M-Rucobo et al., In the lower panel, left is the single particle reconstruction of RNAP and the right presents RNAP-Spt4/5 complex. A finger-like density on the clamp of RNAP is revealed.

B-P-05

CURRENT ADVANCE OF CRYO ELECTRON MICROSCOPY IN REACHING SUB-NANOMETER RESOLUTION PROTEIN STRUCTURES

[157]CHANG, Wei-Hau (章為皓), [2]LIN, Frank (林全信), [3]CHEN, Fu-Rong (陳福榮), [4]MURATA, Kazuyoshi (村田和義), [4]NAGAYAMA, Kuniaki (永山國昭), [5]WANG, Chun-Hsiung (王俊雄), [5]WU, Yi-Min (吳逸民), [5]CHANG, Jen-Wei (張荏韋), [5]HUANG, Shih-Hsin (黃士炘), [6]HSIEH, Dai-Ni (謝岱霓), [6]TU, I-Ping (杜憶萍), [7]CHEN, Yi-Yun (陳怡云), [7]HWU, Yeukuang (胡宇光), [7]Li, Neil (李柏南), [7]Li, Ting-Kuo (李定國)

[1]Department of Biochemical Science and Technology, National Taiwan University, Taipei, Taiwan
[2]Department of Marine Science, National Sun Yat Sen University, Kaohsiung, Taiwan
[3]Department of Engineering System, National Tsing-Hua University, Hsinchu, Taiwan,
[4]Divion of Structural Biology, National Institutes of Physiology, Okazaki, Japan
[5]Institute of Chemistry, [6]Institute of Statistics and [7]Institute of Physics, Academia Sinica, Taipei, Taiwan

Single particle cryo electron microscopy (Cryo-EM) has emerged as a powerful tool in revealing near atomic resolution structures, as mainly demonstrated by Hong Zhou at UCLA and other researchers in USA. The strategy of these groups use is to study icosahedral virus reconstruction to overcome the SNR limit imposed on the images due to radiation damage issue and the results were obtained by very stable and expensive 300 kV field-emission microscope. In Taiwan, though we only have only 200 kV field emission machines, we have demonstrated it is possible to reveal 4 Angstrom structure by using a cutting-edge motion-free camera. In this presentation, we will report two icosahedral virus structures, one abundant in beta-sheet and the other in alpha-helix. Furthermore, to overcome the challenges of obtaining sub-nanometer resolution structure of protein complexes without symmetry, we have formed a consortium with Fu-rong Chen and Nagayama (Okazaki) to boost the SNR with phase plates and with statisticians and theoretical physicists to develop efficient de-noising algorithm.

References

1. J. Shiue, C.-S. Chang, S.-H. Huang, C.-H. Hsu, J.-S. Tsai, W.-H. Chang, Y.-M. Wu, Y.-C. Lin, P.-C. Kuo, Y.-S. Huang, Y. Hwu, J.-J. Kai, F.-G. Tseng and F.-R. Chen (2009), *Journal of Electron Microscopy, 58（3）*
2. C. Wang, C. Hsu, Y. Wu, Y Luo, M. Tu, WH Chang, RH Cheng, CS Lin (2010) *Virus Genes. 41(1):73-80*
3. YM Wu, CH Wang, JW Chang, YY Chen, N. Miyazaki, K. Murata, K. Nagayama5 and WH Chang (2013) *J. Phys. D:* Appl. Phys. 46 494008

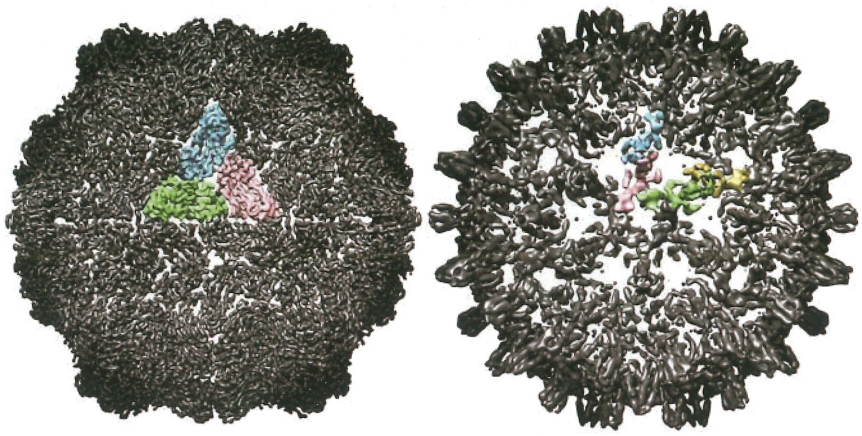

Figure 1. A beta-sheet rich virus compared to an alpha-helix rich virus revealed by a 200 kV cryo-EM followed by motion-correction 3D reconstruction

B-P-06

THE PRELIMINARY STUDY OF THE STRUCTURE OF *SAPINDUS MUKOROSSI* SEED AND ITS PHYSICAL DORMANCY MECHANISM

[1]WANG, Ming-Wei (王名偉), [1]KUO-HUANG, Ling-Long (黃玲瓏) and [2]Ching-Te Chien (簡慶德)

[1]Institute of Ecology and Evolutionary Biology, National Taiwan University, Taipei, Taiwan

[2]Taiwan Forestry Research Institute, Taipei, Taiwan

Chinese soapberry (*Sapindus mukorossi*) is a native species with high potential on economic value in Taiwan, such as the pericarp in cleaning supplies and control agent, the seed kernel pressed to extract oil, and the wood in timber industry. Current studies on Chinese soapberry are focused on the analysis of chemical composition in the pericarp and its structure is less understood. Nevertheless, the structure and chemical composition of its thick seed coat and the related mechanism of its physical dormancy are still unknown. In this study, we use free-hand and paraffin sections, as well as maceration technique to investigate the structure of seed coat and pericarp, the path of water getting into seed, and the changes of the size of hilar slit as soaked in hot water by light and scanning electron microscopy. Besides, the seed coat was also histo-chemically stained. The preliminary results showed: (1) the thick seed coat enclosed an embryo with little endosperm, the filiform aril surrounding the funiculus scar, and the hilar slit located in the scar with a cavity underneath (Fig. 1); (2) the seed coat consisting two kinds of sclerenchyma, the outer palisade cell layers and inner sclereid layers (Fig. 2); (3) the most outer layers of palisade cells lignified and the inner palisade cell and all the inner sclereids suberized (Fig. 3); (4) the hilar slit being the water gap and a positive correlation between its open size and the soaked hot water been verified. In summary, the physical dormancy of Chinese soapberry is caused by the lignified and suberized thick seed coat. For imbibition to break the physical dormancy, the opening of the hilar slit is necessary and the positive correlation between its open size and the soaked hot water might indicate the change of environment.

References

1. N. S. Gama-Arachchige, J. M. Baskin, R. L. Geneve, C. C. Baskin. Identification and characterization of ten new water gaps in seeds and fruits with physical dormancy and classification of water-gap complexes, *Ann Bot.* 112 (2013) 69.
2. J. M. Baskin, C. C. Baskin, X. Li. Taxonomy, anatomy and evolution of physical dormancy in seeds, *Plant Spec. Biol.* 15 (2000) 139.

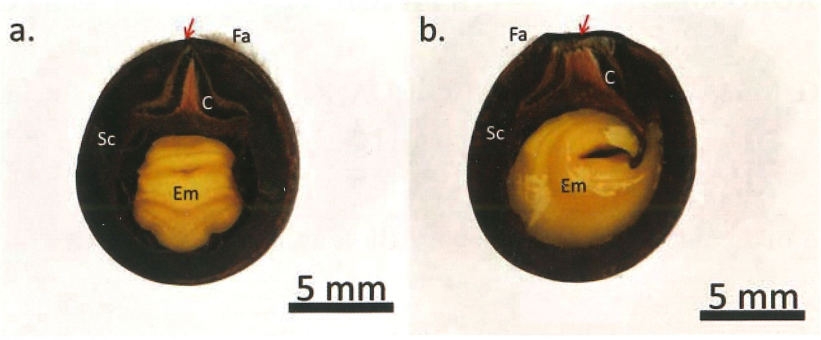

Figure 1. The radial section shows the structure of seed of *Sapindus mukorossi*. Arrows indicate hilar slit. (a) The section is perpendicular to the hilar slit. (b) The section is parallel to the hilar slit. Abbreviation: C, cavity; Em, embryo; Sc, seed coat.

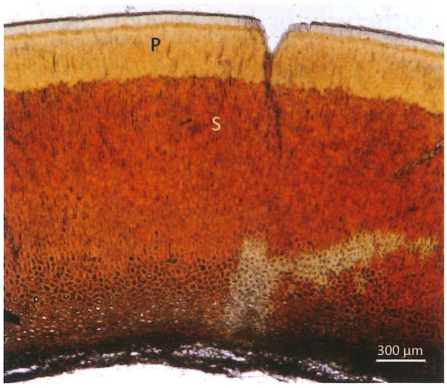

Figure 2. Light micrograph of the structure of the seed coat. Abbreviation: P, palisade cell; S, sclereids

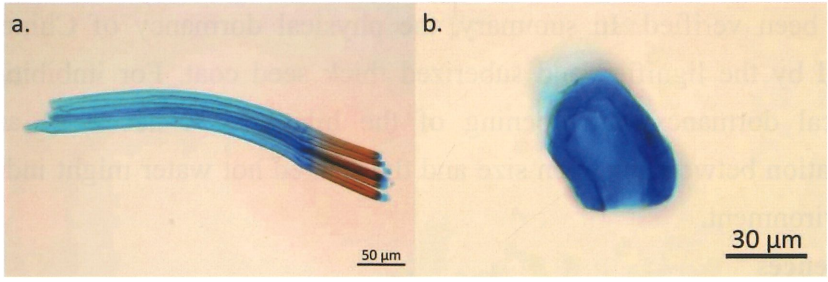

Figure 3. Light micrograph of the seed coat processed by maceration technique. Areas stained red indicate lignification. (a) Palisade cells. (b) Sclereid.

I-01

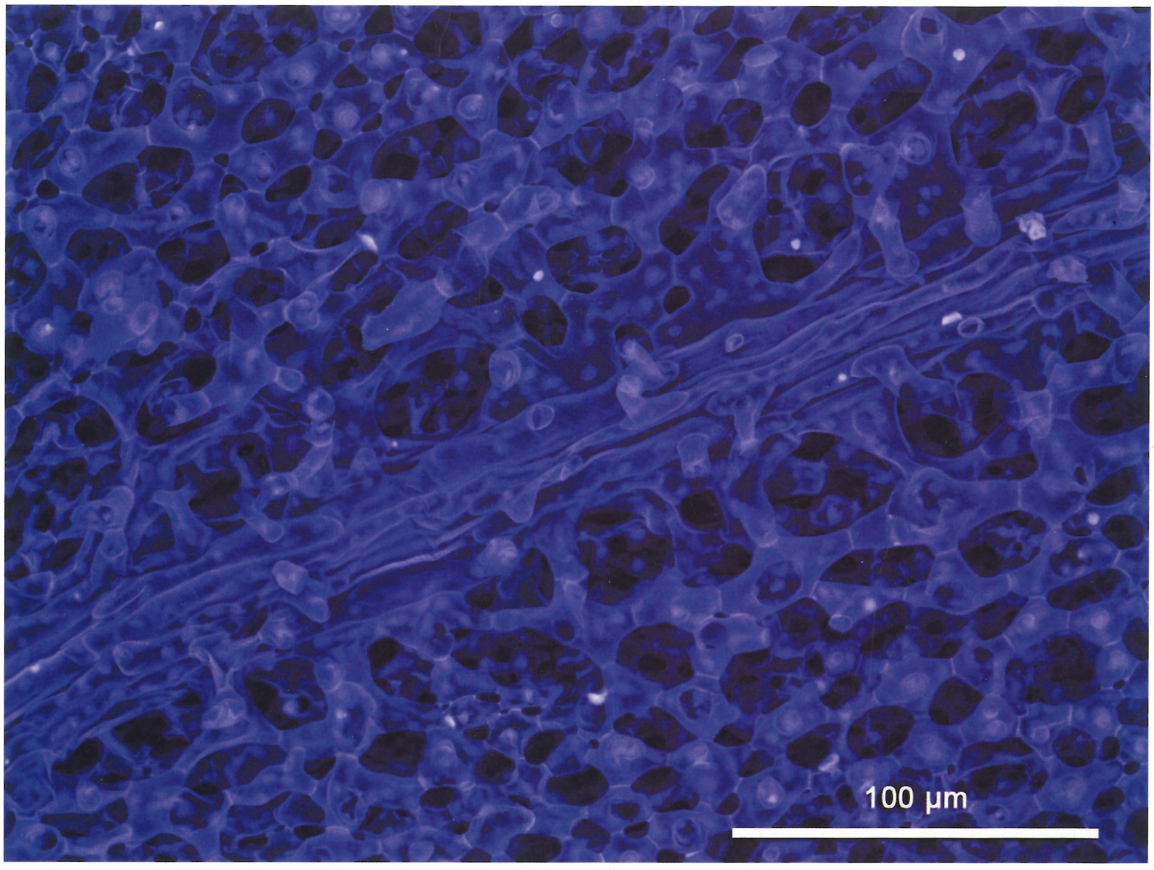

作品名稱　深海的海底隧道

作品內容

神秘的海底隧道盡藏身在葉中的海綿組織內，其中主脈的一條貫穿，如同深藏在深海最深處的水中蛟龍。

作者姓名：李紹輔	單位：中興大學-生命科學系
聯絡電話：0910-985932	E-Mail：freddy1991724@gmail.com

作品名稱　**Superconducting Nano-Carnation 超導康乃馨**	
作品內容 利用水熱法所製備的 FeSe 超導體奈米顆粒之 SEM 影像，此團聚的超導體彷彿盛開的康乃馨。	
作者姓名　張忠傑、許家豪、曾傳銘	**單位**　中央研究院物理所
聯絡電話　(02) 2789-8370	**E-Mail**　ccchang1978@phys.sinica.edu.tw

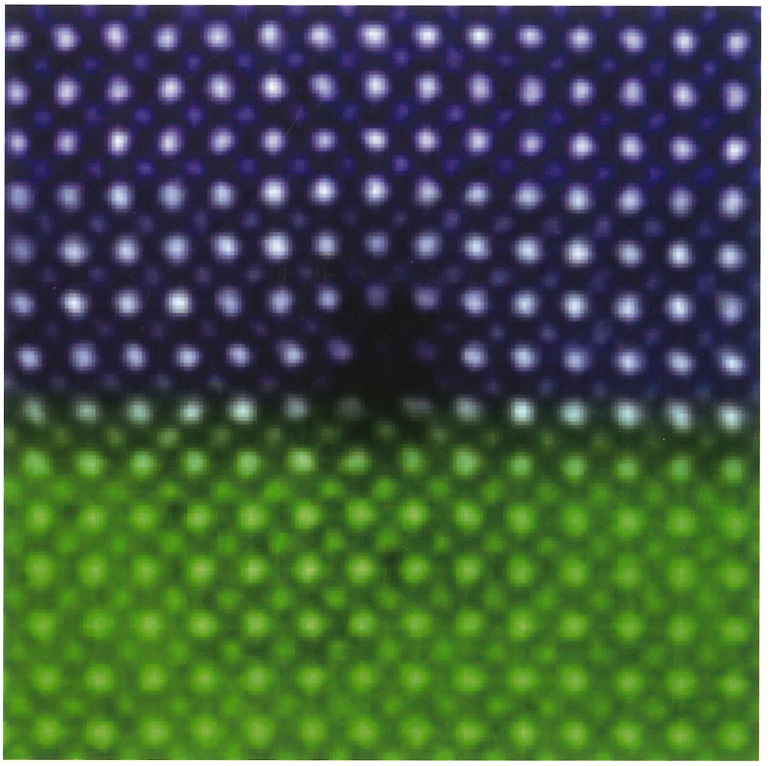

作品名稱　星空・草原・黑洞

作品內容

$(Nd_{0.35}Sr_{0.65})MnO_3$ /$SrTiO_3$ 氧化物界面處失配刃差排(misfit edge dislocation)的原子解析度 STEM-HAADF 影像，如同教科書中常見之示意模型，且經實驗証實此差排應力場如黑洞般，將原本界面之二維電荷全部匯集並蓄積至其中。

作者姓名　張景斌	單位　國立台灣大學凝態科學研究中心
聯絡電話　02-33665210	E-Mail　d96527008@ntu.edu.tw

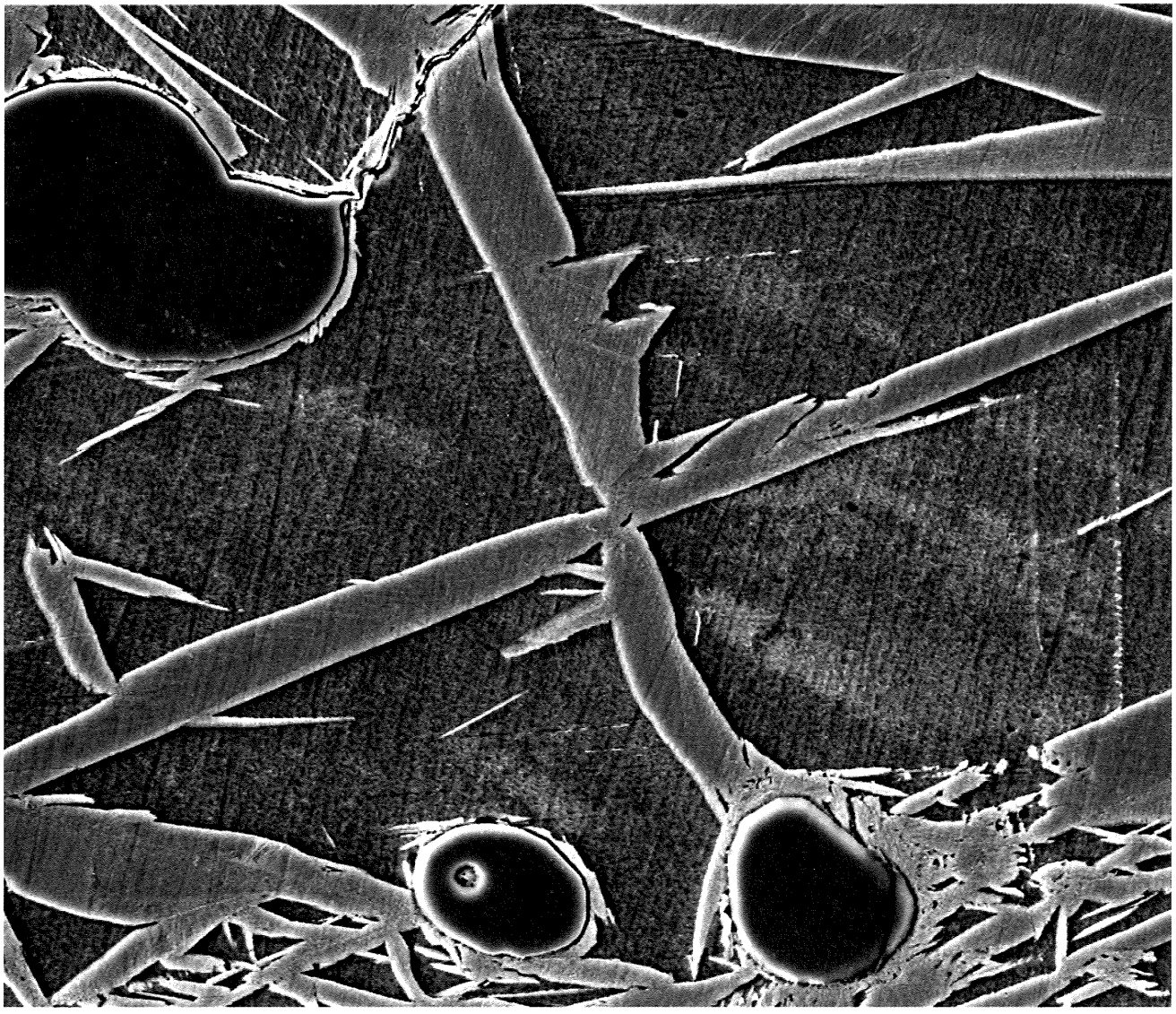

作品名稱　十字型迴力鏢

作品內容

白色邊緣像刀鋒一般，又有十字的形狀，因此取名為十字型迴力鏢。

作者姓名:張雅齡	單位:台灣大學材料所
聯絡:02-33661353	E-Mail:D99527007@ntu.edu.tw

I-05

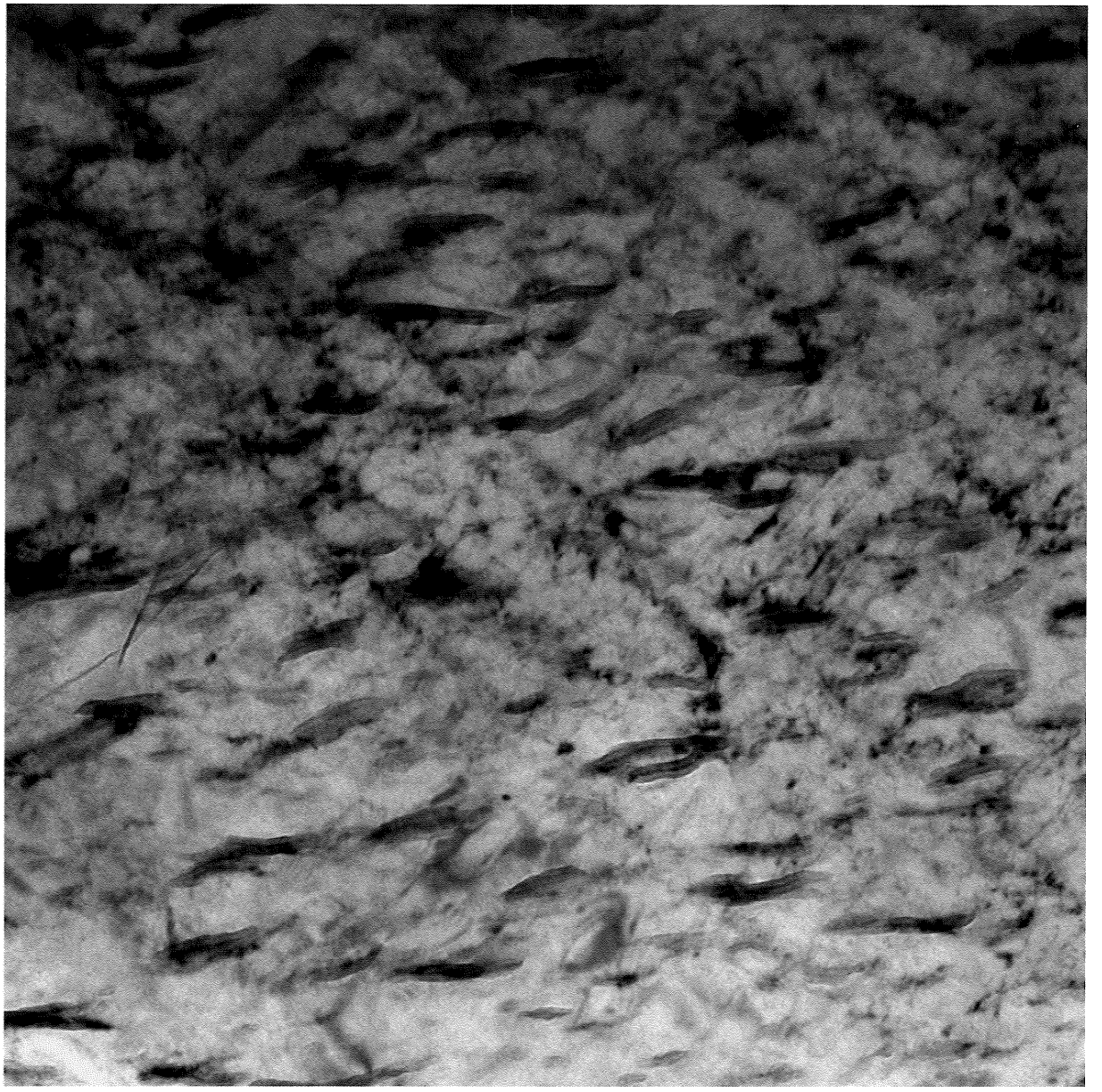

作品名稱　生生不息	
作品內容 魚苗在大海中拼命往前游的景象，象徵生命生生不息。	
作者姓名: 張雅齡	單位: 台灣大學材料所
聯絡電話: 33663748	E-Mail: D99527007@ntu.edu.tw

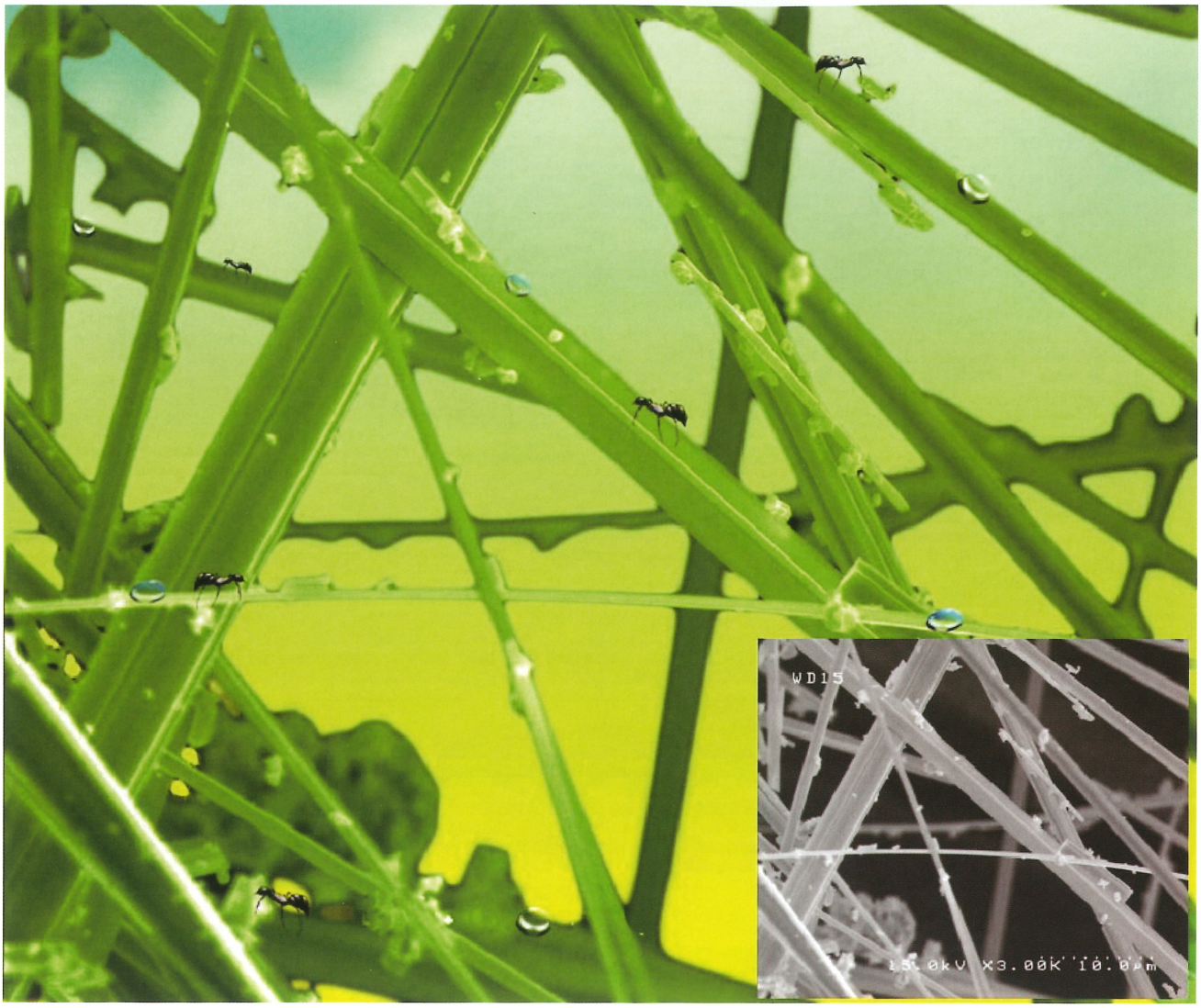

作品名稱　**Life of Ant 螞蟻人生**	
作品內容 Na_xWO_3 奈米線於製程中形成在 Na_xWO_3 塊材表面上，貌似一群螞蟻於枝幹上勤奮地工作著。(右下角為 SEM 原圖影像)	
作者姓名　許家豪、王一智、張忠傑、曾傳銘	**單位**　中央研究院物理所
聯絡電話　(02) 2789-8370	**E-Mail**　chhsu@phys.sinica.edu.tw

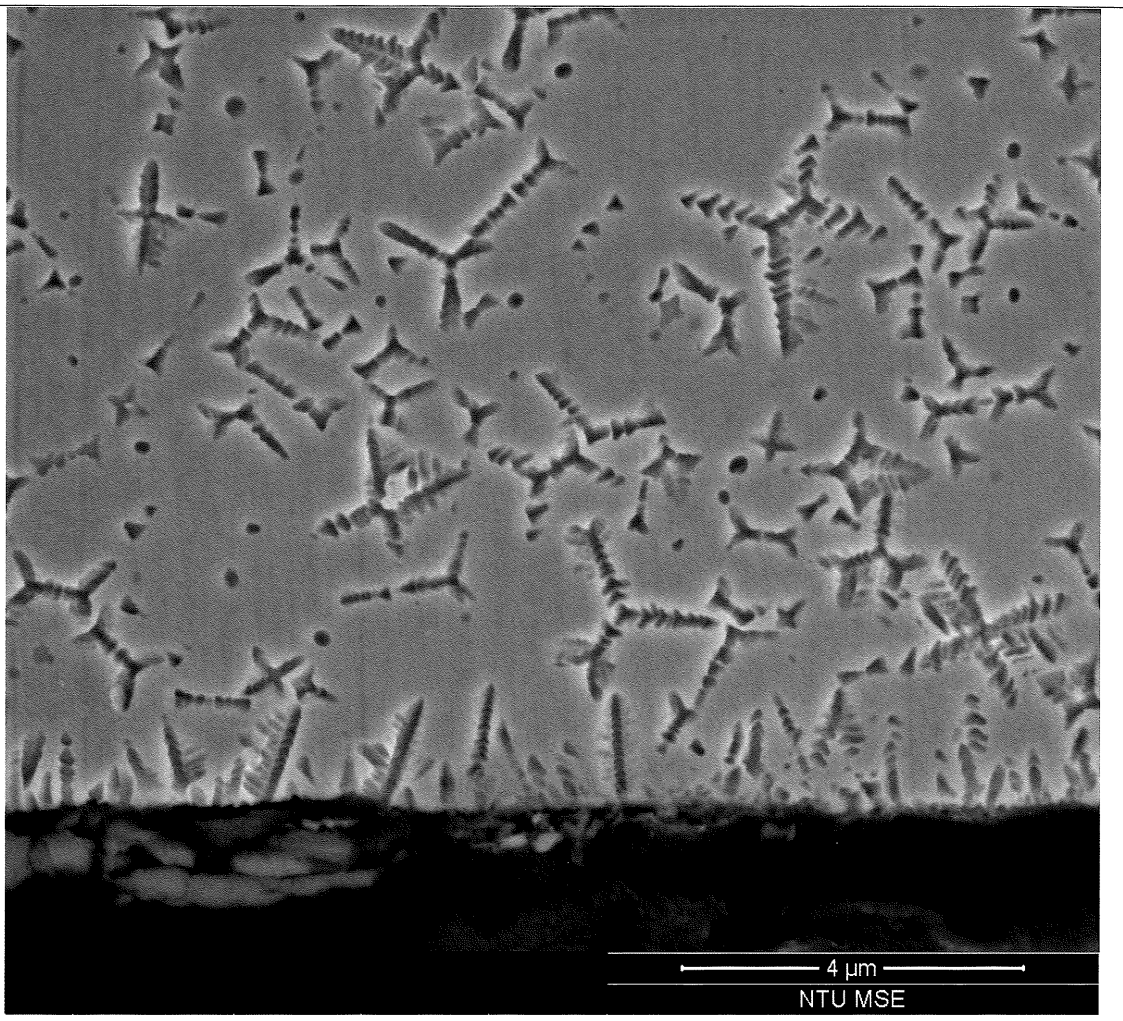

作品名稱　飛舞的雪花結晶	
作品內容 非晶質材料經退火後產生樹狀晶，於表面呈現柱狀排列，如雪花落下	
作者姓名　陳伯宇	單位　國立台灣大學材料所
聯絡電話　(02)3366-3748	E-Mail　d00527002@ntu.edu.tw

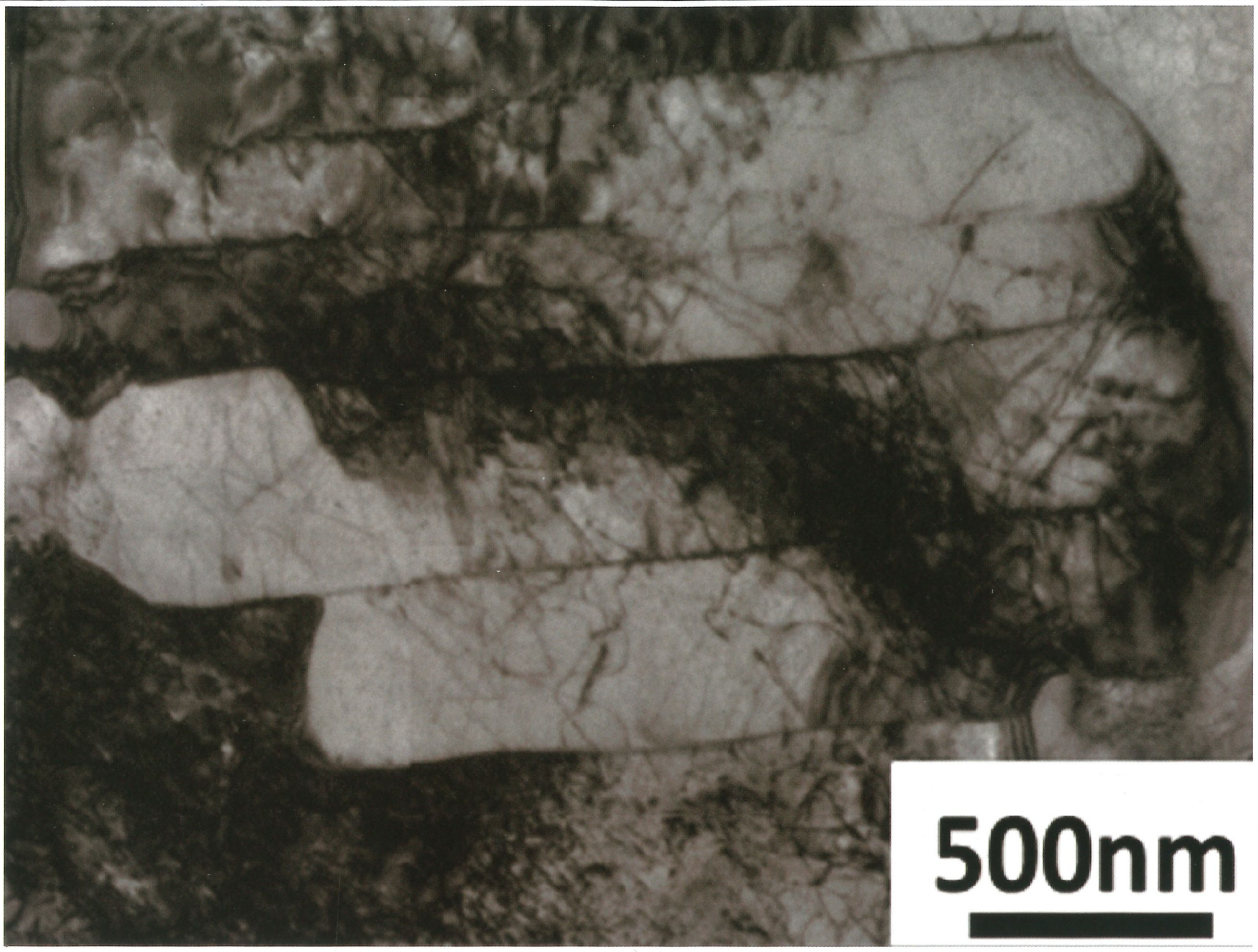

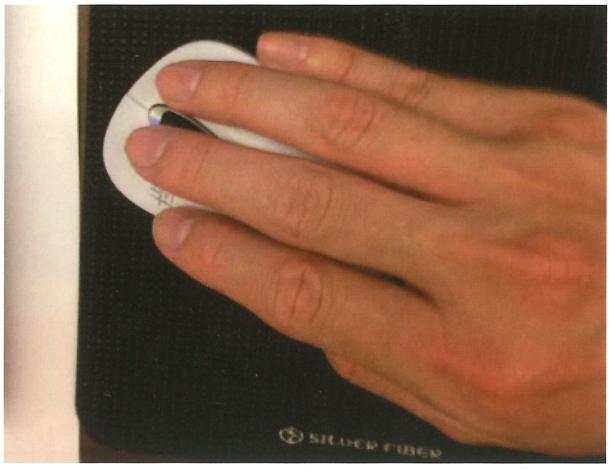

作品名稱　滑鼠上的手背	
作品內容 此結構為長條狀的變韌鐵次晶粒組成的粒狀變韌鐵	
作者姓名:黃柏銘	單位:台大材料所
聯絡電話:02-3366-3748	E-Mail:r95527042@ntu.edu.tw

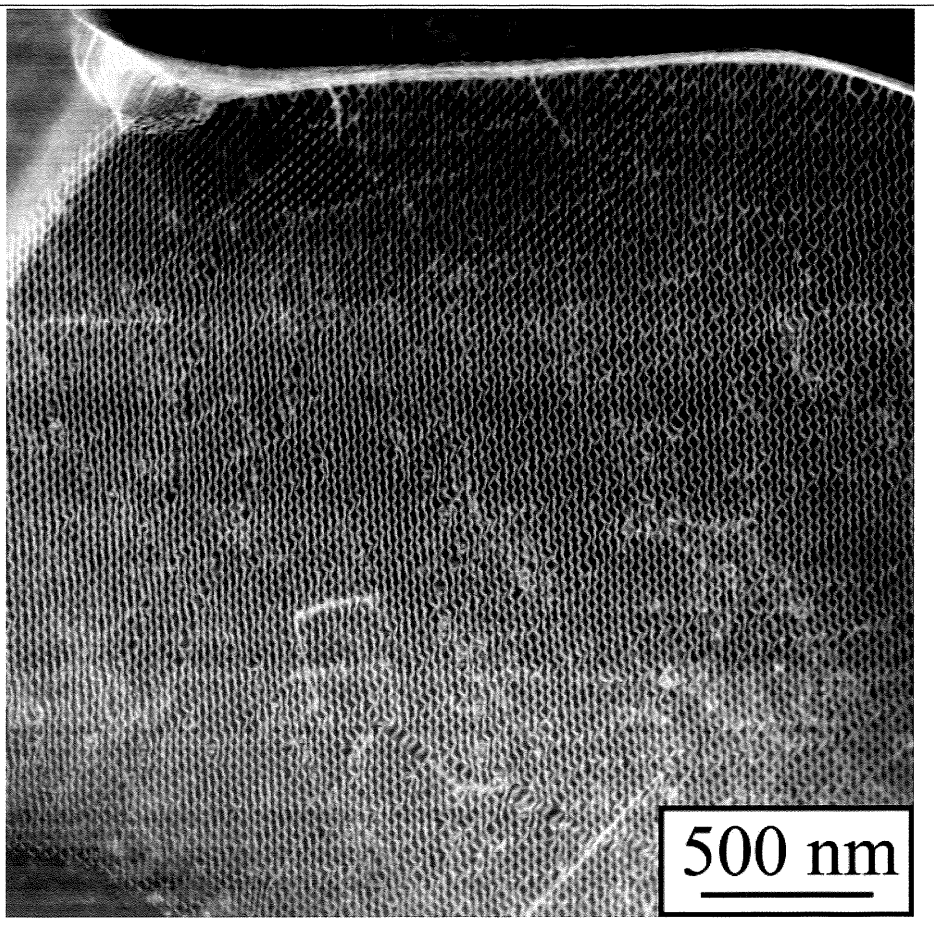

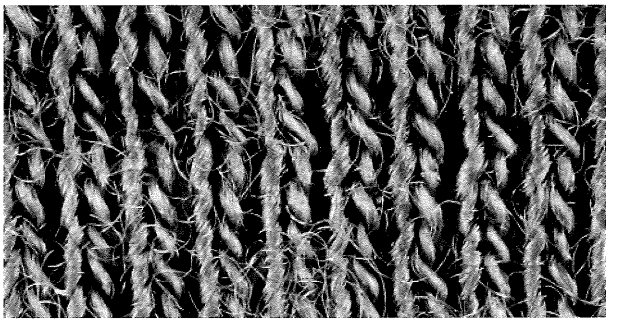

(copy right: Rob Suisted)

作品名稱 ： **Natural fibers texture**	
作品內容 上圖：為在鋼鐵材料當中、肥粒鐵彼此之間低角度晶界，可以發現此低角度晶界由大量差排所構成。差排細密整齊的組織猶如天然纖維的織構(下圖)。	
作者姓名：蔡宇庭	單位：台大材料
聯絡電話：02-33663748	E-Mail：f99527004@ntu.edu.tw

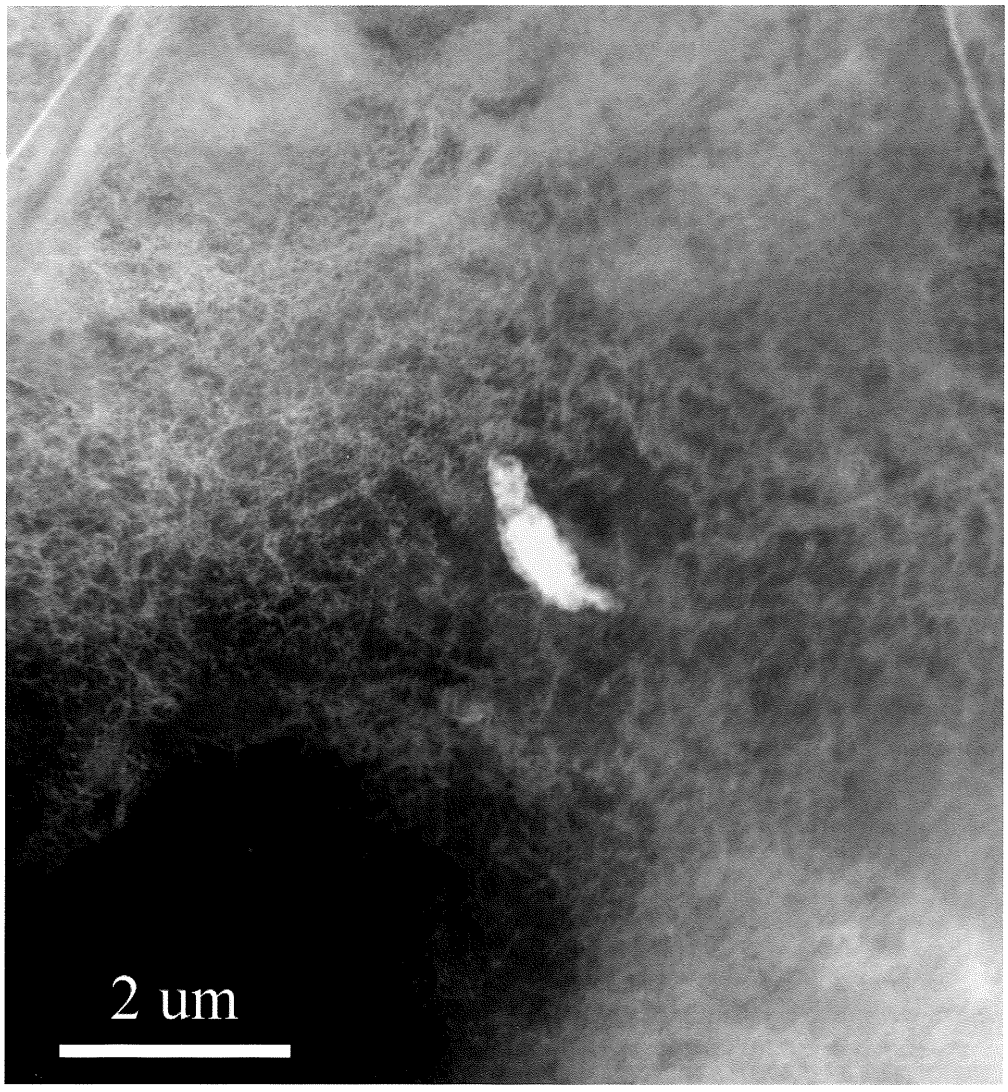

作品名稱　凶險太平洋中閃耀的小島-台灣	
作品內容 雙相鋼中肥粒鐵經過大量塑性變形後利用 STEM 攝得的差排影像，圖中的"台灣"為身在一群差排中的 MA 相。	
作者姓名 蔡劭璞	單位 台大材料所
聯絡電話 0937116385	E-Mail b97507048@ntu.edu.tw

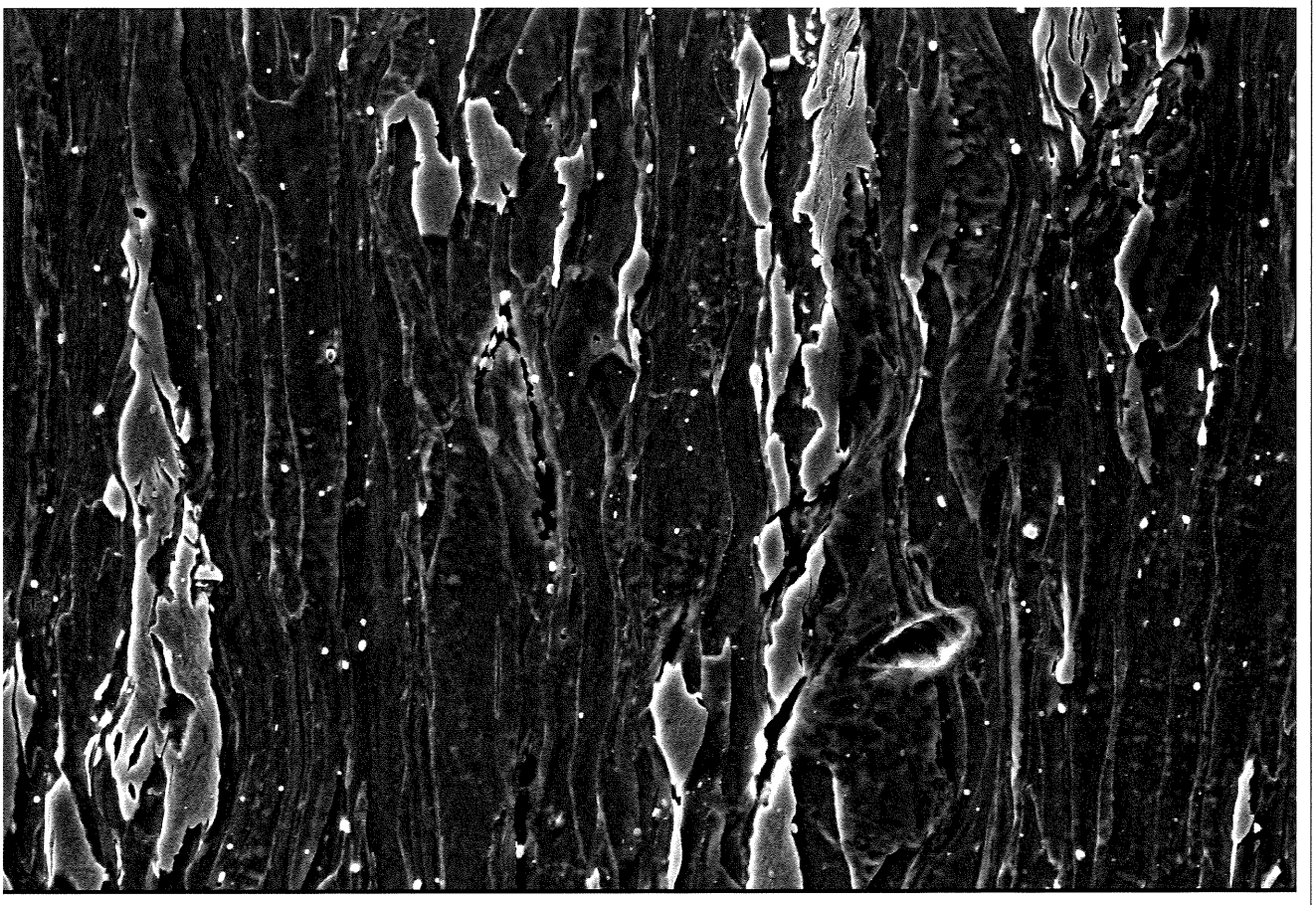

作品名稱　流動

作品內容

經過拉伸之雙相鋼於掃描式電子顯微鏡拍攝的組織樣貌圖，如同生命和宇宙的流動，願意走的和不願意走的，走得慢的和走得快的，總是拉扯，有時決裂。

作者姓名 鄭至閎	單位 台灣大學材料科學與工程學研究所
聯絡電話 0911365699	E-Mail　tabonster@gmail.com

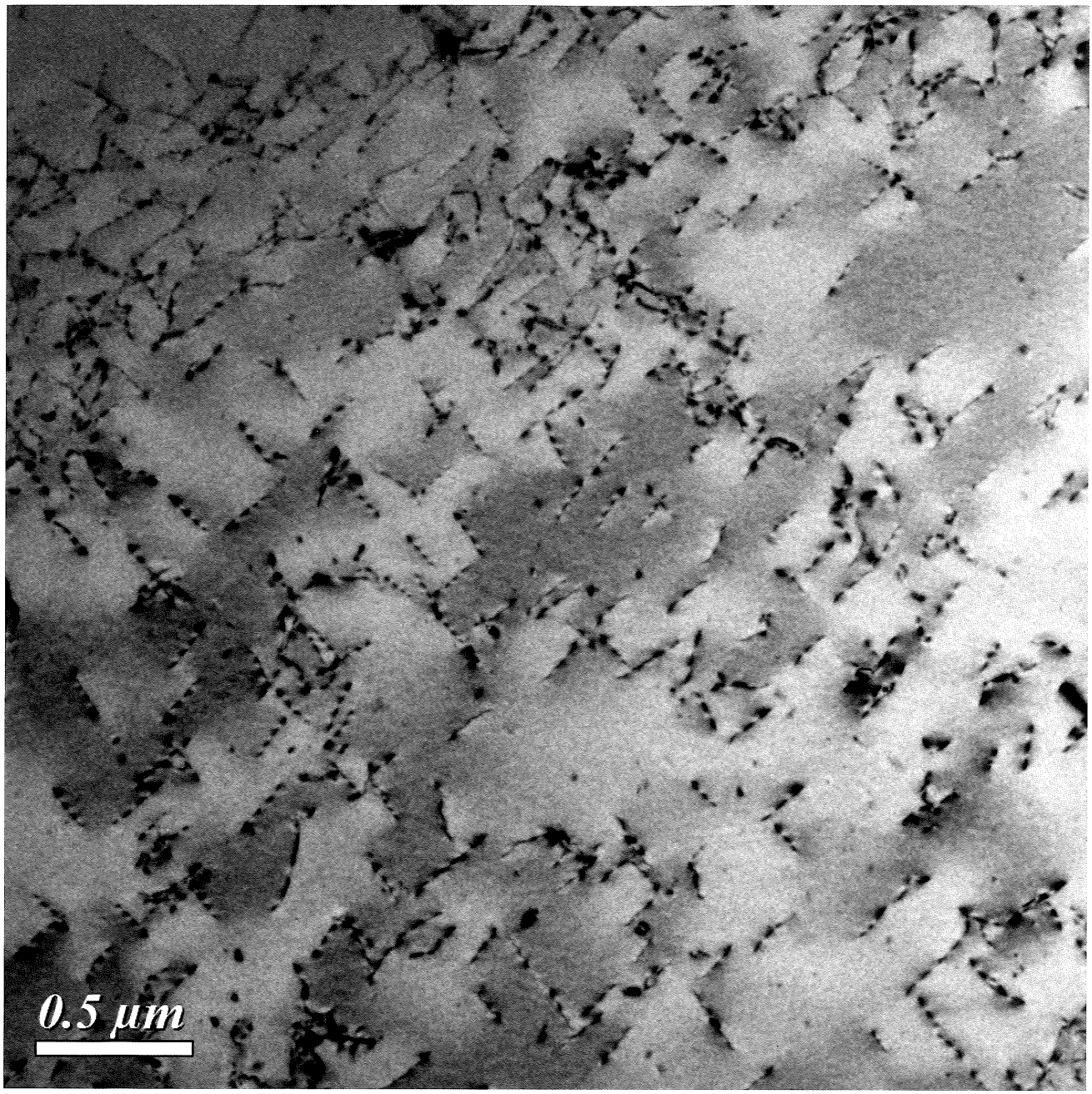

作品名稱　螞蟻雄兵	
作品內容 雙相不銹鋼中散布在肥粒鐵晶粒內的差排線 TEM 圖	
作者姓名:謝亦傑	單位:國立台灣大學材料科學與工程學系暨研究所
聯絡電話:0918022680	E-Mail:r02527001@ntu.edu.tw

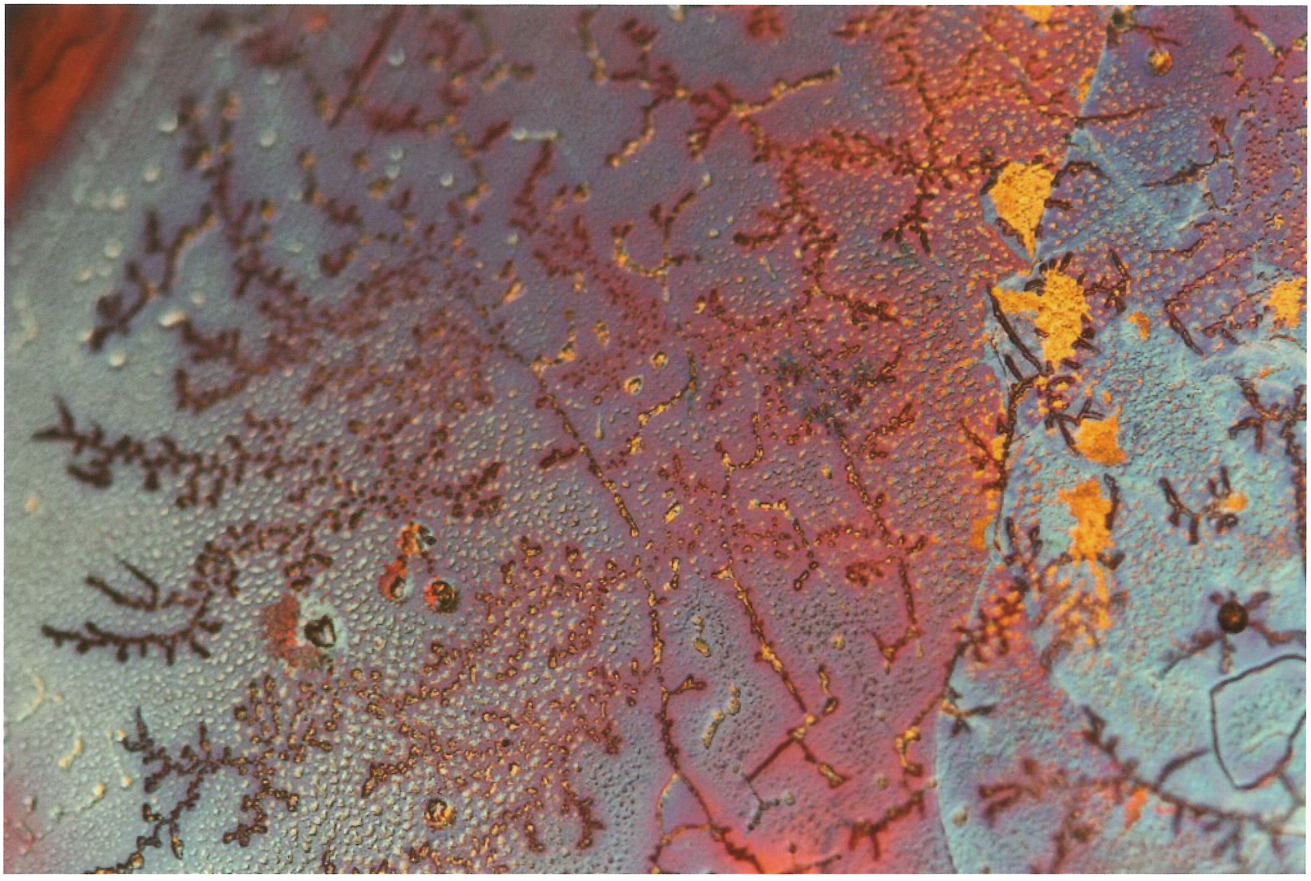

作品名稱　冰雪奇緣 雪花紛飛	
作品內容 NiSi 塊材於高溫退火過程中，與銅蒸氣反應，形成含銅矽化物偏析之樹枝狀結構	
作者姓名 李家豪	單位 國立臺灣大學 材料科學與工程學系
聯絡電話 0987678759	E-Mail b99507025@ntu.edu.tw

I-14

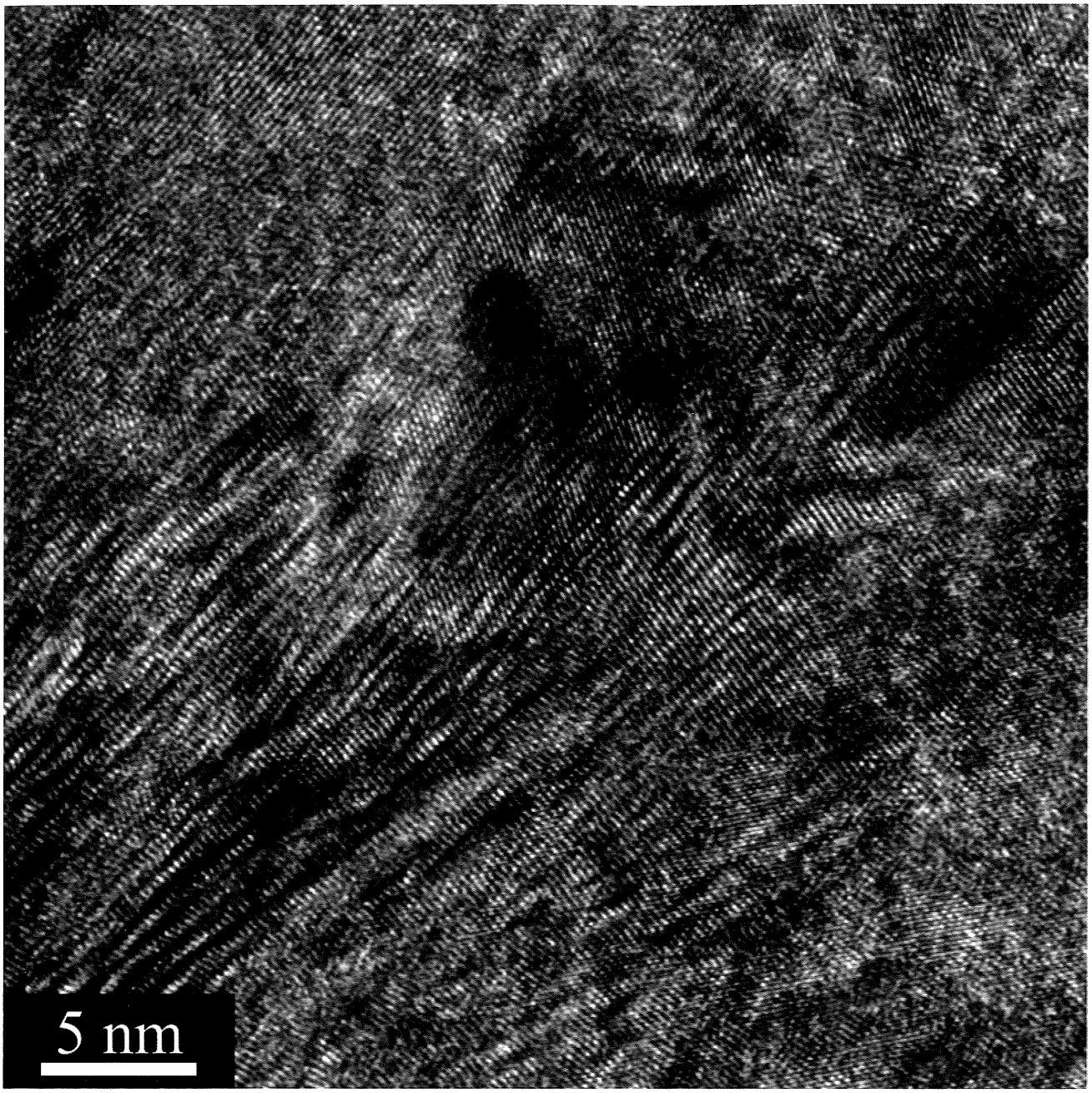

作品名稱：流沙般的晶格

作品內容

Ti-6Al-4V 合金施以熱氫處理後，大量疊差形成於 α_2-Ti_3Al 介金屬相之 HRTEM 顯微照片

作者姓名：王樂民	單位：國防大學理工學院動力及系統工程學系
聯絡電話：0988586065	E-Mail：johnny.ic.wang@gmail.com

作品名稱　這不是香蕉，這是太陽花	
作品內容 以常壓電漿製程製備花狀氧化銅顆粒之 TEM 圖	
作者姓名:蘇昱銘、郭俞麟	單位: 國立台灣科技大學機械工程系
聯絡電話:0926185971	E-Mail: d9803503@mail.ntust.edu.tw

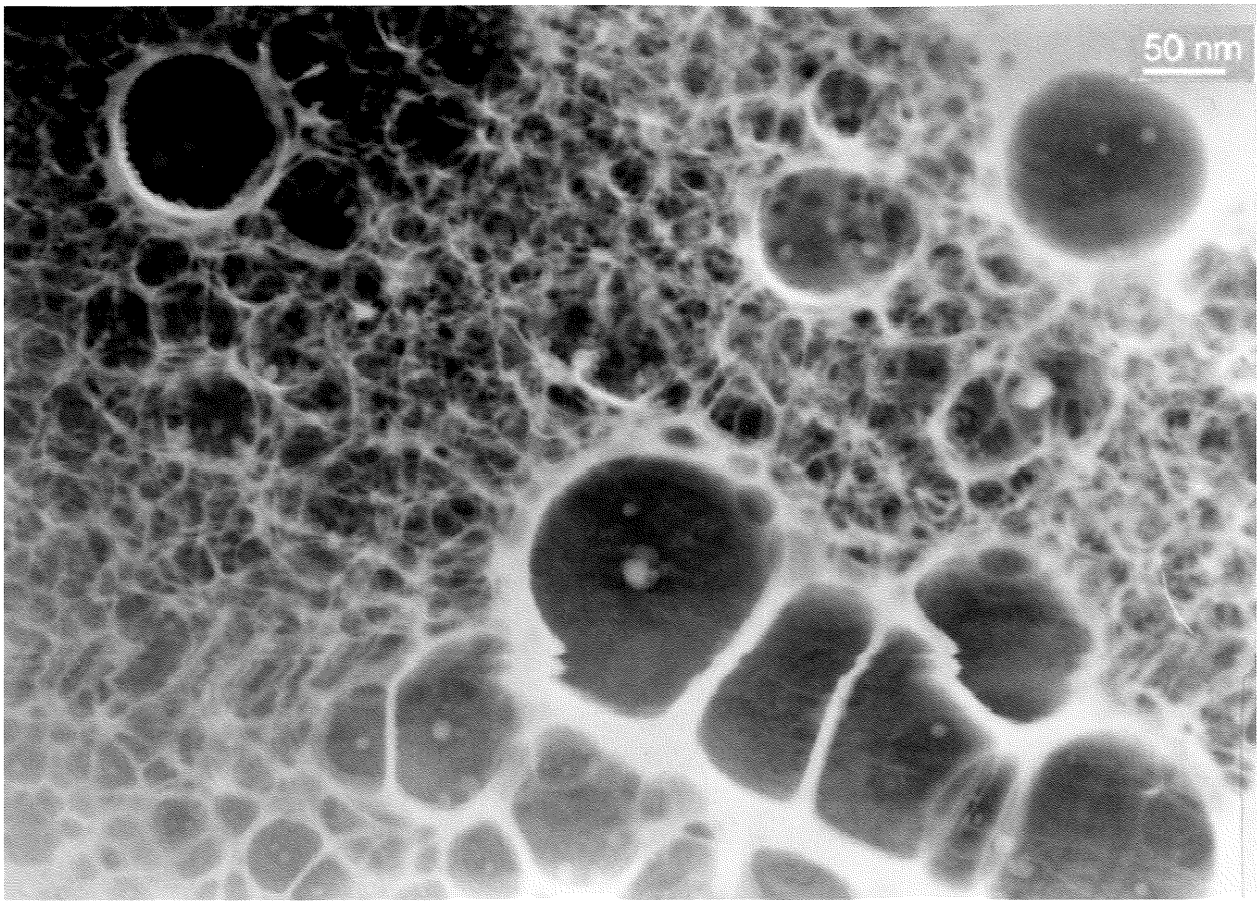

作品名稱　三葉蟲化石

作品內容

躲在泥沙中希望躲過一劫。這一躲竟是幾億年，被未來生物拾起，終於重見天日。

作者姓名	單位
薛柏彥、蔡既瑋、黃子維、彭坤增	明志科技大學
聯絡電話	E-Mail
0928692822	pen5814@mail.mcut.edu.tw

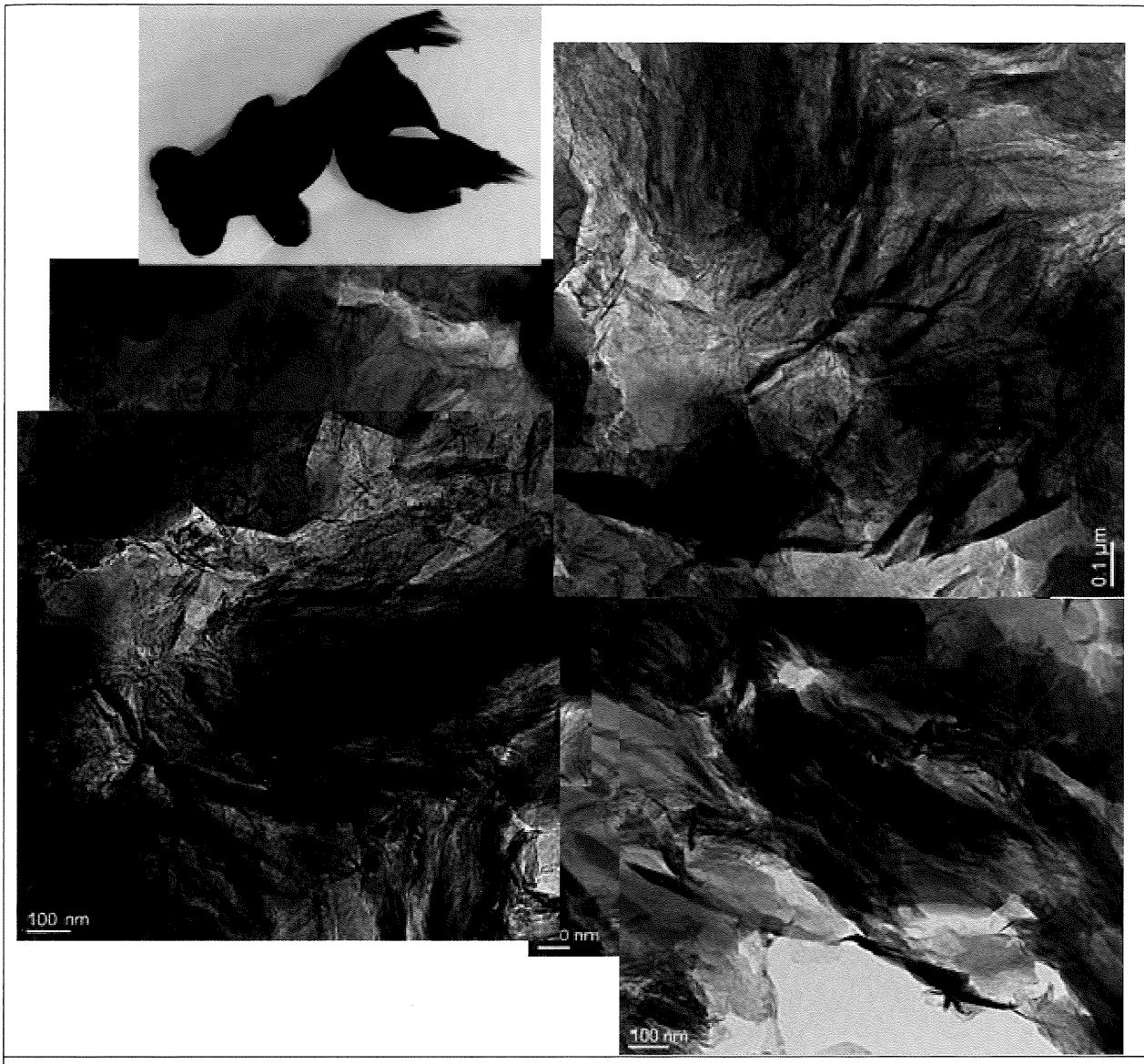

作品名稱　金魚戲水

作品內容

金魚悠遊徜徉在湖水，無憂無慮擺動尾巴婀娜多姿,時間為牠而停止。

作者姓名	單位
楊朝越、楊立爵、黃子維、彭坤增	明志科技大學
聯絡電話	E-Mail
0928692822	pen5814@mail.mcut.edu.tw

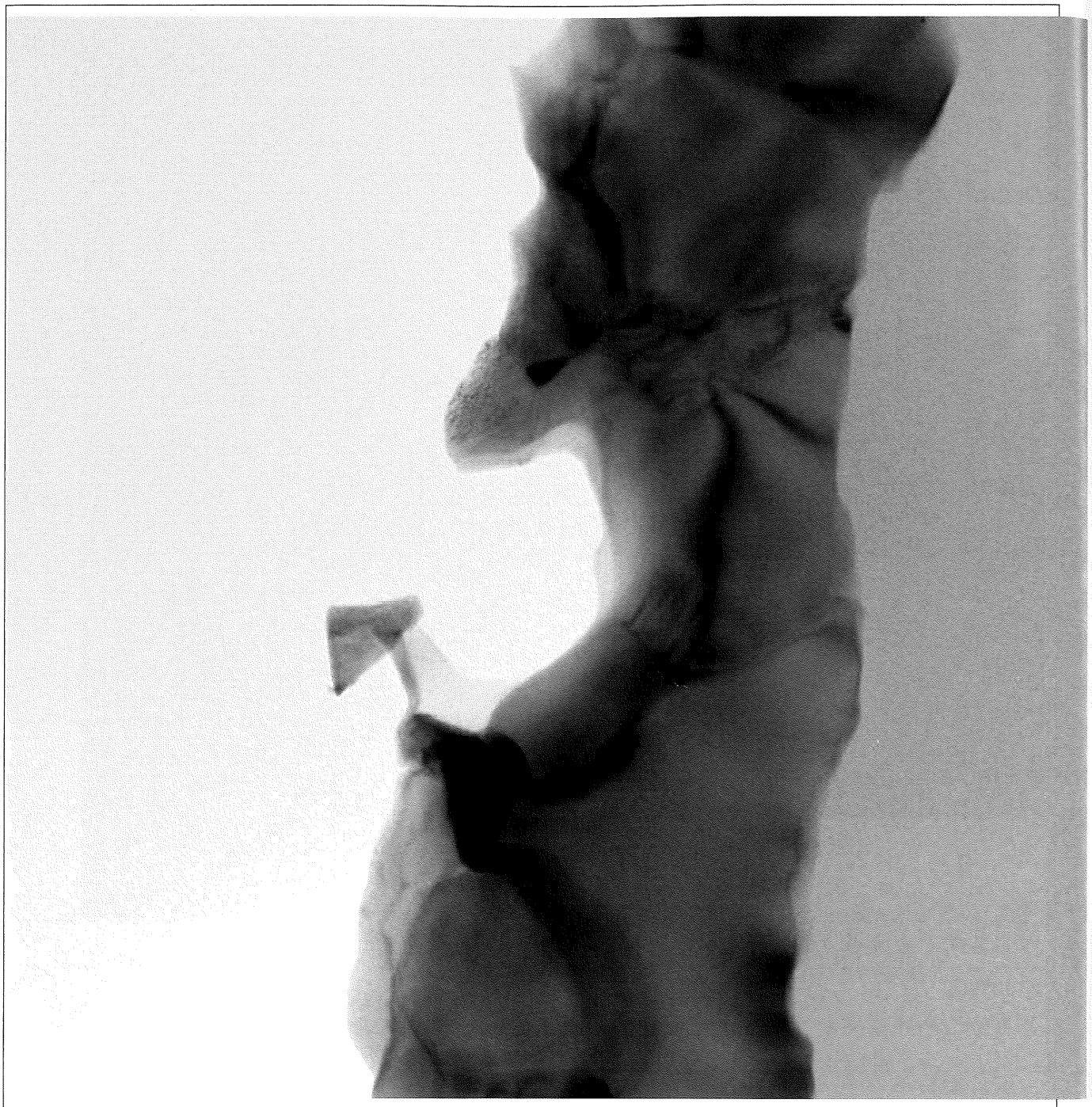

作品名稱　海馬產子	
作品內容 似乎在等待些什麼？海馬寶寶從海馬肚子裡生出來。原本孤單的海馬有了家人，不再孤獨一人。	
作者姓名 楊朝越、楊立爵、蔡尚維、彭坤增	單位 明志科技大學
聯絡電話 0928692822	E-Mail pen5814@mail.mcut.edu.tw

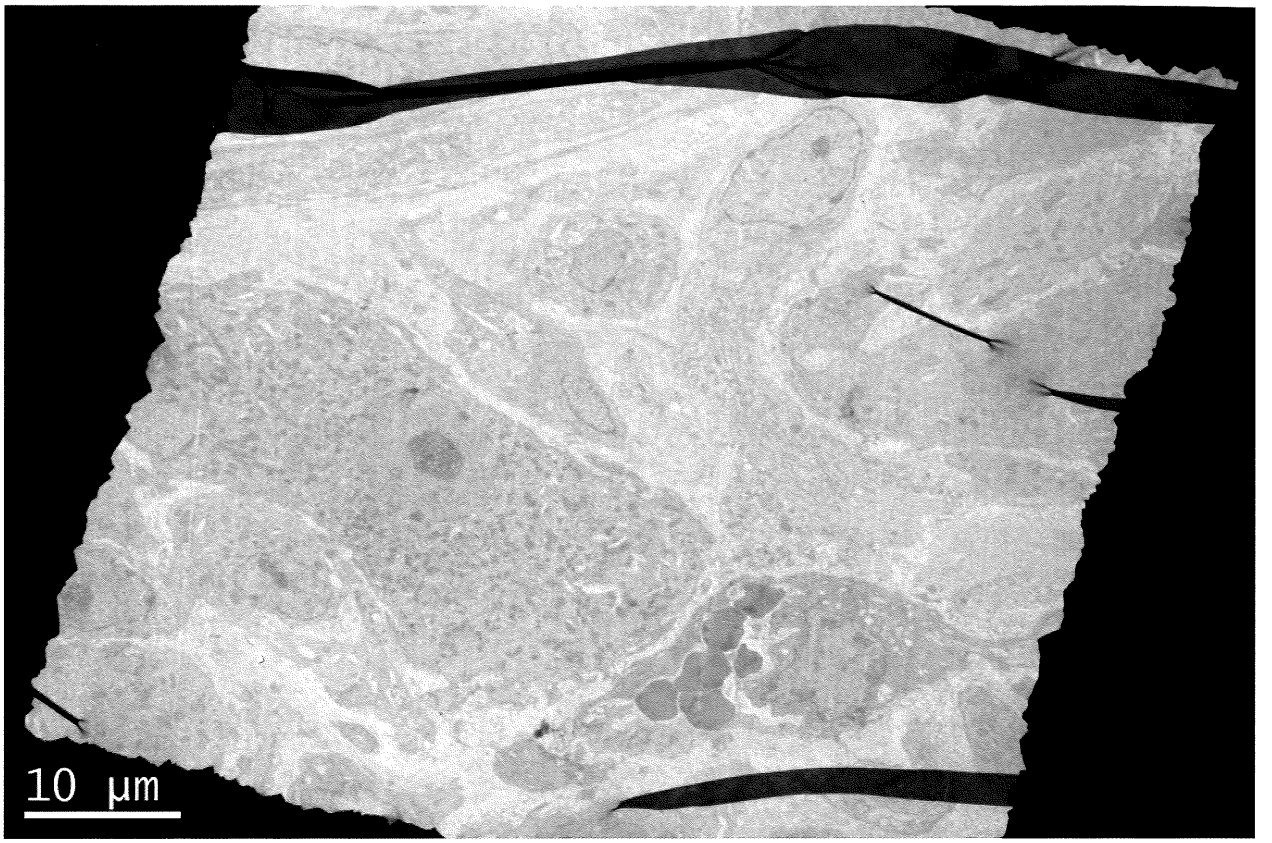

作品名稱　靈魂之窗

作品內容

穿越縱橫交織的窗口，我們觀察並思索生命真實的樣貌，山羊黃體。

作者姓名: 江逸凡 、鄭穹翔	單位：台灣大學獸醫系
聯絡電話：3366-3872	E-Mail：emcheng@ntu.edu.tw

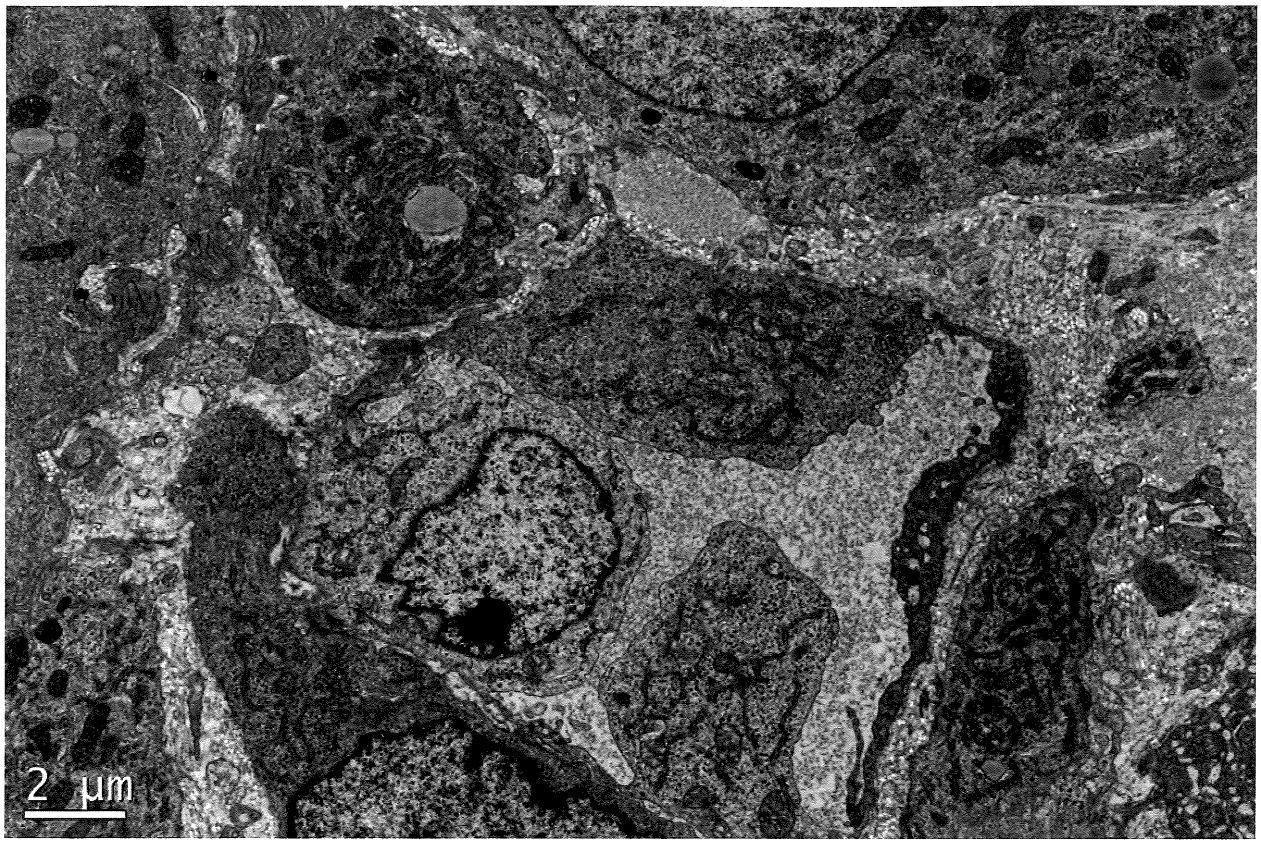

作品名稱　血管新生	
作品內容 穿越藩籬展開新的旅程，將血液注入每一個最小的角落，山羊黃體。	
作者姓名: 江逸凡 、鄭穹翔	單位：台灣大學獸醫系
聯絡電話：3366-3872	E-Mail：emcheng@ntu.edu.tw

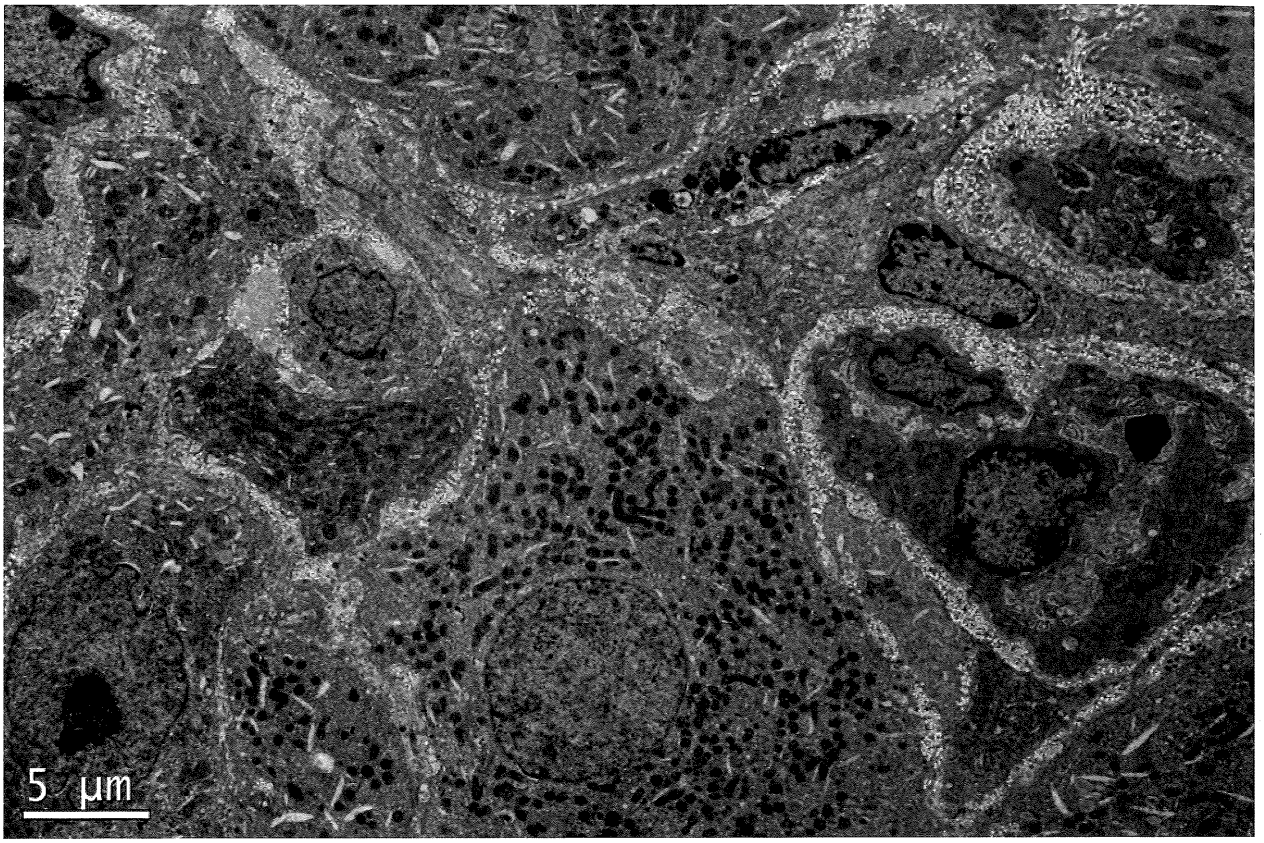

作品名稱　退化之開端
作品內容 功能退化為免疫活化之開端，周期之終結即周期之開始，山羊黃體。

作者姓名	單位
聯絡電話	E-Mail

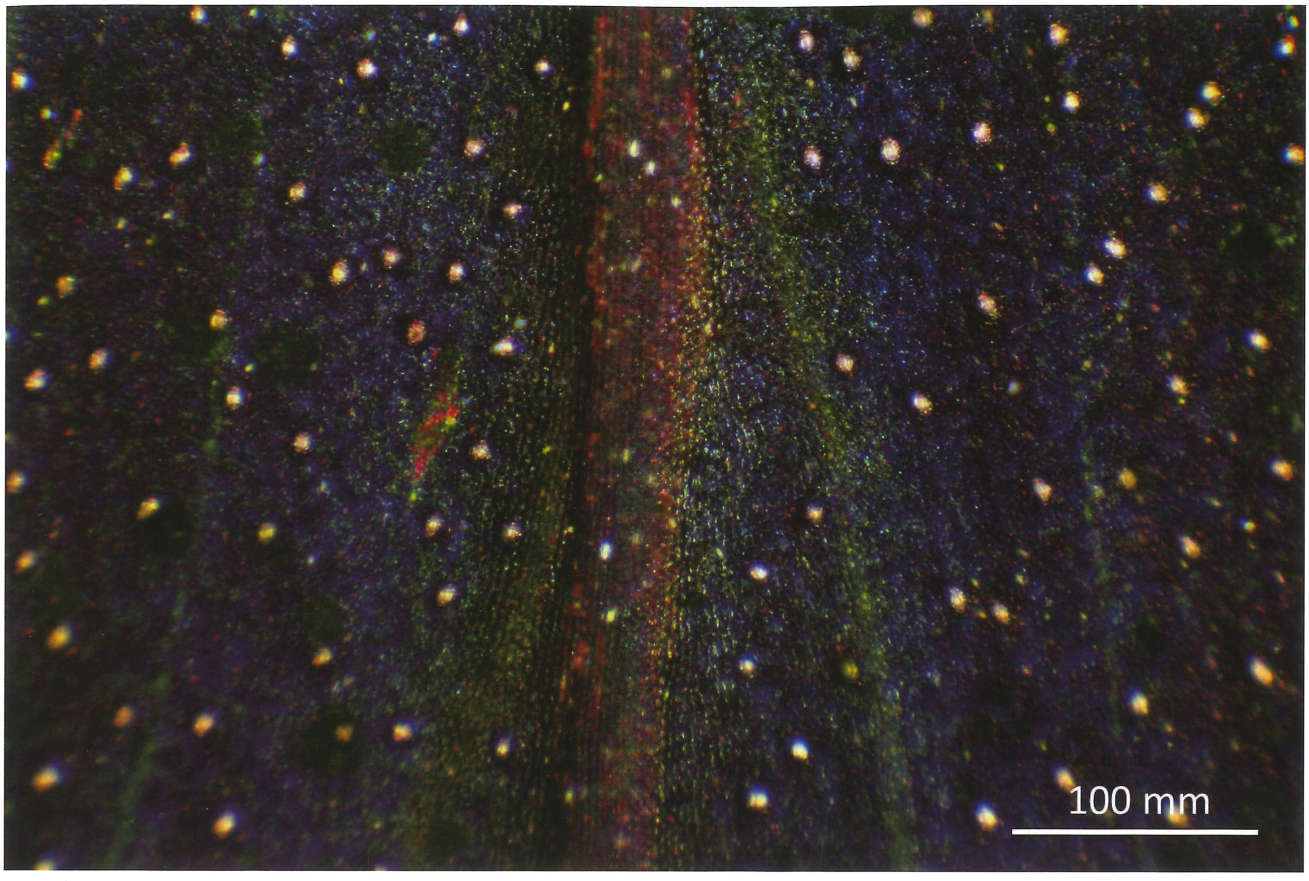

作品名稱　孔雀開屏	
作品內容 一種水生天南星科植物-*Bucephalandra*，上表皮葉面的藍色彩虹，白點為氣孔。	
作者姓名：范綱佑、黃玲瓏	單位: 台灣大學生態演化所
聯絡電話：3366-2510	E-Mail：r02b44007@ntu.edu.tw

作品名稱　九彎十八拐	
作品內容　爵床科植物的花粉，因其花粉外壁所具有的特殊構造，使其像是蜿蜒的北宜公路，故而取名九彎十八拐。	
作者姓名：張家昀、陳香君	單位：台灣大學生命科學系
連絡電話：3366-2498	E-Mail：hjchen@ntu.edu.tw

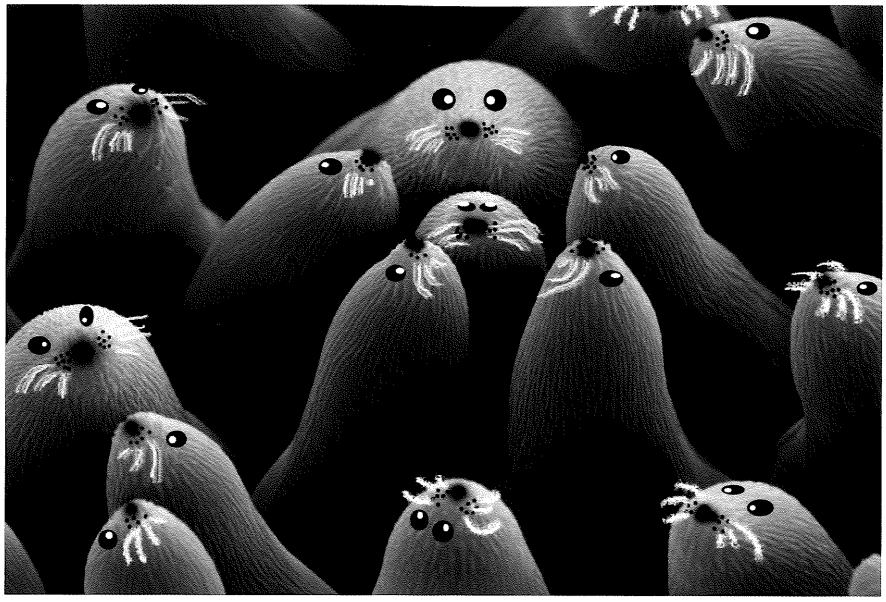

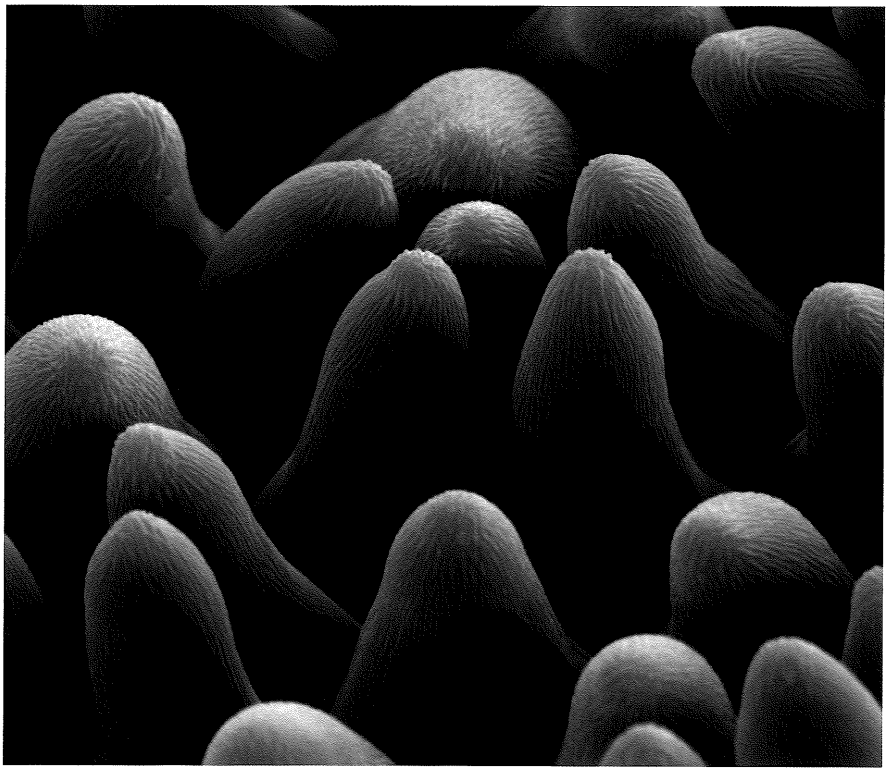

作品名稱：開會中的海豹	
作品內容 佛氏通泉草唇瓣上表皮細胞	
作者姓名：許佳玫 簡萬能	單位：中研院植物暨微生物所
聯絡電話： 27871012	E-Mail：wnjane@gate.sinica.edu.tw

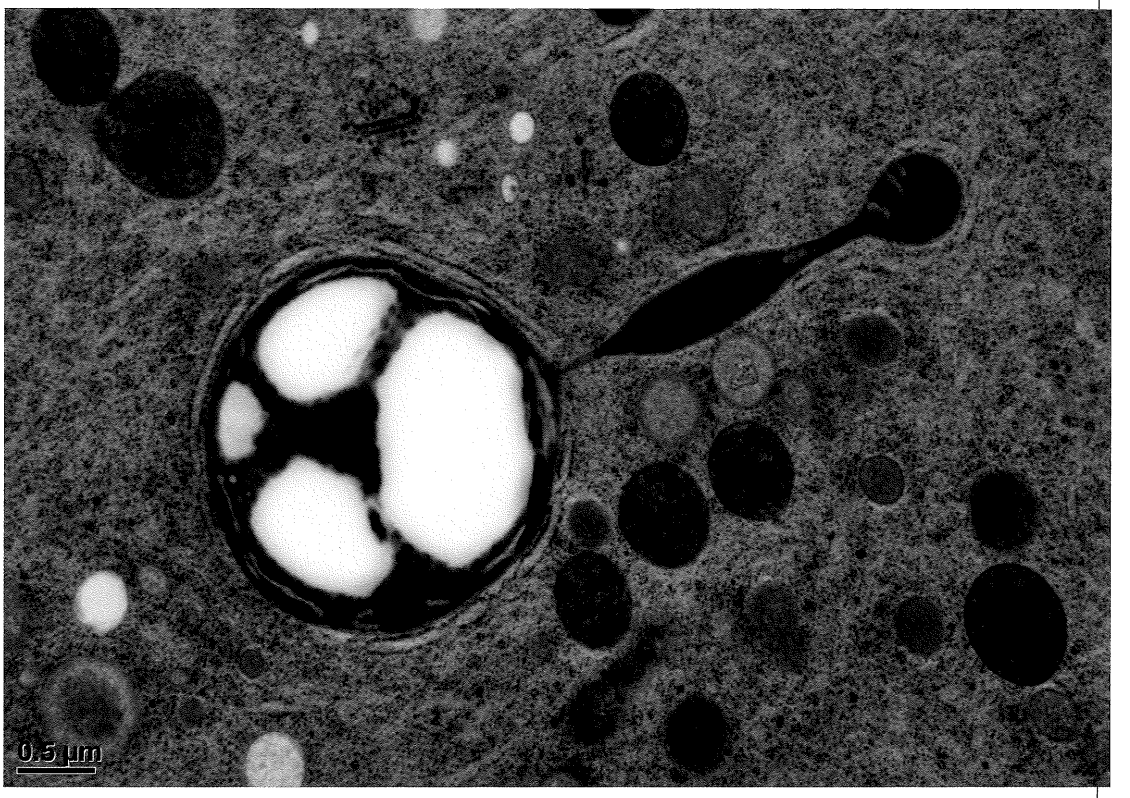

作品名稱：正中靶心 飛鏢	
作品內容 阿拉伯芥根年輕的管細胞	
作者姓名：簡萬能	單位：中研院植物暨微生物所
聯絡電話： 27871012	E-Mail：wnjane@gate.sinica.edu.tw

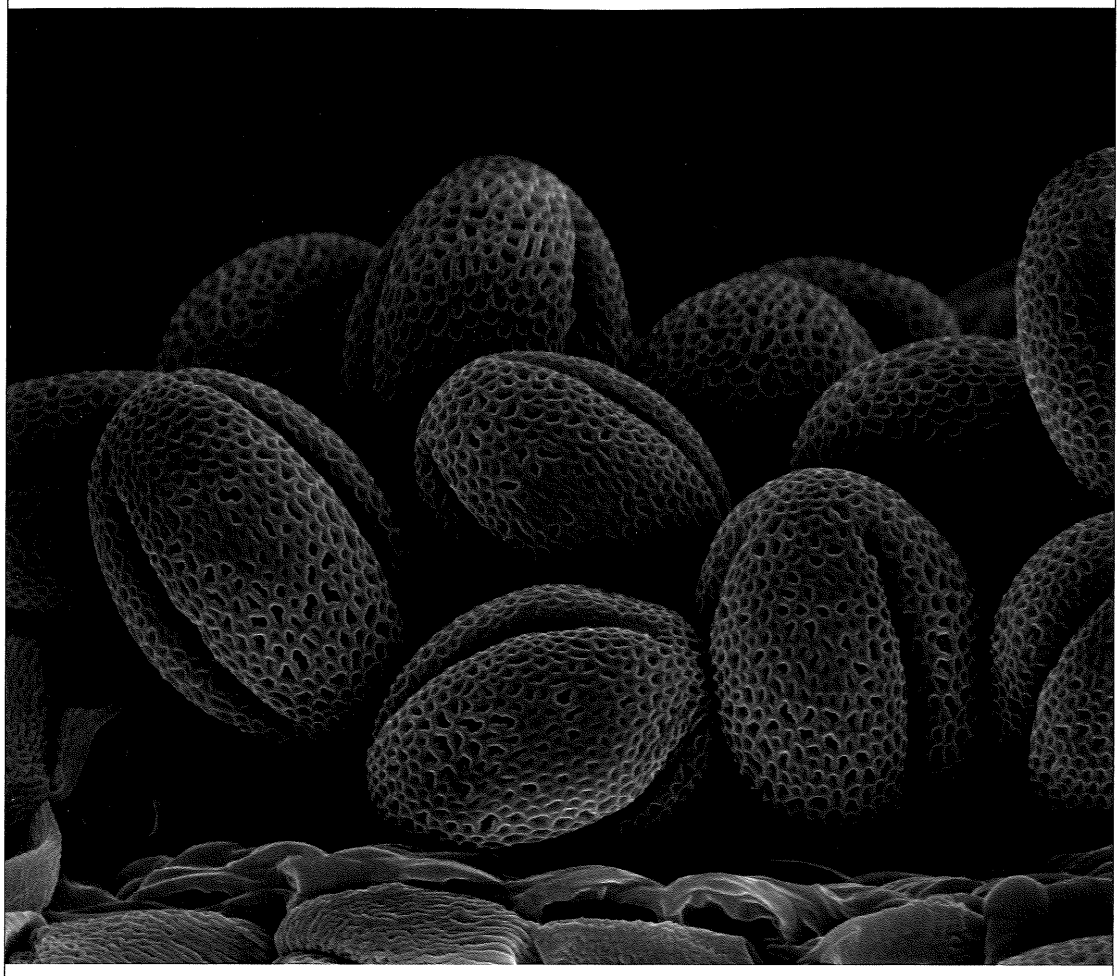

作品名稱：來顆蜜橄欖吧!	
作品內容 阿拉伯芥成熟的花粉	
作者姓名：簡萬能	單位：中研院植物暨微生物所
聯絡電話： 27871012	E-Mail：wnjane@gate.sinica.edu.tw

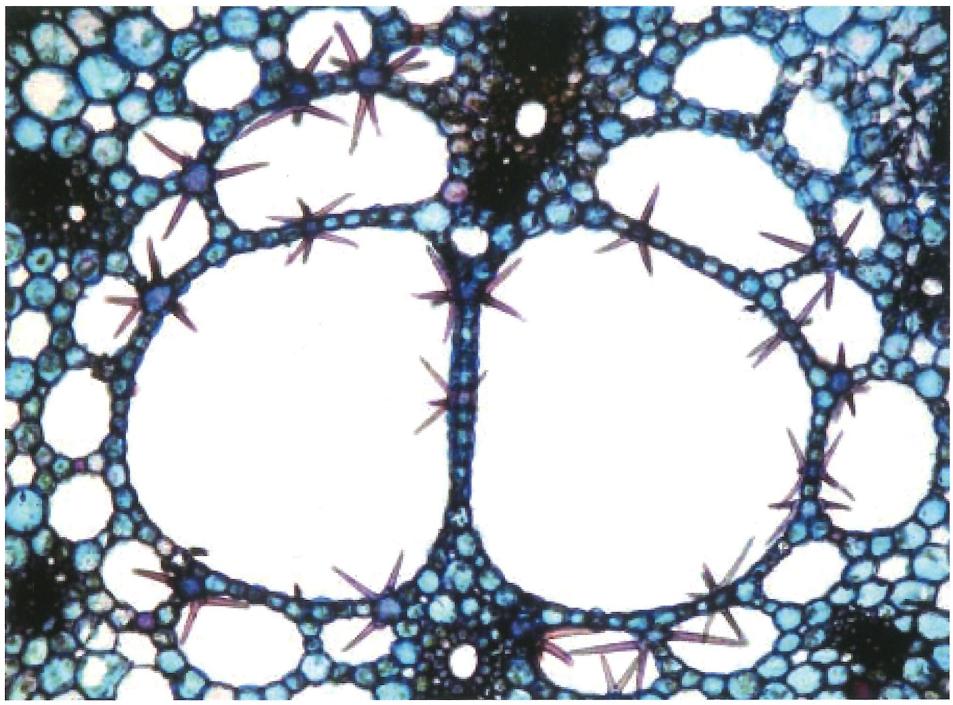

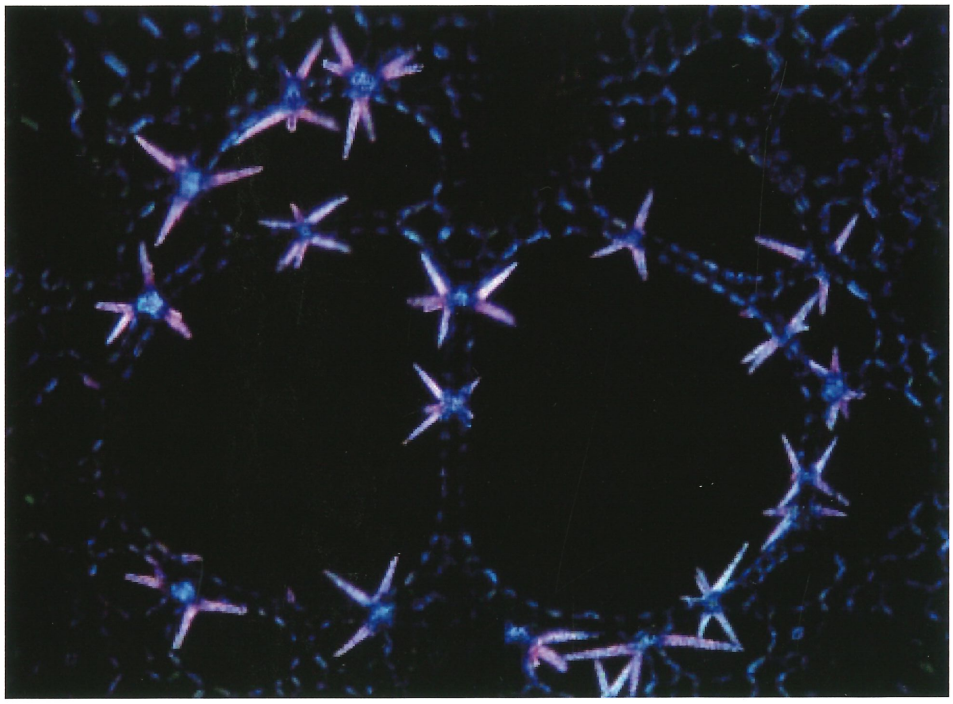

作品名稱：放閃的加菲貓	
作品內容 以 Safranin O 和 Alcian blue 雙重染色(上)且在偏光顯微鏡下(下)的睡蓮葉柄徒手切片，可見如星光閃耀的星狀厚壁細胞，在通氣組織間跳躍飛舞著。Bar = 1 mm	
作者姓名： 洪麗分、黃玲瓏	單位：台灣大學生態演化所
聯絡電話： 3366-2510	E-Mail：d97b44007@ntu.edu.tw

M-O-20	**APPROACHING THE ELASTICITY AND STRAIN LIMITS IN NANOMATERIALS** 韓曉東 北京工業大學	
M-O-21	**ELASTICALLY STRAINED NANOWIRES AND SHEETS** 俞大鵬 北京大學	
M-O-22	**IN SITU OBSERVATION OF OXIDATION OF ZRB2 NANOPARTICLES** 李吉學 浙江大學	
M-O-23	**LOW-DIMENSIONAL MAGNETIC NANOPARTICLES: NANOSCALE CHARACTERISATION, MAGNETIC BEHAVIORS AND THEIR APPLICATIONS** 彭 勇 蘭州大學	
M-O-24	**STRAIN AND SYMMETRY-BREAKING IN FIVE-FOLD TWINS** 于 榮 清華大學	
M-O-25	**AN IN SITU TEM STUDY OF THE SIZE EFFECT ON THE MARTENSITIC TRANSFORMATION IN NANOSCALE NITI SHAPE MEMORY ALLOY** 毛聖成 北京工業大學	
M-O-26	**多鐵材料疇結構的原子構型及其動力學行為** 潘曉晴 南京大學	

M-O-1

ATOMIC SCALE STRUCTURE EVOLUTION OF ELECTRODE MATERIALS IN LITHIUM / SODIUM ION BATTERIES

GU, Lin (谷林)

Institute of Physics, Chinese Academy of Sciences, Beijing 100190, China

Because of the tremendous demanding for energy storage in electric vehicles and electronic consumable devices, lithium batteries have become the most important candidates, which strongly urge effective characterization methods, particularly to observe lithium ions at atomic scale. The recent success in aberration-corrected annular-bright-field (ABF) scanning transmission electron microscopy (STEM) provides a feasible access to a direct interpretation of the atomic structure at sub-angstrom resolution. Such a procedure has been proved to be highly efficient in resolving atomic columns of lithium as shown in our previous work [1-8].

Figure 1 shows a schematic of the ABF geometry with a convergent beam and an annular-shaped bright-field detector. A fine probe with a spot size less than 1 angstrom scans across the specimen with the annular detector defining a collection semiangle at given camera lengths. An ABF electron micrograph of $LiFePO_4$ viewed along [010] orientation is displayed in Fig. 1. It is demonstrated that not only Fe and P are revealed in this micrograph, but also the atomic positions of O and Li. The ABF contrast tends to minimize the variance of the atomic number by following a $Z^{1/3}$ dependency.

With the latest ABF method, we have further studied possible electrochemical reaction mechanisms and detailed structure evolution for (partially) lithiated / delithiated 1D-$LiFePO_4$, 2D- $LiCoO_2$, Li_2MnO_3 and 3D- $Li_4Ti_5O_{12}$ and other lithium-based active materials, which are essential for basic understanding and further material design. In addition, The ABF method can be further extended for atomic-scale investigation of oxygen vacancies and other structure evolution of light atoms.These shed new insight into the lithium / sodium storage mechanism in important cathode materials for Li- / Na- ion batteries.

References

[1] Y. Sun, et al., Nature Commun. 4 (2013) 1870.
[2] R. Wang, et al. Adv. Energy Mater. 3 (2013) 1358.
[3] X. Lu, et al., Adv. Mater. 24 (2012) 3233. (Editor's Choice in Science 336 (2012) 1621.)
[4] X. Lu, et al., Nano Lett. 12 (2012) 6192.
[5] S. Xin, et al., J. Am Chem. Soc. 134 (2012) 18510.
[6] Y. Q. Wang, et al., J. Am Chem. Soc. 134 (2012) 7874.
[7] X. Lu, et al., Energy Environ. Sci. 4 (2011) 2638.

[8] L. Gu, et al., J. Am Chem. Soc. 134 (2011) 4661.
[9] X. Q. Yu, et al., Adv. Energy Mater., in press.
[10] C. B. Zhu, et al., Adv. Func. Mater., in press.

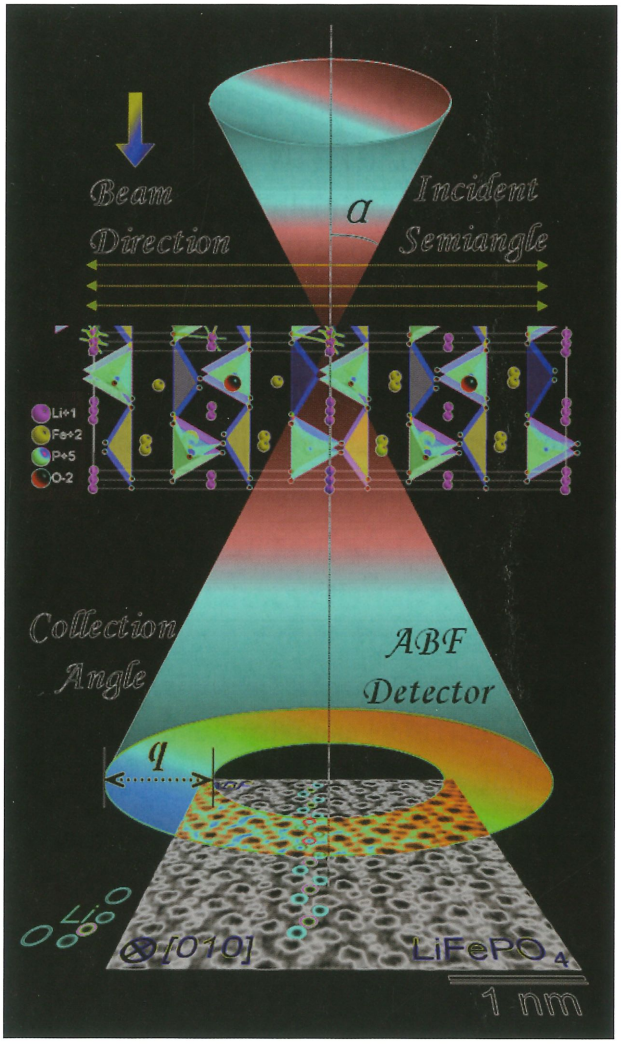

Figure 1. A schematic of the ABF geometry with a convergent beam and an annular-shaped bright-field detector. A fine probe with a spot size less than 1 angstrom scans across the specimen with the annular detector defining a collection semiangle at given camera lengths. An ABF electron micrograph of $LiFePO_4$ viewed along [010] orientation is displayed.

M-O-2

CONDENSATION OF TWO-DIMENSIONAL OXIDE-INTERFACIAL CHARGES INTO ONE-DIMENSIONAL ELECTRON CHAINS BY THE MISFIT-DISLOCATION STRAIN FIELD

Ching-Pin Chang(張景斌),[12] Ming-Wen Chu(朱明文),[1] Horng-Tay Jeng(鄭弘泰),[34] Jauyn Grace Lin(林昭吟),[1] Su-Ling Cheng(鄭淑齡),[12] Jer-Ren Yang(楊哲人),[2] and Cheng-Hsuan Chen(陳正弦)[1]

[1] Center for Condensed Matter Sciences, National Taiwan University, Taipei, Taiwan
[2] Department of Materials Science and Engineering, National Taiwan University, Taipei, Taiwan
[3] Department of Physics, National Tsing Hua University, Hsinchu 300, Taiwan.
[4] Institute of Physics, Academia Sinica, Taipei 115, Taiwan.

The success of semiconductor technology is largely ascribed to controlled impacts of strains and defects on the two-dimensional interfacial charges [1]. Interfacial charges also appear in oxide heterojunctions such as $LaAlO_3/SrTiO_3$ [2] and $(Nd_{0.35}Sr_{0.65})MnO_3/SrTiO_3$ [3]. How the localized strain field of one-dimensional misfit dislocations, defects resulting from the intrinsic misfit strains, would affect the extended oxide-interfacial charges is intriguing and remains unresolved. Here we show the atomic-scale observation of one-dimensional electron chains formed in $(Nd_{0.35}Sr_{0.65})MnO_3/SrTiO_3$ by the condensation of characteristic two-dimensional interfacial charges into the strain field of periodically arrayed misfit dislocations, using chemical mapping and quantification by scanning transmission electron microscopy [4]. The strain-relaxed inter-dislocation regions are readily charge depleted, otherwise decorated by the pristine charges, and the corresponding total-energy calculations unravel the undocumented charge-reservoir role played by the dislocation-strain field. This two-dimensionalto-one-dimensional electronic condensation represents a novel electronic-inhomogeneity mechanism at oxide interfaces and could stimulate further studies of one-dimensional electron density in oxide heterostructures.

References

1. S. T. Pantelides, Phys. Status Solidi A, **210** 175-180 (2013).
2. A. Ohtomo, et al., Nature, **419** 378 (2002).
3. C. P. Chang, et al., Phys. Rev. B, **87** 075129 (2013).
4. M.-W. Chu and C. H. Chen, Acs Nano, **7** 4700 (2013).

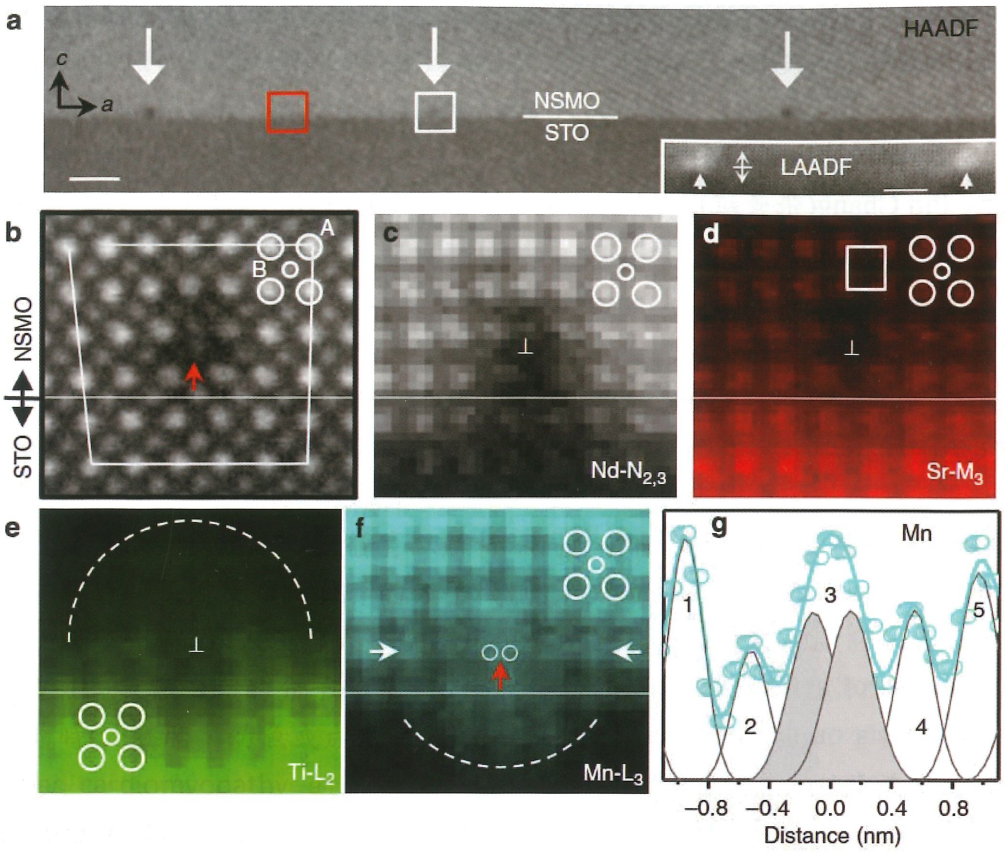

Figure 1. STEM imaging and STEM-EELS chemical mapping of the misfit dislocation at $(Nd_{0.35}Sr_{0.65})MnO_3/SrTiO_3$ interfaces.

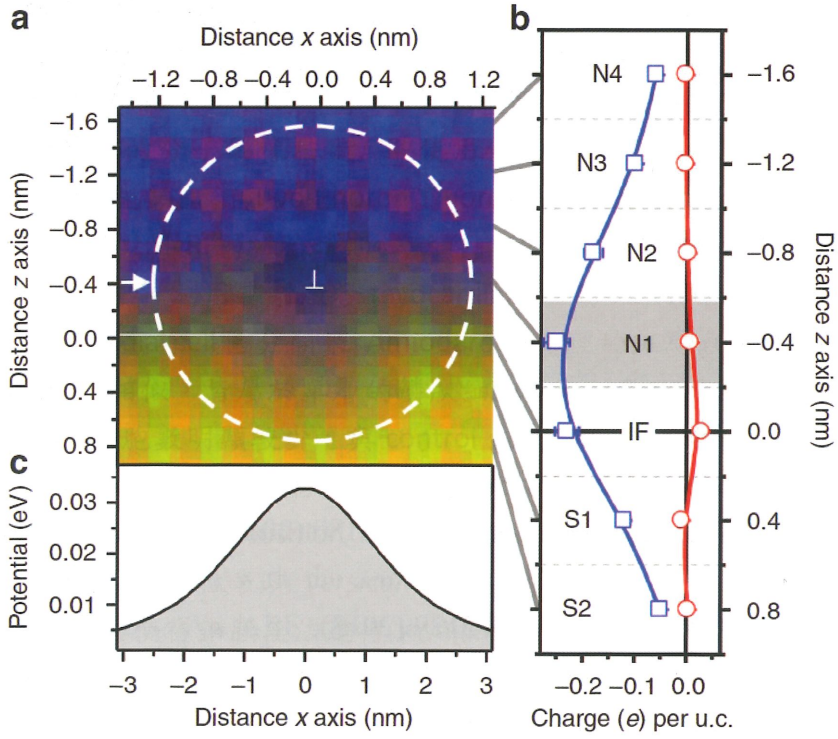

Figure 2. Condensation of the 2D interfacial charges into 1D electron chains by the misfit-dislocation strain field.

M-O-3

TEM STUDY OF CRYSTAL SYMMETRY, DOMAIN STRUCTURE AND DOMAIN-WALL MOBILITY IN $Bi_4Ti_3O_{12}$-BASED FERROELECTRICS OF LAYERED PEROVSKITE

LU Chao-Jing (盧朝靖),* YE Wan-Neng (葉萬能), and YOU Peng (尤朋)

College of Physics Science, Qingdao University, 266071 Qingdao, China

For $Bi_4Ti_3O_{12}$ single crystals, the major component of spontaneous polarization $\boldsymbol{P}_s$ lies along the *a* axis ($P_{s(a)} \approx 50\ \mu C/cm^2$) and the component along the *c* axis is very small ($P_{s(c)} \approx 4\ \mu C/cm^2$). Rare-earth-element substituted $Bi_4Ti_3O_{12}$ ferroelectrics have received much attention due to their applications in nonvolatile memories. Their ferroelectric properties are strongly linked to crystal structures, domain structures and the mobility of domain walls (DWs). Our electron diffraction results indicated unambiguously that both $Bi_4Ti_3O_{12}$ and $Bi_{3.15}Nd_{0.85}Ti_3O_{12}$ (BNdT) belong to the space group of monoclinic $B1a1$ at room temperature rather than orthorhombic $B2cb$ as reported by some publications [J. Appl. Crystallogr. 46, 798 (2013)].

According to space-group theory, 11 types of DWs are predicted to exist possibly in $Bi_4Ti_3O_{12}$-based ferroelectrics and they include 5 types of ferroelectric DWs, anti-phase boundaries (APBs) as well as 5 types of APB-combined ferroelectric DWs. Domain structures and their evolution in both $Bi_4Ti_3O_{12}$ and BNdT single crystals were *in-situ* investigated by using light microscope and transmission electron microscopy (TEM). All the 5 types of ferroelectric DWs were observed in $Bi_4Ti_3O_{12}$. They include 90° DWs of $P_{s(a)}$, 180° DWs of $P_{s(a)}$, 180° DWs of $P_{s(c)}$, 180° DWs of both $P_{s(a)}$ and $\boldsymbol{P}_{s(c)}$, 90° DWs of $P_{s(a)}$ combined 180° DWs of $P_{s(c)}$. Interestingly, no any APBs or APB-combined ferroelectric DWs were seen in $Bi_4Ti_3O_{12}$. In BNdT, in contrast, both irregularly-curved APBs and APB-combined ferroelectric DWs (at least APB-90°DW_a) of high density appear besides the 5 types of ferroelectric DWs. The different domain structures in the two ferroelectrics might result from the part-Nd-substitution induced change in interfacial energy.

The movements of 90° DWs of $\boldsymbol{P}_{s(a)}$, 180° DWs of $\boldsymbol{P}_{s(a)}$, 180° DWs of $\boldsymbol{P}_{s(c)}$ as well as APBs were observed while the nucleation and growth of new 90° domains, 180° domains and anti-phase domains seen. It was found that both the mobility of APBs and the nucleation density of anti-phase domains are high, which might make clear the fatigue-free origin of polarization switching in BNdT. Either the 90° *a-b* switching of the *a*-component of $\boldsymbol{P}_S$ or 180° switching of *c*-component of $\boldsymbol{P}_S$ was never observed before in ferroelectrics of layered perovskite.

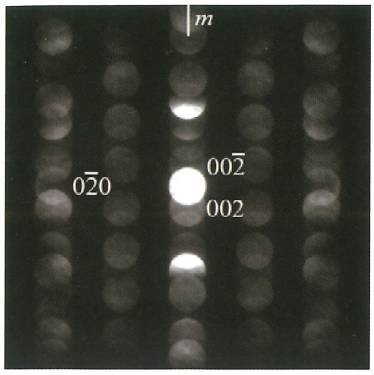

Figure 1. CBED pattern confirming that $Bi_4Ti_3O_{12}$ is of the $B1a1$ space group rather than $B2cb$. Note that the 002 disk is much brighter than the $00\bar{2}$ disk.

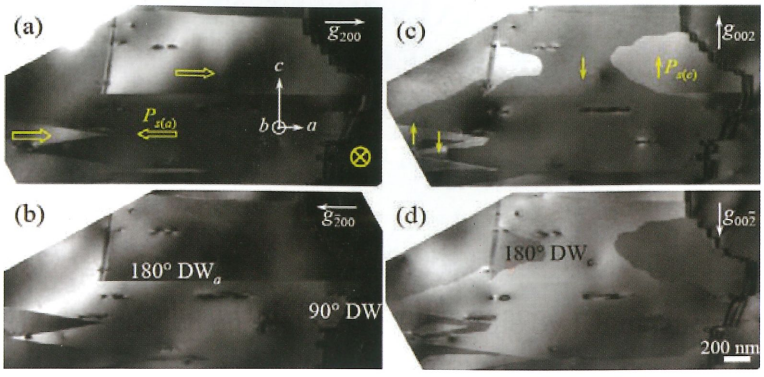

Figure 2. Dark-field TEM images of the same area in $Bi_4Ti_3O_{12}$ crystal. The reversal of bright-dark contrast in (a) and (b) shows 180° *domains* of $\boldsymbol{P}_{s(a)}$ and the contrast reversal in (c) and (d) exhibits 180° domains of $\boldsymbol{P}_{s(c)}$.

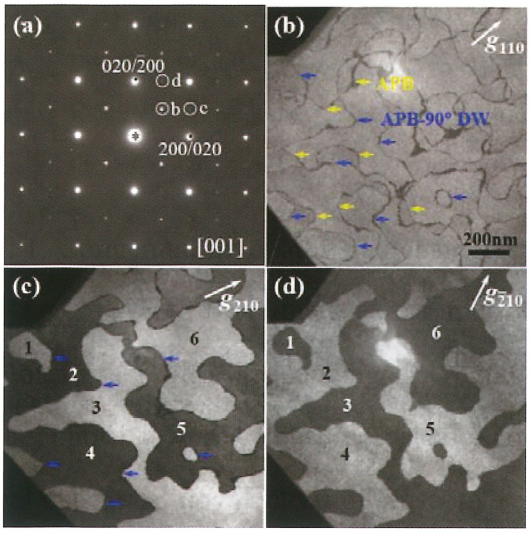

Figure 3. SAED pattern (a) and dark-field TEM images (b-d) of the same area in BNdT crystal. (b) shows curved APBs and APB-combined 90° DWs of high density. The reversal of bright-dark contrast in (c) and (d) exhibits 90° domains of $\boldsymbol{P}_{s(a)}$.

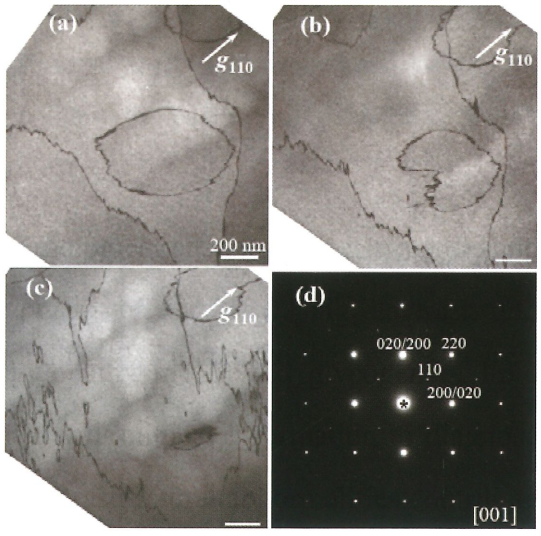

Figure 4. (a-c) dark-field images of the same area showing the evolution of anti-phase domains in BNdT crystal under *e*-beam irradiation. (a) Initial state, (b) during evolution, (c) after evolution. (d) SAED pattern of the same area.

M-O-4

HRTEM STUDY OF BASAL-PRISMATIC STACKING FAULT COMBINATIONS IN COALESCED GAN LAYERS

Chang-Ning Huang (黃常寧),[1,2] Philip A. Shields,[3] Duncan W.E. Allsopp,[3] and Achim Trampert [2]

[1]Department of Chemical and Materials Engineering, Southern Taiwan University of Science and Technology (南臺科技大學), Tainan, Taiwan, R.O.C.

[2]Paul-Drude-Institutare für Festkörperelektronik, Hausvogteiplatz 5-7, 10117 Berlin, Germany

[3]Department of Electronic and Electrical Engineering, University of Bath, Claverton Down, BA2 7A Y, Bath, UK

In order to reduce the dislocation density for high performance light-emitting diodes, GaN nanorods grown as templates for pendeoepitaxial coalescence overgrowth is under discussion. However, novel defects could be created during coalescence of pyramids which are initially grown on the top of nanorods. For example, a step-shaped and a hair-pin basal-prismatic SF combinations can be composed of one prismatic stacking fault (PSF) and two basal plane stacking faults (BSFs) with opposite and the same directions, respectively [1]. Figure 1(a) and (b) show the dark field (DF) images of these two SFs near the coalesced boundaries. The white arrows indicate the PSFs, which terminate two BSFs and sometimes reveal like a zigzag band. Figures 2(a) and 2(b) show high-resolution images of step- and hairpin-shaped basal prismatic SF combination with inclined PSFs projected on the $(11\ \bar{2}\ 0)$ plane with hexagon-like interference pattern indicated by red dash area and red hexagon. Figure 2(c) shows theoretical atomic model proposed by Drum [2]. Figure 2(d) is multi-slice simulated high-resolution image of the inclined prismatic stacking fault based on Drum's model that also has the hexagonal pattern indicated by red hexagon. Consequently, the PSF followed Drum's model with the lower formation energy is formed near the coalesced boundary. Figure 2(e) and 2(f) showed three-dimensional (3-D) schematic drawings of these structures, respectively. This research contributes to the understanding of planar defect formation in III-nitride semiconductor grown by a coalescence process.

References

1. C. N. Huang, P. A. Shields, D.W.E. Allsopp, and A. Trampert, Philos. Mag. 93, 3154 (2013).
2. C. M. Drum, Philos. Mag. 11, 313 (1965).

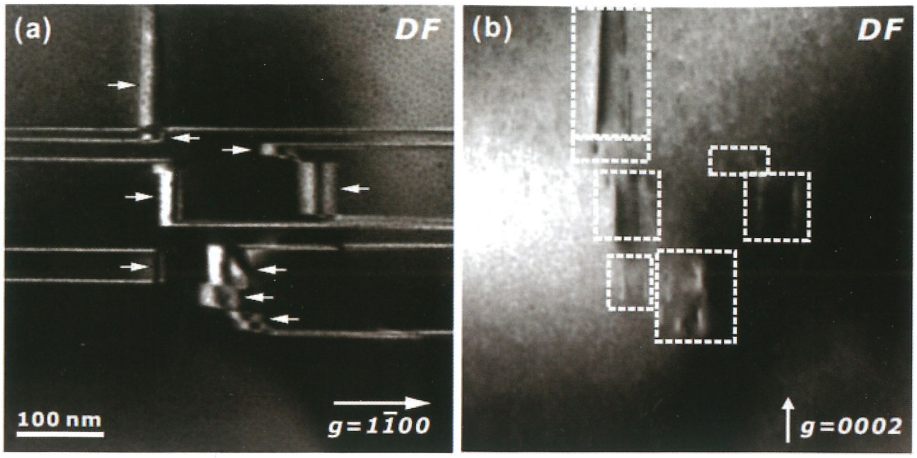

Figure 1. (a) and (b) DF images show the step- and hairpin-shaped basal prismatic SFs near coalesced boundary with g=1$\bar{1}$00 and g=0002 near [1$\bar{1}$20] zone axis. The white arrows indicate prismatic plane stacking faults. The white dash areas indicate the partial dislocations.

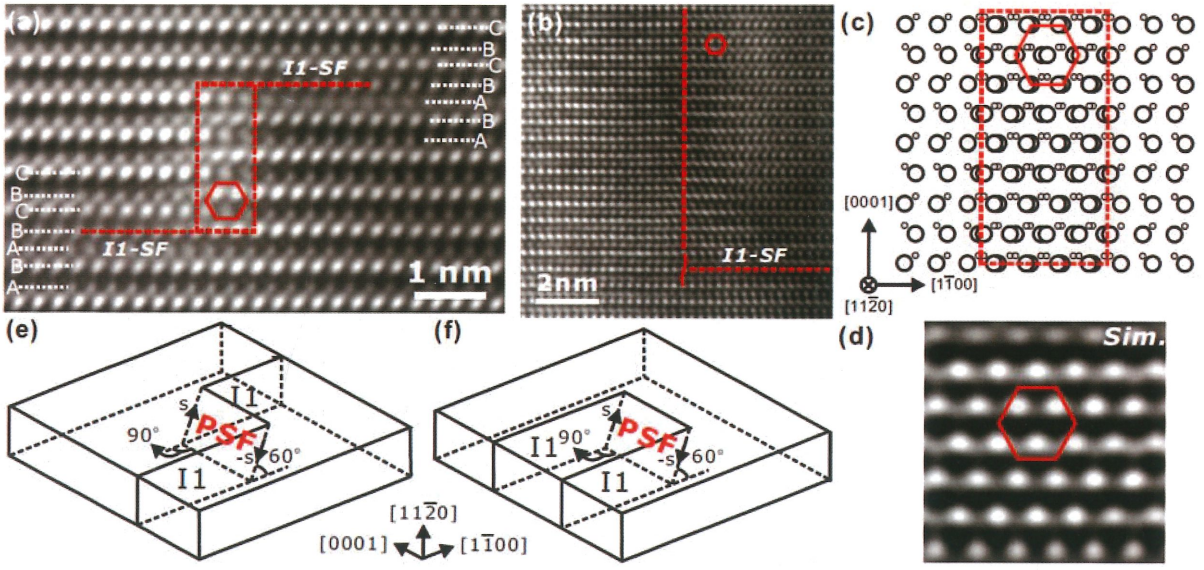

Figure 2. (a) and (b) high-resolution images of step and hair-pin shaped basal prismatic stacking faults. (c) Drum atomic model of the inclined prismatic stacking fault. (d) High resolution simulated image showed the hexagonal contrast. (e) and (f) 3-D schematic drawing of these structures.

M-O-5

SETTING UP A NANOLAB INSIDE A TEM FOR 2D MATERIALS RESEARCH

SUN, Li-Tao (孫立濤)

SEU-FEI Nano-Pico Center, Key Laboratory of MEMS of Ministry of Education,
Southeast University

With the continuous improvement of *in situ* techniques inside transmission electron microscope (TEM), the capabilities of TEM extend beyond structurual characterization to high-precision nanofabrication and property measurement. Based on the idea of "setting up a nanolab inside a TEM", we present our recent progress in 2D Materials research including in situ growth, nanofabrication with atomic resolution, in situ property characterization, nanodevice construction and possible applications (e.g. a 5nm-diameter hole on graphene for third-generation gene sequencing, the spongy graphene as an ultra-efficient sorbent for oils and organic solvents, etc.). Fig. 1 shows in situ nanofabrication of suspended molybdenum sulfide sub-nanometer ribbons with uniform width of 0.35 nm from monolayer MoS2 by electron beam irradiation. The mechanism of electron-beam induced high-resolution nanofabrication was also discussed.

References:

1. L. Sun, F. Banhart, et. al., Science 312, 1199 (2006)
2. J. R-Manzo, M. Terrones, et.al., Nature Nanotechnology 2, 307 (2007)
3. L. Sun, A. Krasheninnikov, et.al., Physical Review Letters 101, 156101(2008)
4. H. Bi, X. Xie, et al., Advanced Functional Materials 22, 4421 (2012)
5. H. Bi, K. Yin, et al., Advanced Materials 24, 5124 (2012)
6. Q. Liu, J. Sun, et al., Advanced Materials 25, 165 (2013)
7. X. Liu, T. Xu, et al., Nature Communications 4, 1776 (2013)
8. H. Qiu, T. Xu, et al., Nature Communications 4, 2642 (2013)
9. X. Li, X. Pan, et al., Nature Communications 5, 3688 (2014)

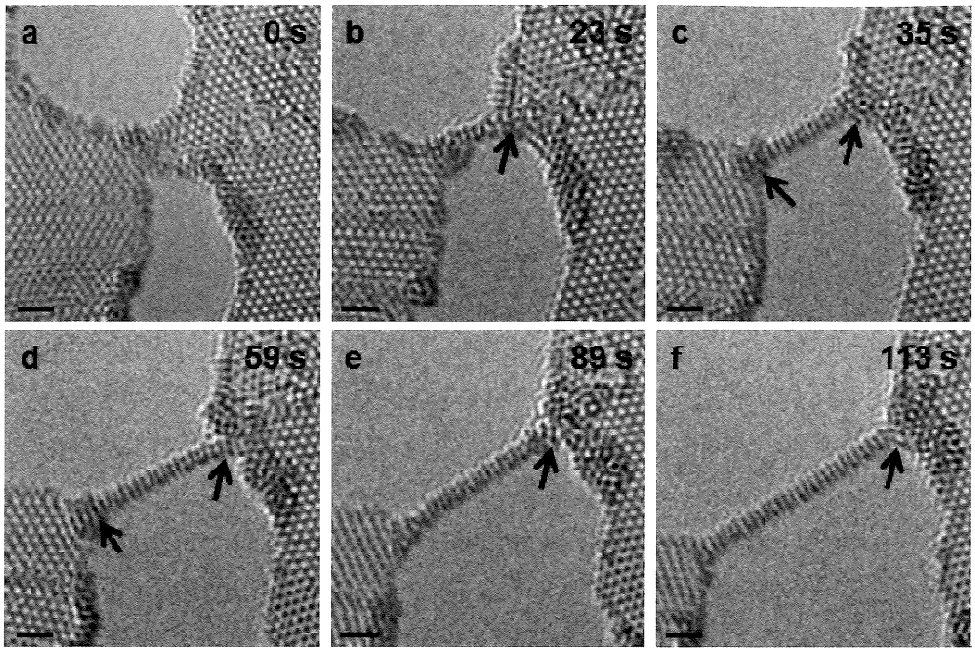

Figure 1. In situ fabrication of suspended molybdenum sulfide sub-nanometer ribbons with uniform width of 0.35 nm (possible narrowest molybdenum sulfide nanoribbon) from monolayer MoS2 by electron irradiation.

M-O-6

TEM IMAGE CONTRAST BEYOND MASS-THICKNESS CONTRAST AND DIFFRACTION CONTRAST

Shih-Wen Tseng (曾湜雯),[1] Shih-Sheng Hung (洪世昇),[1] and Jong-Shing Bow (鮑忠興)[1]

[1]Center for Micro/Nano Science and Technology, National Cheng Kung University, Tainan, Taiwan.

For inorganic solid materials, grains, same composition or different composition, of polycrystal materials are all easily visible by either diffraction contrast or atomic number contrast in TEM images. Recently, due to the development in flexible solar cells and display devices, some organic materials have become important electronic materials [1] which are widely studied by TEM to fully reveal their microstructure to process engineers. One type of these organic materials is supposed to be composed of pseudo-granular structure. However, they are amorphous phases and consisted of light elements, such as C, H, O. These two factors make the granular structure of this organic polymer hardly visible in conventional TEM BF images, governed by mass-thickness contrast and diffraction contrast.

It failed to view the claimed granular structure eventhough the smallest objective aperture and large under focus in TEM image mode (as shown in Figure 1) and the smallest camera length in STEM HAADF image mode were adapted. This granular structure is really visible by using a Gatan Image Filter (GIF) to form images with a specific energy value with a very narrow energy window, three-window elemental map, and two-window ratio map. One set of typical data are shown in Figure 2. Three different setting

References

1. D. W. Steuerman, A. Garcia, M. Dante, R. Q. Yang, J. P. Lofvander, and T. Q. Nguyen, "Imaging the Interfaces of Conjugated Polymer Optoelectronic Devices," Adv. Mater, 0000, 00, 1-8 (2007)
2. J. S. Bow, W. T. Chang, Y. M. Tsou, H. S. Chou, and C. Chiou, "Applications of EELS to Semiconductor Devices Failure Analysis by Using a 300 keV TEM," Proc. ISTFA, 101-105 (2002).

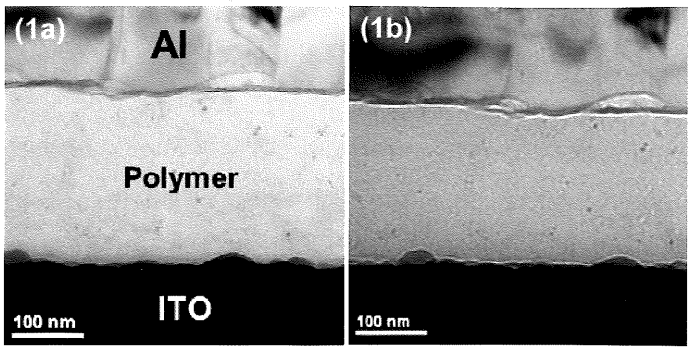

Figure 1. TEM BF images of polymer are not able to reveal its granular structure. (a) normal under focus; (b) large under focus. The smallest objective aperture was used.

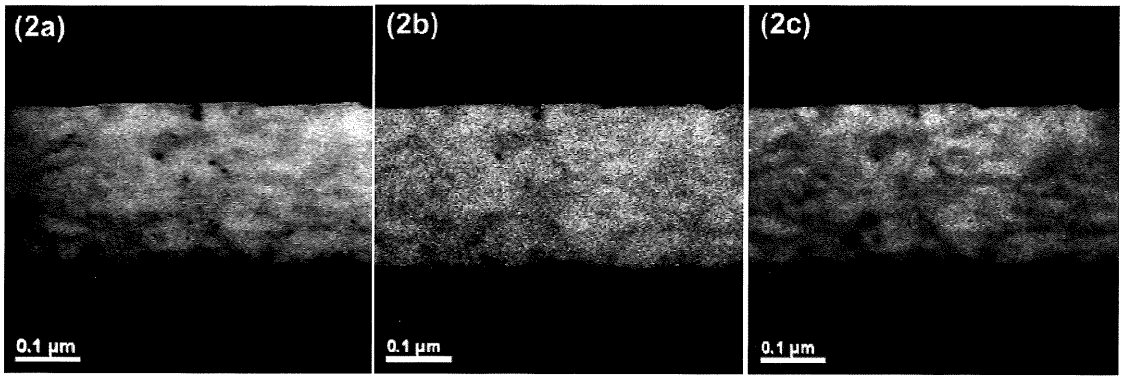

Figure 2. The granular structure of the polymer can be revealed by EELS technqiues. (a) energy selected image ([27 29] eV); (b) C map by three window technique; (c) EELS C ratio image. Those "boundaries" are at same positions in three images.

M-O-7

DEFORMAT ION-INDUCED STRUCTURAL TRANSITION IN BODY-CENTERED CUBIC MOLYBDENUM

WANG, Shu-Juan (王淑娟),[1] WANG, Hao (王浩),[1] Du, Kui(杜奎),[1] ZHANG, Wei (張煒)[1] and SUI, Man-Ling (隋曼齡)[2]

[1] Institute of Metal Research, Chinese Academy of Sciences, Shenyang 110016, China
[2] Beijing University of Technology, Beijing 100124, China

Molybdenum is a refractory metal that is stable in a body-centred cubic structure at all temperatures before melting. Plastic deformation via structural transitions has never been reported for pure molybdenum, while transformation coupled with plasticity is well known for many alloys and ceramics. Here we demonstrate a structural transformation accompanied by shear deformation from an original <001>-oriented body-centred cubic structure to a <110>-oriented face-centred cubic lattice, captured at crack tips during the straining of molybdenum inside a transmission electron microscope at room temperature.[1] The face-centred cubic domains then revert into <111>-oriented body-centred cubic domains, equivalent to a lattice rotation of 54.7°, and ~√15.4% tensile strain is reached, as shown in Fig. 1. The face-centred cubic structure appears to be a well-defined metastable state (Fig. 2), as evidenced by scanning transmission electron microscopy and nanodiffraction, the Nishiyama–Wassermann and Kurdjumov–Sachs relationships between the face-centred cubic and body-centred cubic structures and molecular dynamics simulations. Our findings reveal a deformation mechanism for elemental metals under high-stress deformation conditions.

References

1. S. J. Wang *el al.*, Nat. Comm., 5:3433, DOI:10.1038/ncomms443 (2014).

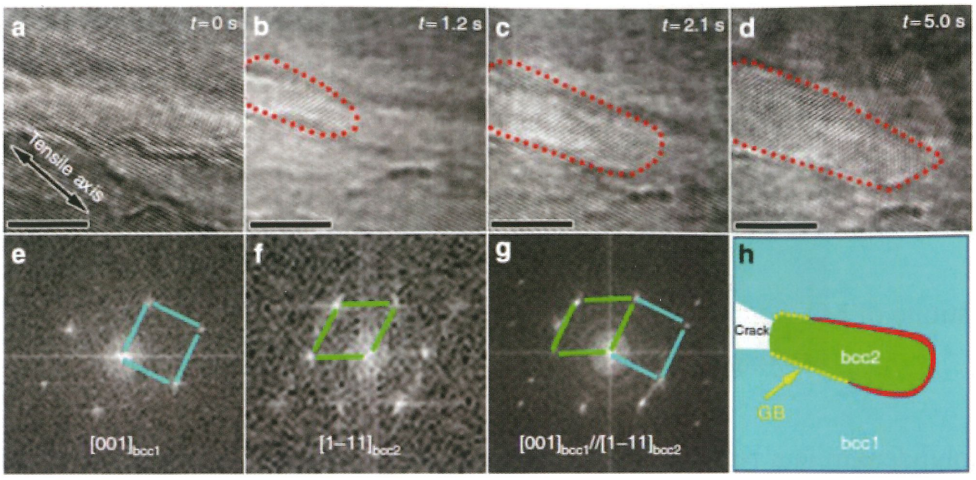

Figure 1. ***In situ*** **electron microscopy observations under tensile loading. a-d,** Time-resolved high-resolution transmission electron microscopy (HRTEM) images taken along the <001> direction of bcc Mo recorded at t = 0 s, 1.2 s, 2.1 s and 5.0 s, respectively. A <111>-oriented grain formed and grown inside the <100>-oriented matrix is outlined by red dots. The scale bar in each figure represents 5 nm. **e-g,** Fast Fourier transformation patterns of HRTEM images from the matrix (bcc1), the newly formed grain (bcc2) and both the matrix and newly formed grain, respectively. **h,** A schematic illustration showing the distribution of bcc1 and bcc2 crystals.

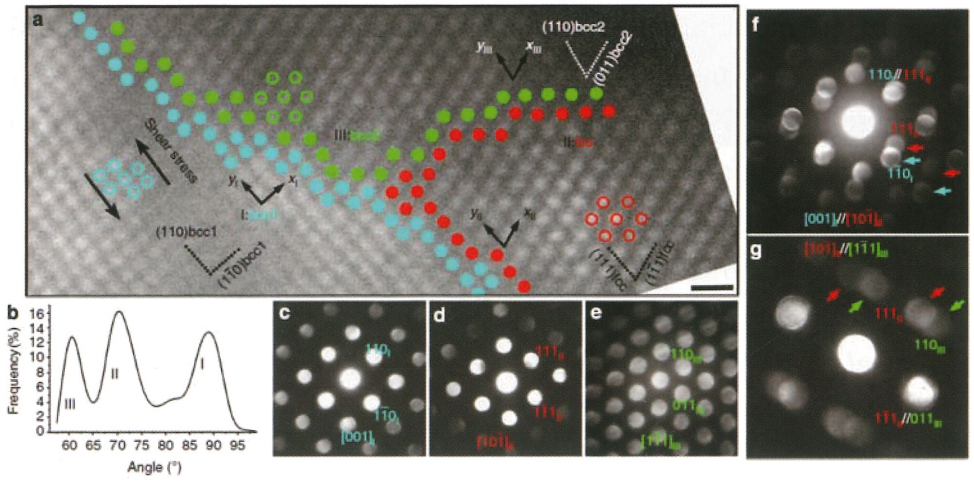

Figure 2. **Three structural variations in Mo. a,** Atomic-resolution high-angle annular dark field scanning transmission electron microscopy (HAADF-STEM) image showing regions I, II, and III with different crystal structures or orientations. Atoms adjacent to the boundaries between the regions are represented using different colors: blue for the original <001>-bcc1 region, red for the <110>-fcc region and green for the <111>-bcc2 region. The scale bar represents 0.5 nm. **b,** Distribution of the measured angle between two basic vectors (*x* and *y*) in the entire imaged area. **c-g,** The electron nanodiffraction patterns from regions I, II, III, I+II and II+III, respectively. The blue, red and green arrows indicate diffraction discs from region I, II and III, respectively, in **f** and **g**.

M-O-8

STRUCTURE DETERMINATION OF SMALL PRECIPITATES IN AL ALLOYS BY QUANTITATIVE ELECTRON MICROSCOPY

J. H. Chen (陳江華),[1] C. L. Wu (伍翠蘭)[1]

[1] Center for High Resolution Electron Microscopy, College of Materials Science and Engineering, Hunan University, Changsha 410082, China

I firstly highlight the latest new developments in modern transmission electron microscopy (TEM). These include through-focus exit-wavefunction reconstruction (TF-EWR) in high-resolution TEM (HRTEM), HRTEM with a spherical aberration (Cs) corrector for the objective lens, high-resolution electron energy-loss spectroscopy (HREELS) with a monochromator, high-resolution scanning TEM (HRSTEM) with a Cs-corrector for the condense lens, and dynamic TEM. Then by examples, I show how these new electron microscopic techniques have led to some breakthroughs in solving key problems in materials science, as well as in nanoscience.

For the new developments in TEM, I will stress the image interpretation problems and the quantitative structure analysis, through discussing the optimum imaging conditions for atomic-resolution imaging.

For the applications of the new TEM techniques, I will firstly illustrate a few excellent examples in the study of dielectric ceramic films, nano-pore devices and other materials. I then focus on our recent study on the automotive aluminum alloys, using atomic-resolution imaging and quantitative structure analysis.

Due to their excellent mechanical properties, the AlMgSi(Cu) alloys occupy a high share of the total aluminum production in the world and are important materials, e.g., for automotive application. With a proper thermal treatment these alloys can be easily pressed in a given form and strengthened by subsequent annealing during which precipitates are formed (which is called precipitation hardening). The precipitation behavior of the solute atoms of alloying elements in the Al matrix, supersaturated after quenching from a higher temperature, plays the key role in forming a desired precipitate microstructure. It has been known for more than 50 years that these alloys are mostly strengthened when small needle-like precipitates are formed [1-3]. These nano-precipitates are called in the literature either as GP(I) and GP(II) zones, or as pre-β″ and β″ phases, or even as Si/Mg co-clusters and GP zones in the early stages [1-2, 4]. The ambiguity in naming reflects that accurate knowledge about these hardening precipitates has not yet been established. To fully understand the early-stage precipitates and their evolution advanced high-resolution transmission electron microscopy (HRTEM) and first principles energy calculations are needed for assessing their atomic structures.

The final structure of these nano-precipites could be determined using electron nano-diffraction, since the final needles may grow large in width up to ~4nm [4]. Unfortunately, for early-stage needles even electron nano-diffraction is difficult to apply, simply because they are too small in width (~2nm). In the present work, we show that the early-stage precipitation in AlMgSi alloys can be understood using advanced HRTEM in association with quantum mechanics first principles energy calculations.

The material we studied is an Al-0.43Mg-1.2Si alloy (weight percent) with 0.15% Cu additions. The homogenized alloy was heated at 560℃ to obtain a full solution of Mg and Si, and then quenched to 20℃. Two annealing conditions were then applied. The specimens were thinned until perforation by electro-polishing for HRTEM investigations.

In conventional HRTEM instruments, the images of the early monoclinic precipitates are easily delocalized and under most imaging conditions they appear as "disordered" clusters, as shown in Figure 1a-b. Hence in order to reveal the structural details of early-stage hardening precipitates, longer particles (>specimen thickness) and advanced atomic imaging in HRTEM have to be selected for the task.

Here we use through-focus exit-wave function reconstruction to image the atomic structure of the growing early-stage needles. From a recorded through-focus series of 20 HRTEM images, we retrieved the electron wave function at the exit-plane of the specimen. The phase of the exit-wave function is then displayed as an atomic-resolution image of the specimen. The obtained atomic-resolution image of a nanoprecipitate, which clearly demonstrates its monoclinic lattice (Figure 1c), is shown in Figure 1d. All the atomic columns are clearly resolved as bright dots.

The present work explains how the hardening nanoprecipitates in AlMgSi alloys are different and why they show the same needle-like morphology and the same monoclinic lattice. It is also shown that the Cu-containing particles, as the precursors of the so-called Q phase can be formed in the early-stage precipitation process of AlMgSi(Cu) alloys.

References

1. Edwards G. A., Stiller K., Dunlop G. L. and Couper M. J., Acta Mater. 46 (1998), 3893-3904
2. Murayama M. and Hono K., Acta Mater. 47 (1999), 1537-1548.
3. Chen J. H., Costan E., van Huis M.A., Xu Q. and Zandbergen H. W., Science 312 (2006), 416-419.
4. Zandbergen H. W., Andersen S. J. and Jansen J., Science 277 (1997), 1221-1225.

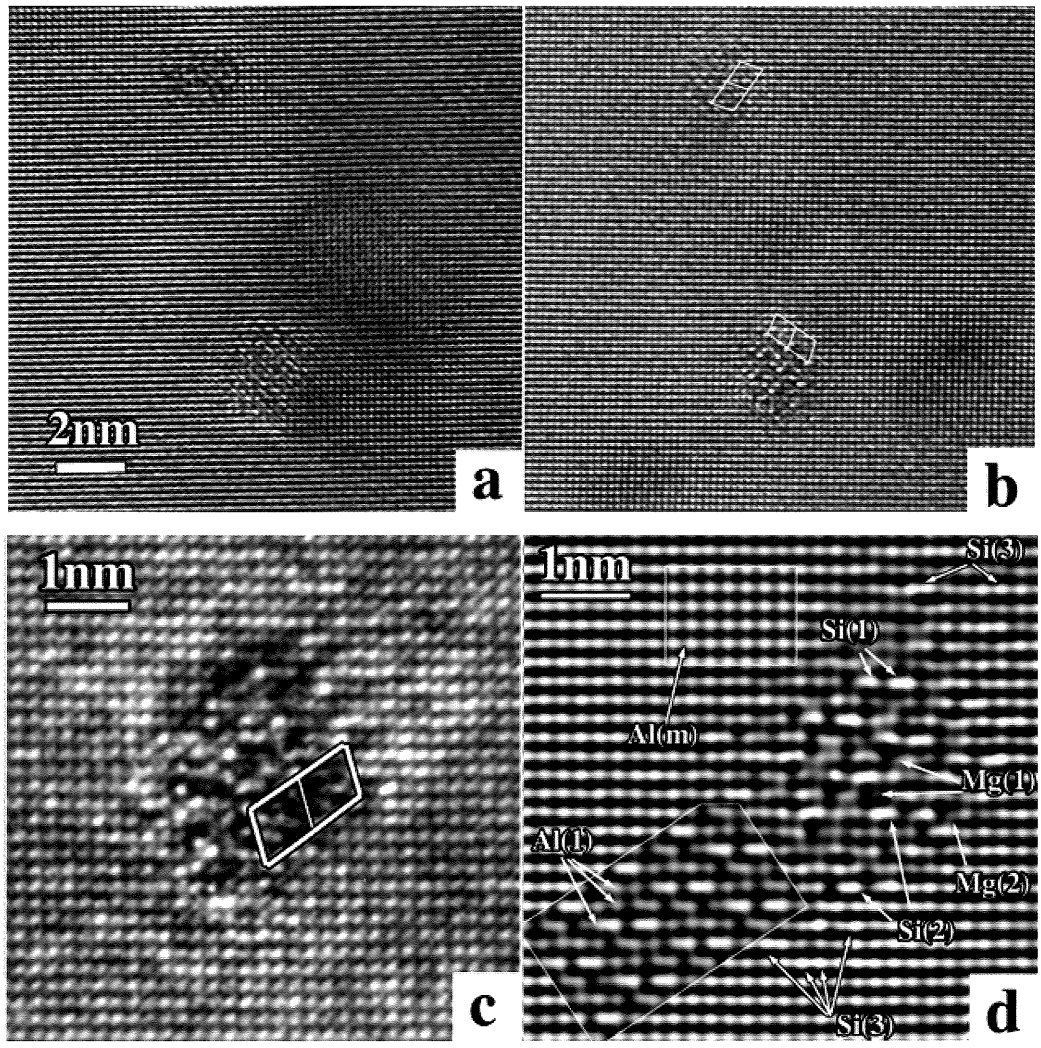

Figure 1 HRTEM images of the hardening nano-precipitates in AlMgSi alloys: from the delocalised lattice image to the atomic-resolution image. a-b) Two early-stage precipitates imaged under different focuses: in a) they appear as "disordered" clusters, but in b) their monoclinic feature is uncovered. c-d) Two images of an early-stage precipitate: c) the original lattice image and d) the atomic-resolution image obtained by using through-focus exit-wave function reconstruction. The insets in d) are the simulated images based on the right structure model of the precipitates.

M-O-9

MANIPULATIONS OF PATTERN CONFIGURATION IN SELF-ASSEMBLED HETEROSTRUCTURES

ZHAN, Qian (詹倩),[1] ZHU, Yuanmin (祝遠民),[1] CHU, Ying-Hao (朱英豪)[2]

[1]Department of Material Physics and Chemistry, University of Science and Technology Beijing, China;

[2]Department of Materials Science and Engineering, National Chiao Tung University, Hsinchu, Taiwan

With a wide range of intriguing structures and physical properties, functional complex oxides that have perovskite, perovskite-related and spinel crystal structures can offer tremendous opportunities to develop next generation electronic devices.[1-2] Among complex correlated oxide heterostructures, a vertical nanocomposite architecture has drawn a widely spotlight due to the strong coupling benefitting from the various hetero-interfaces.[3]

In this work, $BiFeO_3$-$CoFe_2O_4$ (or $NiFe_2O_4$) nanocomposite thin films, as a model system of perovskite-spinel heterostructure, were demonstrated a novel nanostructure configuration with new orientation relationships and heterointerface structures by transmission electron microscopy and related techniques. The substrates with different structural distortions and lattice parameters were selected, such as the ideal cubic perovskite $SrTiO_3$, highly distorted orthorhombic perovskite $DyScO_3$ and $NdGaO_3$. The results show that $CoFe_2O_4$/$NiFe_2O_4$ nanopillars were embedded in the $BiFeO_3$ matrix exhibiting various configurations and extended through the whole films in all of the cases. However, rather than traditional cube-on-cube orientation relationship, the crystal orientation of spinel nanopillars can be tuned along [001], [011], and [111] respectively, while that of the $BiFeO_3$ matrix is fixed in [001] matching the substrates. The different interface structures between the two component phases and also the substrate at an atomic scale have been investigated by high resolution transmission electron microscopy. We conclude that the plentiful combination forms of nanostructures and regulations on the crystallographic orientation of the constituent phases can be understood by the effect of surface energy anisotropy, atomic structure continuity and strain state at the heterointerface.

Reference:

1. Aiping Chen, et al. Microstructure, vertical strain control and tunable functionalities in self-assembled, vertically aligned nanocomposite thin films. Acta Mater.,61 2783 (2013).
2. L. W. Martin, et al. Multiferroic and magnetoelectric heterostructures. Acta Mater., 60 2449 (2012).
3. S. C. Liao, et al, Misorientation control and functionality design of nanopillars in

self-assembled perovskite-spinel heteroepitaxial nanostructures. ACS Nano, 5 4118 (2011).

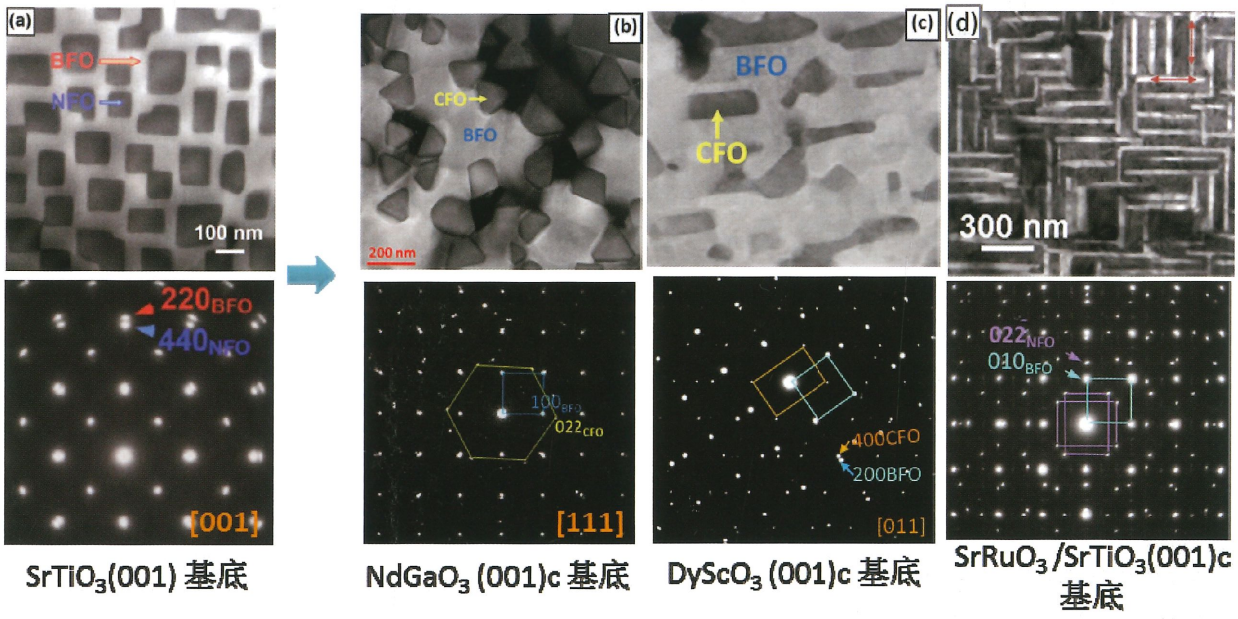

Figure 1. $BiFeO_3$-$CoFe_2O_4$/$NiFe_2O_4$ films on different distorted perovskite substrates with various morphologies and orientations.

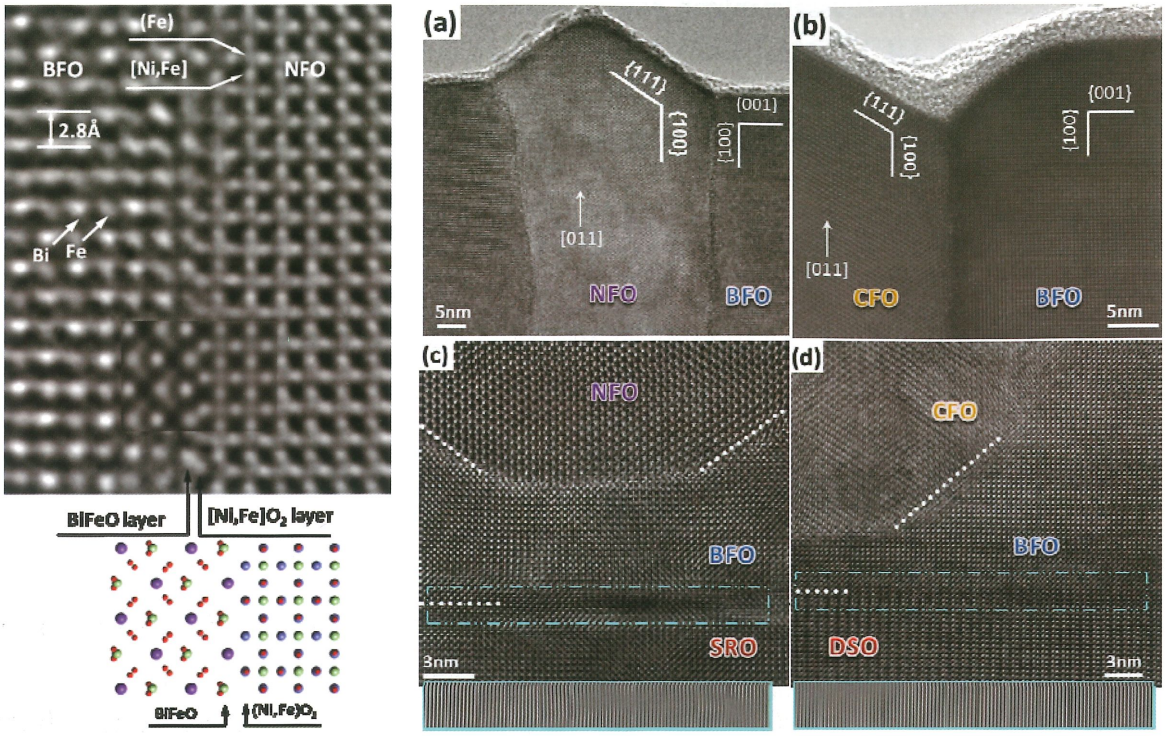

Figure 2. Heterointerfaces and strain state in $BiFeO_3$-$CoFe_2O_4$/$NiFe_2O_4$ film system.

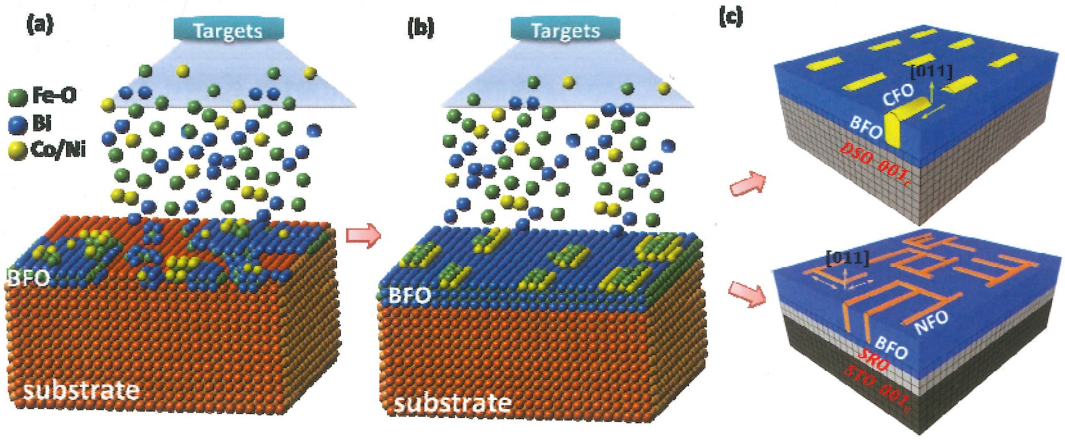

Figure 3. Schematic model of the growth procedure for spinel nanoplates with three deposition stages.

M-O-10

ELECTRON BACKSCATTER DIFFRACTION STUDY ON TWINNING BEHAVIOR IN MAGNESIUM ALLOY

XIN, REN-LONG (辛仁龍),[1] GUO, Chang-Fa(郭長發),[1] and LIU, Qing(劉慶)[1]

[1]College of Materials Science and Engineering, Chongqing University, Chongqing, China

Twinning is an important deformation mechanism for Mg alloys in which there are insufficient operative slip systems to offer continuous deformation especially at room temperature. During plastic deformation the lattice rotation and grain subdivision caused by twinning can largely affect microstructural evolution and strain hardening behaviors. Therefore, an in-depth understanding of twinning behavior and mechanism is important for the development of new alloys and novel processing methods. The present work aims to understand the characteristics and variant selection mechanism of {10-12}<-1011> twinning.

The grain orientation effect on twinning was analyzed by calculating Schmid factors relative to specific applied deformation. The effect from neighboring grains was understood by analyzing grain boundary misorientation and a geometric compatibility factor (m'). As shown in Figure 1, the geometric compatibility factor is defined as: $m'=\cos\psi * \cos\kappa$, where ψ (κ) is the angle between twinning plane normal (twinning shear direction) of two neighboring grains. Figure 2 shows that various twin patterns such as independent or intersecting multi-twins in a grain, paired twins in two neighboring grains, and twin chains across many grains were observed in the 3% compressed AZ31 sample [1]. Paired {10-12} twins are likely formed when the Schmid factors of both twins and their strain compatibility factor are very high. The paired twins can propagate throughout the grains and transfer to more neighboring grains. Such continuous twin-twin transfer behavior across more than three neighboring grains result in the formation of twin chains. Long {10-12} twin bands have been observed in a rolled Mg alloy [2]. Schmid factor analysis reveals that for each twin in the band, there are two variants favorable for the applied rolling deformation. However, these two variants have quite different m' and all the variants have selected the one with the highest m', indicating that local strain transfer plays an important role in variant selections of twinning.

References

1. R. L. Xin, C. F. Guo, Z. R. Xu, G. D. Liu, X. X. Huang and Q. Liu, Scr. Mater., **74** 96 (2014).
2. C. F. Guo, R. L. Xin, C. H. Ding and Q. Liu, Mater. Sci. & Eng. A, 609 92 (2014).

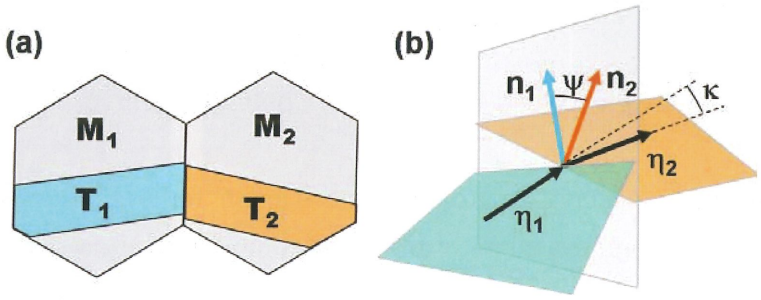

Figure 1. (a) Schematic illustrations of two neighboring twins (T_1 and T_2) in a twin band (M_1 and M_2 are the corresponding parent grains). (b) Geometric relationship between the active twinning systems in M_1 and M_2. n and η are the twinning plane normal and shear direction, respectively.

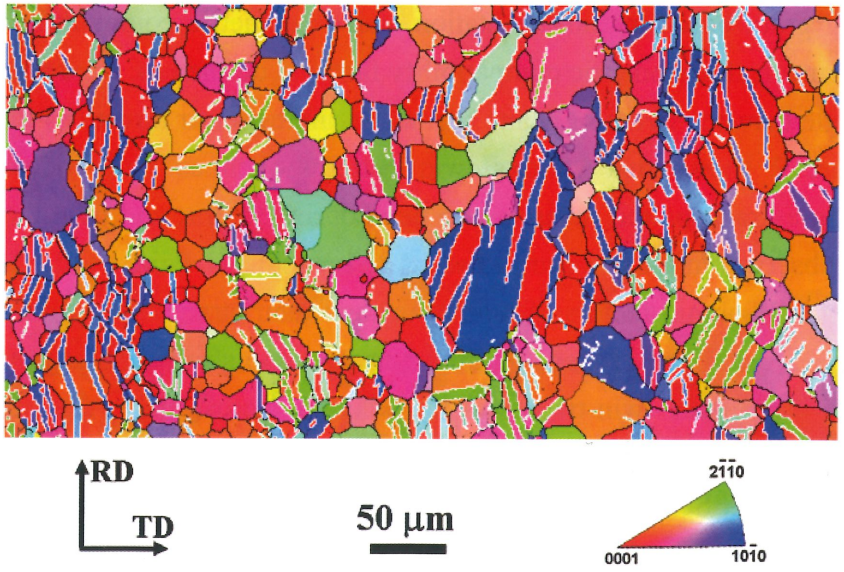

Figure 2. The microstructure of the sample deformed to an engineering strain of 3%. The {10-12} twin boundaries were indicated by white lines. Various twin patterns such as multi-twins in a grain, paired twins in two neighboring grains and twin chains across many twins were observed.

M-O-11

IN SITU STUDY OF FACET-DEPENDENT HETEROGENEOUS CATALYSIS

WANG Yong (王勇)

Center of Electron Microscopy and State Key Laboratory of Silicon Materials, Department of Materials Science and Engineering, Zhejiang University, Hangzhou, China

Heterogeneous catalysis, also referred as surface catalysis, is of paramount significance in chemical technology and industrial processes, where efficiency heavily relies on the properties of catalyst surfaces [1,2]. Most of catalysts are noble metal nanocrystals with anisotropic nature; thus knowledge about reaction characteristics on different catalyst crystal facets is pivotal for improving the activities of heterogeneous catalysis. Although previous spectroscopy and microscopy studies have provided pieces of circumstantial evidences on this regard; however, a direct observation at the atomic level of the facet-dependent activity of nanocrystal-catalysts remains challenging. In this report, we present a direct experimental observation of a crystal facet-dependent catalysis on a single nanocrystal-catalyst through an in situ study of a model catalysis platform, platinum-catalyzed oxidation of graphene layers, in an environmental transmission electron microscope [3]. Our experimental setup for the first time implements a simultaneous recording of diverse catalytic activities on different facets on a single particle at atomic resolution, revealing that Pt{100} is more active for the graphene oxidation than Pt{111}. Density functional theory calculation shows that the Pt{100} facets favor both the adsorption and dissociation of oxygen species (O_2 and O) compared to the Pt{111} facets, and this facilitates C-C bond breaking, promoting a faster oxidation of graphene to CO_2 on Pt{100}. Our study not only directly demonstrates crystal facet-dependent catalysis in situ but also offers a novel approach for the dynamical study of the catalytic mechanism of heterogeneous catalysts at the atomic level.

References

1. G. Somorjai , Science 227 902 (1985).
2. F. Tao, M. Salmeron, Science 331 171 (2011).
3. W. Yuan, Y. Jiang, Y. Wang, Z. Zhang et al. 2014, submitted.

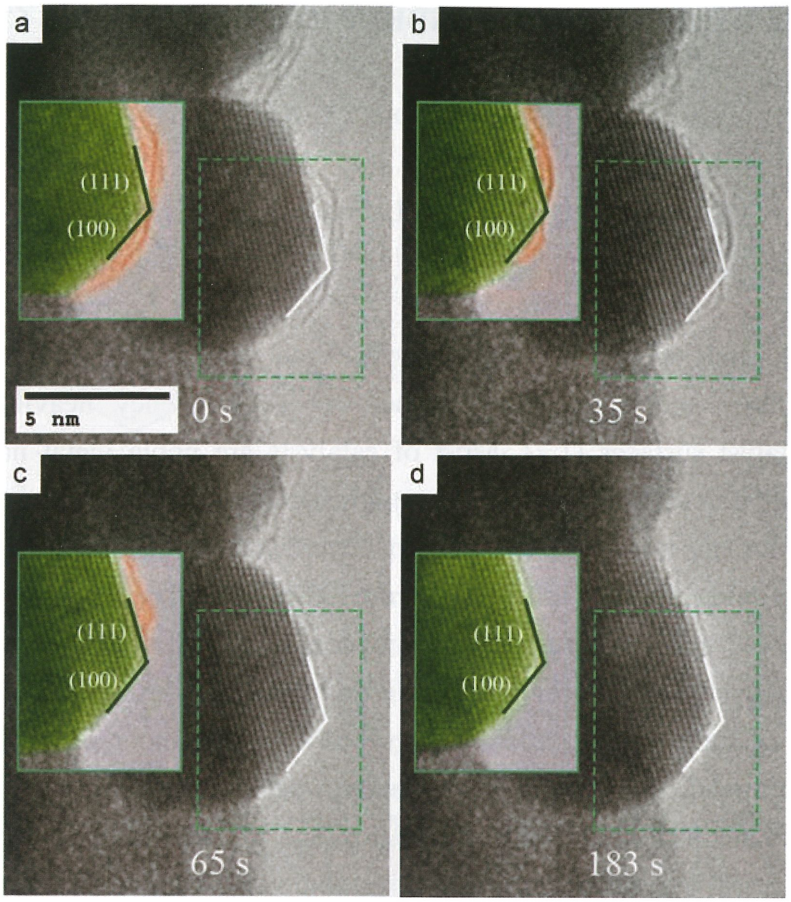

Figure 1. TEM images of the dynamic oxidation of the graphene layers catalyzed by the Pt nanocrystals with time.

M-O-12

IN SITU TEM STUDIES OF RESISTANCE SWITCHING IN TITANATE BASED DEVICE

YANG, Yang (楊陽),[1] LÜ, Wei-Ming (呂偉明),[1] YAO, Yuan (姚淵),[1] JI Rong-Sun (孫繼榮),[1] and YU, Ri-Cheng (禹日成)[1]

[1]Beijing National Laboratory of Condensed Matter Physics, Institute of Physics, Chinese Academy of Sciences, Beijing 100190, P. R. China

Compared with the ferroelectric random access memory, the resistance random-access memory (RRAM) possesses the distinct advantage because of its simple fabrication process, fast read and write speed, high storage density and multi-level storage application. So RRAM is becoming one of the rapid development fields both in semiconductor engineering and scientific researches[1-5]. After decades of efforts, the research on resistance switching (RS) behavior in transition metal oxides has shifted to the stage of verifying the proposed models by direct experimental evidences. We investigated RS behavior and oxygen content variation of $La_{0.85}Sr_{0.15}TiO_3/SrTiO_3$:Nb (LSTO/STON) by *in situ* transmission electron microscopy observation and *in situ* electron energy loss spectrum (EELS) characterization under external electric field. RS behavior was found by *in situ* I-V measurement in TEM after the "forming" process. Simultaneous with the observation, significant changes of oxygen content at the Pt/LSTO interface were identified, as shown in Fig. 1 and Fig. 2. Under different voltages, the shape of the O-K EELS peaks changes regularly at the position of Pt/LSTO interface. Our experimental results[6] imply that the conductive channels should be formed by the oxygen vacancy at the Pt/LSTO interface and support that the RS behavior in this device originates from the local variation of oxygen content. We illustrate a schematic diagram in Fig. 3. Moreover, *in situ* TEM characterization displays the advantage - to reveal the origin of various RS behaviors.

References

1. R. Waser, R. Dittmann, G. Staikov and K. Szot, Adv. Mater., **21** 2632 (2009).
2. A. Ignatiev, et al., Phase Trans., **81** 791 (2008).
3. A. Sawa, Mater. Today, **11** 28 (2008).
4. H. Schroeder, R. Pandian and J. Miao, Phys. Status Solidi A, **208** 300 (2011).
5. K. M. Kim, D. S. Jeong and C. S. Hwang, Nanotechnol., **22** 254002 (2011).
6. Y. Yang, W. M. Lü, Y. Yao, J. R. Sun, C. Z. Gu, L. Gu, Y. G. Wang, X. F. Duan and R. R. Yu, Scien. Rep., **4** 3890 (2014).

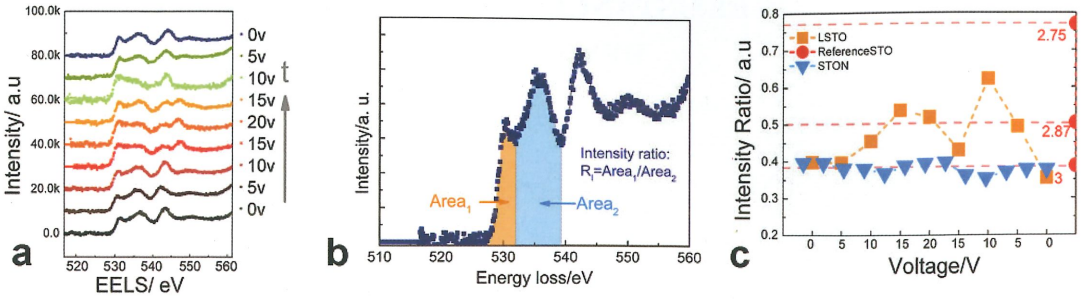

Figure 1. The oxygen content fluctuation adjusted by applied bias in the "forming" process.

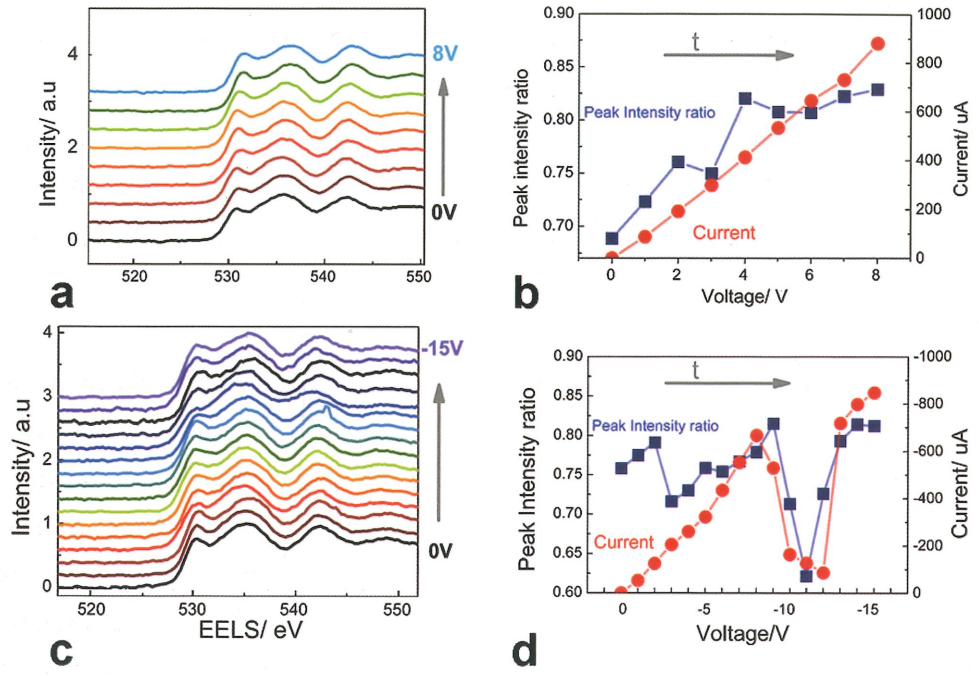

Figure 2. O-K edge and the intensity ratio under voltages with corresponding current in the RS process.

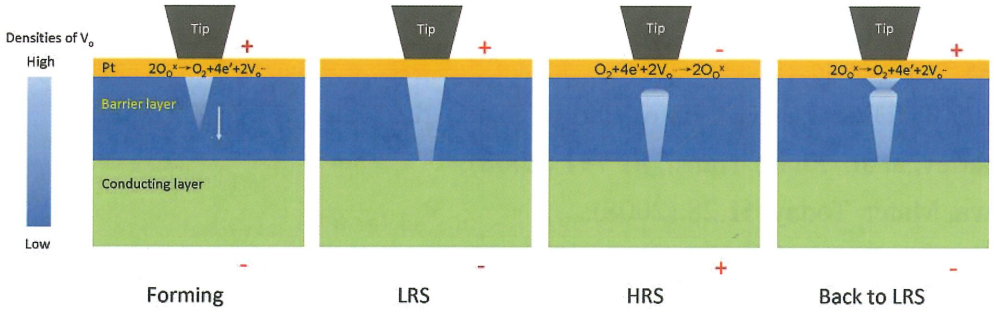

Figure 3. Schematic diagram of resistance switching of the device. The red symbols "+" and "-" indicate the direction of applied voltage.

M-O-13

QUANTITATIVE CHARACTERIZATION OF CHARGE DISTRIBUTIONS IN NANOSTRUCTURES USING COMPREHENSIVE TEM TECHNIQUES

Li, Luying (李露穎)[1,2]

[1] Wuhan National Laboratory for Optoelectronics, Huazhong University of Science and Technology, Wuhan, 430074, China

[2]Department of Physics, Arizona State University, Tempe, Arizona 85287, USA

Epitaxial germanium QDs embedded in boron-doped silicon have been studied using off-axis electron holography to estimate the number of holes associated with a single QD. Holes were confined near the base of the pyramidal Ge QDs. About 30 holes were localized to the investigated dot, which is comparable to the average number of holes confined to each Ge dot using a C-V measurement [1]. HAADF scanning transmission electron microscopy images and off-axis electron holograms were obtained from specific Ge/Si core/shell NWs. The excess phase shifts measured across the NWs indicated the presence of holes inside the Ge cores [2].

Homogeneous ZB/WZ heterostructural junctions have been studied in ZnSe nanobelts and InAs nanopillars. For ZnSe nanobelts, Polarity continuity is determined through aberration-corrected HAADF imaging. The hypothesized saw-tooth-like potential profile is directly revealed at the nanoscale using off-axis electron holography, and spontaneous polarization is identified as the predominant factor causing the experimental profile [3]. For InAs nanopillars, the electric field related to spontaneous polarization within the ZB region is revealed at nanometer scale using off-axis electron holography. Through probe-corrected HAADF imaging, strain-induced variations of local spontaneous polarization are determined with atomic resolution. Moreover, spontaneous polarization values along the interface normal are calculated and possible explanations are provided [4].

References

1. L. Li, S. Ketharanathan, J. Drucker and M. R. McCartney, Appl. Phys. Lett., 94, 232108 (2009).
2. L. Li, D. J. Smith, E. Dailey, P. Madras, J. Drucker and M. R. McCartney, Nano Lett., 11, 493 (2011).
3. L. Li, L. Jin, J. Wang, D. J. Smith, W. Yin, Y. Yan, H. Sang, W. Choy and M. R. McCartney, Adv. Mater., 24, 1328 (2012).
4. L. Li, Z. Gan, M. R. McCartney, H. Liang, H. Yu, W. Yin, Y. Yan, Y. Gao, J. Wang and D. J. Smith, Adv. Mater., 26, 1052 (2014).

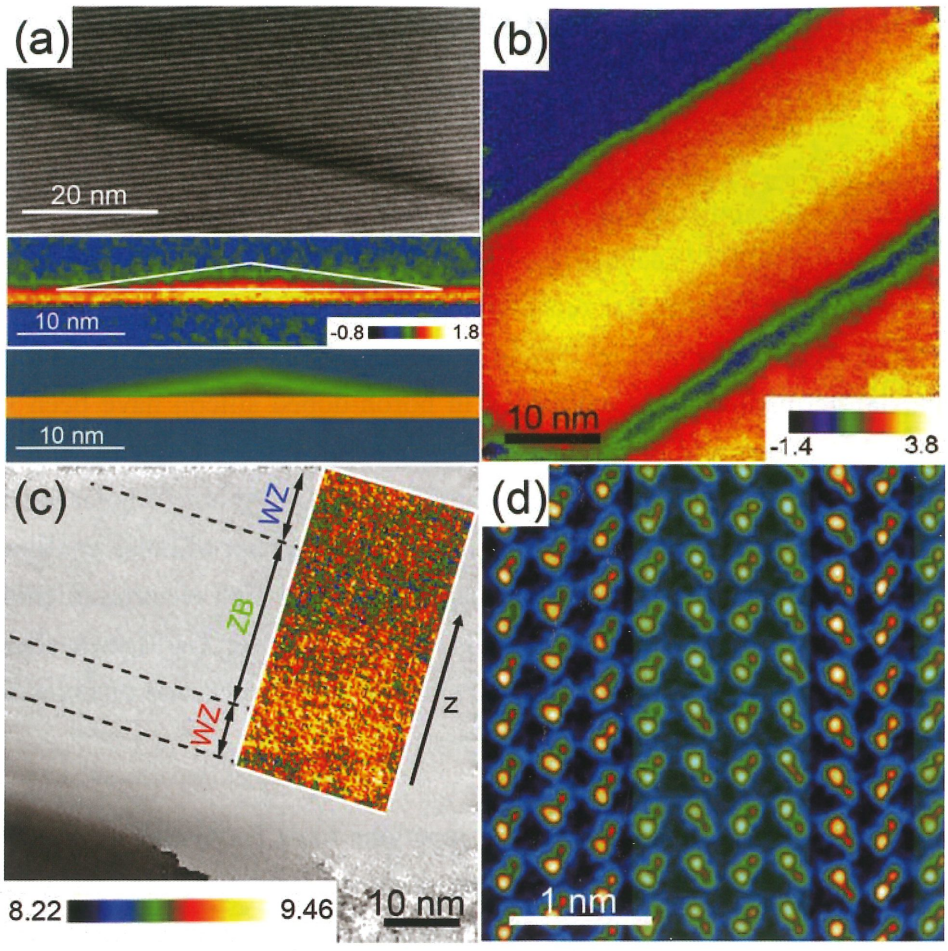

Figure 1. (a) Electron hologram and phase image of a Ge quantum dots embedded in Si substrate showing hole accumulation near the base of the dot. (b) Phase image of a Ge/Si core/shell nanowire where holes reside in the Ge core. (c) Phase image of ZB/WZ heterostructural junctions within ZnSe nanobelt with saw-tooth-like phase profile across the interfaces. (d) HAADF image of ZB/WZ interfaces in InAs nanopillars at atomic resolution.

M-O-14

STRAIN AND STABILITY OF SI/GE AXIAL HETEROJUNCTION NANOWIRES

Cheng-Yen Wen (溫政彥), [1] Frances M. Ross,[2] Mark C. Reuter,[2] Dong Su,[3] and Eric A. Stach[3]

[1]Department of Materials Science and Engineering, National Taiwan University, Taipei, Taiwan

[2]IBM T. J. Watson Research Center, Yorktown Heights, New York

[3]Center for Functional Nanomaterials, Brookhaven National Laboratory, Upton, New York

The growth of semiconductor heterojunction nanowires is beneficial for electronic devices in several ways. Firstly, the growth processes are compatible with existing semiconductor technology. Secondly, the small diameter of nanowires provides efficient lattice-mismatch-induced strain energy dissipation pathways - fabrication of heterojunctions for bandgap engineering is more feasible in nanowires, showing great potentials for future electronic, optoelectronic, and energy applications [1, 2]. In this study, we use solid alloy catalysts to grow Si and Ge heterojunction nanowires via the vapor-solid-solid method, which, in contrast to the standard vapor-liquid-solid method, does not have the intermixing problem for the growth of heterojunctions. Ultra-thin Ge layers (less than 1 nm) can be grown inside Si nanowires without the formation of misfit dislocations (Fig. 1(a)). Besides, the composition change at the junctions is very abrupt, e.g. less than 1 nm from Si to Ge and about 1 nm from Ge to Si (Fig. 1(b)).

As a result of the structural perfection of the heterojunction interfaces, coherent strains exist at the interface. Such strains may strongly influence the physical properties of the Si and Ge lattices and hence the performance of devices built from this type of heterojunction structure [3]. To evaluate the strain, we use the Geometrical Phase Analysis method to map the strain distribution around the heterojunctions. The incorporation of Ge does cause the vertical (axial) lattice distortion, as seen in Fig. 1(c), whereas the horizontal (radial) strain is very small, as shown in Fig. 1(d), indicating that the Ge lattice is strained by the Si lattice. The lattice stain can easily cause the structural instability of the Si/Ge/Si heterojunctions and, thus, lower the permissible thermal budget for the post-growth thermal processes.

References

1. T. E. Clark, P. Nimmatoori, K.-K. Lew, L. Pan, J. M. Redwing, and E. C. Dickey, Nano Lett., **8**, 1246 (2008).
2. C. Lieber, Nano Lett., **2**, 81 (2002).
3. J. G. Swadener and S. T. Picraux, J. Appl. Phys., **105**, 044310 (2009).

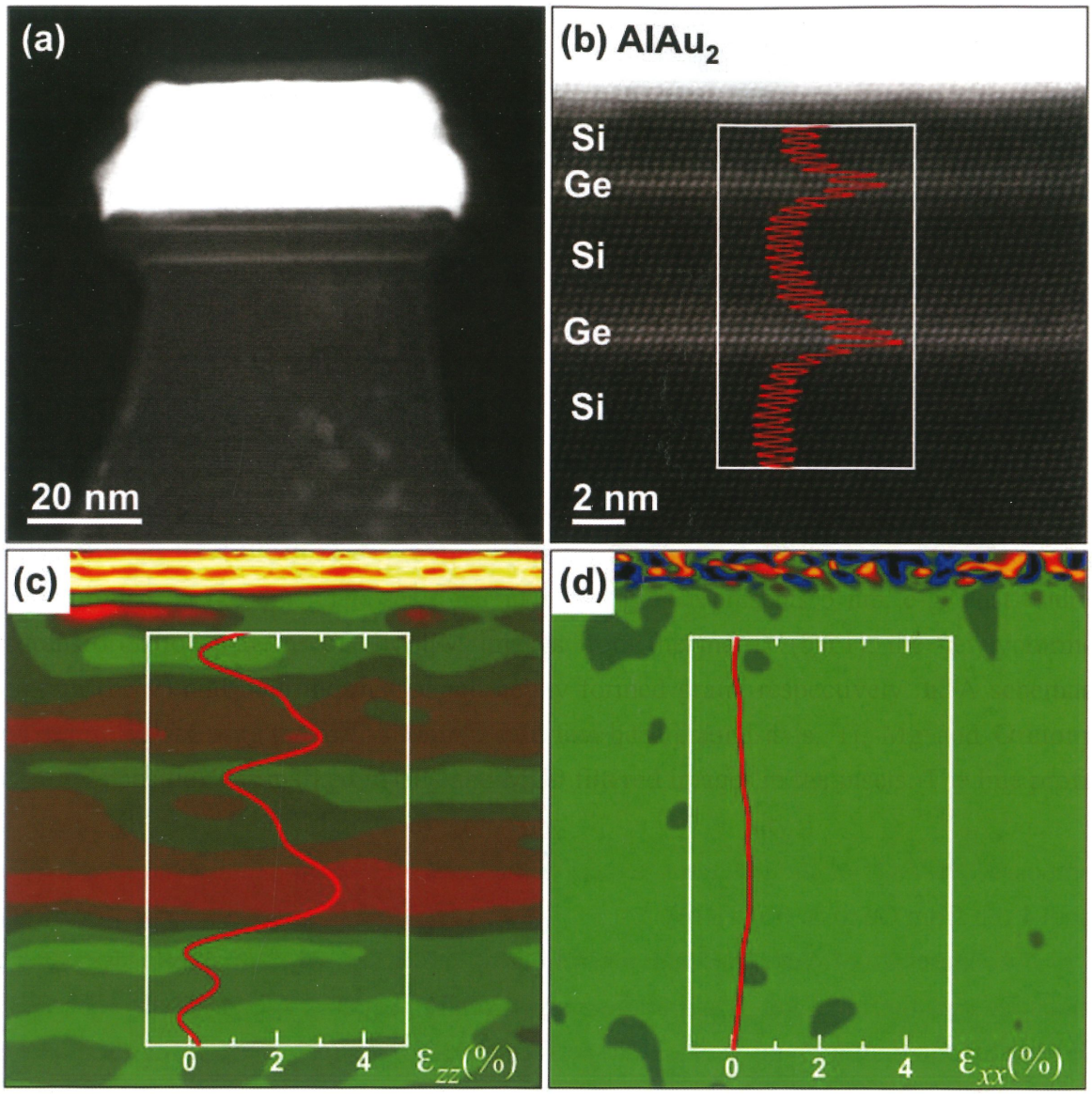

Figure 1. (a) High-angle annular dark-field scanning transmission electron microscopy (HAADF-STEM) image of a Si nanowire containing a couple thin Ge layers. (b) HAADF-STEM lattice image showing abrupt composition changes at the Si-Ge heterojunctions. The inset if the STEM intensity profile along the lattice planes. (c-d) Geometrical Phase Analysis maps of vertical (axial) strain and horizontal (radial) strain, respectively, of the Si-Ge heterojunctions. The insets are profiles of the strain values averaged over the whole width of the maps.

M-O-15

FABRICATION AND HEALING OF FACETED NANOPORES IN MAGNESIUM

WU, Shu-Jing (吳淑靜),[1] SHENG, Hua-Ping (盛華平),[1] CAO, Fan (曹凡),[1] LIU, Yu (劉玉),[1] LIU, Chun (劉春),[1] ZHENG, He (鄭赫),[1] ZHAO, Dong-Shan (趙東山),[1] and WANG, Jian-Bo (王建波)[1]

[1]School of Physics and Technology, Center for Electron Microscopy and MOE Key Laboratory of Artificial Micro- and Nano-structures, Wuhan University, Wuhan, China

Solid state nanopore-based sensing has emerged as a promising candidate for the detection and characterization of biomolecules. To date, most of the fabricated nanopores in various materials such as SiO_2 [1], are circular with no obvious facets, due to the isotropic property in amorphous materials. While faceted nanopores can be potentially employed in rapid electrical detection and analysis of biomacromolecule with various shapes, the relevant investigation has been rarely reported. In what follows, we demonstrate that faceted nanopores with various shapes can be successfully fabricated in magnesium via focused e-beam inside transmission electron microscope (TEM). Associated with orientation, the nanopore shapes varied when manipulating the e-beam irradiation direction (Fig. 1). The crystallographic planes corresponding to the edges of nanopores are discussed [2, 3].

Furthermore, when the e-beam was spread out, the nanopores would continuously shrink and finally disappear. Such atomic-scale healing dynamics are directly recorded by the in situ high-resolution transmission electron microscopy (HRTEM) techniques, as evidenced by the layer-by-layer growth of atomic planes at the nanopore periphery (Fig. 2) [4]. Without e-beam illumination, the nanopore would retain its shape, implying an e-beam-assisted healing mechanism. Hence, by manipulating the e-beam (e.g., irradiation direction and duration), the nanopore shape and size could be effectively controlled along different directions. Our results are highly relevant to the nanopore patterning in metallic materials and are of fundamental importance concerning the potential applications, such as nanopore-based sensor, etc.

References

1. A. J. Storm, *et al.*, Nat. Mater., **2** 537 (2003).
2. S. Wu, *et al.*, Appl. Phys. Lett., **103** 243101 (2013).
3. H. Zheng, *et al.*, Appl. Phys. Lett., **104** 141906 (2014).
4. H. Zheng, *et al.*, Sci. Rep., **3** 1920 (2013).

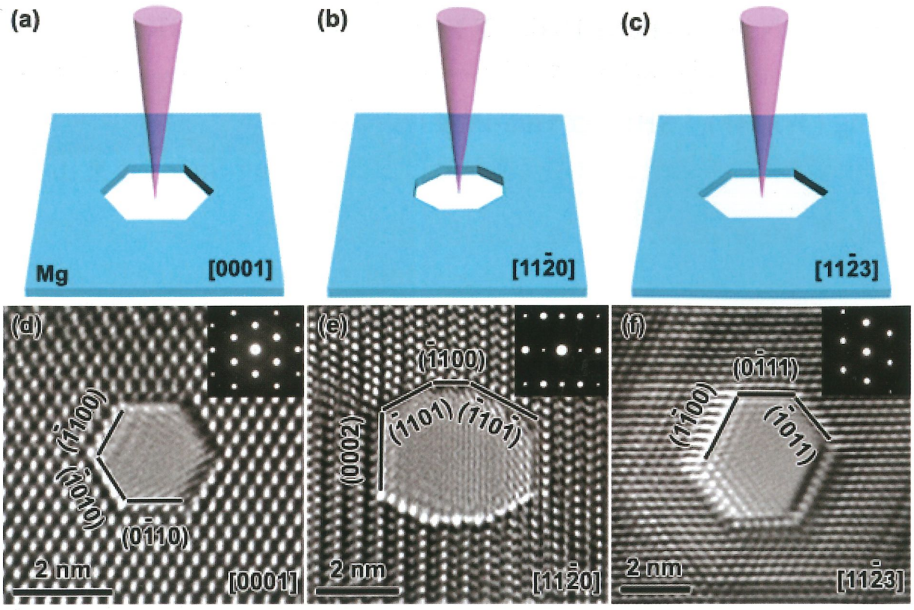

Figure 1. (a-c) A schematic illustration and (d-f) HRTEM images of nanopores along the (a) [0001], (b) [11-20], and (c) [11-23] zone axes, correspondingly. The insets in (d-f) show the SAED patterns of the corresponding regions, respectively.

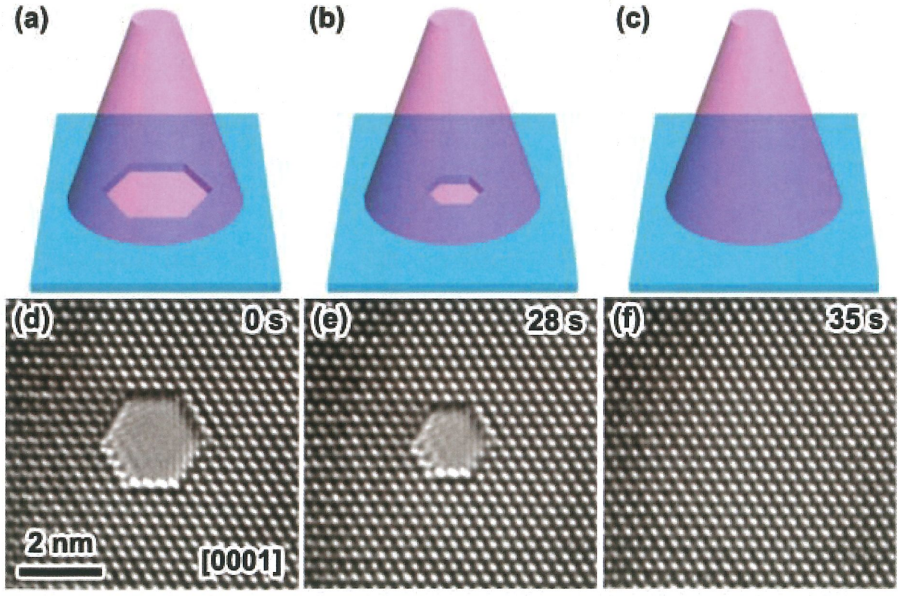

Figure 2. (a-c) A schematic illustration and (d-f) time-lapsed experimental images showing the healing of an individual nanopore under wide-field e-beam irradiation along the [0001] zone axis.

M-O-16

PHASE TRANSFORMATIONS IN THE NITROCARBURIZING SURFACE OF CARBON STEEL IN THE PROCESS OF NITROCARBURIZING AT 560-580°C

C. L. Wu (伍翠蘭), W. L. Chen (陳汪林), J. H. Chen (陳江華)

Center for High Resolution Electron Microscopy, College of Materials Science and Engineering, Hunan University, Changsha 410082, China

Ferritic nitrocarburizing is a widely employed industry process by which a strengthened nitrocarburized surface can be formed on mechanical tools or parts made of steels. Mainly composed of the ε-Fe_{2-3}(C,N) and the γ′-Fe_4(C,N) carbonitride phases as well as the α-Fe phase, the nitrocarburized surface has featured microstructures and properties that are directly related to the phase transformations occurring in the surface layers. Thus far, the following phase transformation sequence for the surface has generally been accepted: α-Fe + N/C → ε → γ′. In the present work, these phase transformations were systematically revisited by microstructure and property characterizations in association with a controlled nitrocarburizing process by which the microstructures and properties of the surface are adjustable. Our study demonstrates that, to fully understand the microstructure and the property of a nitrocarburized surface, it is necessary to adopt the hase transformation sequence: α-Fe + N/C→ γ-N/C + N/C → γ′ + N/C → ε, in which the existence of a transitional austenite phase containing N/C-atoms (γ-N/C) must be assumed and the γ′ phase actually forms prior to the ε phase.

References

1. W.L. Chen, C.L. Wu*, Z.R. Liu, S. Ni, Y. Hong, Y. Zhang, J.H. Chen, Phase transformations in the nitrocarburizing surface of carbon steels revisited by microstructure and property characterizations, Acta Materialia, 2013,61:3963–3972.
2. W.L. Chen, C.L. Wu*, J.H. Chen, Aigui He, An electron microscopy study of vein-like grain boundary microstructure in nitrocarburized low carbon steels, J. Mater. Sci. Technol., 2013, 29(7): 669-672.
3. He AG, Chen WL, Wu CL, The morphology and crystallographic orientation of γ '-Fe4(C,N) phase in diffusion layer of plasma nitrocarburized 08F steel, J Chin Electr Microsc Soc 2012;31:22 (in chinese).
4. Gontijo LC, Machado R, Miola EJ, Casteletti LC, Nascente PAP. Surf Coat Technol 2004;183:10.
5. Somers MAJ, Christiansen. J Phase Equilib 2005; 26:520.
6. Gerardin D, Morniroli JP, Michel H, Gantois M. J Mater Sci 1981;16:159.

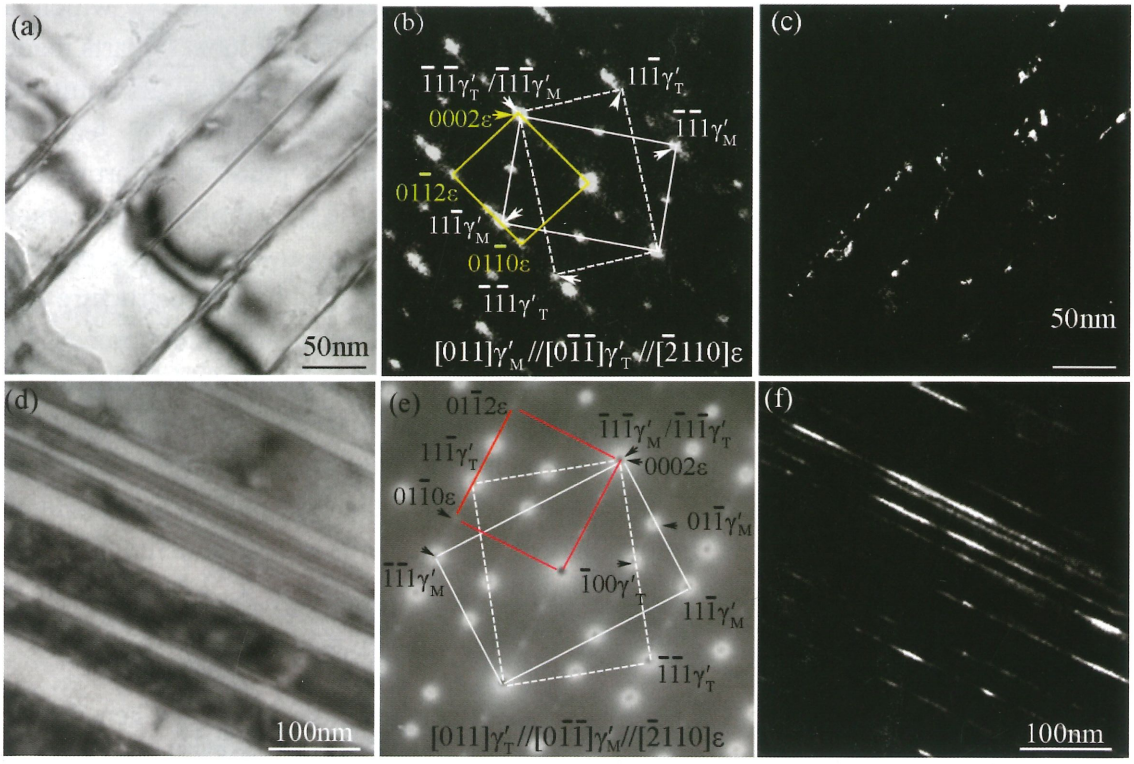

Fig.1. (a) The TEM BF image of a γ′ grain ； (b) the SAED pattern taken along the $[011]_{\gamma'}//[0\bar{1}\bar{1}]_{\gamma'T}//[\bar{2}110]_{\varepsilon}$ direction and its indexing; (c) The DF image formed using $(0\bar{1}10)_{\varepsilon}$ reflection shown in (b).

INCOHERENT AND COHERENT IMAGING FOR TOMOGRAPHY OF NANO PARTICLE

Chen F. R. (陳福榮)[1], Tsai C. Y. [1], Yuan-Chih Chang (張淵智)[2], Van Dyck, D.[3]

[1] National Tsing Hua University, Hsin-Chu, Taiwan
[2] Academic Sinica, Taiwan
[3] University of Antwerp, Belgium

Transmission electron microscopy (TEM) has been well recognized for its power in spatial resolution to the sub-Å level, especially, with aberration-corrected optics. However, the ultimate goal of electron microscopy is not only to obtain nice images but also to advance materials science. This means that EM has to evolve from describing to understanding materials properties. It is wellknown that all the structure-property relations are encoded in the positions of the atoms and the shape of particle, specially, in the case of catalysts and biological species. The future EM is then to be considered as a communication channel between object and observer and the images as data planes from which the 3D atom positions and the shape of the sample can be extracted quantitatively. Although, with the newest generation of Cs corrected EM's the resolution is sufficient to resolve the individual atoms and to refine their position with picometer precision. The drawbacks of high resolution TEM are two folds. First, it gives only 2D projected structural information. And second, the passband of the lens transfer at the low spatial frequencies is very poor and such that the information about shape is lost.

In my talk, I will show that how we develop a novel theory and method for incoherent and coherent TEM imaging technique to determine 3D shape of nano-object with atomic resolution. For coherent imaging, our approach is to retrieve the three-dimensional atomic structure of nanocrystals from the electron exit wave function of a single projection image. The method employs wave propagation to determine the local exit surface of a sample together with the mass of each atomic column. Intensities are scaled by the mean inner potential of the sample and single atom sensitivity is expected since aberration-corrected electron microscopes are now available with such extraordinary capabilities. The validity of the approach is tested with a simulated exit wave function of a gold wedge, as shown in the fig. 1(a) and 1(b). The fig. 1(c) shows the reconstructed tomogram for the wedge Au crystal.

For incoherent imaging, in the field of structure biology, there are two transmission electron microscopy (TEM) related techniques to reconstruct the three dimensional structure: single particle analysis and electron tomography. These two techniques rely on averaging numerous particles from many different orientations to improve the signal---to---noise ratio in cryo---mode for high resolution structural studies of biological object. They are therefore a

computational intensive techniques. Hence, there is need for a new imaging scheme to enhance the contrast and shorten the processing time. Here we present a new route to enhance the contrast by hollow cone imaging technique for biological objects using thermal diffuse scattered (TDS) electrons. Hollow cone imaging is incoherent and thus does not interfere with the central beam therefore it generates the amplitude contrast. Furthermore, the TDS signal is linear to the mass-thickness and easy to interpret and so it is suitable for soft material tomography. Here Fig. 2. we report the first results on the application of TDS to single particle analysis of proteins. The proof of the concept of the method has been demonstrated experimentally for Chaperonin GroEL as a standard protein since it is stable, easy to obtain and the structure is well-known.

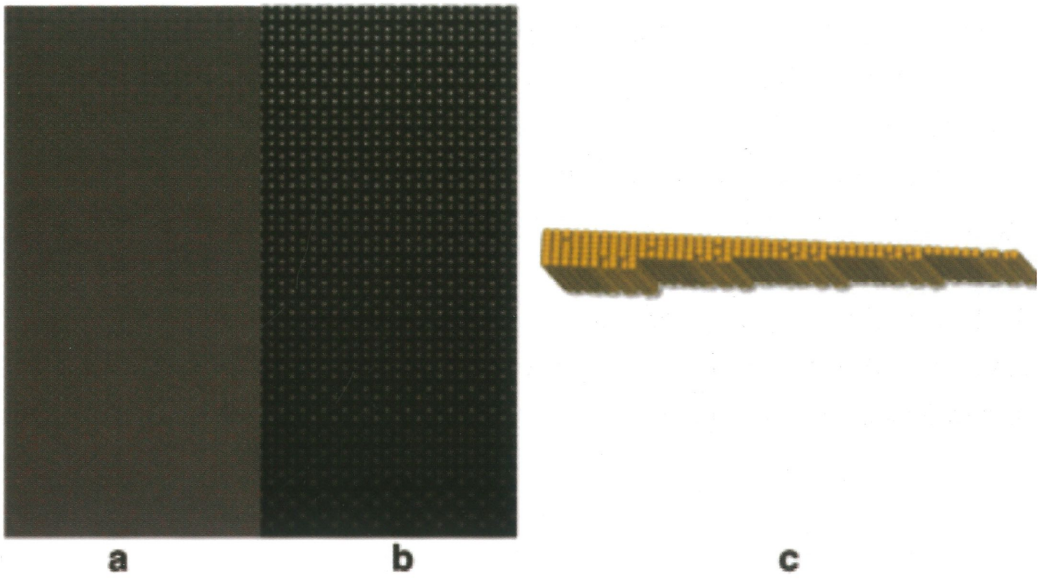

Fig. 1(a) modulus of he simulated exit wave for Au wedge crystal (b) phase of simulated exit wave of Au wedge crystal (c) reconstructed tomogram from 1(a) and 1(b).

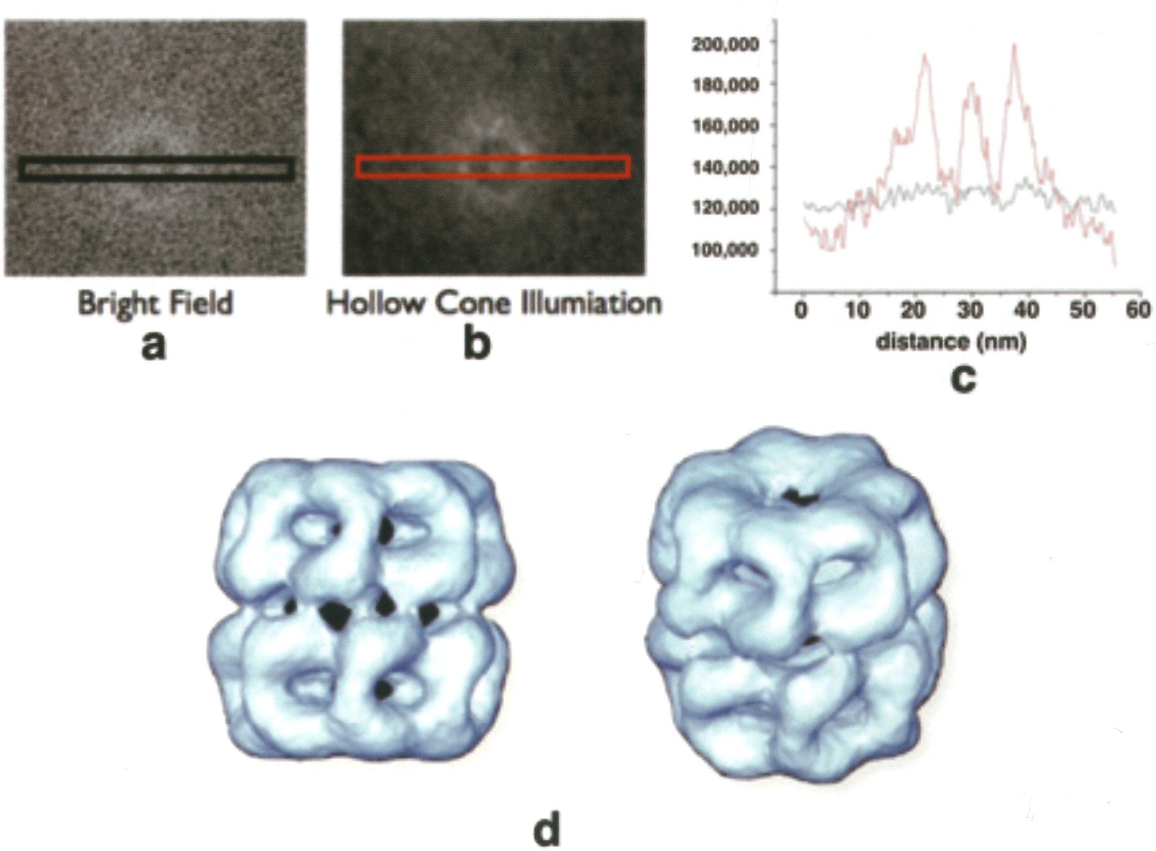

Fig. 2 (a) Bright field image of GroEL (b) Hollow cone image (HCI) of GroEl (c) Intensity profile across the image in 2(a) and 2(b)

M-O-18

TEM INVESTIGATION OF INTERPHASE PRECIPITATED NANOMETRE-SIZED CARBIDES IN THE ADVANCED LOW-ALLOY STEELS

Jer-Ren Yang (楊哲人)

Department of Materials Science and Engineering, National Taiwan University, Taipei, Taiwan

In this work, the investigation of transmission electron microscopy has elucidated the morphologies of the interphase precipitated carbides in an experimental Ti-Mo-bearing steel into three types: (1) planar interphase precipitation with regular sheet spacing (designated as PIP), (2) curved interphase precipitation with regular sheet spacing (designated as Regular CIP), and (3) curved interphase precipitation with irregular sheet spacing (designated as Irregular CIP). The planar sheets of carbides have also been analyzed and found to be oriented close to ferrite planes {211}, {210} and {111}; the results of transmission electron microscopy provide strong evidence to suggest that the development of interphase-precipitated carbides can be associated with the growth of incoherent ferrite/austenite interface by the ledge mechanism. The sheet spacing and inter-carbide spacing in the sheet have been measured and estimated in this work. The sheet spacing is found to be finer than the inter-carbide spacing in the sheet for all samples investigated. The result reflects that the distribution of interphase-precipitated carbides is anisotropic and cannot be considered random distribution. The relevance of the Orowan mechanism to the non-random distribution of interphase-precipitated carbides has been considered. The contribution of the dispersion of interphase-precipitated carbides to the yield strength of the steel studied has been estimated. It is revealed that an optimum component about 400 MPa contributed by interphase-precipitated carbides can be achieved, and the finding is consistent with the hardness data. Other examples of the different alloy steels are also addressed.

References

1. H. W. Yen, P. Y. Chen, C. Y. Huang and J. R. Yang, "Interphase precipitation of nanometer-sized carbides in a titanium-molybdenum-bearing low-carbon steel", Acta Materialia, 59(2011) pp. 6264-6274.

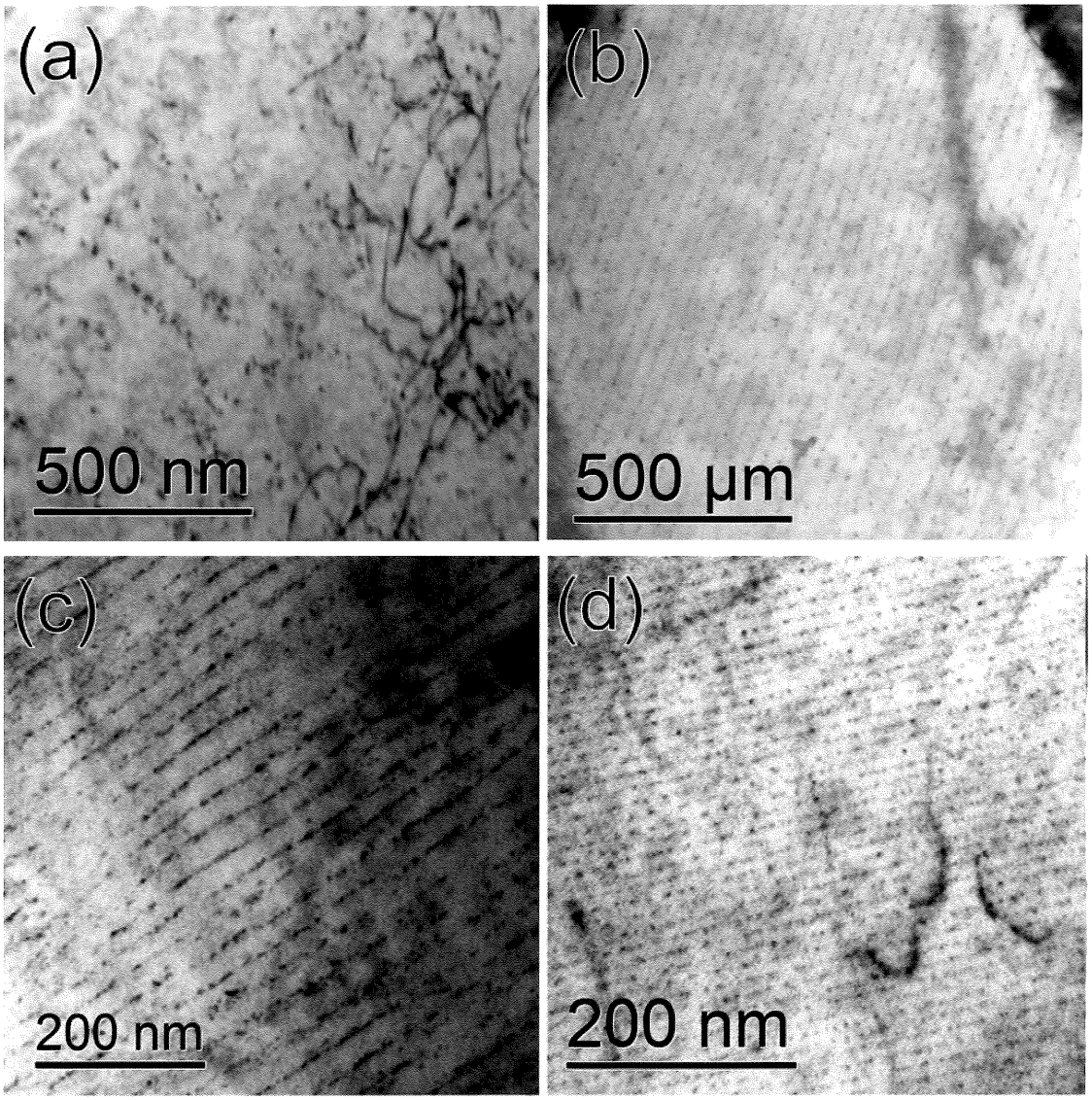

Figure 1 TEM micrographs showing (a) curved interphase precipitation with irregular sheet spacing (Irregular CIP), (b) curved interphase precipitation with regular sheet spacing (Regular CIP), (c) a mixture of PIP and Regular CIP, and (d) planar interphase precipitation with regular sheet spacing (PIP).

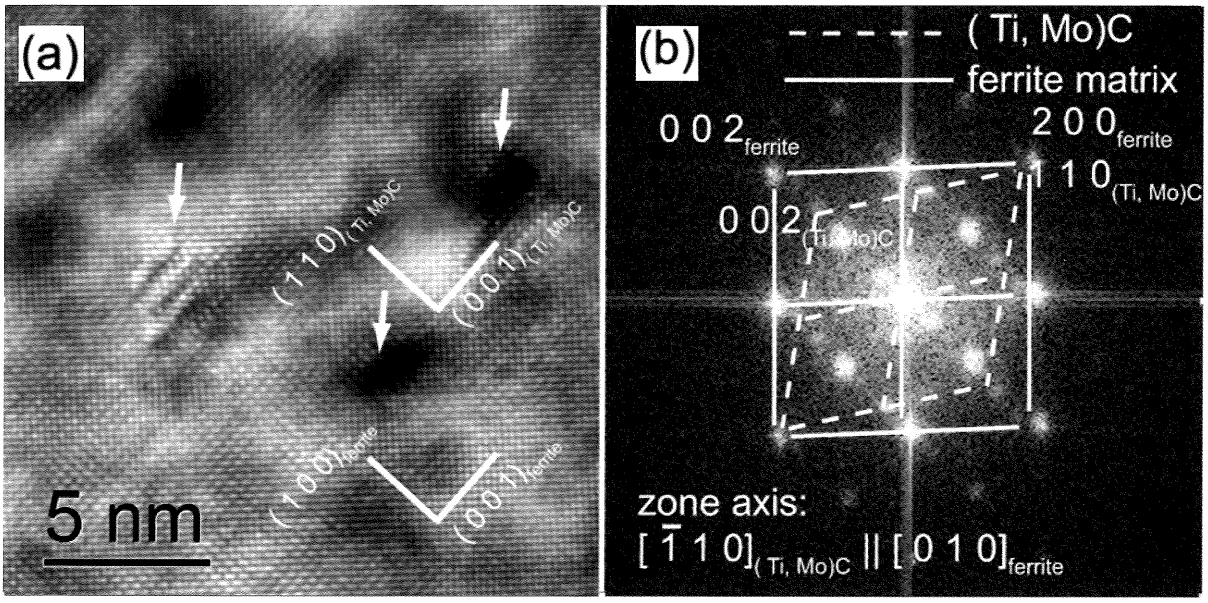

Fig.2 (a) HRTEM image of nanomerter-sized (Ti,Mo)C carbides (indicated by the arrows); (b) the corresponding fast Fourier transformed diffractogram.

B-O-1

A MINORITY SUBPOPULATION OF CD133+/EGFRVIII+/EGFR_ CELLS IN GLIOMA ACQUIRES STEMNESS AND CONTRIBUTES TO GEFITINIB RESISTANCE

Xu-Jie Liu, Wen-Tao Wu, Wei-Hua Wu, Feng Yin, Si-Hai Ma, Xiu-Xiu Liu, Yi-Nan Liu, Kai-Yu Liu, Jin-Ming Zhang, Qi-Hua* He & Li Shen

Peking University Health Science Center

Aims: To study the contribution of epidermal growth factor receptor variant III (EGFRvIII) to glioblastoma multiforme (GBM) stemness and gefitinib resistance.

Methods: CD133+ and CD133_ cells were separated from EGFRvIII+ clinical specimens of three patients with newly diagnosed GBM. Then, RT-PCR was performed to evaluate EGFRvIII and EGFR expression in CD133+ and CD133_ cells. The tumorigenicity and stemness of CD133+ cells was verified by intracranial implantation of 5 9 103 cells into immunodeficient NOD/SCID mice. Finally, cells were evaluated for their sensitivity to EGFR tyrosine kinase inhibition by gefitinib.

Results: RT-PCR results showed that the sorted CD133+ cells expressed EGFRvIII exclusively, while the CD133_ cells expressed both EGFRvIII and EGFR. At 6–8 weeks postimplantation, CD133+/EGFRvIII+/EGFR_ cells formed intracranial tumors. Cell counting kit-8 results showed that the IC50 values of the three isolated EGFRvIII+ cell lines treated with gefitinib were 14.44, 16.00, and 14.66 lM, respectively, whereas the IC50 value of an isolated EGFRvIII_ cell line was 8.57 lM.

Conclusions: EGFRvIII contributes to the stemness of cancer stem cells through coexpression with CD133 in GBMs. Furthermore, CD133+/EGFRvIII+/EGFR_ cells have the ability to initiate tumor formation and may contribute to gefitinib resistance.

References

1. Ekstrand AJ, James CD, Cavenee WK, Seliger B, Pettersson RF, Collins VP. Genes for epidermal growth factor receptor, transforming growth factor alpha, and epidermal growth factor and their expression in human gliomas in vivo. Cancer Res 1991; 51:2164–2172.
2. Ekstrand AJ, Sugawa N, James CD, Collins VP. Amplified and rearranged epidermal growth factor receptor genes in human glioblastomas reveal deletions of sequences encoding portions of the N- and/or C-terminal tails. Proc Natl Acad Sci USA 1992;89:4309–4913.
3. Nishikawa R, Ji XD, Harmon RC, et al. Huang, A mutant epidermal growth factor receptor common in human glioma confers enhanced tumorigenicity. Proc Natl Acad Sci USA 1994;91:7727–7731.

4. Feldkamp MM, Lala P, Lau N, Roncari L, Guha A. Expression of activated epidermal growth factor receptors, Ras-guanosine triphosphate, and mitogen-activated protein kinase in human glioblastoma multiforme specimens. Neurosurgery 1999;45:1442–1453.
5. Lammering G, Hewit TH, Valerie K, et al. EGFRvIIImediated radioresistance through a strong cytoprotective response. Oncogene 2003;22:5545–5553.
6. Singh SK, Hawkins C, Clarke ID, et al. Identification of human brain tumour initiating cells. Nature 2004;432:396–401.
7. Yuan X, Curtin J, Xiong Y, et al. Epidermal growth factor receptor variant III contributes to cancer stem cell phenotypes in invasivebreast carcinoma. Cancer Res 2012;72:2657–2671.
8. Visvader JE, Lindeman GJ. Cancer stem cells: Current status and evolving complexities. Cell Stem Cell 2012;10:717–728.

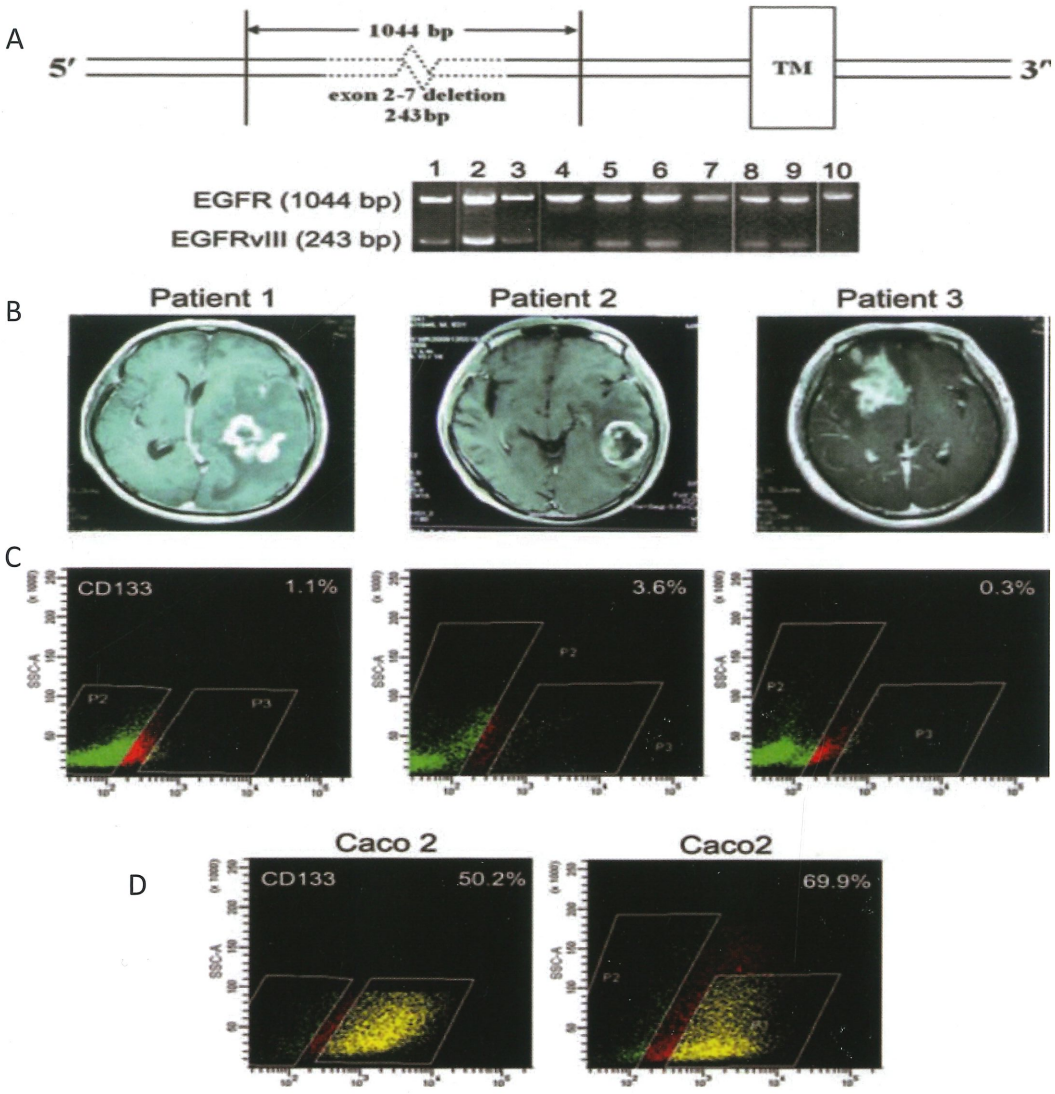

Figure 1 RT-PCR results showed that all 10 GBM clinical specimens were wild-type EGFR+, and eight of the 10 were EGFRvIII+ (A). Lanes correspond to the patient number. DNA fragments of 1044 bp and 243 bp in size represented EGFR and EGFRvIII, respectively. MRI showed space-occupying lesions in all three patients (B). Patient No. 1. Spaceoccupying lesions were located in the left temporal lobe rear, and the midline structure shifted right. Patient No. 2 showed a class round abnormal signal shadow, and rich blood supply space-occupying lesions were located inthe left temporal lobe rear. Patient No. 3 showed space-occupying lesions in the right frontal lobe, the right lateral ventricle was compressed by the tumor, and the midline structure shifted left. Flow cytometric analysis showed that the percentages of CD133+ cells from each patient were 1.1%, 3.6%, and 0.3% (C). The Caco2 cell line with CD133 overexpression was used as a positive control (D).

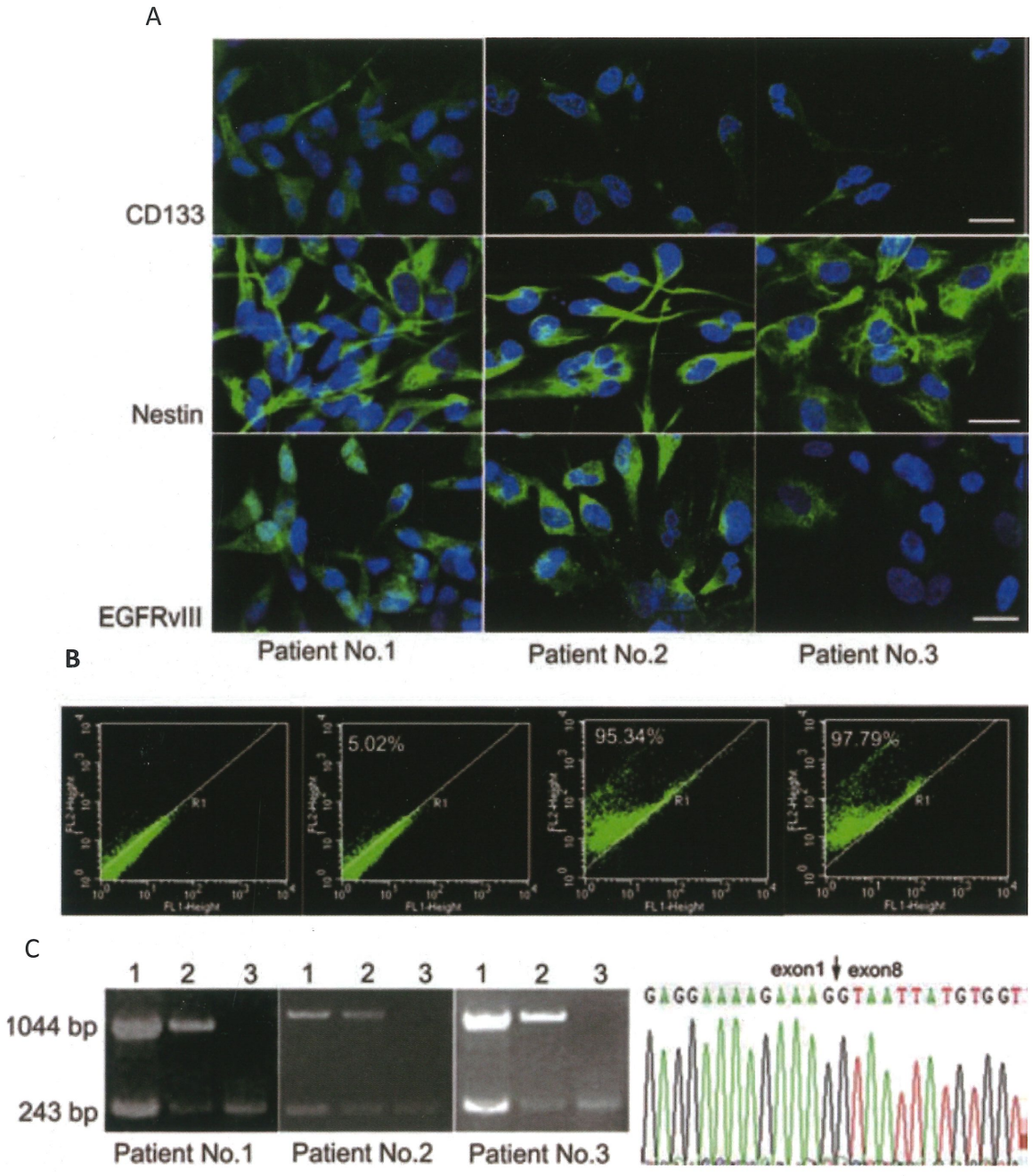

Figure 2 The results of immunofluorescence assays showed that CD133, nestin, and EGFRvIII were all expressed in cells derived from the three patient specimens (A). For cells from Patient No. 1, the percentages of CD133 cells were 95.34% and 97.79% after initial and secondary MACS was performed, respectively. (B). The first left panel is the blank control, and the second left panel is the isotype control using IgG instead of the anti-CD133 antibody as the primary antibody. The sorting results of cells from Patient No. 2 and 3 are not shown here. RT-PCR results showed that CD133+ cells were EGFRvIII+ but EGFR_ (C). Lanes 1 and 2, corresponding to primary nonsorted cells and sorted CD133_ cells, respectively, showed two bands including EGFR (1044 bp) and EGFRvIII (243 bp), while CD133+ cells in lane 3 only showed the 243-bp band. Sequencing results confirmed expression of the EGFRvIII gene.

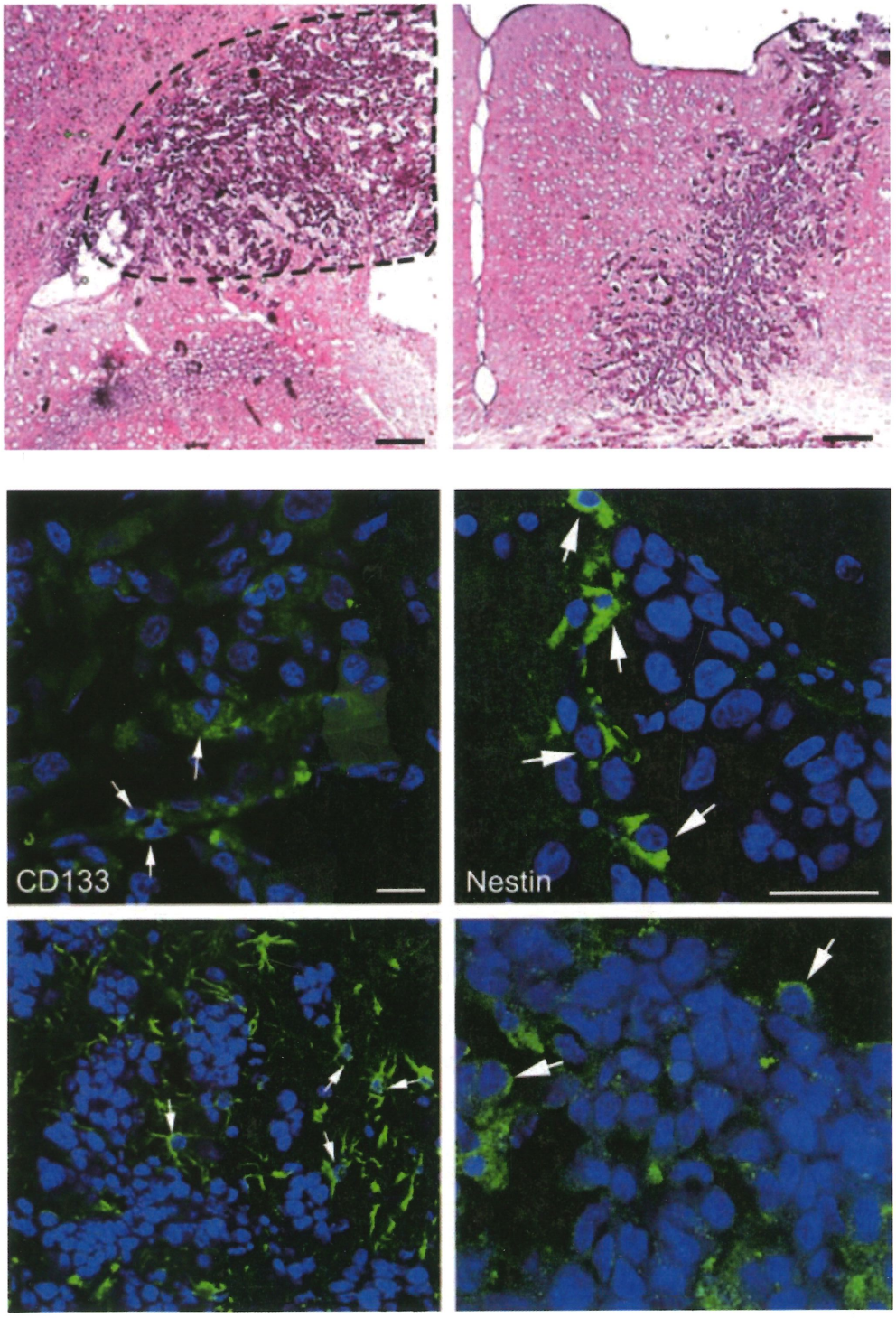

Figure 3 H&E staining of the brain tissues of NOD/SCID mice. Space-occupying lesions in the area between the cerebral cortex and dorsal hippocampus CA3, as well as many atypical and prominent nuclei, were found in highmagnification D, and F, 200 lm; E, 40 lm).

B-O-2

CURRENT ADVANCE OF CRYO ELECTRON MICROSCOPY IN REACHING SUB-NANOMETER RESOLUTION PROTEIN STRUCTURES

[157]CHANG, Wei-Hau (章為皓), [2]LIN, Frank (林全信), [3]CHEN, Fu-Rong (陳福榮), [4]MURATA, Kazuyoshi (村田和義), [4]NAGAYAMA, Kuniaki (永山國昭), [5]WANG, Chun-Hsiung (王俊雄), [5]WU, Yi-Min (吳逸民), [5]CHANG, Jen-Wei (張荏韋), [5]HUANG, Shih-Hsin (黃士炘), [6]HSIEH, Dai-Ni (謝岱霓), [6]TU, I-Ping (杜憶萍), [7]CHEN, Yi-Yun (陳怡云), [7]HWU, Yeukuang (胡宇光), [7]Li, Neil (李柏南), [7]Li, Ting-Kuo (李定國)

[1]Department of Biochemical Science and Technology, National Taiwan University, Taipei, Taiwan
[2]Department of Marine Science, National Sun Yat Sen University, Kaohsiung, Taiwan
[3]Department of Engineering System, National Tsing-Hua University, Hsinchu, Taiwan
[4]Divion of Structural Biology, National Institutes of Physiology, Okazaki, Japan
[5]Institute of Chemistry
[6]Institute of Statistics and [7]Institute of Physics, Academia Sinica, Taipei, Taiwan

Single Particle cryo electron microscopy (Cryo-EM) has emerged as a powerful tool in revealing near atomic resolution structures, as mainly demonstrated by Hong Zhou at UCLA and other researchers in USA. The strategy of these groups use is to study icosahedral virus reconstruction to overcome the SNR limit imposed on the images due to radiation damage issue and the results were obtained by very stable and expensive 300 kV field-emission microscope. In Taiwan, though we only have only 200 kV field emission machines, we have demonstrated it is possible to reveal 4 Angstrom structure by using a cutting-edge motion-free camera. In this presentation, we will report two icosahedral virus structures, one abundant in beta-sheet and the other in alpha-helix. Furthermore, to overcome the challenges of obtaining sub-nanometer resolution structure of protein complexes without symmetry, we have formed a consortium with Fu-rong Chen and Nagayama (Okazaki) to boost the SNR with phase plates and with statisticians and theoretical physicists to develop efficient de-noising algorithm.

References

1. J. Shiue, C.-S. Chang, S.-H. Huang, C.-H. Hsu, J.-S. Tsai, W.-H. Chang, Y.-M. Wu, Y.-C. Lin, P.-C. Kuo, Y.-S. Huang, Y. Hwu, J.-J. Kai, F.-G. Tseng and F.-R. Chen (2009), *Journal of Electron Microscopy, 58（3）*
2. C. Wang, C. Hsu, Y. Wu, Y Luo, M. Tu, WH Chang, RH Cheng, CS Lin (2010) *Virus Genes. 41(1):73-80*
3. YM Wu, CH Wang, JW Chang, YY Chen, N. Miyazaki, K. Murata, K. Nagayama5 and WH Chang (2013) *J. Phys. D:* Appl. Phys. 46 494008

B-O-3

EXPLORING THE POLYMER FORM OF ARABIDOPSIS HISTONE DEACETYLASE 6 BY ELECTRON MICROSCOPY TO REVEAL ITS COMPOSITION

[1]Wang, Wen-Jiun (王雯君) and [1,2*]Cheng, Yi-Sheng (鄭貽生)

[1]Institute of Plant Biology, National Taiwan University, Taipei, Taiwan
[2]Department of Life Science, National Taiwan University, Taipei, Taiwan

The *Arabidopsis thaliana* histone deacetylase 6 (AtHDA6) has diverse roles to regulate genome stability, development status and environmental stress responses in plants. In this study, we used recombinant protein of AtHDA6 as a guide to reveal AtHDA6 protein structure in a large polymer form. Transmission electron microscopy (TEM) was used to collect the images of AtHDA6 and the image results of AtHDA6 showed that is spherical with a ~25 nm object. For functional assays, we identified different expression patterns of HDAC activity between the endogenous and recombinant HDA6 proteins. Furthermore, mass spectrometry data showed that two phosphorylation sites in AtHDA6 has been identified in the C-terminal region of the protein. In summary, our results could provide an experimental basis for plant HDAC structures and would investigate the mechanisms of how PTMs manipulate HDAC enzymatic activity.

References

1. A. Brandl, T. Heinzel and O. H. Kramer. (2009) Histone deacetylases: salesmen and customers in the post-translational modification market. Biol Cell 101: 193-205
2. J. M. Kim, T. K. To and M. Seki (2012) An epigenetic integrator: new insights into genome regulation, environmental stress responses and developmental controls by Histone Deacetylase 6. Plant Cell Physiol 53: 794-800

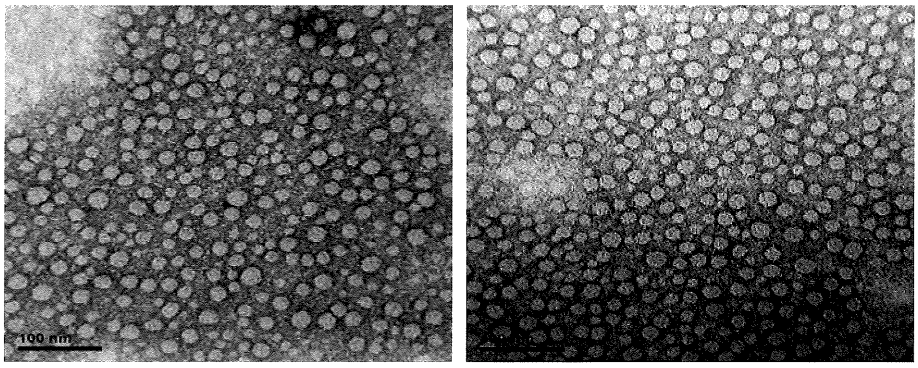

A

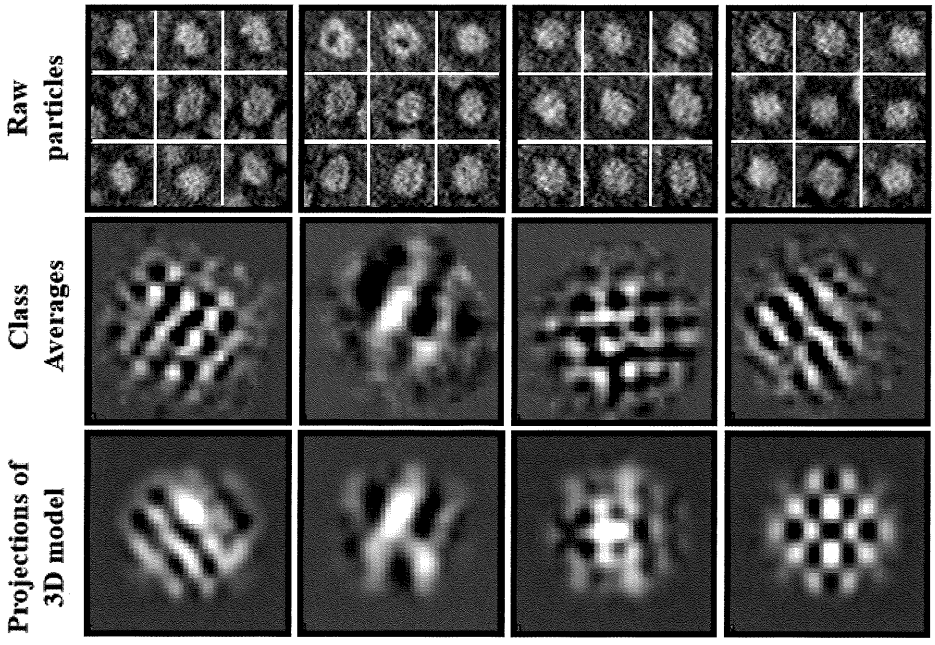

B

Figure 1. Examination of AtHDA6 protein superstructure by Transmission Electron Microscopy (TEM). (A) A representative area of a CCD image of AtHDA6 particles. Particles are circular or oval. (B) Three representative views of selected and windowed raw particles of AtHDA6 (top column) and their class averages (middle column) were compared to their corresponding views of the same projections in 3D model of AtHDA6 (bottom column).

B-O-4

PROBING ORGANELLE QUALITY CONTROL BY LIGHT

YANG, WEI YUAN (楊維元)

Institute of Biological Chemistry, Academia Sinica, Taipei, Taiwan

Autophagy is a trafficking process that enables eukaryotic cells to transport cytoplasmic materials into lysosomes for recycling and degradation, and one of its prominent functions is the selective elimination of dysfunctional organelles. This allows cells to rid themselves of unwanted stress to maintain health and avoid the activation of cell death. One vivid example of this is Parkin-mediated mitophagy: mitochondria defective in protein import results in their selective elimination through the autophagic machinery. The lack of proper mitophagy has been implicated as one cause of Parkinson's disease. Autophagy is therefore a vital strategy for cellular quality control of organelles. Here I will discuss the prospect of utilizing organelle-specific photosensitizers to probe these processes inside living cells.

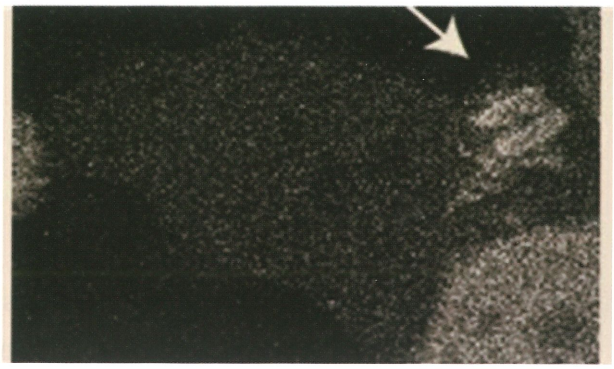

Figure 1. A cell undergoing Parkin-mediated mitophagy at a spatially restricted site (white arrow) upon light-activation.

B-O-5

ARCHITECTURAL MAPPING OF PRIMARY CILIA USING SUPERRESOLUTION MICROSCOPY

[1]YANG, Tony Tung-Lin (楊東霖) and [1]LIAO, Jung-Chi (廖仲麒)

[1]Institute of Atomic and Molecular Sciences, Academia Sinica, Taipei, Taiwan

Recent studies have identified important regulating elements for transition zone (TZ) gating in cilia. However, the architecture of the TZ region and its arrangement relative to intraflagellar transport (IFT) proteins remain largely unknown, hindering the mechanistic understanding of the regulation mechanisms. One of the major challenges comes from the tiny volume at the ciliary base packed with numerous proteins, with the diameter of the TZ close to the diffraction limit of conventional microscopes. Using a custom-built stimulated emission depletion (STED) superresolution microscope, we revealed relative localizations of TZ proteins, IFT proteins, transition fiber (TF) proteins, and centriole proteins. We found Tctn2 at the outmost periphery of the TZ close to the ciliary membrane, with Tmem67 adjacent to it. RPGRIP1L was localized toward the axoneme at the same axial level as Tctn2 and Tmem67. Surprisingly, Cep290 was localized at the proximal side of the TZ close to the distal end of the centrin-labeled basal body. The lateral width was unexpectedly close to the width of the basal body, distant from the potential Y-links region of the TZ. IFT88 was also surprisingly distributed in two distinct patterns, forming three puncta or a Y shape at the ciliary base (Figure 1). Two proximal puncta of the three puncta pattern were localized at the proximal side of TF protein, while one distal punctum was localized at the distal side of RPGRIP1L. The Y-shaped pattern also had its distal punctum at the same location as the distal punctum of the three-puncta pattern. Perturbation of cell growth conditions causes changes in the distribution patterns of IFT88, shedding light on the regulation of IFT passage through the TZ.

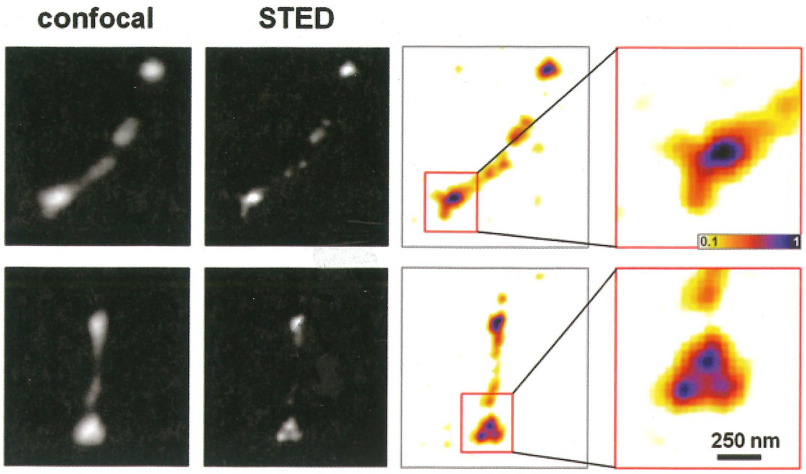

Figure 1. Superresolution STED imaging revealing novel multiple distribution patterns of IFT88 in primary cilia of human fibroblasts. Confocal images showed high intensity clusters of immunolabeled IFT88 at the basal end of primary cilia. These images lacked the resolution to properly characterize the structural differences among these clusters. Corresponding STED images illustrate distinguishable distribution patterns of IFT88. After 48-hour serum starvation, about 74% (N = 28) of primary cilia possessed a branched pattern of IFT88 (upper panels) where a bright punctum was connected to two branches toward the basal end with an angle to the axoneme direction. About 26% (N = 10) of primary cilia possessed a three-puncta pattern (lower panels) forming a triangle at the basal end of the primary cilia.

B-O-6

MULTI-HARMONIC GENERATION MICROSCOPY FOR IN VIVO VIRTUAL BIOPSY IMAGING OF HUMAN SKIN

[1,2]SUN, Chi-Kuang (孫啟光)

[1]Molecular Imaging Center, National Taiwan University, Taipei, Taiwan
[2]Department of Electrical Engineering and Graduate Institute of Photonics and Optoelectronics, National Taiwan University, Taipei, Taiwan

Virtual biopsy techniques, for imaging cells and tissues at microscopic details capable of differentiating benign from malignant lesions non-invasively, are highly desirable. Without removing tissues, in vivo virtual biopsy not only avoids or minimizes the various disadvantages associated with the physically invasive biopsy procedure, but also reduces the cost and time for traditional pathological decision. Optical virtual biopsy could also potentially provide a more comprehensive bedside non-invasive total lesion scanning for improved clinical disease classification and therapeutic guidelines, and a feasible way for continuous disease monitoring during and after treatment.

We have recently successfully developed a state-of-the-art optical virtual biopsy system based on the least invasive multi-harmonic generation microscopy (HGM) [1-6]. The system aimed to detect subclinical life-threatening disease and to assist diagnostic decision making for clinically evident diseases. Pre-scanning of the lesion with this system also reduces sampling errors in physical biopsy and helps surgeons to determine the safety margins. In this talk, I will review our recent effort to clinically [4-6] evaluate the potential of the developed HGM biopsy system to differentiate malignancy from normal tissues. Our in vivo clinical study indicated that the multi-harmonic generation biopsy system outperforms current confocal and two-photon based techniques in providing higher penetration depth, higher spatial resolution, minimized photodamage and phototoxicity, reduced dye-toxicity due to minimized use of external fluorophores, and lowest photobleaching. This system enables 3D subsurface imaging in vivo without the need for surgical approach.

This work is sponsored by National Health Research Institute of Taiwan.

References

1. S.-W. Chu, *et al.*, Opt. Lett. 26 (2001) 1909.
2. C.-K. Sun, *et al.*, Opt. Lett. 28 (2003) 2488.
3. S.-P. Tai, *et al.*, *Advanced Materials* 19 (2007) 4520.
4. S.-Y. Chen, *et al.*, *IEEE J. Sel. Top. Quant. Electron.* 16 (2010) 478.
5. Y.-H. Liao, *et al.*, *Biomed. Opt. Express* 4 (2013) 77.
6. M.-R. Tsai, *et al.*, *J. Biomed. Opt.* 19 (2014) 036001.

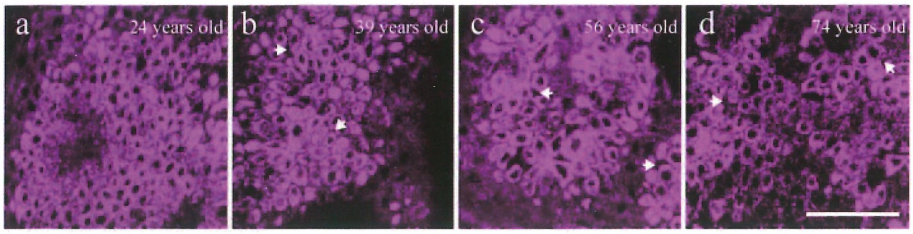

Figure 1. Four representative *in vivo* third harmonic generation (THG) images of epidermal basal cells obtained from the volar forearm of (a) 24-, (b) 39-, (c) 56-, and (d) 74-year-old volunteers. The widened THG-dark intercellular spaces between basal keratinocytes were indicated by arrows in (b-d). Scale bar = 50 μm.

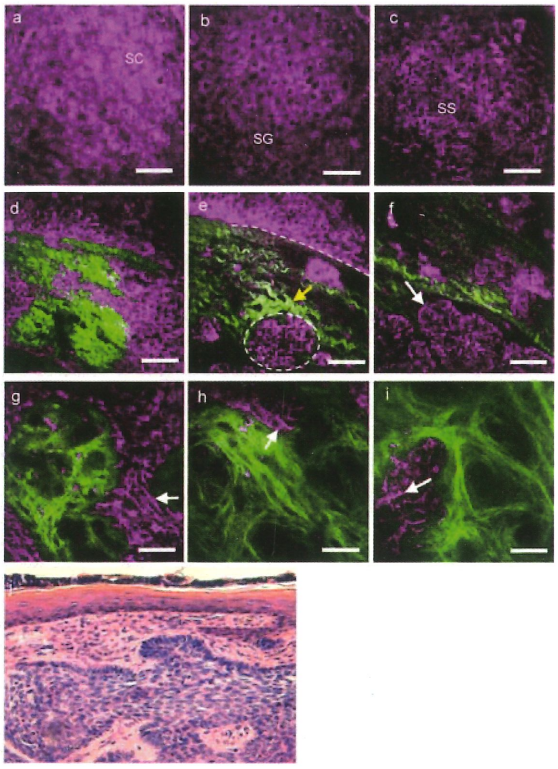

Figure 2. (a)-(f) A representative series of *in vivo* HGM images of a case of basal cell carcinoma (BCC) at different depths relative to the surface (5, 25, 40, 60, 75 and 90 μm) revealed proliferation of polymorphous THG-bright tumor cells from the stratum basale (d) and continuously extended into the dermis (dashed circle; e) from one BCC patient. Several tumor nests (arrow; f) were found in the dermis. The tumor cells appeared irregular, elongated, and peripheral palisaded (dashed line; e). Collagen bundles (yellow arrow; e) surrounding the tumor nests were more thickened and coarse than the normal counterpart. A characteristic feature noted was the presence of a large number of cells with dendritic processes (arrow; f) and the feature also can be found from the other patient with deeply invasive BCC at different depths relative to the surface (80, 150, and 270 μm) (arrows; g-i). SC, stratum corneum; SG, stratum granulosum; SS, stratum spinosum. Bars = 50 μm.

B-O-7

EFFECTS OF TOUGU XIAOTONG CAPSULE ON KNEE MORPHOLOGY IN RABBITS WITH KNEE OSTEOARTHRITIS

CHEN WENLIE (陳文列)*, HUANG YUNMEI (黃雲梅), LIN RUHUI (林如輝), CHEN SAINAN (陳賽楠), HUANG MEIYA (黃美雅), WU GUANGWEN (吳廣文), LI XIHAI (李西海), WU ZHUILE (吳追樂),LI ZUANFANG (李鑽芳), LIAO NAISHUN (廖乃順), LI XIAODONG (李孝棟) and LIU XIANXIANG (劉獻祥)

[1]Fujian Academy of Integrative Medicine
[2]National Laboratory of Traditional Chinese Medicine Pharmacology (Cell structure and function)
[3]Fujian Key Laboratory of Integrative Medicine on Geriatrics, Fujian University of Traditional Chinese Medicine, Fuzhou 350122, China

Tougu Xiaotong capsule (TGXTC) can reduce the symptoms of osteoarthritis (OA). Using a rabbit model of knee osteoarthritis, we determined the effects of TGXTC in the subchondral bone, and then explored its protective role in both cartilage and subchondral bone. The three experimental groups included a normal control, osteoarthritis model and TGXTC groups. After drug administration, the tibia and femur were harvested for observation of cartilage by light microscopy and transmission electron microscopy and of subchondral bone by micro-CT, transmission and scanning electron microscopy. We found moderate to severe cartilage injury in the model group, with increased subchondral bone trabecular number and thickness, subchondral sclerosis. Compared with the model group, the TGXTC groups had significantly mitigated cartilage injury, reduced trabecular number and thickness, and accelerated trabecular separation. These results suggest that TGXTC can mitigate cartilage injury and subchondral sclerosis and delay the pathological development of osteoarthritis.

Foundation: This study was supported by the Key Project of Fujian Province Department of Science and Technology (No.2012Y4006), the Natural Science Foundation of Fujian Province (No. 2014J0101-13141146), the Developmental Fund of CHEN Keji Integrative Medicine (No.CKJ2011004) and the National Natural Science Foundation of China (No.81202712).

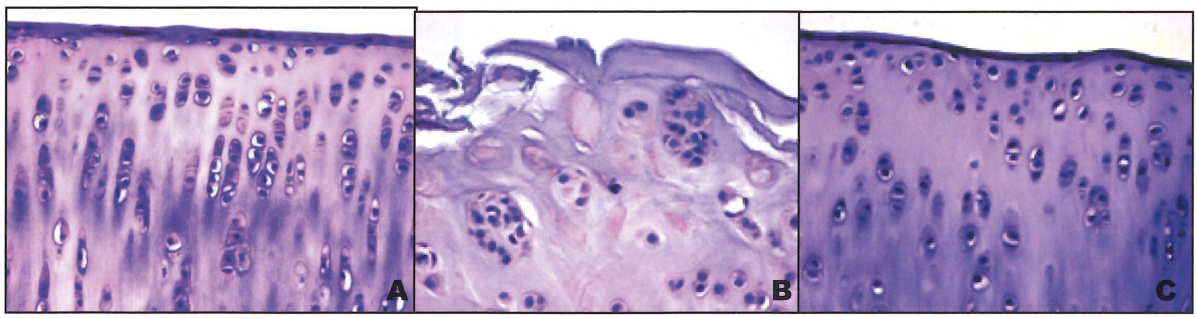

Figure 1. Cartilage microstructure. HE staining, LM. (A) Normal control., (B) OA model, (C) TGXTC groups.

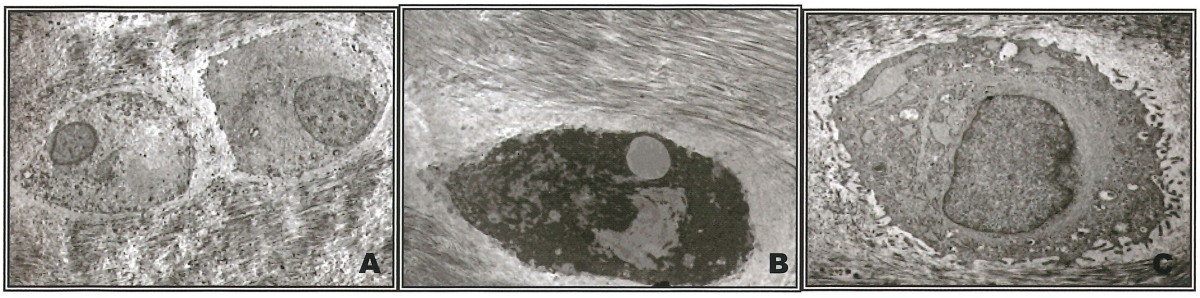

Figure 2. Cartilage ultrastructure. TEM. (A) Normal control., (B) OA model, (C) TGXTC groups.

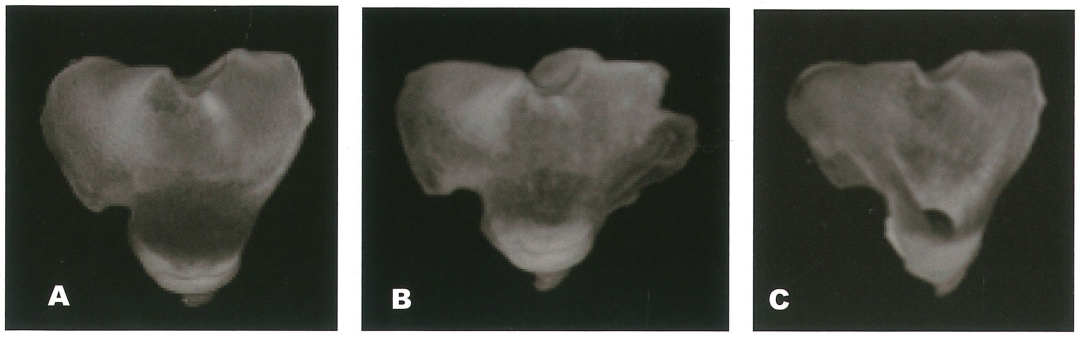

Figure 3.Tibial platform structure. Micro-CT. (A) Normal control., (B) OA model, (C) TGXTC groups.

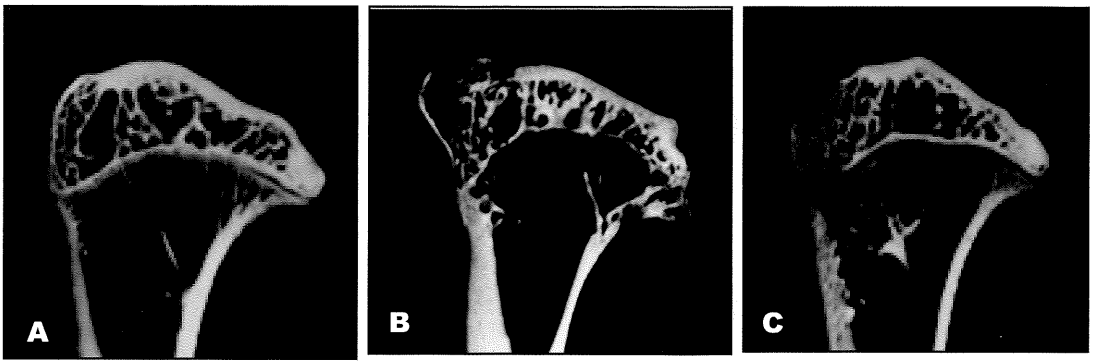

Figure 4. Subchondral bone structure. Micro-CT. (A) Normal control., (B) OA model, (C) TGXTC groups.

Figure 6. Subchondral bone microstructure. SEM. (A) Normal control., (B) OA model, (C) TGXTC groups.

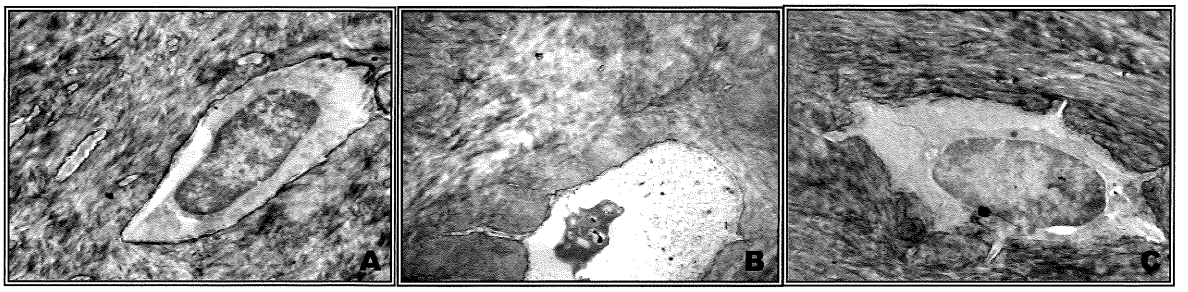

Figure7. Ultrastructure of Bone cell in Subchondral bone. TEM. (A) Normal control., (B) OA model, (C) TGXTC groups.

B-O-8

IN SITU VISUALIZING T-TUBULE/SR JUNCTION REVEALS NOVEL ARRANGEMENT OF RYANODINE RECEPTOR-1 USING ELECTRON TOMOGRAPHY

Yongji Yang *, Xiaowei Song, Ying Tang, Changhai Lei, Mi Cao, Yafeng Shen

Department of Biophysics, Second Military Medical University, 800 Xiangyin Road, Shanghai 200433, China

Background, Membrane-integral proteins are critical executants of life activities. It is still lack of efficient technologies to determine the structures and arrangement of membrane-integral proteins in their native phospholipid-bilayer environment. Here, we confirmed the possibility of using Cryo-Electron Tomography to visualize ryanodine receptor-1 (RyR1) in its close-to-life state. **Results**, We found that RyR1 was distributed in subregion of sarcoplasmic reticulum (SR) membrane, where T-tubule was most closely neighboring. Interestingly, we visualized the relationship between RyR1 and SR membrane for the first time, showing that most mass of RyR1, in umbrella-shape, was exposed to SR, whereas only a small portion, in stalk-shape, was exposed to the cytoplasic environment. Based on this observation, we established a new modulating model of RyR1, in which, we postulated that dihydropyridine receptor (DHPR) directly interacted with the stalk-shaped part of RyR1, while FK-506 binding protein 12 kDa (FKBP12) directly interacted with the umbrella-shape of RyR1 to regulate the process of calcium releasing from SR during excitation-contraction coupling. **Conclusions**, Electron Tomography could be used as an efficient method to determine the structure and arrangement of single membrane-integral protein within intact cells in its native context of membranes, SR, vesicles and other molecular complexes.

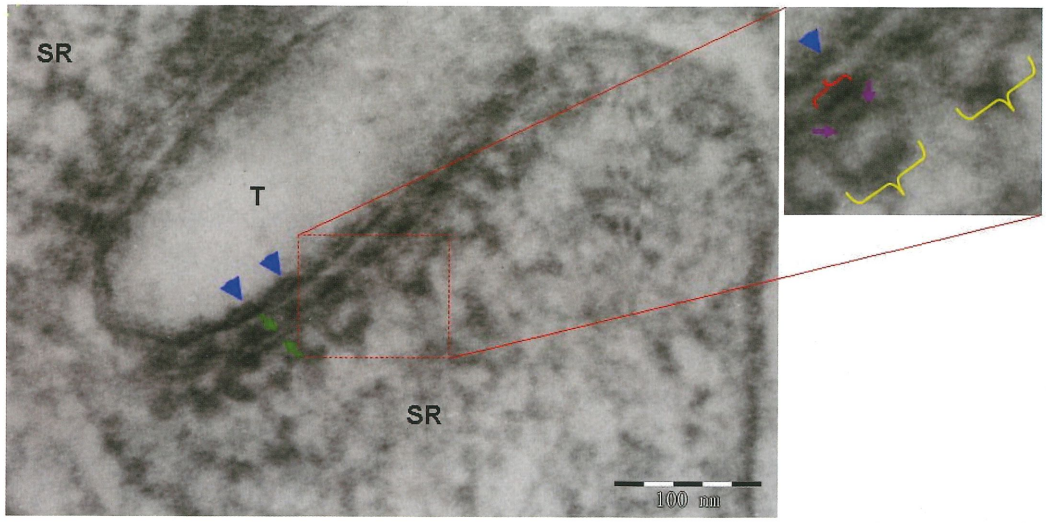

Figure 1. *In situ* visualizing the T-Tubule/Sarcoplasmic Reticulum junction in 2 dimensional picture using Electron Microscopy. The T-Tubule membrane and Sarcoplasmic Reticulum membrane was closely neighboring with each other. In SR membrane, Ryanodine receptor-1 was embedded and adopted the shape of a mushroom at the size of 25-34 nm averagely. (Bar=100nm)

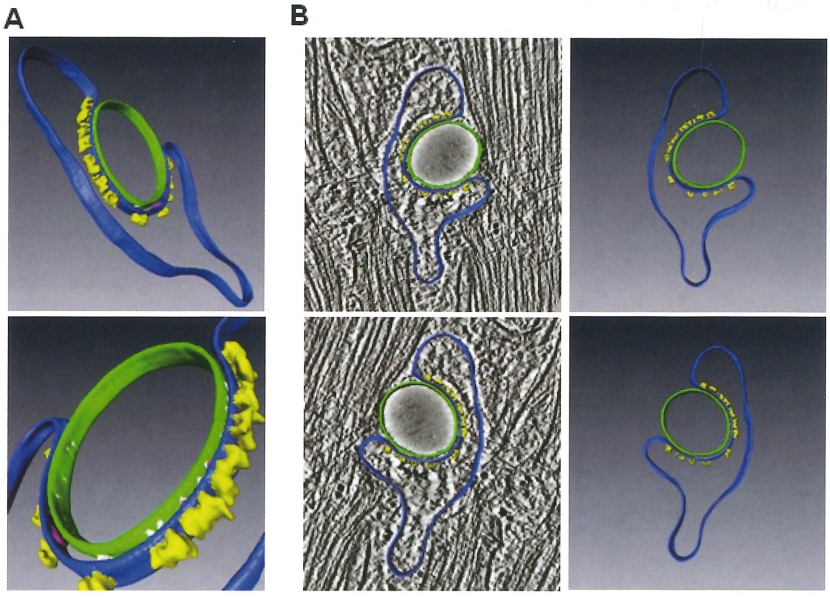

Figure 2. Surface-rendered views of the final 3D map of the T-Tubule/SR junction from different direction using IMOD software construction. The density fitting usage of computational methods combined with Electron Tomography showed whole structure of T-Tubule/SR junction. (A) Most mass of RyR1 was observed to be placed in the SR membrane from the top view of the SR face. (B) From side view of the cartoons, RyR1 embedded in SR membrane and adopted a mushroom shape in whole. The umbrella-shaped assembly of RyR1 was exposed to SR environment, whereas stalk-shaped part was embedded in the SR membrane and exposed to the cytoplasm.

B-O-9

INITIATION CELLS OF CLONAL PLANTLETS IN THREE SPECIES OF CRASSULACEAE

Jiansheng Guo, Yangyang He, Xianghuan Cui, Xiling Du, Jian Zhu*

Department of Molecular and Cell Biology, School of Life Science and Technology, Tongji University, Shanghai 200092, China.

Abstract: During regenerated process, the initiation cells from different organs can be reprogrammed to produce new individual, a process that requires coordination of cell cycle reactivation with acquisition of other cellular morphological characteristics. However, the factors that influence the variety of regeneration have not been determined yet. Here, we report the regeneration of *Kalanchoe daigremontiana*, *Graptopetalum paraguayense* and *Crassula portulacea* and analyze the effect of the initial cells of regeneration to the formation of buds and plantlets in three species in Crassulaceae. Some samples prepared by high pressure freezing and freeze substitution. In addition, the roles of WUSCHEL (WUS) and CUP-SHAPED COTYLEDON 1(CUC1) in the regeneration of these three species are analyzed through qRT-PCR during development of buds. Our results indicated that the pre-existing stem cell-like cells in the position of regeneration of *Kalanchoe daigremontiana*, *Graptopetalum paraguayense* and *Crassula portulacea* are responsible for the formation of buds and plantlets. They have arrested in different phases of the cell cycle and show different cell morphological characteristics and cell counts. The accumulation of auxin and cytokinin in the position where buds formed indicated a very important function, special for the cell cycle reactivation and different demand during regeneration in three species. These differences in three species may influence the pattern and the complexity of asexual reproduction in these three species in Crassulaceae. In summary, the research on initiating cells in the three species leaded us to believe the pre-existing stem cells in plant played an important

role in asexual reproduction. The morphological structure, cell cycle and sensibility of plant hormone to initiating cells may reflect their different states, and could start asexual reproduction under the stimulus enough. Taking the number, differentiated degree and demand to plant hormone of the three initiating cell types into consideration, we believed that more initiating cells, lower differentiated degree and appropriate hormone were conducive to asexual reproduction. In addition, the enrichment of WUS and CUC1 during asexual reproduction suggested their positive role in the development of plantlets. Our studies compared the origination of asexual reproduction in three Crassulaceae species and provided abundant theoretical data for the origin and development of asexual plantlets.

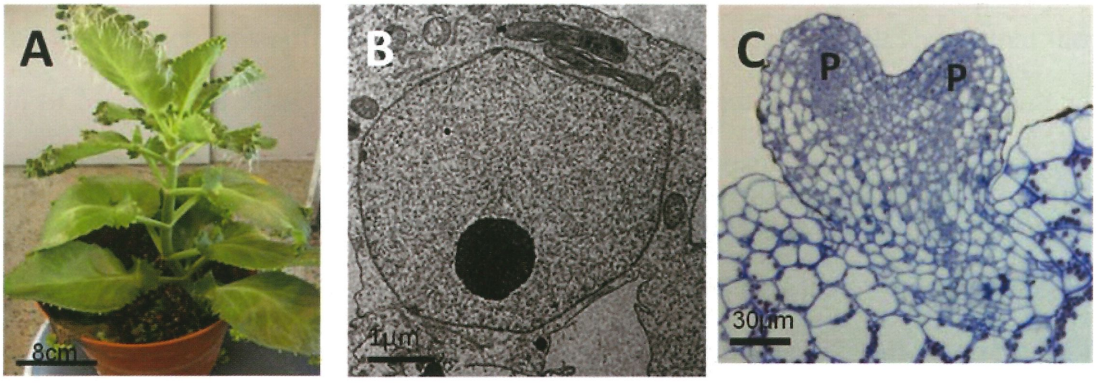

A- *Kalanchoe daigremontiana;* B-Ultrastructure of an itiation cell; C-A section of Bud

D-*Graptopetalum paraguayense;* E-Adventitious buds at the base of the leaf; F-The ultrastructure of an initiated cell

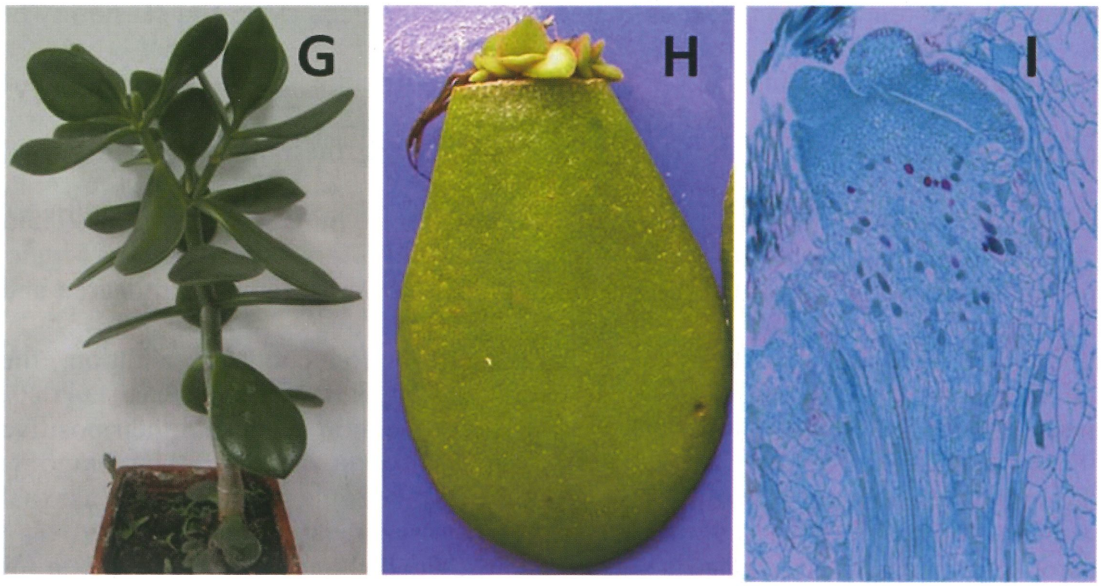

G-*Crassula portulacea;* H-Adventitious buds; I-A section of the bud

B-O-10

RESEARCH ON INFECTIOUS PROCESS OF MAIZE CHLOROTIC MOTTLE VIRUS BY TRANSMISSION ELECTRON MICROSCOPE

WANG, Chun-Yan (王春艳), WANG, Qiang（王強）,LI, Zhen-He (李正和), HONG, Jian (洪健)

Institute of Biotechnology, Zhejiang University, Hangzhou 310058, China

Maize chlorotic mottle virus (MCMV) is the only member of the *Machlomovirus* genus in the family of *Tombusviridae*[1]. It can replicate in a large scale in the plant cells when it infects the maize. The cytopathology of MCMV is analyzed by observing the electron microscope images by conventional sample preparation method and the possible assembly process is speculated. It is found that there is a large number of fibrous material located in the mitochondria and to a certain period, the fibrous material is released into the cytoplasm resulted from the collapse of the mitochondria. Software prediction result shows that the coat protein of MCMV has 99% possibility to be located in the mitochondria. Thus, Immunogold labeling technology is utilized to verify the hypothesis using the specific mono-clonal antibody against the MCMV virions. The multivesicular bodies derived from the peroxisomes are also found in the mesophyll cells of maize leaves infected by MCMV which is reported to be the replication sites for some other positive-strand RNA viruses [2]. Unique to MCMV, the vesicles in the multivesicular bodies have different sizes and the bigger ones are filled with obvious amorphous substance, which is speculated to be the nucleic acid in replication. Immunogold labeling technology is utilized to further confirm the result by labeling the dsRNA with J2 monoclonal body, which can bind dsRNA specifically. In addition, numberous proliferation of membranes was observed in the MCMV infected plant tissues and complete MCMV virions are detected in vesicles, which thus are speculated to be the assembly location of MCMV virions before the viruses are released into the cytoplasm.

References

1. King AMQ, Lefkowitz E, Adams MJ, Carstens EB. Virus Taxonomy: Ninth Report of the International Committee on Taxonomy of Viruses. Vol 9. San Diego, CA: Elsevier Academic Press; 2011. pp. 256–267.

2. Kopek BG1, Perkins G, Miller DJ, Ellisman MH, Ahlquist P. Plos Biology. Vol 5. Issue 9.2007.pp.2022-2034.

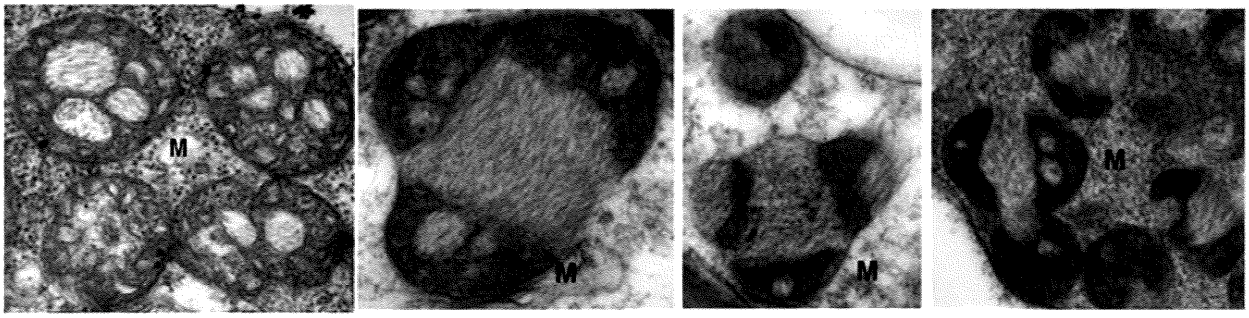

Figure 1. Hypothesis of the release process of the fibrous material from mitochondria into the cytoplasm (A) Early stage of the production of the fibrous materials in the mitochondria (B) Fibrous materials are accumulated in the distorted mitochondria (C) Mitochondria is filled with fibrous materials but still with integrity(D)Mitochondria is broken and the fibrous materials are released into the cytoplasm. Mitochondria is marked by M.

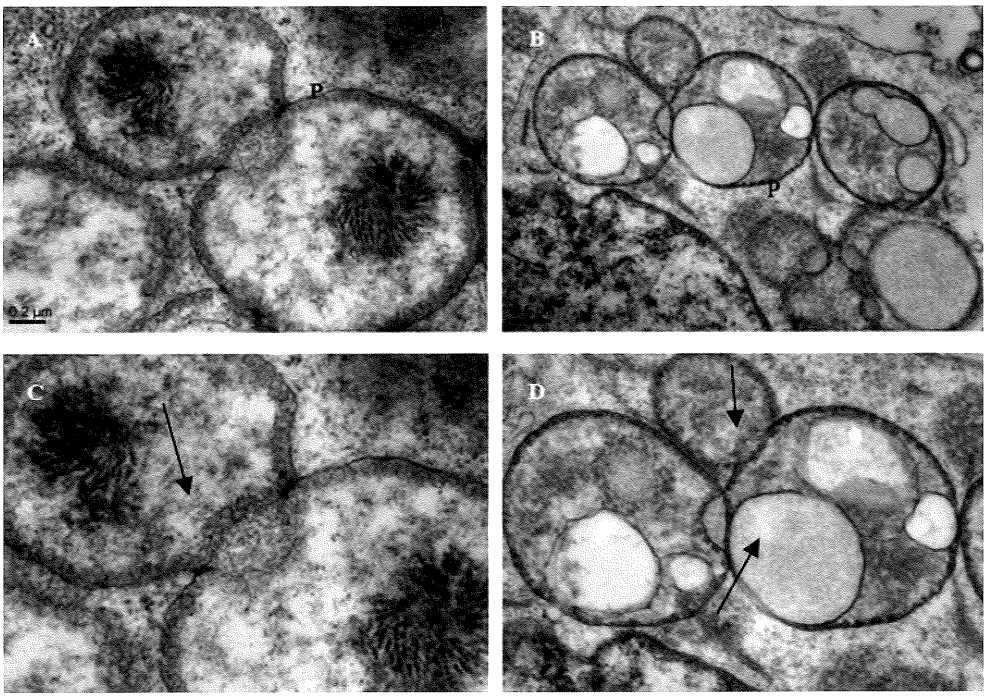

Figure 2.Multivesicular bodies found in the MCMV infected maize leaves (A) Multiple bubbles are found around the edge of the peroxidase with a diameter of 50nm as indicated by arrows in (C); (B) Another type of Multivesicular bodies are detected with the small bubbles around the edge of the peroxidase and bigger bubbles with amorphous materials in the internal as indicated by arrows (D). Peroxidase is marked by P.

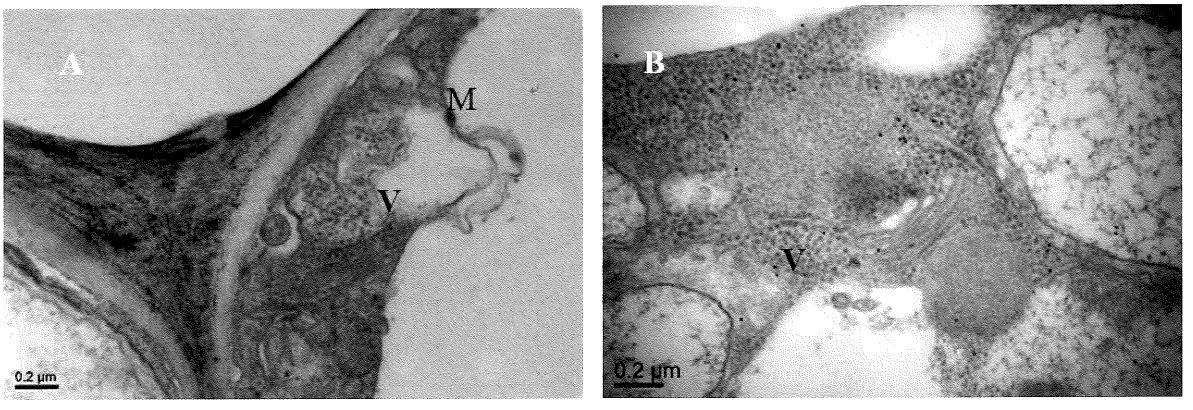

Figure 3.Possible mechanism of the assembly of MCMV virions. (A) Proliferation of membranes is detected in the cytoplasm and complete MCMV virions are found to be packaged into membrane structures (B) Numerous virions are scattered in the cytoplasm without being contained in vesicles. Virions are marked by V and membrane structures are marked by M.

B-O-11

THE DIAGNOSTIC VALUE OF ELECTRON MICROSCOPE IN MUSCULAR DISORDERS

Hongjun Ma[1], Jing Hu[2], Qi Bing[2] , Li Men[1], Guisheng Liu[1]

[1]Electron microscope center of Hebei Medical University, Shijiazhuang

[2]Department of Neuromuscular disease, The 3rd hospital of Hebei Medical University, Shijiazhuang

Objective: To investigate the ultrastructural changes of the classification and differential diagnosis of skeletal muscle disease, and summarizes the characteristics of ultrapathological changes in various types of skeletal muscle disease by electron microscopy .

Methods: To collecte the pathological data of light microscopy and electron microscopy of patients who with various types of skeletal muscle myopathy disease and visited the department of neuromuscular disease of the 3rd Hospital of Hebei Medical University 2005-2012 retrospectively, analyzed and compared the ultrapathological changes.

Results: 1. Congenital myopathy had characteristic pathological changes in cell structure and morphology in both light and electron microscopy, can be identified typing diagnosis and screen for further gene sequencing; 2. Metabolic myopathy manifested glycogen of lipid elements abnormal in the light microscope, combined with clinical information to diagnose the initial classification, electron microscopy revealed ultrastructural abnormalities contribute to typing diagnosis, Diagnosis was confirmed by genetic testing.

Conclusions: 1. Light microscopy and electron microscopy is the basis tool of genetic skeletal disorders typing diagnosis and differential diagnosis; 2. Electron microscopy ultrapathological structural abnormalities found in the sarcoplasm can define some type of myopathy such as congenital myopathy, metabolic myopathy, etc; 3. Ultrapathological analysis is important in pathological pathogenesis of skeletal disease research; 4. Ultrapathological features help guide the gene sequencing to determine the final diagnosis.

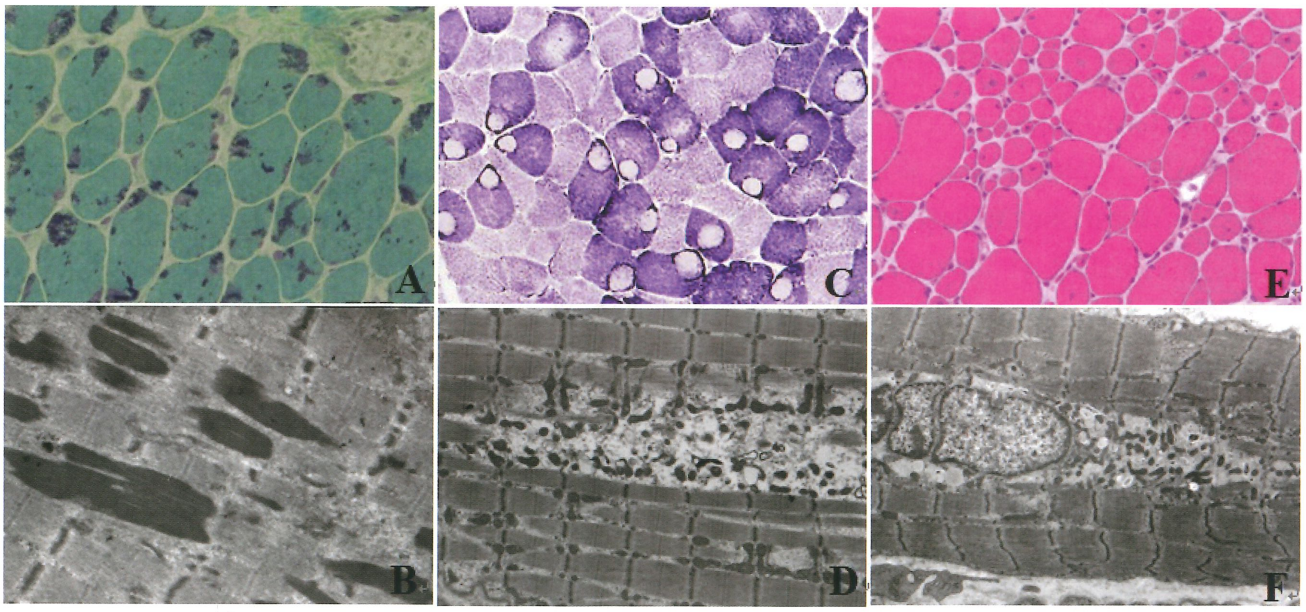

Fig.1: Congenital myopathy: A-B（nemaline myopathy）C-D（central core disease）E-F（centronucleus myopthy）A：MGT×200；C：NADH×200；E：HE×200；B：×10000，D、F：×8000.

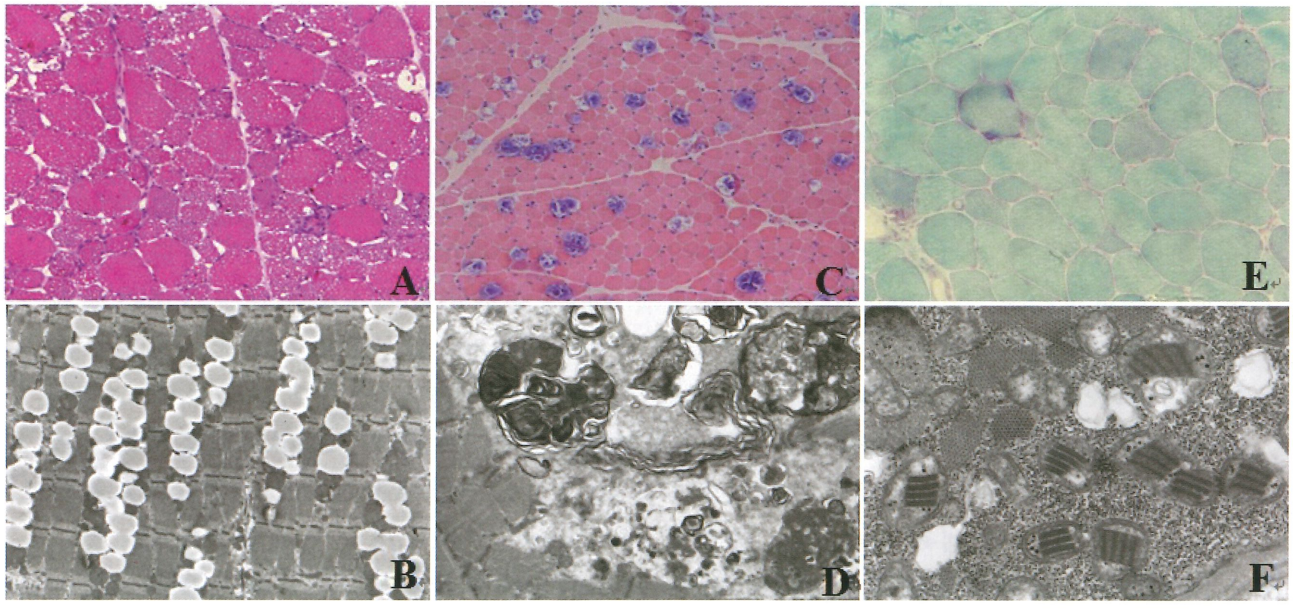

Fig.2: Metabolic myopathy: A-B（metabolic myopathy）C-D（Pompe disease）E-F（metabolic myopathy）A、C：HE×100；E：MGT×200；B：×6000；D、F：×20000.

B-O-12

利用螢光顯微鏡活體研究魚類組織形成的分子機制及其應用

[1]HUANG, Chiu-Ju (黃秋茹), [2]HO, Yi-Lwun (何奕倫), [2]HSIEH, Fong-Jou (謝豐舟) [3]CHEN, Ying-Hsin (陳穎信), [4]SUN, Chi-Kuang (孫啟光) and [1]TSAI, Huai-Jen(蔡懷楨)

[1] 台大生科院分子細胞所 [2] 台大醫學院臨床醫學所 [3] 三軍總醫院 [4] 台大電資院光電所

魚類是所有動物中最早擁有心臟器官的脊椎動物。而斑馬魚最近成為用來研究心臟病最好的模式魚種。本實驗室是全世界第一個成功建立了整個心臟可以被綠色螢光活性標識的轉殖斑馬魚品系 Tg(cmlc2:GFPP)[1]。有了這種繼代穩定遺傳的轉殖魚品系，再配合螢光顯微鏡就可以動態追蹤心臟發育以解析不同發育階段的功能性基因及蛋白質；尋找心臟發育有關的新基因及心臟發育的分子機制；和建立類似人類心臟病的模式動物及藥物的篩選及開發。例如本人與台大醫院臨床醫學所謝豐舟教授及心臟科何奕倫醫師合作，建立一種斑馬魚類心臟的分子影像、心室收縮功能測定及心跳動圖[2]，接著又成功地建立可以隨時(於胚胎、幼魚或成魚時期)誘導降低 cardiac troponin C 蛋白而產生心律不整之 dilated cardiomyopathy 的魚個體，這種 defective phenotype 非常類似人類 incomplete atrioventricular blocking disease 之心臟疾病[3]。其次，本人實驗室也與三軍總醫院陳穎信醫師合作研究 Amiodarone 對胚胎發育的影響。Amiodarone 為第三型抗心律不整藥物，用以舒緩多種心律不整症狀，但對初期懷孕婦女之胎兒影響仍未知。為了解懷孕婦女誤用藥物對胎兒發育的影響，因此選用斑馬魚作為模式物種。發現 Amiodarone 浸泡的斑馬魚胚胎心臟會血液逆流。為了能不傷害魚體，能在最真實的狀況下長期觀察斑馬魚胚胎心臟及瓣膜的發育，本實驗室與台大電機系光電所孫啟光教授開發了以魚類胚胎為活体的分子影像技術，即使用倍頻光學顯微術(Harmonic Optical Microscopy)搭配雙光子螢光顯微術(Two-Photon Fluorescence Microscopy)在活體直接觀察基因轉殖斑馬魚 Tg(cmlc2:HcRFP)胚胎時期心臟瓣膜的形成而不必犧牲標本進行極麻煩的瓣膜切片。在此系統中，利用雷射激發 myocardial cell 的 HcRed 紅螢光，可以很清楚的將內層黃色的 endocardial cell 區分開來。Amiodarone 處理的斑馬魚胚胎，endocardial cell 在 48 hpf 與 control 組相似，皆屬於單層的鱗狀細胞; 但到了 72 hpf，形成了較小較不完整的 endocushion，細胞數明顯較少，與 control 組充滿細胞的 endocushion 大不相同；另外，也沒有看到 endocushion 的生長，AVC endocardial cell 仍為單層的細胞。直刊死亡前的 87 hpf 都無法觀察到 endocushion 細胞的聚集與瓣膜的生長。進一步地，我們瞭解到 Amiodarone 會造成異位性表現 *versican*，而抑制 *snai1b* 的表現，接著造成 *VE-cadherin* 的過量表現，最後使得瓣膜無法進行 invagination 而產生瓣膜缺失[4]。很明顯地，利用 Harmonic Optical Microscopy 和 Two-Photon Fluorescence Microscopy 再搭配轉殖斑馬魚品系的遺伝特質就可以很清楚地觀察斑馬魚心臟瓣膜發育的各個時期，非常適合用來進行斑馬魚心臟瓣膜發育的研究。

References

1. C. J. Huang, C. T. Tu, C. D. Hsiao, F. J. Hsieh and H. J. Tsai. *Dev. Dynamics* (2003) 228:30.
2. Y. L. Ho, Y. H. Lin, I. J. Tsai, F. J. Hsieh and H. J. Tsai. (2007) *J. Formosa Med. Assoc.* 106:181.
3. Y. L. Ho, Y. H. Lin, W. Y. Tsai, F. J. Hsieh and H. J. Tsai. (2009) *Circ. J.* 73:1691.
4. Y. H. Chen, R. J. Hsu, T. Y. Chen, Y. K. Hunag, H. C. Lee, S. C. Hu, H. J. Harn, J. R. Jeng, C. K. Sun, S. Z. Lin and H. J. Tsai. (2012) *Reprod. Toxicol.* 33: 233.

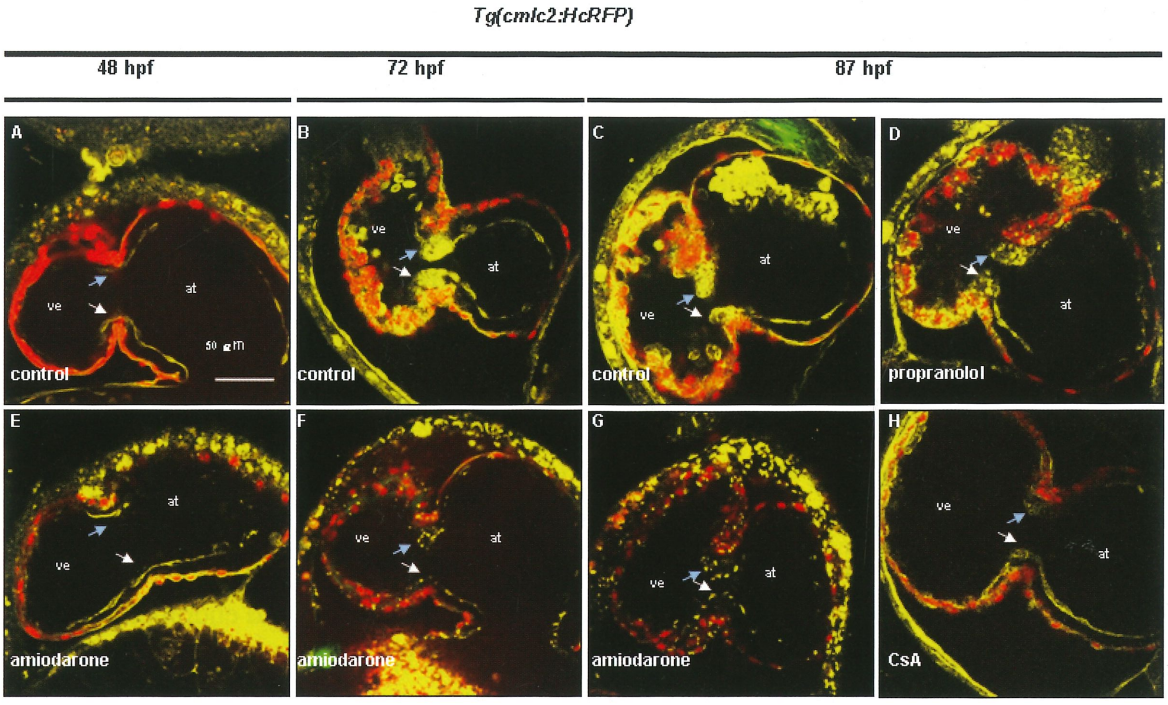

B-O-13

THE PROTECTIVE EFFECTS OF ENDOTHELIAL PROGENITOR CELLS FROM WHARTON'S JELLY IN HUMAN UMBILICAL CORD ON VASCULAR DISEASES

[1]LIANG, Chan-Jung (梁展榮), [1]WANG, Shu-Huei(王淑慧), [1]SHEN, Wen-Ching(沈紋君) and [1]CHEN, Yuh-Lien(陳玉怜)

[1] Department of Anatomy and Cell Biology, College of Medicine, National Taiwan University, Taipei, Taiwan

The number of endothelial progenitor cells (EPCs) that can be obtained from adult bone marrow and peripheral blood to treat cardiovascular diseases is limited. The goal was to examine the endothelial potential of Wharton jelly in human umbilical cord (WJ)-derived stem cells and evaluate their potential to affect neointimal formation after vascular injury. Mesenchymal cells (MCs) were isolated from WJ and cultured in endothelial growth medium. Differentiation into endothelial progenitor cells (WJ-EPCs) was demonstrated by incorporation of acetylated low-density lipoprotein and expression of the endothelial-specific markers. Transplantation of WJ-EPCs into wire-injured femoral arteries in mice led to rapid reendothelialization. The neointima/media area ratio was reduced and strong expression of pigment epithelium-derived factor (PEDF) compared to saline-or MC- treated mice at 4 weeks after injury. In addition, we evaluated the effects of WJ-EPC transplantation on hind limb injury caused by femoral artery ligation in mice with streptozotocin (STZ)-induced diabetes. We found that the ischemic hind limb in mice with STZ-induced diabetes showed decreased blood flow and capillary density and increased apoptosis of skeletal muscle and endothelial cells and that these effects were significantly inhibited by injection of WJ-EPCs. In addition, HIF-1α and IL-8 were highly expressed in transplanted WJ-EPCs in the ischemic skeletal tissues and were present at high levels in hypoxia-treated cultured WJ-EPCs. HIF-1α and IL-8 increase migration and vascular tube formation of EPCs. In the present study, we demonstrated the presence of a cell population within WJ that has the potential to differentiate into WJ-EPCs. Transplantation of WJ-EPCs may play a crucial role in reestablishing endothelial integrity in injured vessels, thereby inhibiting neointimal hyperplasia. In addition, transplantation of these WJ-EPCs represents an innovative therapeutic strategy for treating diabetic ischemic tissues. These findings have implications for a novel and practical cell-based therapy for vascular diseases.

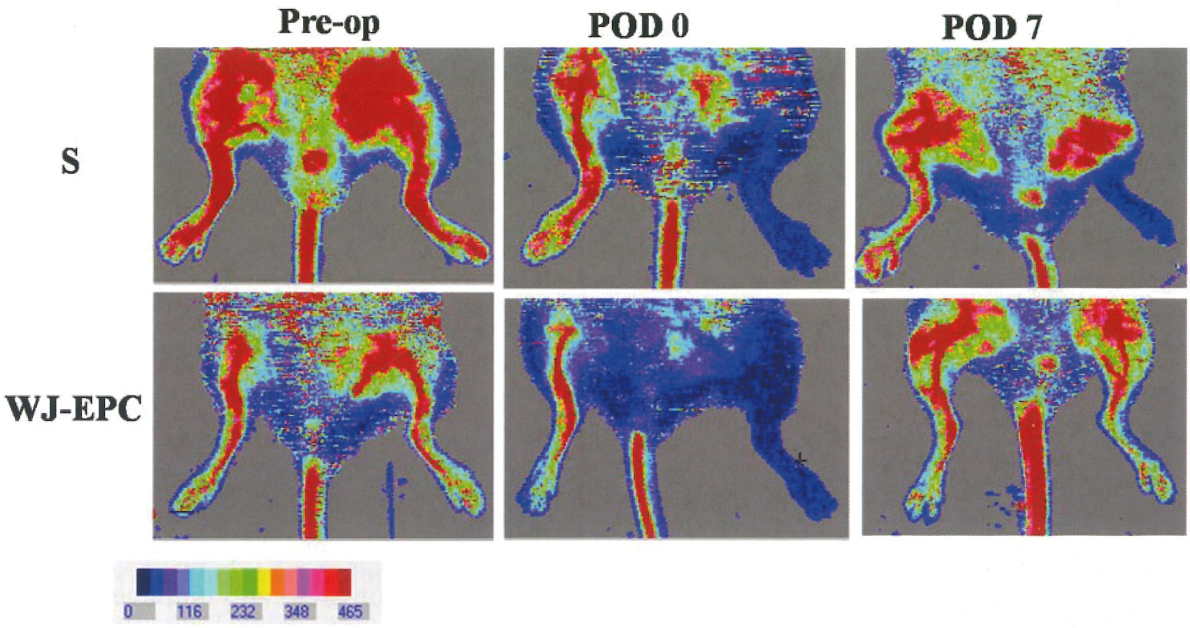

Figure 1. Wharton jelly-derived endothelial progenitor cell (WJ-EPC) transplantation improves blood flow in hind limb ischemia in diabetic mice. STZ-injected diabetic mice underwent left femoral artery ligation and the diabetic mice were injected intramuscularly with saline (S) or WJ-EPC (WJ-EPC). Laser Doppler perfusion images were taken before surgery (Pre-op) and immediately after surgery (POD 0) or at 7 days after surgery (POD 7).

B-O-14

THE ULTRASTRUCTURAL CHANGES OF CORPORA LUTEA AND LUTEAL CELLS DURING STEROIDOGENESIS IN GOATS

[1]Jiang, Yi-Fan (江逸凡), [2]Cheng, Chiung-Hsiang (鄭穹翔),[1]Wu, Leang-Shin (吳兩新) [1]Chiu, Chih-Hsien (邱智賢)

[1]Department of Animal Science and Technology, National Taiwan University, Taipei, Taiwan
[2]School of Veterinary Medicine, National Taiwan University, Taipei, Taiwan

Corpora lutea (CLs) are transient progesterone(P_4)-secreting glands necessary for reproduction in mammals. In present studies, the experiments were designed to investigate the developments of goat CLs in various stages. Our analyses revealed proper patterned capillaries in middle CLs, while shrunken luteal cells, expanding regression areas and immune cells with lobed nuclei were identified in the late. These shrunken cells showed the figures of both autophagy and apoptosis, indicating that programmed cell death might involve CL regression. The active endothelial cells suggested activated angiogenesis in early CLs. The stabilized capillaries and the accumulation of extracellular matrix (ECM) fibers indicated the absence of angiogenesis in the late. The large luteal cells (LLCs) assembled to form microvillar channels on their surface. With globular structures discerned in the channels, the selective uptake pathway for cholesterol utilization could be significant in goat LLCs. In the cytoplasm, secretion granules and the mitochondria-associated membrane (MAM) were recognized throughout the cycles, while some swollen cisternal ERs were identified only in the early and middle stages. The mitochondria with tubular cristae increased in early and middle LLCs. However, the mitochondria swelled and the cristae shifted to lamellar type in the late, suggesting that plasticity of organelles could contribute to steroidogenesis in goat CLs. To make the connection between ultrastructure and steriodogenesis, we observed the ultrastructure of a caprine luteal cell line, CLC-D, under steroidogenic treatments. And the morphological shift of mitochondria from lamellar to tubular cristae after the treatments was observed. In conclusion, our results suggested the angiogenesis in early CLs and the programmed cell death in the late. The luteal cellular ultrastructures vary depending on stages, and the plasticity of mitochondria might involve steroidogenesis. However, further connections among cellular functions, structures and gene expressions remain to be explored.

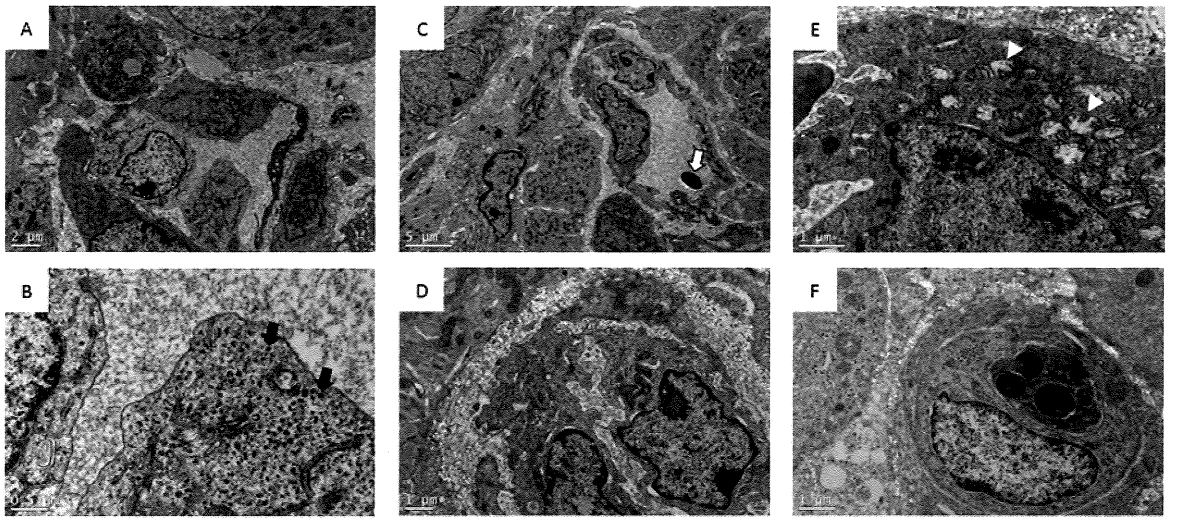

Figure 1. The morphology of capillaries in goat CL during the estrous cycle. A: A capillary on Day 4, with dark stained ERs observed in the endothelia cells. **B**: The cytoplasm of an endothelial cell under a high magnification from **A**. Black arrow: Ribosomes in the cytoplasm. **C**: A capillary on Day 14, with an erythrocyte observed in the vessel (white arrow). **D**: A high magnification view of **C**. The cytoplasm of endothelia cells shows homogenous staining. **E**: An endothelial cell on Day 8, with some swollen mitochondria (white arrow heads). **F:** A capillary on Day 16, with the assembly of endothelia cells circularly arranged in closer proximity.

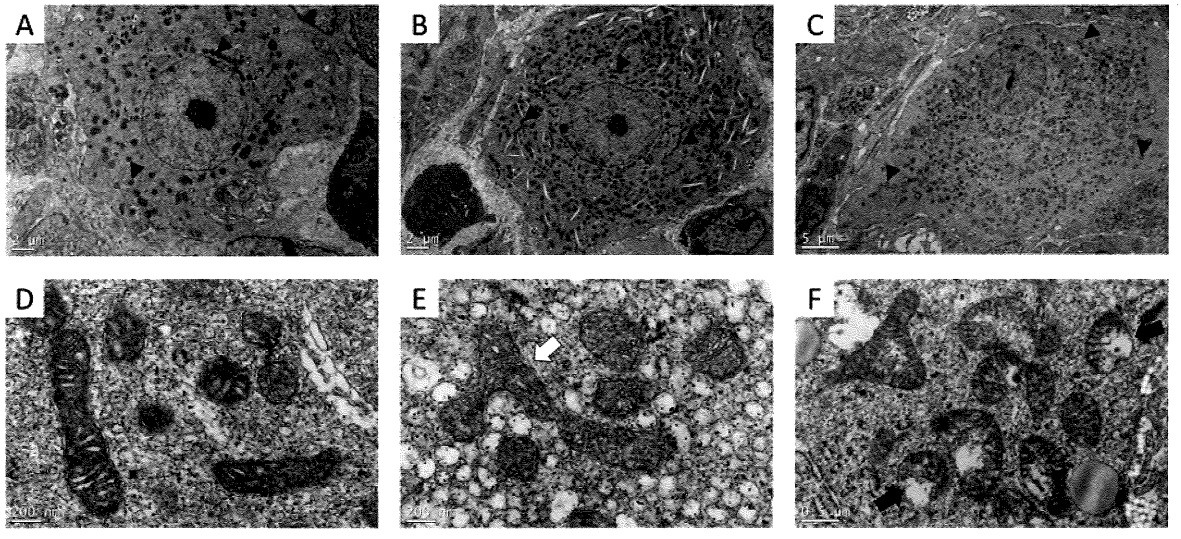

Figure 2. The distribution of mitochondria and the morphological changes in goat LLCs during the cycles. A-C: LLCs on Days 4, 14, and 16, respectively, with the mitochondria discernible in its cytoplasm (black arrow heads). **D**: The mitochondria on Day 14. Under high magnifications, mitochondria show tubular cristae and dark-stained matrixes. **E**: A branched mitochondrion on Day 12 (the white arrow). **F**: The swollen matrixes and lamellar cristae in mitochondria on Day 16 (black arrows).

B-O-15

APPLICATION OF FREEZING TECHNIQUES IN PLANT SAMPLE PREPARATION OF ELECTRON MICROSCOPY

Hsu, Chia-Mei, Chou, Yi-Chia, and Jane, Wann-Neng (簡萬能)

Institute of Plant and Microbial Biology, Academia Sinica (中央研究院植物暨微生物學研究所) 128, Academia Road, Sec 2, Nankang, 11529 Taipei, Taiwan

In general, sample preparation of scanning electron microscopy must undergo chemical fixation, washing, dehydration, critical point drying and coating. Because the procedure of sample preparation is complex, it need much time (over 24 hours). The most limitation of this conventional processing for plant sample is usually shrinking and distorted (Fig. 1).

Comparing to conventional SEM, sample preparation of cryo-SEM is easy and processes rapidly. However, the processing must be at low temperature. The fresh sample loading on stub is frozen by liquid nitrogen or high pressure freezer, and then transfers to preparation chamber. After sublimation (etching) or/and fracturing, the sample should be coating and then transfer to cryo stage of SEM chamber. The advantages of cryo-SEM are including: sample viewed in its fully hydrated state (Fig. 2) and like live; high resolution capability; soluble materials retained; less relocation of highly diffusable elements; little mechanical damage; no exposure to toxic reagents; extra information obtained by fracturing (Figs. 3 & 4), etc.

Sample preparation of transmission electron microscopy must generally undergo chemical fixation, washing, dehydration, infiltration, polymerization, trimming, sectioning and staining. Protein denature, loss (Fig. 5) and relocation of cellular contents are occurred in this process, so we may get many artifact images. In biological sample preparation, cryo fixation is better than chemical fixation. Cryo fixation can preserve good ultrastructure (Fig. 6) and biological signals. Freeze substitution is ice substituted by organic solvents at low temperature, and can decrease displacement and loss of cellular contents including soluble elements.

High pressure freezing combined with freeze substitution is the best sample preparation of transmission electron microscopy using tissue sectioning. The good frozen thickness of high pressure freezing is over 400μm. The inner structure of plant tissue, including vascular tissue of root (Fig. 7), mesophyll of leaf, tapetum and pollen grains of anther, ovules in ovary, can be observed. We can get not only more sigals but also good ultrastructure (Fig. 8), when we do immunolabeling.

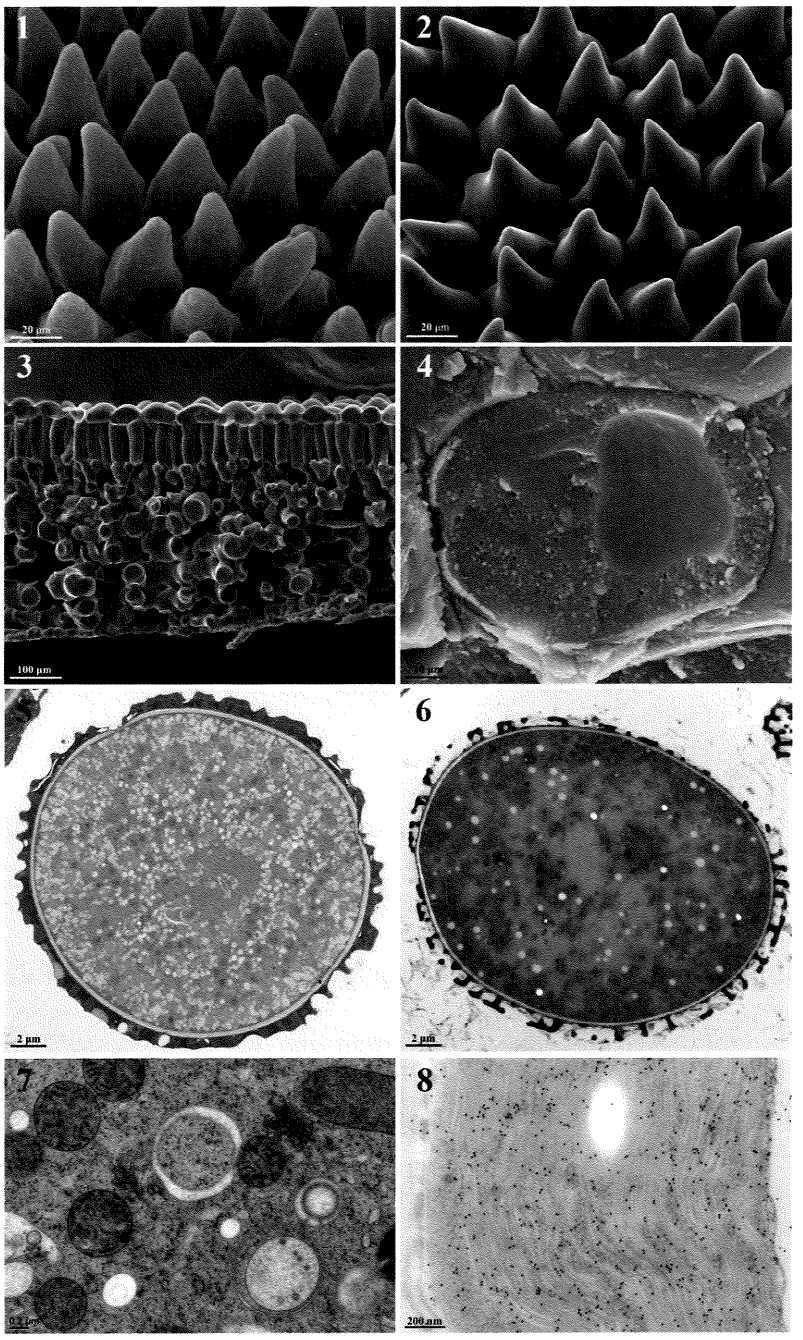

Fig. 1. SEM image. Figs. 2-4. Cryo-SEM image. Fig. 1. Upper epidermis of petal in *Mazus fauriei* using chemical fixation and CPD. Fig. 2. Upper epidermis of petal in *Mazus fauriei* using cryo fixation. Fig. 3. Cross section of leaf in *Torenia fournieri* using cryo fixation and fracturing. Fig. 4. Section of pollen grain in *Zea mays* using high pressure freezing and fracturing. Fig. 5-8. TEM image. Fig. 5. Chemical fixation. Figs. 6-8. High pressure freezing and freeze substitution. Fig. 5. Pollen grain of *Arabidopsis thaliana*.n Fig. 6. Pollen grain of *Arabidopsis thaliana*. Spurr's resin is used. Fig. 7. Tracheary element of root vascular tissue in *Arabidopsis thaliana*. Spurr's resin is used. Fig. 8. Chloroplast of leaf in *Nicotiana tabacum* transgenic plant. LR Gold resin is used and immunolabeling is anti-actin.

B-O-16

TRICHOME MORPHOLOGY AND ESSENTIAL OILS REPELLENCY OF *Crossostephium chinense, Plectranthus amboinicia and Vitex rotundifolia*

Shiang-Jiuun Chen[1] (陳香君), Che-yu Shiu[1] (許哲瑜), Ling-long Kuo-Huang[1] (黃玲瓏), Hsiang-Ting Huang[2] (黃祥庭) and Rong-Nan Huang[2] (黃榮南)

[1] Institute of Ecology and Evolutionary Biology, National Taiwan University, Taipei 10617
[2] Department of Entomology, National Taiwan University, Taipei 10617

The epidermal protuberances of leaf surface trichomes (leaf hairs) have long been considered a plant's first line of defense. They function as physical (morphology) or chemical (secretion) barriers against attaching herbivoures and pathogens, as well as protecting plants against UV-B radiation, water loss or heat stress. In addition to repellence to pests, the trichome secretion (essential oil, EO) also exhibits therapeutic function. Previous studies mainly focused on the content of essential oil and their application (repellent and therapeutic), detailed knowledge of the secreted structure, trichome, is still lacking. Therefore, these studies aim to dissect the anatomical structure of trichomes from three common aroma plants, *Crossostephium chinense*, *Plectranthus amboinicia and Vitex rotundifolia* in related to their repellency of essential oils toward cabbage moth (*Plutella xylostella* L.) and two-spotted spider mite (*Tetranychus urticae* Koch). The results show that the leaves of *P. amboinica* are covered with numerous capitate trichomes with longer stalk cell near midrib at lower epidermis, and shorter stalk cell are widely distributed on upper epidermis. In contrast, there was only the later covering on the leaves of *C. chinense and V. rotundifolia*. The existence of both the phenolic compounds and polysaccharides in the three herbs are evidenced by histochemical tests. The deterrent efficiency of 0.01% EO from three herbals to cabbage moth and two-spotted mite were 45.61% and 36.72% (*P. amboinicus*), 38.85% and 39.18% (*V. rotundifolia*), 28.84% and 19.53% (*C.chinense*) respectively. These three herbal are easy to plant, cultivate

and further dissection of the morphological structure and the deterrence of three herbs could facilitate the development of EO as alternatives for synthetic pesticides.

References

1. P. Thanomchat, Y. Paopun, C. Kongpakdee, Structural Investigation of Trichomes and Stomata of *Plectranthus amboinicus* (Lour.) Spreng. *Journal of the Microscopy Society of Thailand* (2011) 4, 65-69.
2. P. L.Valverde, J. Fornoni, and J. Nunez-Farfan, Defensive role of leaf trichomes in resistance to herbivorous insects in Datura stramonium. *Journal of Evolutionary Biology* (2001) 14, 424-432.

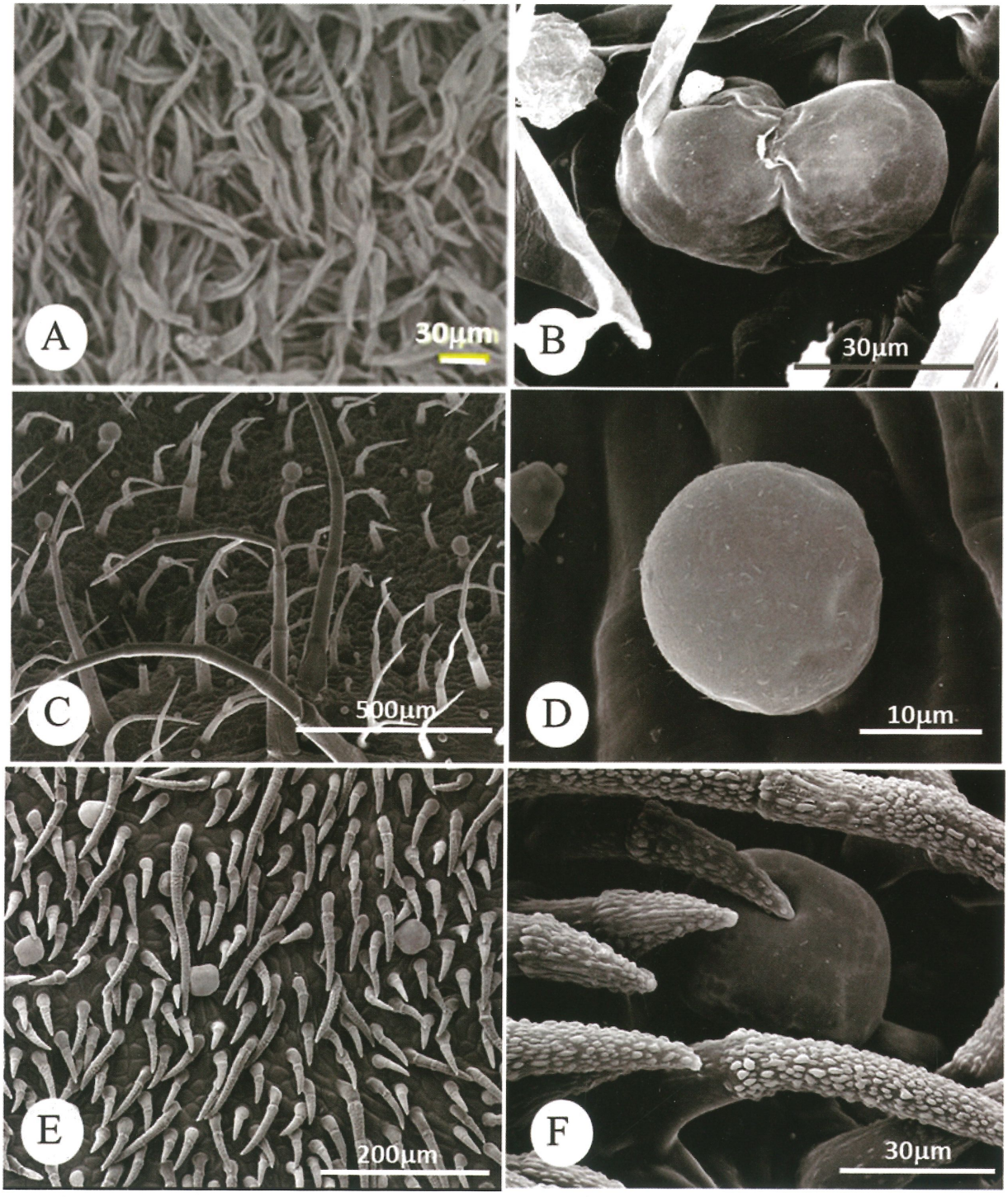

SEM micrographs show the trichomes morphology of three herbs. Figure A & B, *Crossostephium chinense.* (A) High density of T-type trichome at abaxial side of leaf. (B) Capitate glandular trichome with 2-head cell. Figure C & D, *Plectranthus amboinicia.* (C) 2 types non-glandular trichomes and 2 types glandular on abaxial side of leaf. (D) Glandular trichome with short stalk. Figure E & F, *Vitex rotundifolia.* (E) Dimorphic trichomes at abaxial side of leaf. (F) Non-glandular trichomes with small warts on the surface and capitate glandular trichomes distribute sparsely.

B-O-17

DISTRIBUTION PATTERNS OF SMALL SUGARS IN DEVELOPING SEEDS OF MAIZE

Chi-Chih Wu and Chih-Hua Tsou

Institute of Plant and Microbial Biology, Academia Sinica, Taipei

There is a long-term need to examine in situ localization and distribution of molecules, such as small sugars, that are related to cellular activities at subcellular or cellular level. These sugars, including glucose, fructose and sucrose, are suggested to be highly involved in many metabolic pathways and physiological activities directly or indirectly, especially during angiosperm seed development. Unfortunately, due to the high solubility and small molecular weight of these sugars, most regular processes of sample preparations likely result in the alternation of distribution of these small sugars. Here, we report a process to investigate in situ distribution patterns of small sugars in developing maize seeds.

To eliminate potential artificial effects of chemical solutions, we applied cryo-fixation with liquid nitrogen to fix whole maize seeds, and then embedded seeds with the optimal cutting temperature (OCT) compound. Subsequently, embedded maize seeds were cut at the thickness of 16 micrometer by a cryo-microtome. We then isolated homogenous tissues including starchy endosperm, milky endosperm, embryo, basal endosperm transfer layer (BETL) and placenta-chalazal cells (P-C) using a laser capture microdissection microscope. Small sugars were extracted from dissected samples and quantified by using a high performance anion exchange chromatographer with pulsed amperometric dectector (HPAEC-PAD). Furthermore, in order to map the fine distribution patters of small sugars at the subcellular level, we used a matrix-assisted laser desorption/ionization mass spectrometer (MALDI) to scan and analyze sections of developing maize seeds.

By using an HPAEC-PAD to quantify small sugars in different homogenous tissues of maize seeds, concentrations of small sugars differ in different tissue and relative ratio of small sugars changes over developmental stages. It is suggested that the concentration of small sugars is associated with physiological activities of different tissues of maize seeds.

Interestingly, the uneven ratio of glucose to fructose may be duo to different metabolic rates of these two monosaccharaides in living cells. Additionally, concentration of small sugars changes dramatically within a narrow range. In summary, our preliminary results fit the prediction of Shannon's hypothesis about the distribution patterns of small sugars in developing maize seeds. The outcome also provides the first fine distribution of small sugars in maize seeds with less artificial disturbance.

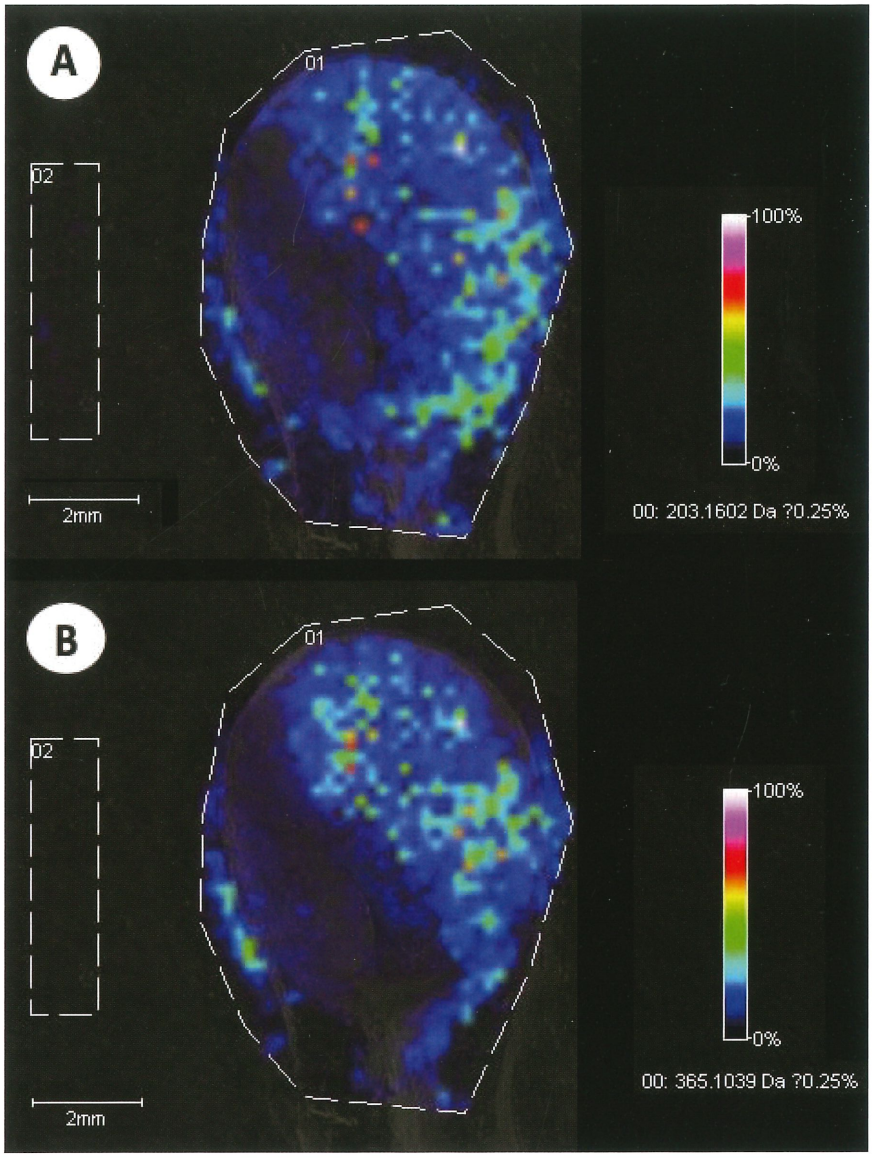

Figure1. MALDI-images of the longitudinal section of a B73 maize seed at 22 days after pollination. (A) Distribution and relative intensity of glucose (m/z+ = 203) (B) Distribution and relative intensity of sucrose (m/z+) = 365. The pattern of glucose is different from that of sucrose, especially in the area of BETL and P-C, which is consistent with the activity of invertase. (The region of the Number 1 is the scanning area of a maize seed; the region of the Number 2 is the canning area of a background for a control; the width of a laser spot is 100 micrometer; the walking distance of a laser spot is 200 micrometer)

B-O-18

14-3-3 通過 NFL 頭部結構域的相互作用調控神經絲的組裝

陳建國

北京大學生命科學學院,北京 100871

神經絲是由 NFL,NFM 和 NFH 三種蛋白組裝而成異源多聚體。這種直徑為 10nm 的絲狀結構是神經細胞骨架的主要成分,在細胞極性化形態結構和功能的維持、細胞器及生物大分子的定位等方面發揮重要作用。人類的一些遺傳性疾病,如人腓骨肌萎縮症(Charcot-Marie-Tooth disease,CMT)也與神經絲蛋白基因的變異相關。CMT 的臨床表現為四肢肌無力和萎縮並伴隨感覺喪失。NFL 突變引起 CMT 的機制並不清楚。本文從 14-3-3 與 NFL 的相互作用入手,闡明 14-3-3 對神經絲組裝的調控作用,以及編碼 NFL 基因一些位點的突變與 CMT 的關係。 哺乳動物細胞共編碼表達 7 種 14-3-3 蛋白,其中一些類型的 14-3-3 蛋白,如 14-3-3γ 等在大腦中的含量非常豐富。通過 GST- pull down、免疫共沉澱以及免疫螢光標記等方法證明了 7 種 14-3-3 蛋白都能與 NFL 相互作用,其中 14-3-3γ 和 NFL 的相互作用最強,而且這種相互作用不依賴于其它中間絲蛋白。通過 NFL 缺失突變體和磷脂酶抑制劑處理結果顯示 14-3-3 特異性地與磷酸化的 NFL 頭部結構域結合。進一步對 NFL 的頭部結構域 Ser 磷酸化位點進行突變分析的結果顯示,14-3-3 與 NFL 頭部結構域的相互作用與多個磷酸化位點相關,其中 Ser43,Ser55 位點磷酸化尤為重要,而且受 PKA 激酶的調節。螢光漂白恢復實驗顯示 14-3-3 能夠促進 NFL 動態交換,過表達 14-3-3 會引起 NFL/NFM 共組裝而成的神經絲解聚,抑制 14-3-3 的結合則導致 NFL 突變體異常聚集。由此可見,14-3-3 對神經絲的組裝、以及纖維和細胞質基質中亞單位的動態交換具有重要調節作用。人類 CMT 病人 NFL 的三種突變體 P8Q,P8L 和 P22S 明顯影響與 14-3-3 的結合,並導致 NFL 突變體在細胞質內異常聚集,影響神經絲的組裝,而過表達 14-3-3 能減少 NFL 突變體的聚集,可能會對 CMT 有一定緩解作用。 綜上所述,14-3-3 作為 NFL 相互作用蛋白,在調節 NFL 的組裝神經絲蛋白亞單位的交換,防止 NFL 異常聚集等方面發揮作用,這些結果有望為人類 CMT 的治療提供新的靶點。

B-O-19

新中心體蛋白 LRRC45 的功能分析

滕俊琳

北京大學生命科學學院,北京 100871

中心體由中心粒和中心粒周圍物質(PCM)組成,是動物細胞中最主要的微管組織中心。在間期細胞中,兩個中心粒間存在一種鬆散的蛋白連接體,使其不會相互分開,這保證了細胞中只有一個微管組織中心存在。連接體蛋白在 G2 期後期會被 Nek2A 等激酶磷酸化,導致中心體間連接逐漸減弱。核膜破裂後,完全解除連接的兩個中心體在 Eg5 的作用下移向兩極,參與紡錘體的組裝。然而,有關間期細胞中心粒間蛋白連接體的組分和動態行為並不清楚。我們分析了中心體蛋白 LRRC45 在細胞週期中的功能。LRRC45 全長有 670 個氨基酸組成,其 N 端有 6 個富含亮氨酸的重複(leucine rich repeat,LRR)結構域,在 C 端含有一個較長的 coiled-coil 結構域。免疫螢光和免疫電鏡觀察結果顯示 LRRC45 主要定位於中心粒近端及中心粒之間連接處。過表達 LRRC45 全長或者其 C-端能在細胞質內組裝成絲狀結構,該蛋白的中心體定位依賴于其 C 端的 coiled-coil 結構域。電鏡觀察結果顯示 LRRC45 與中心體連接蛋白 rootletin 形成的纖維結構十分類似,與 rootletin 一樣,該蛋白在中心體近端的定位依賴于 C-Nap1。通過 RNA 干涉實驗敲低 LRRC45 在 U2OS 細胞中的表達量不影響細胞週期及細胞增殖,但會造成間期細胞中心體的提前分離。質譜分析和體外實驗的結果顯示在有絲分裂前 LRRC45 的 S335 和 S661 位點可以被 Nek2A 磷酸化,其結果是中心粒間的蛋白質絲狀連接解體,中心體移向兩極。因此,LRRC45 作為中心粒間蛋白連接體的重要組分在保障間期細胞微管組織中心的結構方便發揮重要作用。

電子顯微鏡 TEM/SEM 專用耗材

客・製・化・設・備・設・計・服・務

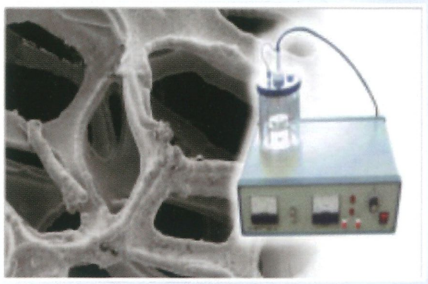

桌上型鍍金機＆濺鍍靶材

TEM 銅網/鎳網/金網/鉬網
TEM 銅環/鎳環/金環/鉬環

單盤研磨拋光機

慢速精密鑽石刀片切割機

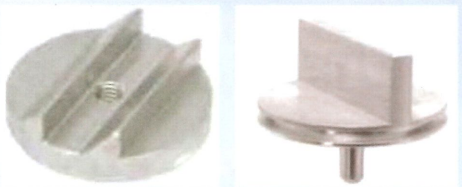

SEM 試片座

導電銅膠帶　導電碳膠帶

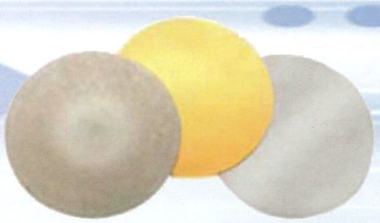

濺鍍機專用濺鍍靶材

薄膜試片盒

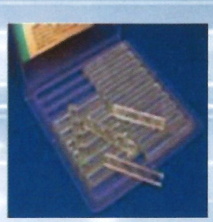

135℃ 熱熔膠

G1膠/AB膠

切割研磨拋光耗材

50格試片保存盒及鑷子

金相顯微鏡

TEM/SEM
試片製作
代測分析 服務

佳佑儀器
有限公司

地址：30091新竹市牛埔東路1-2號13F
電話：(03)530-2385　傳真：(03)530-6186
網址：www.jja.com.tw
E-mail：konica@jja.com.tw

Right results...Real-time

Only Oxford Instruments has the expertise to deliver:

- Large area detectors that deliver outstanding speed and sensitivity
- Algorithms that automatically and accurately identify all the elements
- Process engines that deliver the correct results in real-time...every time

Right results in real-time ...it's what we do!

To see how to obtain the right result visit www.oxford-instruments.com/results

OXFORD INSTRUMENTS

The Business of Science®

2465

電子顯微鏡樣品製備利器

Living up to Life

Leica
MICROSYSTEMS

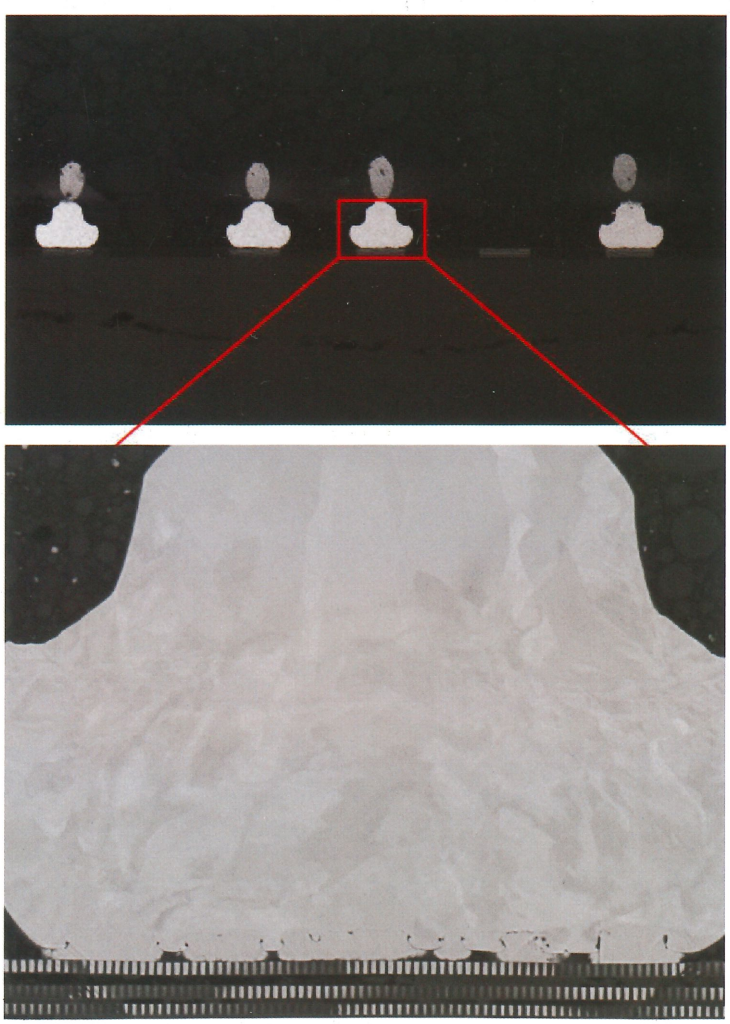

EM Target Preparation at highest quality level

The complete workflow
by Leica Microsystems

LEICA EM TXP
Target Surfacing System

LEICA EM RES102
Ion Beam Milling System

LEICA EM TIC3X
Ion Beam Slope Cutter

台灣總代理 友聯光學有限公司

地址:台北縣汐止市新台五路1段81號4樓之3
電話：02-26980508
E-mail：unionopt@ms11.hinet.net
網址: http://www.unionoptical.com.tw/

超泰科技有限公司
E. B. TECH. CO., LTD

專業的電子顯微鏡,材料分析儀器,耗材,相關設備代理商

Electron Microscope , Analysis instruments, Sample preparation tools

FEI 高低真空場發射掃描電子顯微鏡

FISCHIONE INSTRUMENTS 離子減薄機(Ion Miller)

FEI 場發射掃描/穿透式電子顯微鏡

FISCHIONE INSTRUMENTS 電漿清淨機(Plasma Cleaner)

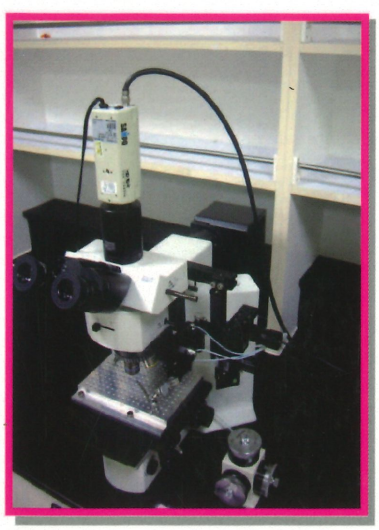

EBT 光學及試片吸針系統

gatan

OXFORD INSTRUMENTS

EDAX advanced microanalysis solutions

BRUKER Innovation with Integrity

ELECTRON MICROSCOPY SCIENCES

電子顯微鏡相關設備耗材

台北市信義區吳興街156巷16弄7號1樓
電話:(02)2733-2576 傳真:(02)2733-5546
Http://www.ebtech.com.tw
E-mail:service@ebtech.com.tw